UNIVERSTITAT POLITÈCNICA DE VALÈNCIA

CENTRO DE INVESTIGACIÓN E INNOVACIÓN EN BIOINGENIERÍA

DEPARTAMENTO DE INGENIERÍA ELECTRÓNICA

PhD Thesis

Development of a novel high resolution and high throughput biosensing technology based on a Monolithic High Fundamental Frequency Quartz Crystal Microbalance (MHFF-QCM). Validation in food control

María del Señor Calero Alcarria

December 2021

Directed by

Yolanda Jiménez Jiménez

Román Fernández Díaz

RESUMEN

La sociedad actual demanda un mayor control en la seguridad y calidad de los alimentos que se consumen. Esta preocupación se ve reflejada en los diferentes planes estatales y europeos de investigación científica, los cuales, plantean la necesidad de innovar y desarrollar nuevas técnicas analíticas que cubran los requerimientos actuales. En el presente documento se aborda el problema de la presencia de residuos químicos en la miel. El origen de los mismos se debe, fundamentalmente, a los tramientos veterinarios con los que se tratan enfermedades y parásitos en las abejas, y a los tratamientos agrícolas con los que las abejas se ponen en contacto cuando recolectan el néctar en cultivos próximos a las colmenas. La Agencia Europea de Seguridad Alimentaria (EFSA) confirma esta realidad al notificar numerosas alertas sanitarias en la miel.

En los últimos años, los métodos de análisis basados en inmunosensores piezoeléctricos se han posicionado como la base de una técnica de cribado muy prometedora, la cual puede ser empleada como técnica complementaria a las clásicas de cromatografía, gracias a su sencillez, rapidez y bajo coste. La tecnología de resonadores High-Fundamental Frequency Quartz Crystal Microbalance with Dissipation (HFF-QCMD) combina la detección directa en tiempo real, alta sensibilidad y selectividad con un fácil manejo y coste reducido en comparación con otras técnicas. Además, está tecnología permite aumentar el rendimiento del análisis mediante el diseño de arrays de resonadores en un mismo sustrato (Monolithic HFF-QCMD). En este documento se presenta el diseño de un array de 24 sensores HFF-QCMD, junto con un cartucho de micro-fluídica que traza diversos microcanales sobre los diferentes elementos sensores, a los que hace llegar la muestra de miel diluida a analizar. El cartucho actúa también como interfaz para realizar la conexión entre el array de resonadores y el instrumento de caracterización de los mismos. Para obtener el máximo partido del array diseñado, se desarrolla un método de medida robusto y fiable que permite elevar la tasa de adquisición de datos para facilitar la toma de registros eléctricos de un elevado número de resonadores de forma simultánea, e incluso en varios armónicos del modo fundamental de resonancia. La gran sensibilidad de la tecnología HFF-QCMD a los eventos bioquímicos a caracterizar se extiende también a otro tipo eventos externos, como son los cambios de temperatura o presión, lo que es necesario minimizar con el fin de reducir el impacto que estas perturbaciones no deseadas

provocan en la estabilidad y fiabilidad de la medida. Con este fin, se desarrolla un algoritmo de procesado de señal basado en la Discrete Transform Wavelet (DTW). Finalmente, todos los desarrollos tecnológicos realizados se validan mediante la implementación de un inmunoensayo para la detección simultánea, en muestras de mieles reales, de residuos químicos de naturaleza química muy diferente, a saber, el fungicida tiabendazol y el antibiótico sulfatiazol.

RESUM

La societat actual demanda un major control en la seguretat i qualitat dels aliments que es consumeixen. Aquesta preocupació es veu reflectida en els diferents plans estatals i europeus d'investigació científica, els quals, plantegen la necessitat d'innovar i desenvolupar noves tècniques analítiques que cobrisquen els requeriments actuals. En el present document s'aborda el problema de la presència de residus químics en la mel. L'origen dels mateixos es deu, fonamentalment, als tractaments veterinaris amb els quals es tracten malalties i paràsits en les abelles, i als tractaments agrícoles amb els quals les abelles es posen en contacte quan recol·lecten el nèctar en cultius pròxims als ruscos. L'Agència Europea de Seguretat Alimentària (EFSA) confirma aquesta realitat notificant nombroses alertes sanitàries en la mel.

En els últims anys, els mètodes d'anàlisis basades en immunosensors piezoelèctrics s'han posicionat com la base d'una tècnica de garbellat molt prometedora, la qual pot ser emprada com a tècnica complementària a les clàssiques de cromatografia, gràcies a la seua senzillesa, rapidesa i baix cost. La tecnologia de ressonadors High-Fundamental Frequency Quartz Crystal Microbalance with Dissipation (HFF-QCMD) combina la detecció directa en temps real, alta sensibilitat i selectivitat amb un fàcil maneig i cost reduït en comparació amb altres tècniques. A més, està tecnologia permet augmentar el rendiment del anàlisi mitjançant el disseny d'arrays de ressonadors en un mateix substrat (Monolithic HFF-QCMD). En aquest document es presenta el disseny d'un array de 24 sensors HFF-QCMD, juntament amb un cartutx de microfluídica que estableix diversos microcanals sobre els diferents elements sensors, als quals fa arribar la mostra de mel diluïda a analitzar. El cartutx actua també com a interfície per a realitzar la connexió entre l'array de ressonadors i l'instrument de caracterització d'aquests. Per a traure el màxim partit a l'array dissenyat, es desenvolupa un mètode de mesura robust i fiable que permet elevar la taxa d'adquisició de dades per a facilitar la presa de registres elèctrics d'un elevat

nombre de ressonadors de manera simultània, i fins i tot en diversos harmònics del mode fonamental de ressonància. La gran sensibilitat de la tecnologia HFF-QCMD als esdeveniments bioquímics a caracteritzar s'estén també a un altre tipus esdeveniments externs, com són els canvis de temperatura o pressió, la qual cosa és necessari minimitzar amb la finalitat de reduir l'impacte que aquestes pertorbacions no desitjades provoquen en l'estabilitat i fiabilitat de la mesura. A aquest efecte, es desenvolupa un algorisme de processament de senyal basat en la Discrete Transform Wavelet (DTW). Finalment, tots els desenvolupaments tecnològics realitzats es validen mitjançant la implementació d'un immunoassaig per a la detecció simultània, en mostres de mel reals, de residus químics de naturalesa química molt diferent, a saber, el fungicida tiabendazol i l'antibiòtic sulfatiazol.

SUMMARY

Currently, society demands greater control over the safety and quality of the food consumed. This concern is reflected in the different states and European plans for scientific research, which establish the necessity to innovate and develop new analytical techniques that meet current requirements. This document addresses the problem of the presence of chemical residues in honey. Its origin is fundamentally due to the veterinary treatments against diseases and parasites in bees, and also to the agricultural treatments with which the bees come into contact when they collect the nectar in crops close to the hives. The European Food Safety Agency (EFSA) confirms this reality by notifying numerous health alerts in honey.

In recent years, analysis methods based on piezoelectric immunosensors have been positioned as the basis of a very promising screening technique, which can be used as a complementary technique to the classic chromatography, thanks to its simplicity, speed and low cost. High-Fundamental Frequency Quartz Crystal Microbalance with Dissipation (HFF-QCMD) resonator technology combines direct real-time detection, high sensitivity and selectivity with easy handling and low cost compared to other techniques. In addition, this technology allows increasing the performance of the analysis through the design of resonator arrays on the same substrate (Monolithic HFF-QCMD). This document presents the design of an array of 24 HFF-QCMD sensors, together with a microfluidic cartridge that establish various microchannels on the different sensor elements, to provide them the diluted honey sample to be analyzed. The cartridge also

acts as an interface to make the connection between the array of resonators and the characterization instrument. To get the most out of the designed array, a robust and reliable measurement method has been developed that allows increasing the data acquisition rate to facilitate electrical parameters readout from a high number of resonators simultaneously, and even in several harmonics of the fundamental resonance mode. The great sensitivity of the HFF-QCMD technology to the biochemical events to be characterized also is extended to other types of external events, such as changes in temperature or pressure, which must be minimized in order to reduce the impact that these unwanted disturbances cause in the stability and reliability of the measurement. To this end, a signal processing algorithm based on the Discrete Transform Wavelet (DTW) is developed. Finally, all the technological developments carried out are validated through the implementation of an immunoassay for the simultaneous detection, in real honey samples, of chemical residues of very different chemical nature, namely, the fungicide thiabendazole and the antibiotic sulfathiazole.

Agradecimientos

Cuando comencé esta aventura no sabía a donde me llevaría o qué supondría y sin duda no hubiera sido lo mismo sin todos aquellos que han estado junto a mí en este camino.

En primer lugar, mi agradecimiento a mis directores de tesis. Gracias porque vuestra confianza en mí ha sido fundamental. Sé que no he podido encontrar mejores maestros, os admiro y sois un espejo en el que mirarse en todos los aspectos. Mi suerte ha sido conoceros.

Yolanda, un ejemplo de constancia y trabajo que imitar. Saber que eras mi directora en cada paso, me daba la seguridad y tranquilidad de que, aunque las cosas no siempre salieran bien podría apoyarme en ti y seguiríamos avanzando. Gracias por tu dedicación y por tu cariño.

Gracias por tu paciencia y por tu forma de enseñar, Román. La energía que transmites nos hace un poco mejores a todos los que te tenemos cerca. Gracias por tu fuerza y alegría que siempre hace que los días malos lo sean un poco menos, y por siempre tener tiempo para escuchar.

A todo el equipo que forma o ha formado parte de AWSensors, gracias. Todos de una forma u otra me habéis ayudado, enseñado y apoyado desde el primer momento que entré por las puertas de la empresa hace 6 años. Se qué compartís la alegría de cerrar esta etapa conmigo.

Agradecer a cada uno de los profesionales que he podido conocer en este tiempo y que me han guiado y ayudado a sacar adelante este trabajo.

Gracias a mis amigos, por hacer vuestras mis alegrías compartiendo nervios, risas y dolores de cabeza. Gracias por todos los abrazos, cerca o lejos, *pero sabes que siempre puedes contar conmigo.*

Y por último mi familia, sin vosotros esto no hubiera sido posible. Todo lo bueno que pueda tener es gracias a vosotros. Gracias por estar siempre, por apoyarme, por enseñarme a seguir intentándolo, por quererme sin condiciones y, sobre todo, por ser el lugar al que siempre volver. Os quiero.

A mis padres y hermanos

Preface

This doctoral thesis focuses on the development of an array of high-fundamental frequency quartz crystal microbalances and its subsequent use and validation as an immunosensor for the detection of pesticides and antibiotics in honey.

The document is structured in six chapters. It begins with a description of the context research, together with the funding sources that have made this research line possible. Due to the multidisciplinary nature of this thesis, Chapter 1 is divided into three main parts. In the first part, honey legal framework is described, as well as the risk that presence of pesticides and antibiotics has for human health. To conclude this first part, the traditional techniques used for the detection of pesticides and antibiotics in honey, together with their advantages and disadvantages, are discussed. This discussion reveals the necessity to propose new complementary or alternative analysis techniques to the classical ones used in honey packing industry. The chapter continues with a state of the art of biosensors, in general, and of piezoelectric immunosensors, in particular, as a suitable technology to achieve key features demanded by food control industry. In particular, Monolithic High-Fundamental Quartz Crystal Microbalance with Dissipation (MHFF-QCMD) is proposed as the technological evolution of HFF-QCM to accomplish them. Finally, chapter concludes with the main challenges to address in terms of optimizing MFHH-QCM design for practical applications. Chapter 2 defines the objectives of the thesis. Chapter 3 includes the results achieved in this research. This chapter is divided into five parts corresponding to five articles published in several scientific journals. The first article includes the development of a monolithic array for biosensing applications, including its design and its experimental characterization. The second article contains the design and validation of a microchannel microfluidic sensing cartridge for bioanalytical applications of MHFF-QCMD. In the third article, a fast method for monitoring shifts in the resonance frequency and dissipation of the resonant elements of a monolithic array in biosensing applications is developed and validated. Fourth article contains a real-time method for improving stability of MHFF-QCMD operation under harsh environmental conditions based on the discrete wavelet transform. Finally, the fifth article contains the validation of the technological developments

achieved in all previous articles through the implementation of a proof of concept for the simultaneous detection of pesticides and antibiotics in honey.

Chapter 4 contains the final conclusions of the thesis and the futures lines of work. Chapter 5 provides information annexed to the results presented. The scientific production derived from the research work accomplished is included in Chapter 6.

Context of research

Food safety and quality is one of the main concerns raised both at national and European level. Food adulteration has legal and economic repercussions and affects public health. As Spain is the most important producer of honey in Europe, the development of novel methods to determine the quality of this product, which improve or complement existing ones, is of great interest. This doctoral thesis is framed within this challenge.

The doctoral thesis has been developed within the research project "Diseño de un biosensor de AND basado en tecnología HFF-QCM para la detección de sustancias adulterantes en miel (AGL2016-77702-R)" of the "Ministerio de Ciencia e Innovación" within its call for grants for R+D+i projects of 2016 "Programa estatal de investigación, desarrollo e innovación orientada a los retos de la Sociedad".

Additionally, the doctoral student of this thesis was awarded a 4-year pre-doctoral research grant funded by "Ministerio de Economía, Industria y Competitividad" (BES-2017-080246).

The development of the research presented in this document has been made possible thanks to the collaboration of three research groups and two private entities:

1. LABMIEL (Laboratory for the quality control of honey and bee products) of the "Instituto Universitario de Ingeniería de Alimentos para el Desarrollo" (IUIAD) from Universitat Politècnica de València. This group cooperates permanently with beekeeping companies in the Valencian Community for several years. Those companies have expressed the need to develop novel techniques that allow to detect the presence of chemical residues, such as pesticides and antibiotics in honey, in a quickly and easily way. This would reduce costs in the analysis tasks. LABMIEL group has long experience in the use of classical chromatographic techniques for the detection of those residues.
2. Biosensors group from the "Centro de Investigación e Innovación en Bioingeniería" (Ci2B) from Universitat Politècnica de València. This group has a long experience in developing high-resolution acoustic sensors, the cells housing them and electronic instrumentation necessary for sensor characterization. From several years, there has been a closely cooperation with Immunotechnology group of Ci2B described below.

3. Immunotechnology group from the “Centro de Investigación e Innovación en Bioingeniería” (Ci2B) from Universitat Politècnica of Valencia. This group has developed the monoclonal antibodies necessary to provide the sensor with the necessary selectivity for the detection of a specific target. In particular, it has developed the biosensor immunoreagents for the detection of one of the chemical compounds used in this work: thiabendazole.
4. AWSensors is a spin-off private company of the Universitat Politècnica de València. The company was founded by some researchers from the Biosensors group with the aim to transfer to society the knowledge and technology developed in its research environment. Currently, the activity of the company primarily geared towards the production and commercialization of high precision instrumentation based on electronic systems for characterization of QCM sensors. Joint activities with the research and development department of the company has made possible the development of a MHFF-QCM array together with the housing cartridge. AWSensors have also provided electronic instrumentation to perform measurements as well as access to the clean room located in its facilities.
5. Quartz Pro Sweden AB private company dedicated to the manufacturing of Quartz Crystals, Crystal Oscillators and QCM sensors. Quartz Pro has hosted the doctoral student to show her the facilities required for the manufacturing of QCM sensors, and to train her in the different processes involved in its fabrication.

INDEX

LIST OF FIGURES

LIST OF TABLES

1. Introduction

Concern for the safety and quality of food consumed by human beings is growing. The EFSA (European Food Safety Authority) has been notified of the presence of hazardous chemical residues in food. There are many foods on which numerous alerts have come up in recent years (oils, milk and dairy, egg, chicken and poultry…). Among all of them, the quality and veracity of honey have aroused great interest due to the numerous health alerts that have occurred. The report of the EFSA about honey highlights and alerts of the chemical residues impact on the health of bees and consequently on honey and pollen consumers. The existence of chemical residues in honey has its origin in agricultural treatments with pesticides, mainly neonicotinoids [1]–[4], with which bees come into contact when collecting nectar but also to veterinary treatments such as acaricides or antibiotics used to treat bee diseases [5]. Its presence in honey has become a public health problem that involves the authorities, the beekeeping sector and the scientific community, making honey one of the foods under exhaustive controls [6]–[8].

There are several widely established and used analytical techniques with honey. The reference technique is High-Performance Liquid Chromatography-Mass Spectrometry/Mass Spectrometry (HPLC-MS/MS). This technique has clearly and well-defined measurement protocols and provides highly reliable and accurate results with LoDs (Limits of Detection) required by current legislation. However, chromatography is a complex technique that requires qualified personnel and to carry out complex sample pre-treatments which involve polluting reagents. In addition, this analysis method uses expensive equipments, which are usually only found in specialized and centralized laboratories. Another disadvantage of these techniques is the high time cost involved in sample analysis. There are other solutions on the market based on optical luminescent tests and radioactive particle counters that, although they allow rapid detection of residues with a lower cost than chromatography, do not reach the required LoDs. Currently, a widely used technique is ELISA (Enzyme Linked Immunosorbent Assay), a type of immunoassay based on antigen-antibody interaction. This technique is less expensive than chromatography. Its main drawback concern with the use of molecular labels, which can compromise the bio-chemical activity [9], [10]. All previously mentioned techniques are not easily automated, which prevents its use for on-line analysis [11].

This scenario reveals the necessity to develop new techniques that provide a rapid analysis and alert of the existence of substances in honey harmful to public health with high reliability. In this sense, different scientific research plans promote and finance

innovation in this field to satisfy the aforementioned needs. New analytical techniques to be developed must meet certain requirements to be suitable for use. Low cost, high sensitivity and selectivity, as well as real time detection along with high reliability are some of the needs to be covered. It is also a requirement to provide an easy-to-use technique so that highly qualified personnel are not essential, this would allow deployment of the instrument in food control laboratories of beekeeping companies. These novel techniques can be either alternative or complementary to the already existent ones. Next, a brief description about the relevance of beekeeping sector in Spain and the legal framework of chemical residues in honey is presented.

1.1. Honey

Honey is a very sweet, sticky, viscous, yellow substance made by bees by transforming the nectar of the flowers and secretions from living plants. It is stored in hive combs and used by human beings as a sweetener. It is a food with a high immediate energy power, easy to digest and assimilate. Its sweetness is due to glucose and fructose. The composition of honey depends on the floral origin, climatic factors, state of the colony, collection methods and bee breed, among others. For the most part, the composition of honey are carbohydrates (80%), where glucose stands out 30% and fructose 40%. Other components are acids, minerals, proteins, aromatic elements, and vitamins. Despite containing vitamins, minerals and other organic components, they are present in very small quantities, so their contribution is not significant for health. Regarding its physical properties, they depend on floral origin, water content or temperature [12].

1.1.1. Relevance of beekeeping sector in Spain

In Spain, the beekeeping sector represents 0.44% of the final livestock production. The production of beehive products (honey, beeswax and pollen) is estimated to be around 62 million euros per year, with a steady growth in recent years. This growth has been observed both in the number of beehives, as well as farms and beekeepers. Apart from the economic benefits, the growth of this sector is of vital importance if we consider its contribution to the convergence of nature through the pollination of crops.

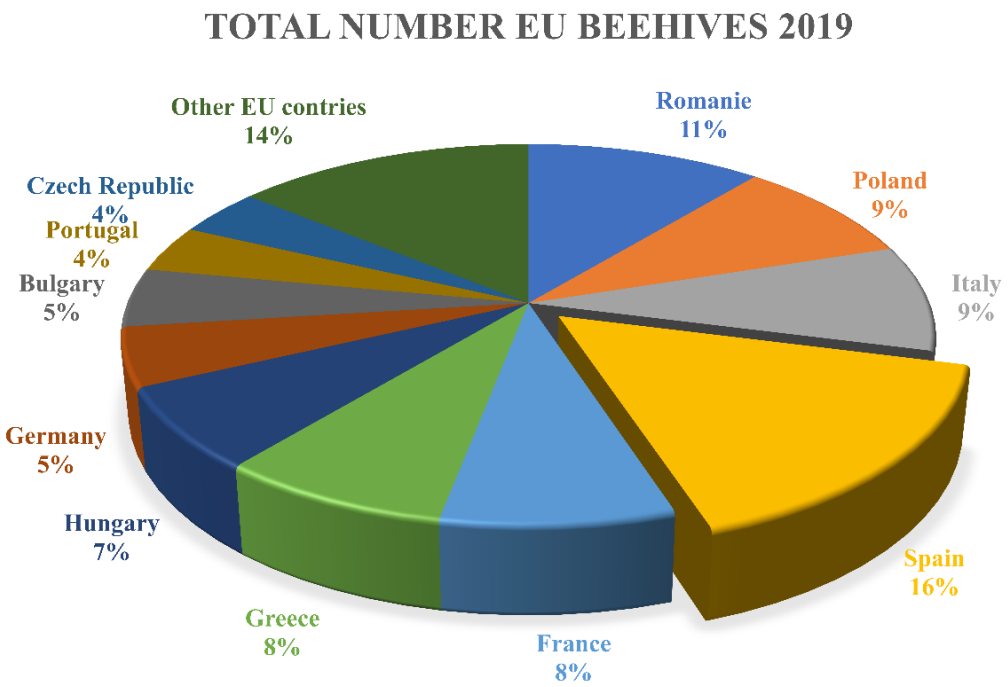

Figure 1.1 Total number of beehives by country in the European Union

Figure 1.1 provides data about the situation of Spanish beekeeping sector compared to the rest of the European Union (EU) countries. Spain has the highest number of beehives in UE (16%), 80% of them are managed by professional beekeepers[1]. These numbers imply a professionalization of Spanish beekeeping above the European average (22% professional beekeepers). This great growth of the sector is due to the international effect, which has led to an increase in honey exports (see Figure 1.2).

[1] Professional beekeeper: the one that manages more than 150 beehives

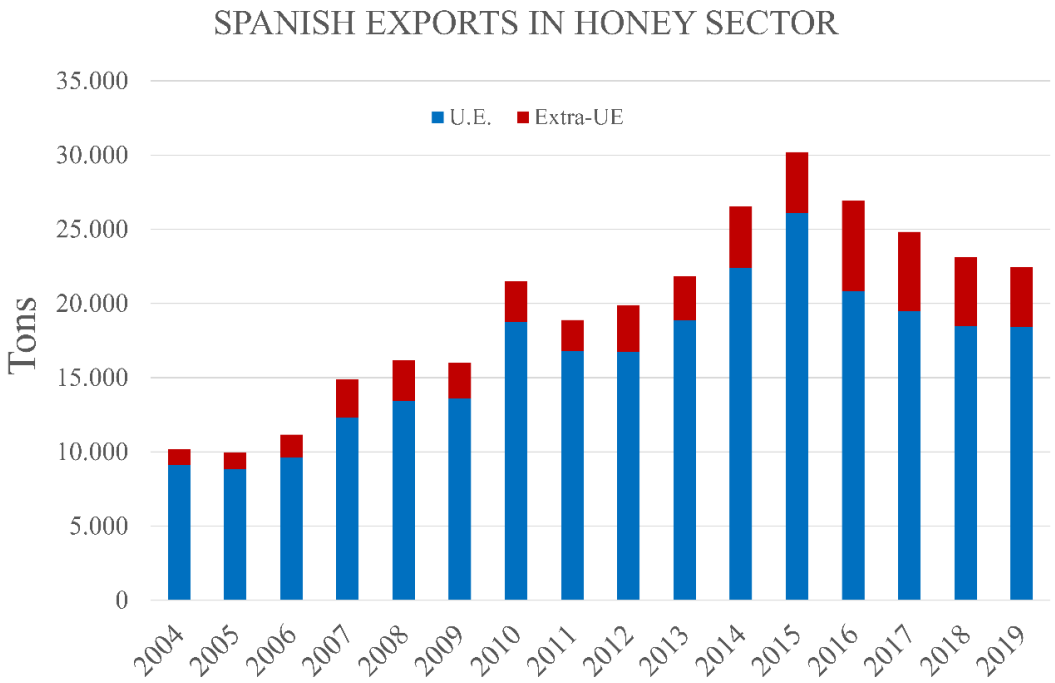

Figure 1.2. Evolution of the tons of Spanish honey exported

In EU, regulation (EU) 1308/2013 establishes a common organisation of the markets in agricultural products, in general, and in beehive products, in particular. This regulation includes a series of actions that are transmitted through the National Beekeeping Programs. These programs, which are renewed every three years, are financed by the corresponding member state and by the European Commission in equal parts. Since 1998, when the application of these programs began, Spanish beekeeping has received more than 140 million euros, ranking as the member state that has received the most financial resources, and has executed more than 90% of the established plans. In the current triennium (2020-2022) the budget for Spain is 14% of the total. The National Beekeeping Program in Spain includes eight action lines: technical consistency, fight against attacks on hive, rationalization of transhumance, analysis of bee products, repopulation of the hive, applied research in beekeeping, market monitoring studies and improvement of the quality. These actions seek to professionalize and modernize the sector, as well as to improve production and marketing systems.

One of the missions of aid measures granted by national plans for beekeeping is to support the implementation of research programs to reduce the risk derived from the use of phytosanitary and/or antibiotic products. The concern for food safety and quality is reflected in both the national plan for scientific and technical research and innovation (Spanish Ministry of Science and Innovation) and the Horizon Europe program (European Commission).

1.1.2. Legal framework

All definitions of honey highlight the fact that it is a natural product, i.e. it must have been produced by bees. One of the concerns of the Food and Agriculture Organization of the United Nations (FAO) has to do with safe and good food to every person in the world. With this aim, in 1963 the international standards of the Codex Alimentarius were created to contribute to the safety and quality of food products. Codex Alimentarius includes a series of standards on basic foods, whether processed, semi-processed or raw. The Codex specifies that honey must be free from any additives and contaminants, so this product is under food regulations worldwide. Nevertheless, the fraudulent practice of selling adulterated honey has occurred for a long time, and nowadays is widespread. Moreover, the practices carried out by the stockbreeders and agricultural industry in the treatment of diseases with livestock or pest control in crops can cause the presence of traces of the chemical residues, such as pesticides or antibiotics, in honey. According to the Codex Alimentarius "traces left by pesticides in treated products or those left by veterinary drugs in animals are called residues" [13]. Nowadays, the presence of such chemical residues is unavoidable and, in this context, current legislation tries to ensure that they are in small quantities so that they are not harmful to persons who ingest them. In this sense, Codex Alimentarius collects the Maximum Residue Limits (MRLs) legally allowed both for residues from veterinary medicines or for pesticides. The indications provided by the Codex do not replace compliance with the national or UE legislation, instead, they rather represent a common framework in which to underpin.

To ensure the correct and safe distribution of honey, the EU Council established Directive 74/409/EEC contains honey definition, its composition, the different types of honey that can be sold in the market, and how they should be provided (packaging, conservation…). This information provides to the consumer the knowledge about the quality of the honey. Updated quality criteria of this food (authenticity, freshness and safety) are determined by Directive 2001/110/EC (amendment Directive 2014/64/EU).

Regarding the analytical methods for the detection of residues of pharmacologically active substances, the Commission Implementing Regulation EU 2021/808 refers to the performance of these methods, collecting all the definitions necessary to understand and to interpret the analysis of food samples and their results. Moreover, the Commission of the European Communities Decision 97/747/EC fixes the levels and sampling frequencies to control substances and residues in animal products. In its chapter 4, it collects the

aspects referring to honey. On the other hand, Council Directive 96/23/EC of 29 April 1996 establishes a series of standards to control certain substances and their residues both in live animals and in products of animal origin such as honey. Its annexes detail what the groups of substances that must be detected when performing analyses are. In the case of honey, these are veterinary drugs and contaminants such as (1) antibacterial substances, including sulphonamides, quinolones; (2) other veterinary drugs, such as carbamates and pyrethroids; and (3) other substances and environmental contaminants, such as organochlorine compounds including PcBs, organophosphorus compounds and chemical elements.

At the European level, Rapid Alert System for Food and Feed (RASFF) system is activated whenever the authorities detect the presence or risk of chemical contaminants in food for humans and/or feed for livestock. This system facilitates the exchange of information about the risk detected among European Commission, EFSA, European Space Agency (ESA) and the food safety authorities of the 28 member countries of the EU, together with Norway, Liechtenstein, Iceland and Switzerland. In this way, members belonging to this system are informed in real time about the risk, this allows them to take the appropriate measures to protect the consumer: namely, to inform the public, to withdraw the product from the market, to carry out controls ...

1.1.3. Presence of chemical residues in honey

Any of the products related to bees (honey, pollen, wax, royal jelly...) is likely to contain residues of the chemicals used by the beekeeping sector. These residues can also have their origin in various agricultural practices or even in environmental pollution. The greatest concern about the possible danger that these chemicals may cause focuses on honey since it is the beehive product of greater consumption.

The exhaustive controls carried out on multitude of foods, including honey, reveal that the intake of pesticides or antibiotics by consumers is not high. However, a prolonged consumption of these chemical substances over time can damage human health. Next, a brief description about the two chemical residues (a pesticide and an antibiotic) used in the proof of concept performed in this thesis is included.

1.1.3.1. Pesticides: Thiabendazole in the beekeeping sector.

Since the beginning of agriculture practices, there has been the challenge of avoiding the loss of crops due to insects, rodents, plant diseases, weeds, pests, etc. In ancient Greece, sulphur was used to exterminate pests, this could be considered as the beginning of the use of pesticides. According to the International Code of Conduct of FAO, a pesticide is "any substance or mixture of substances of chemical or biological ingredients intended for repelling, destroying or controlling any pest, or for regulating plant growth".

A radical change in agriculture and livestock took place with the industrial revolution. New farming techniques and agricultural machinery increased and facilitated production. Large-scale fumigation then also arose, which made it possible to control pests and therefore to increase production. The use of synthetic products experienced a very significant increase during the Second World War, especially that of a chlorine-based insecticide, DDT (Dichlorodiphenyltrichloroethane).

Clearly, the losses that would occur in crops if these chemicals were not used would be dramatic. However, despite of evidence that its use increases production, there is also an increasing awareness and concern about the consequences that its maintained consumption can cause in humans due to its toxicity. This is why the EU carries out strict toxicological controls on agrochemical products to authorize their manufacture and consumption (Directive 91/414/CEE). The need to create standards that establish pesticide-specific MRLs for each food along with the procedure for requesting new MRLs can be found elsewhere (Regulation (EC) No 396/2005). Next, more information about the pesticide analysed in this thesis, Thiabendazole, is included.

Thiabendazole (TBZ), known in the food industry with the code E233, is a preservative antifungal and antiparasitic agent mainly used for the treatment of mold and, in general, fungal diseases in fruit and vegetables. It is used in the treatment of worms, such as ascariasis, and is an ingredient in the wax applied on the skin of citrus fruits such as orange.

In hives, it is one of the treatments preventively used to avoid fungal infections such as chalkbrood. The regulation of the European Commission 37/2010 includes the MRLs for the following pesticides in honey: amitraz (200 µg/kg) and coumaphos (100 µg/kg). Regulation 2017/1164 includes MRLs for metalaxyl and thiabendazole (0.05mg/kg)

while Regulation 2017/623 sets this same MRL value for acequinocyl, diflufenican and pyraclostrobin in honey. The MRL value of 0.05mg/kg given for TBZ represents the lower limit that can be measured analytically.

1.1.3.2. Antibiotics: Sulfathiazole in the beekeeping sector

Despite some earlier discoveries and developments, the accidental penicillin discovery in 1928 by Alexander Fleming is considered the beginning of antibiotics. It was in the 1950s that the use of antibiotics began to spread not only in humans, but also in the veterinary field.

Antibiotics are defined as the chemical substance produced by a microorganism which has an antimicrobial function [14]. According to the World Health Organization (WHO), antibiotics are "medicines used to prevent and treat bacterial infections". The origin of this substance can be either natural or semisynthetic. In the former case, the antibiotic is obtained from cultures of microorganisms, such as fungi or bacteria. Whereas in the latter case, it is generated from a basic nucleus obtained naturally, then some of its chemical characteristics are modified in order to improve its properties: expand its range of action, facilitate its use, reduce its side effects... Antibiotics can be classified into two groups: bactericides and bacteriostatics. The formers are those capable of killing specific bacteria. The latter are used to inhibit, stop or reduce the growth of bacteria in the organism thus allowing the immune system to develop its defence mechanisms against the microorganism.

The widespread use of antibiotics has increased and worsened the problem of bacteria resistance to them. Resistance to antibiotics happens naturally since bacteria mutate in response to that medicine. The infections that new bacteria produce are more difficult to treat and therefore can be more dangerous. Antibiotic resistance is increasing worryingly and will increase in severity if proper and controlled use of antibiotics is not performed. Livestock and agriculture sector have had an important role in the evolution of this problem. Very widespread practices over the years, such as the use of antibiotics to promote the growth of animals or as preventive treatments against possible diseases in healthy animals have contributed to the resistance problem. The vaccination of animals or the improvement of hygiene on farms are, among others, some of the recommendations made by the WHO to the agriculture and livestock sector to reduce and control the

increase in antibiotic resistance. In EU, the use of antibiotics in the livestock sector with a non-therapeutic nature is forbidden, therefore absence is the requirement and there are no established MRLs.

Among the bacteria that can affect bees are those that produce American foulbrood and European foulbrood. In the case of American foulbrood, a serious degenerative process occurs in the larvae and can cause their death. Drugs widely used for the treatment of this disease are sulphonamides and, among these, sulfathiazole (SFZ), a fast-acting antimicrobial. As mentioned before, the use of sulphonamides in Europe is not allowed in beekeeping sector, since it is known and widely studied that their residues appear in honey. Any country producing and exporting honey in the EU must currently pass controls for the presence of this antibiotic family.

1.2. Analytical techniques used in the analysis of residues in honey

To comply with the requirements demanded by the different national and EU administrations, it is necessary to analyze different honeys that are produced and exported between the member countries. This section contains a brief description of two representative analytical techniques employed in honey analysis: Chromatography and ELISA. The former can be considered as a reference technique in honey analysis, the latter, although not as sensitive as Chromatography, is the most representative of the current screening techniques.

1.2.1. Chromatography

One of the classical quantitative techniques for analyzing honey, considered as a reference technique, is chromatography. This technique consists of separating the components, or solutes, of a mixture based on the relative amounts of each solute distributed between a moving fluid stream, called the mobile phase, and a contiguous stationary phase. The different components of the mixture travel through the stationary phase at different speeds, causing them to separate from one another. The mobile phase may be either a liquid or a gas, while the stationary phase is either a solid or a liquid [15]. Chromatography can be used with two different objectives: 1) to separate the components of the mixture, so that they are obtained purer and can be used later; or 2) to measure the proportion of each of the components, in this case, very small amounts of sample are

needed. According to how the stationary phase is placed, the chromatographic techniques can be divided into:

- Planar: the stationary phase is located on a flat plate or on a piece of paper.
- Column: the stationary phase is located within a column. In this case, a subclassification can be made according to the mobile phase:
    - Liquid chromatography
    - Gas chromatography
    - Supercritical Fluid Chromatography

Within liquid chromatography, HPLC stands out, which is the most widely used chromatographic technique nowadays. On the one hand, this technique achieves the LoDs required in honey analysis and can be used to simultaneously detect chemical residues with a similar chemical composition, for instance several pesticides [16]. However, simultaneous analysis of chemical residues with very different chemical composition, for instance pesticides and antibiotics, is not possible when good LoDs are required. On the other hand, HPLC is a technique that must be carried out by highly qualified personnel (whose learning can last from 3 to 6 months), it is economically expensive (both cost of equipment and analysis) and requires analysis times in the order of one hour.

Since honey is a complex matrix, HPLC technique requires pre-treatment of the sample before its injection into the chromatographic equipment. The aim of this pre-treatment is the extraction of the analytes from the honey matrix. There are numerous sample pre-treatment techniques for pesticide and antibiotic analysis that can be applied to different food matrices, including honey. Each one presents advantages and disadvantages that must be evaluated in each case, according to the needs, volume of samples to be analysed or level of technification of the laboratory. The following table shows a summary of the different extraction techniques, more detailed comparative information can be found elsewhere [17].

Extraction Technique	Use for antibiotics and pesticides extraction in honey	Advantages	Disadvantages
Liquid-Liquid Extraction (LLE)	Blasco et al., 2004; Pirard et al., 2007; Souza Tette et al., 2016	Non sophisticated material required Low cost	Large amount of sample High consumption of toxic solvents Slow Risk of cross contamination due to the multiple steps involved Possible formation of emulsions Requires a subsequent filtration
Liquid-Liquid Ultrasound Assisted Extraction (LLUSAE)	Rezić et al., 2005	Low cost Allows the extraction of thermolabile pesticides Quick Not depend on the matrix More efficient than LLE	High consumption of solvents Requires posterior filtration High sample quantity (2-30g)
Supercritical Fluid Extraction (SFE)	Atienza et al., 1993; Jiménez, Atienza & Bernal, 1995; Blasco et al., 2003; Rissato et al., 2004	Quick Low Consumption of solvents High Selectivity Small amounts of sample required Automated Final pure and concentrated extract	Large number of variables to optimize High technification and high cost of equipment Not suitable for polar organic compounds
Solid-Phase Extraction (SPE)	Debayle, Dessalces & Grenier-Loustalot, 2008; Amendola, Pelosi & Dommarco, 2010 -García-Chao et al., 2010; Bonzini et al., 2011;Juan-Borrás et al., 2015	Simplicity; Robustness; Quick High Sensitivity Low consumption of solvents Extraction of numerous pesticides from a sample Volatile and non-volatile extraction No emulsions Great Variety of adsorbents	Low performance in number of samples Cartridge material can generate interference and absorb the analyte Adsorbent packaging must be uniform to avoid low efficiency
Matrix Solid-Phase Dispersion (MSPD)	Albero, Sánchez-Brunete & Tadeo, 2001; Sánchez-Brunete et al., 2002	Quicker than SE Lowe solvent consumption than SE No previous dilution steps of solid and semisolid samples (necessary for SPE) No emulsions High sensitivity	Not suitable for dry samples Sample quantity is limited.
Stir Bar Sorptive Extraction (SBSE)	Blasco et al., 2004	Like SPME but higher %recovery, higher sensitivity, higher precision	Desorption cannot be done directly in the injector without a special desorption unit
Solid-Phase Microextraction (SPME)	Jiménez et al., 1998; Volante et al., 2001; Blasco et al., 2004; Yu, Wu & Xing, 2004	Problems associated with SPE are eliminated Quick extraction High sensitivity No solvent consumption Automatized Low cost	Reproducibility problems
Single-Drop Microextraction (SDME)	Tsiropoulos & Amvrazi, 2011	Low solvent consumption Low cost Low sample quantity	Difficult optimization Presence of contaminants
QuEChERs (Quick, Easy, Cheap, Effective, Rugged, Safe)	Kamel, 2010; Sampaio et al., 2012; Proietto Galeano et al., 2013; Kujawski et al., 2014;Calatayud-Vernich et al., 2016	Quick extraction Low solvent consumption Low Cost Low technological requirement Few steps Possible to extract large number of polar and non-polar pesticides	Low selectivity in the extraction Possible formation of emulsions Manual extraction Low concentrated extracts

Table 1.1. Extraction methods of pesticides and antibiotics in honey for chromatography [17].

1.2.2. Screening techniques: Enzyme-Linked ImmunoSorbent Assay (ELISA)

Directive 96/23/EC classifies detection methods as confirmatory or screening. The former are used once the test samples have been determined from the screening methods and provide information that allows the identification and/or quantification of the substance in the sample to be analysed. These are techniques like chromatography discussed in the previous section. The latter are faster and cheaper methods that detect the presence of residues in the samples, generally, above the MRLs. According to Commission Decision 2002/657/EC (2002), screening methods have the following features: "(1) They are used to detect the presence of a substance or class of substances at the level of interest. (2) They have the capability for a high sample throughput. (3) They are used to sift large numbers of samples for potential non-compliant results. (4) They are specifically designed to avoid false compliant results". Their capability to analyse a large number of samples is considered their main advantage, together with their low cost when they are compared with chromatography. However, screening methods not always reach the demanded detection limits, which is their main disadvantage. Screening techniques allow discarding those samples in which residues are detected (positives), so that only those samples with a negative diagnosis are analysed by means of confirmatory methods, thus reducing the time and economical cost of the analysis.

In turn, screening methods can be classified as microbiological or biochemical. Microbiological are qualitative methods that detect the presence of residues above the MRLs or their absence. They are the most widely used methods for the detection of residues in food [41]–[43], and are based on the sensitivity of bacteria to antibiotics. In particular, they are based on growth inhibition tests of the microorganism at antibiotic concentrations above the MRL in a sample. Biochemical methods are developed based on the antigen-antibody recognition for the detection of the analyte, which makes them more specific than the microbiological ones. A more comprehensive review of the most widely used biochemical screening methods can be found elsewhere [44]. Following, a short review about one of the most widely used biochemical screening methods, ELISA, is introduced.

ELISA is a very popular immunoassay technique in which the immobilized antigen is detected through its binding with an antibody linked to an enzyme that generates a detectable signal, such as a colour change, some minutes after the reaction takes place.

Therefore, it is an indirect analyte detection method that relies on optical techniques, such as spectrophotometry, to complete the detection assay. ELISA can be used both to detect the presence of an analyte in the sample (qualitative), and to measure the concentration at which it is found (quantitative). In the latter case, it is necessary to generate a calibration curve using known analyte concentrations. In the last decades, an increase in the use of immunoassays as analytical techniques has taken place, becoming to be considered as complementary, or even an alternative, to the chromatography classical techniques. ELISA technique is used in several applications: medical diagnostic, detection of pathologies in plants or industry quality controls, between others. Specifically for honey, ELISA tests have been developed to detect insecticides such as imidacloprid and thiamethoxam or antibiotics such as sulphonamides, tetracyclines [44].

The concentrations of analytes to be detected are getting lower and lower and ELISA technique has sensitivity limitations in this regard. Its LoD is usually around 0.1µg/L [45]. Another drawback of the technique is the short period of time elapsed between the enzyme reaction and the read-out data, when this period time is over, the read-out can be erroneous [46]. In addition, some investigations have revealed the fact that the binding of the enzyme and the antibody prevents or hinders the antigen-antibody binding [10].

In 1985 the chemiluminescence immunoassay (CLIA/CLEIA) arose as an effective combination of immunoreaction and chemiluminescent system. Since then, it has been applied broadly to the clinical diagnosis, environmental analysis, food safety, biomedical research … This technique is based on the same concept as ELISA, with the difference that it uses a chemiluminescent indicator linked to the antigen or antibody. Therefore, when the detection reaction occurs, the light emission, instead of a colour change as would be observed in ELISA, is measured. This meant an improvement in the sensitivity of the immunoassays (0.001 µg/L). Some of its advantages include fast reaction times, long-lived emission signal, high signal-to-noise ratio and stability at room temperature for the duration of the assay. Its main disadvantage is the need to have specific equipment capable of carrying out chemiluminescence readings, which tend to be expensive.

Table 1.2 summarizes the most relevant aspects of the HPLC-MS/MS and ELISA techniques in terms of set-up preparation time, time invested in the analysis of a sample, cost of the equipment, sample analysis cost, user training time, multi-analysis capability and pre-processing of the sample.

	HPLC	ELISA
Set up preparation	Weeks/Months[2]	6 to 12 months[3]
Time cost of the sample analysis	1h to 1.5h	1.5h to 3h
Cost of the equipment	150,000€ – 200,000€	15,000€ – 20,000€
Cost per sample analysis	100€ - 150€	10€ (If a least 40 samples are run simultaneously)[4]
Time cost of training	3 to 6 months	2 to 3 weeks
Multi-analysis	When analytes have a similar chemical composition	Up to 40 samples simultaneously.
Pre-treatment[5]	Complex (see Table 1.1)	Simple (only water dilution is required)

Table 1.2. Comparison between the relevant aspects of HPLC and ELISA techniques

The presented review reveals that conventional analytical methods, currently employed as reference, require trained personnel in centralized laboratories to perform time-consuming experiments with costly, large, and bulky devices. Owing to their simplicity, reduced size, good sensitivity and low cost, novel biosensors may play a fundamental role in the very near future becoming an alternative or complementary analytical tool in health care, food security and environmental monitoring applications. Next, a brief explanation about biosensors with a deep focus on a type of acoustic biosensor is included.

1.3. Biosensors

Clark and Lyons are the precursors of the biosensor concept, which was reflected in an article published in 1962 [47]. They presented the development of a biosensor to measure glucose levels by means of an electrochemical detector on which they immobilized an

[2] Orientative estimation when the set-up is prepared for a new analyte
[3] Also includes the inmunoreagents development, as well as haptens synthesis (See section 1.3.1.1). Depending on the chemical difficulty of the analyte, since it is necessary to synthesize the appropriate haptens to immunize the mice. The success of this task is quite unpredictable.
[4] Plates contain 96 wells. Taking into account standards and duplicates it is possible to give results for 40 samples simultaneously
[5] Refers to the sample processing before its injection

enzyme. Since that time, the development of biosensors has grown largely thanks to advances in technology. Research in the field of biosensors is marked by the need for faster and reliable medical diagnosis or for food industry security controls. Quick results after sample analysis can improve disease care and reduce economic losses in food industry.

Biosensors are analytical devices incorporating a biological (or a biologically derived) material which is integrated within a physicochemical transducing microsystem. In particular, it is the ensemble of (1) a biological recognition layer that specifically detects a substance by taking advantage of the specificity of biomolecular interactions; (2) a transducer that converts the bio-recognition event into a signal that can be processed; and (3) the characterization system that records the signal provided by the transducer. As depicted in Figure 1.3, the bio-recognition layer can be formed by enzymes, immunoreceptors (antigens or antibodies), microorganisms, DNA, aptamers, or even synthetic species, such as molecularly imprinted polymers (MIPs) [9]. This layer is immobilized onto the surface of a transducer. The most widely used transducers in the field of food technology are electrochemical, optical and acoustical.

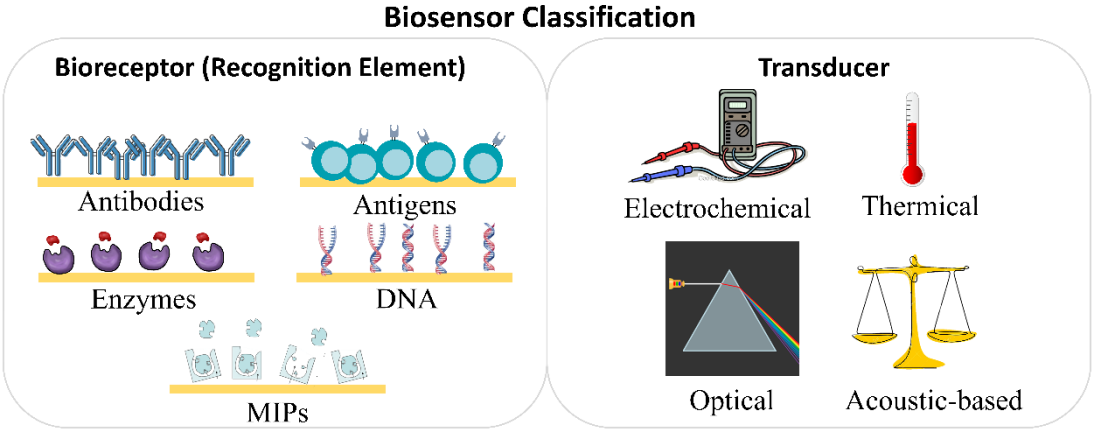

Figure 1.3. Biosensor's classification according to transduction mechanism and to the biorecognition layer.

The signal provided by the tranducer changes according to the biological event that takes place in the medium in contact with it. This signal is recorded by the transducer characterization system and, subsequently, processed by the appropriate software. The processed signal provides information about the biological interaction and, in turn, about the physical magnitude under study. One of the main requirements of the characterization system is to maintain a low noise level in order not to mask the signal produced by the transducer. Moreover, the abovementioned bio-recognition event occurs in the natural

liquid environment of molecules involved, this requires a fluidic or microfluidic system that allows fluids to be confined in a volume close to the transducer. Figure 1.4 ilustrates the previous description for the case of the biosensor developed in this thesis. Biosensors used in this doctoral thesis are based on piezoelectric acoustic transducers with immunoreceptors immobilized over its surface. This type of biosensor is called immunosensor and will be described with more detail in the next section.

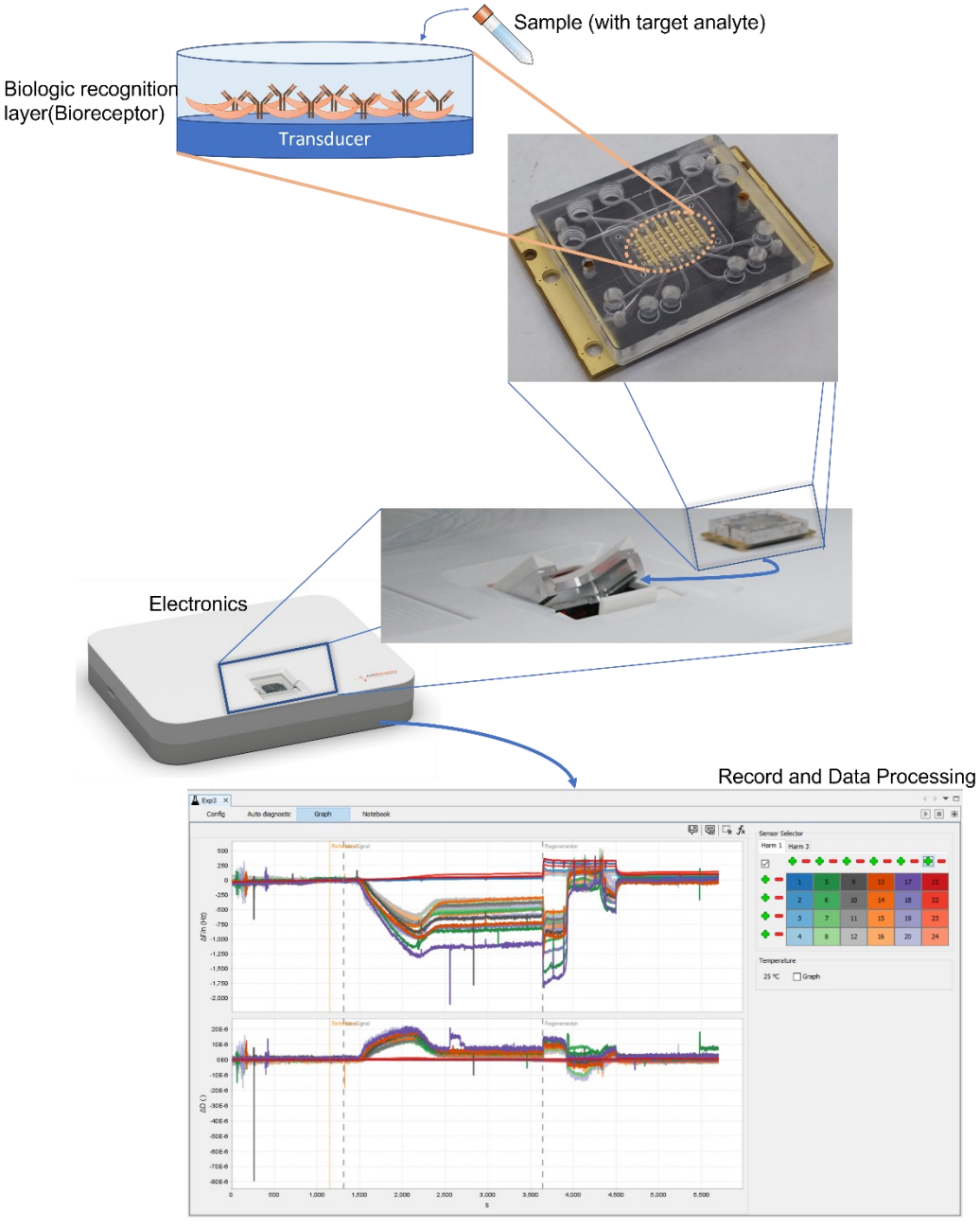

Figure 1.4. General schematic of a biosensor

1.3.1. Immunosensors

Among the different types of biosensors there is one in which the biological compound that detects the analyte is an immunoreagent. This type of biosensor is known as immunosensor [48], and is based on an immunochemical reaction between an antigen and its specific antibody. Immunosensors combine the selectivity of immunological reactions with the sensitivity of the transducer. Although it depends on the transducer, immunosensors are known to be highly sensitive, since they can detect concentrations of biomolecules in the range of nanomolar to femtomolar.

In order to facilitate the detection of the event corresponding to the antigen-antibody binding, which is usually difficult to quantify, it is very common to use the labelling technique. In this technique, a chemical substance (i.e. an enzyme or a fluorescent compound) that produces a colour or a light emission change is chemically added to the antigen or antibody, thus producing a light signal, which can be detected by means of fluorometric, colorimetric of luminometric methods [48]. Label-based techniques force to carry out the quantitative measurement of the reaction once the biochemical recognition has occurred, which make them not-real-time techniques. This feature can be considered as a disadvantage in those applications in which the kinetics of the reaction provides information. In addition, as it was previously indicated, some research suggests that the biochemical reaction can be compromised by the enzyme [10]. In contrast, some immunosensors do not use labels, thus, providing a direct detection. In a label-free immunosensor, one of the immunoreagents is immobilized on the surface of the transducer and, when the interaction occurs, a real-time signal is generated. This is the main advantage of label-free immunosensors compared to labelled immunoassays. Moreover, the latest generations of immunosensors based on acoustic or optic transducers have reached those sensitivity levels of labelled immunoassays [49]. However, up to now, a main challenge remains, since immunosensors have not succeeded in reproducing the multi-analysis capacity of screening techniques such as ELISA, thus, preventing immunosensors from becoming a high-throughput screening technique.

1.3.1.1. Immunoassay Formats

An antibody is a protein produced by the body, both in people and in animals, as an immune response to a foreign substance (antigen) to protect itself. At present, they can also be produced in a controlled way in specialized laboratories. To do this, the

corresponding antigen is injected into an animal, usually lab mice or rabbits, so that its immune system naturally generates the specific antibody against the antigen. In most of the immunosensors, one of the immunoreagents (antigen or antibody) is immobilized on the surface of the transducer, so they can be classified into two immunoassay formats: conjugate-coated format and antibody-coated format.

In the case of low-molecular weight organic molecules, such as the pesticides and antibiotics that concern us in this thesis, the immune system does not usually recognize them, in other words, are non-immunogenic molecules. Therefore, no antibodies are generated in response to them. To overcome this, a conjugated hapten is synthesized. The molecule of the analyte to be detected is chemically modified to introduce into its structure some chemical groups to facilitate its union with proteins, this "modified" analyte is called "hapten". Binding of the hapten to the carrier protein produces a high-molecular weight molecule called "conjugated hapten". Hapten is used as an injectable antigen in animals, to generate specific antibodies against the analyte, and as a conjugate in the immunoassay.

When detection of low-molecular weight molecules is required, it is recommended to immobilize the hapten-conjugate (conjugate-coated format). In this immunoassay format, the binding of the antibody to the immobilized hapten-conjugate produces a greater signal change in the transducer when compared with the antibody-coated format. Conjugate-coated format requires performing a competitive immunoassay, where the free analyte competes with the immobilized hapten-conjugate to bind to a limiting concentration of antibody. In a competitive immunoassay, the higher the concentration of the analyte the lower the signals provided by the transducer. This generates a typical standard calibration curve that shows the inversely proportional relationship between the concentration of the analyte to be detected and the signal generated by the transducer (see Figure 1.5).

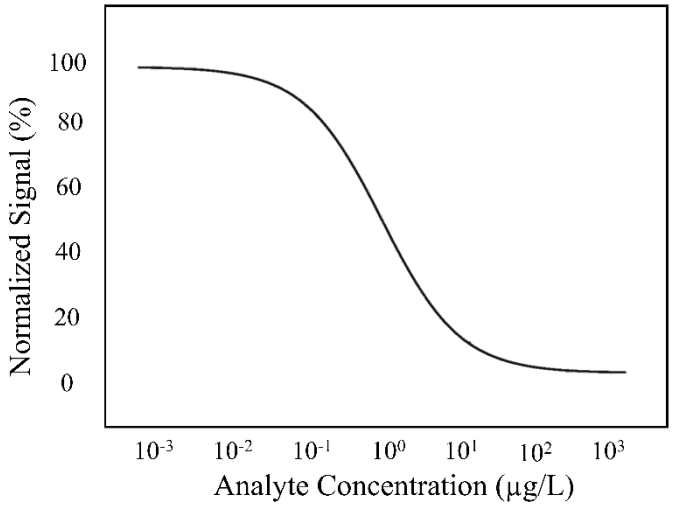

Figure 1.5. Typical standard calibration curve in a competitive immunoassay

Hapten-conjugate format is also the preferred one rather than its counterpart for sensor regeneration processes. These processes are necessary in order to reuse the functionalized transducer in new immunoassays. Antibody layers are less stable than hapten-conjugate layers under the reagents used for the regeneration, since these reagents can modify the chemical structure of the antibody. In addition, the immobilization of the antibody is a very complex process when compared with antigen immobilization.

The development of immunosensors requires extensive prior work regarding the production of the immunoreagents and their immobilization on the transducer surface, which is beyond the scope of this thesis. More detailed information about this topic can be found elsewhere [50].

1.4. Piezoelectric Acoustic Transducers

There are several types of label-free immunosensors according to the method used to perform the measurement, among them optical and acoustic immunosensors have experienced a rapid growth in food control industry and Point of Care (PoC) applications. [9], [51], [52].

Optical immunosensors, like those based on SPR, can be very sensitive, but they usually require more expensive instrumentation to be characterized, thus, limiting their capacity for high-throughput screening analysis. In addition, the signals provided by these transducers may depend on the optical properties of the media in which the immunoreactives are immersed [53]. Immunosensors based on acoustic wave technology can work with a broad range of surfaces and contacting media, since optical properties of

the latest do not affect the measurement. They were used in their origin to measure mass in the range of μg/cm^2 to pg/cm^2. However, nowadays it has been demonstrated that they are more than a microbalance, since they are sensitive to changes in mechanical or electrical properties of the media in contact with the transducer (stiffness, viscosity, conductivity, permittivity, pH…). They are also sensitive to other external disturbances such as temperature or pressure changes, which, in some applications, can become a disadvantage [54]. Regarding the instrumentation required to characterize this type of transducers, it is less expensive than its optical counterparts are. This is an advantage for the development of high-throughput and "in-situ" applications which are very demanded both for food control industry and PoC applications [55].

According to the guiding mechanism of the acoustic wave and its way of propagation through the media, acoustic transducers can be classified in Bulk Acoustic Wave (BAW) devices (wave propagation is through the substrate unguided), Surface Acoustic Wave (SAW) devices (wave propagation is along a surface of the substrate guided or unguided) and Acoustic Plate mode (APM) devices (waves are guided by reflection from multiple surfaces). It is also possible to classify them by considering the movement of the particles with respect either to the direction of propagation of the wave (*longitudinal* or *transverse*), or to the surface of the device (*vertical* or *horizontal*). *Vertical* waves are normal to the device surface, while *horizontal* waves are parallel to it. In the case of *transverse* waves, also called shear waves, the displacement of the particles is perpendicular to the propagation direction of the wave. In *longitudinal* waves both, particle displacement and wave propagation, are in the same direction [56]. The most used acoustic wave biosensors are those based on Thickness Shear Mode (TSM) devices[57], which belong to the group of BAW devices. Among TSM devices, Quartz Crystal Resonators (QCRs) stick out for being one of the most used, being thus the transducer employed in this thesis.

Quartz is a piezoelectric material. The term "piezo" means "pressure" in Greek, thus, the term "piezoelectric" means "generation of electricity by pressure" and defines the phenomenon that describes the appearance of positive and negative charges on the material surfaces when compressed. This compression causes the deformation of its crystalline structure, which gives rise to the appearance of small dipoles. The crystal is then polarized, and an electric field appears. When two electrodes connected by a conductive wire are placed on both sides of the crystal, the internal electric field generates

a flow of the free electrons in the wire. When the exerted pressure on the crystal stops, the polarization disappears, and the flow of charges ceases. Thus, the quartz crystal behaves like a transducer since the mechanical energy used to deform the material is transformed into electrical energy. In the same way, the application of an electric field on the material through the two electrodes placed on its surfaces causes the crystal deformation. If such a field is applied periodically, the crystal will periodically deform. Among all the excitation frequencies of the electric field, there is one that causes the crystal deformation to be maximum. This frequency is known as resonance frequency, for this reason, quartz crystals are also known as piezoelectric resonators.

1.5. Quartz Crystal Microbalance

In their first uses, quartz crystals were used as frequency reference standards in the oscillators designed to generate the carriers of radio stations. The resonance frequencies of these crystals were adjusted by deposition of very small masses on the crystal until the desired frequency was achieved. This application was based on the studies of Lord Rayleigh, who showed that small changes in the inertia of a mechanical vibration system modified its resonance frequency; but it was not until years after that it began to be used as a sensor [58]. In 1959, Sauerbrey demonstrated that the variation in the resonance frequency of a quartz crystal was proportional to the mass added on it, as long as this added mass formed a very thin and uniform layer [59].

$$\Delta f_r = -2f_r^2 \frac{\rho_f h_f}{\sqrt{\rho_q c_q}} \qquad (1)$$

Where f_r is the resonance frequency of the transducer; ρ_f and ρ_q are the mass density of the film layer and the quartz, respectively; h_f is the thicknesses of the film layer and c_q the stiffness quartz coefficient. The extension of the validity of the Sauerbrey equation to deposited masses of any material is based on the hypothesis that a sufficiently thin film of material deposited on the quartz surface only affects the resonant frequency of the crystal by the inertia of the added layer, that is, by its mass. With this assumption, it is tacitly assumed that the film does not deform and, therefore, its elastic properties do not take part in the vibration frequency of the resonant system. This operation regime of the transducer is called “gravimetric regime” [60]. In the beginning, quartz crystal was used to measure masses in the order of μg/cm^2, hence the term Quartz Crystal Microbalance (QCM). Later, studies showed that QCRs were capable of measuring masses around

0.0005-0.001 μg/cm^2. This great sensitivity is due to the tremendous acceleration to which the particles deposited on the surface of the crystal are subjected, which is proportional to the square of their vibration frequency. In the 80s, the stability of a quartz crystal controlled oscillator was demonstrated when it was in contact with a liquid medium (until that moment it was believed that when a fluid was deposited on the sensor, it would stop oscillating) [61]. This gave the opportunity to use the quartz crystal to carry out detection processes that occurred better in liquid than in gas, which is the case of biosensors. On the other hand, when the thickness of the film placed on the quartz crystal becomes thicker, it is not possible to continue considering that the acoustic wave does not deform the material when passing through it. Under these conditions, the sensor can not longer be considered as a simple microbalance due to the fact that, apart from the mass variations, changes in the viscoelastic properties of the deposited material also produce changes in its resonance frequency [62]. This operation regime is called "non-gravimetric regime" [63]. The operation of the sensor in this regime broadens the range of applications in which this sensor can be used, for instance, in the characterization of materials or fluids [64].

When the sensor is covered with thicker layers, the acoustic waves generated by the crystal penetrate into those materials, deforming them. This produces the variation of the speed and amplitude of the acoustic wave. Due to the electromechanical coupling of quartz, changes in the mechanical properties of the layers through which the wave propagates are translated into changes in the electrical properties of the resonator, which can be measured in terms of variations in its electrical impedance spectrum. Tracking of these variations gives information about the mechanical properties of the layers. Most of the times, it is not necessary to measure the full impedance spectrum to obtain the properties of a certain material, but only the amplitude and phase of the impedance at some characteristic frequencies. This depends on the total amount of unknown properties to be determined [65]. In a typical QCM experiment, the relevant electric parameters of the resonant sensors acquired are the shifts in the resonance frequency, f_r, and the dissipation, D (equivalent to the half-bandwidth). These magnitudes, measured at one or more overtones, are related to the physical and/or biochemical properties of the layers deposited over them through various models, which can be found elsewhere [60], [66]. This new evolution of QCM technology is currently known as Quartz Crystal Microbalance with Dissipation (QCMD)[48], [60].

QCRs are manufactured from AT-cut quartz. The cut determines the vibration mode of the crystal, in addition to other characteristics such as unwanted vibration modes or the influence of temperature on the vibration frequency. To achieve a low number of unwanted vibration modes, as well as a low value of the frequency temperature coefficient, the AT-cut quartz is used. This type of quartz cut is obtained by cutting crystal plates with an angle of 35.15º with respect to the Z axis of crystallized quartz crystals with the shape of a hexagonal prism [67]. Traditional QCRs are manufactured by depositing gold electrodes on each face of an AT-cut quartz plate. When an alternating potential between the electrodes is applied, a shear-like deformation occurs at the same frequency as that of the potential, generating an acoustic wave that propagates in the thickness direction. This acoustic wave is reflected off at the crystal surfaces, generating incident and reflected waves. For a certain relationship between the excitation frequency of the electric potential and the thickness of the crystal (see Eq. (2)) the speed and amplitude of those mentioned incident and reflected waves set equal, generating a standing wave, and therefore, the resonance of the crystal. The relationship between the plate thickness, h_q and the resonance frequency f_r is the following [68]:

$$f_r = \frac{N}{h_q} \tag{2}$$

where N is the frequency constant, and for AT-cut quartz is given by:

$$N = \frac{1}{2}\sqrt{\frac{\overline{c_{66}}}{\rho_q}} \tag{3}$$

Where $\overline{c_{66}}$ is the effective stiffness modulus. Solving for the values of Table 1.4 results a frequency constant value of N = 1664 $kHz{\cdot}mm$ for AT quartz. A direct correspondence can be established between Eq. (2) and Sauerbrey equation.

Parameter	Value	Description
ε_{22}	3.982×10^{-11} $A^2{\cdot}s^4{\cdot}kg^{-1}{\cdot}m^{-3}$	Permittivity
η_q	9.27×10^{-3} Pa·s	Effective viscosity
$\bar{c}_{66}$	2.947×10^{10} $N{\cdot}m^{-2}$	Effective modulus of stiffness
e_{26}	9.657×10^{-2} $A{\cdot}s{\cdot}m^{-2}$	Piezoelectric constant
ρ_q	2651 $Kg{\cdot}m^{-3}$	Density

Table 1.3. Physical properties of a quartz crystal in AT cut

Traditional QCRs work at fundamental resonance frequencies between 5 and 10 MHz, which, according to Eq. (1), correspond to crystal thicknesses between 332.8 μm and 166.4 μm, respectively. Fundamental resonance frequency determines a crucial property of the resonator: the sensitivity S_σ, which corresponds to the frequency shift that the sensor provides (Δf_r) against a variation in the surface mass density of the deposited layer ($\Delta\sigma$). Theoretical sensitivity can be obtained directly from Sauerbry Equation (see Eq. (1)) or, after some manipulation from Eq. (2):

$$S_\sigma = \frac{\Delta f_r}{\Delta\sigma} = -\frac{2}{\rho_q v_q} f_r^2 \ (Hz\ cm^2 ng^{-1}) \tag{4}$$

Where v_q is the wave's shear propagation velocity in the AT-cut quartz crystal ($v_q = \sqrt{\overline{c_{66}}/\rho_q}$).

The use of traditional QCM technology for biochemical and biotechnology applications is widely known [69]–[72]. Increasing the sensitivity is one of the fundamental objectives that has been pursued over the years to satisfy the demand for lower limits of detection. The solution to this challenge, as reflected in Eq. (4), comes from the evolution of traditional QCM into High Fundamental Frequency- QCMD (HFF-QCMD) sensors. HFF-QCMD are based on the same physical principle as the QCMD but with higher fundamental resonance frequencies, between 50 and 150MHz. Increasing the fundamental resonance frequency of these devices is achieved by reducing the thickness of the crystals. This thickness reduction has additional implications in the resonator dimensions. It will be necessary to determine the optimal geometry of the electrodes to ensure sufficient separation between the fundamental thickness shear mode and the first spurious mode. The "plate-back" equation, used in the design of common quartz resonators (5-10MHz), indicates how the lateral dimensions of the electrode affect the presence of inharmonic modes close to the fundamental mode. A minimum thickness of the electrodes will also be required in order to ensure good electrical conductivity and that the effect of "energy trapping" is generated under the electrode area, which improves the quality factor of the sensor [73]. The main problem that arises when working at these frequencies is the fragility of the sensor, since for a fundamental frequency of 150 MHz the thickness of the crystal is reduced to about 11 μm. The most appropriate way to solve the fragility problem is through Inverted Mesa technology [69]. In practice, the improvement has so far been more modest than predicted by theory [74]. An enhancement

of two orders of magnitude in both sensitivity and LOD has been reported in biosensing applications using HFF-QCMD sensors up to 150MHz [75]–[82]. Nevertheless, HFF resonators offer a unique approach to miniaturizing and parallelizing QCMD-based assays through the design of the monolithic resonator arrays with low-volume elements, thus also improving the throughput and reducing reagent consumption.

A new and improved QCRs generation based on HFF-QCMD concept could be employed in applications that range from Point of-Care (PoC) devices for disease diagnostics, health monitoring, and treatment monitoring in personalized medicine [47], [48] to devices for analysis of active substances and pathogens in food and environmental safety [10].

In the next section, the remaining challenges for QCM technology to further progress in those aspects demanded by current novel applications are explained.

1.5.1. New QCM sensors generation and current challenges

Reduction of the dimensions of the HFF-QCMD resonators establishes one of the advantages of this technology: its integration capacity. This characteristic makes possible manufacturing monolithic arrays (MHFF-QCMD) with independent resonators in a single reduced-size wafer [83], [84], [93]–[96], [85]–[92]. MHFF-QCMD has multiple advantages: low cost per sensor, less sample/reagent consumption, ability to detect minute amounts of analytes in complex samples, shorter detection assay time and faster sensing response. This makes them suitable to meet the basic requirements of High-Throughput Screening (HTS) applications, where multiple analytes must be detected simultaneously.

MHFF-QCMD can be considered as the next generation of QCMD sensors, however, it remains in its infancy [97] and much work has to be done in terms of optimizing its design for practical applications [98], [99]. The **first challenge** to undertake has to do with interferences between array elements. More insight to ensure independent operation of the individual sensor elements is a key challenge to address. Interaction between sensors can be mediated electrically, mechanically or via de fluidic path. Design criteria of the electrodes, as well as, of the sensors' dimensions in the array to reduce inharmonic modes and to minimize crosstalk (electrical interaction) are dealt with more detail in section 3.1.1.

Second challenge concerns the stringent requirements that HFF-QCMD operation places on the readout circuit. On the one hand, the increase in the fundamental resonance frequency, which leads to an improvement in sensitivity, implies a reduction in the quality factor of the sensors. This means reducing frequency stability, making necessary developing low noise characterization systems and improved measurement and processing methods. On the other hand, multiple overtone measurements are increasingly recognized as an important extension of the QCM technique. Probing the resonator at multiple overtones, providing both Δf_r and ΔD, allows enhancing the physical and biological interpretation of very different phenomena that take place over the sensor surface. [83].When working with HFF-QCM arrays, fast operation readout systems are necessary to measure in real time Δf_r and ΔD for each element of the array in several overtones. This issue will be discussed with more detail in section 3.2.1.

The aforementioned advantages of the MHFF-QCMD technology make it valid to be used as basis for Lab-on-a-chip devices (LoC) and, thus, cover some of the drawbacks of conventional bulk analytical methods that relay on expensive centralized facilities [100], [101]. In this sense, it is also important to face the **third challenge** when working with MHFF-QCMD technology: the development of adequate electrical, mechanical and fluidic interfaces. Since most applications are carried out in liquid medium, it is essential to have a suitable fluid cell. The planar surface in MHFF-QCMD makes easier the integration of a top microfluidic layer, which defines the small volume flow channels in every individual element of the array, confining the liquid over the surface of the sensor, while isolating the electrical contact. Biocompatibility, low cost and easy manufacturing and assembly are much demanded features for microfluidic cells that are part of disposable or non-disposable cartridges [98]. Fluidic cells have already been developed for several low-frequency single QCMD sensors [84], [102]–[104] or for single sensors over 50MHz [91], [98], [105]–[109]. Currently, advanced commercial systems offer measurements with at most four sensors at a time, each of which has to be operated individually. Therefore, the development of cartridges for monolithic QCMD arrays continues being one of the challenges to address. Microfluidic field has the potential to enable new capabilities and applications in the areas of biology and chemistry. An integration strategy between PCB, array and microfluidics will be described in section 3.3.1.

Fourth challenge is related to the processing of the electrical signal acquired for improving results interpretation. Although MQCM technology is well-suited for biosensing, there are still remaining challenges that prevent its adoption for portable applications. The stability of the sensor can be strongly affected by some effects intrinsic to the sensor setup (such as mechanical stress exerted by the measurement cell or electronic noise of the characterization system) and external factors (such as temperature, humidity, vibrations, or pressure) [110]. Low stability could mask the signal of interest, which, in turn, could produce a LoD deterioration and a lack of reliability in the measurements. Isolating the sensor response from those factors is not trivial and increases the complexity and cost of the testing equipment, often preventing the development of lightweight and portable instruments appropriate for real-time applications. To address LoC solutions with real portable biosensing devices a more complex signal conditioning stage, combining different strategies, is required. At some point, selective filtering [111], principal component analysis (PCA) [112], wavelets, or combinations of PCA with neuronal networks [113] have been used in literature. Each one of these techniques has its pros and cons, which will be summarized in section 3.4.1.

The objective of this thesis is to address with MHFF-QCM challenges previously described and to contribute to their achievement with further technological developments, which will be tested by means of a proof of concept in the field of food safety

1.6. References

[1] P. R. Whitehorn, S. O'Connor, F. L. Wackers, and D. Goulson, "Neonicotinoid Pesticide Reduces Bumble Bee Colony Growth and Queen Production," *Science (80-.).*, vol. 336, no. 6079, pp. 351–352, Apr. 2012.

[2] M. Henry *et al.*, "A Common Pesticide Decreases Foraging Success and Survival in Honey Bees," *Science (80-.).*, vol. 336, no. 6079, pp. 348–350, Apr. 2012.

[3] D. vanEngelsdorp and M. D. Meixner, "A historical review of managed honey bee populations in Europe and the United States and the factors that may affect them," *J. Invertebr. Pathol.*, vol. 103, pp. S80–S95, Jan. 2010.

[4] C. H. Krupke, G. J. Hunt, B. D. Eitzer, G. Andino, and K. Given, "Multiple Routes of Pesticide Exposure for Honey Bees Living Near Agricultural Fields," *PLoS One*, vol. 7, no. 1, p. e29268, Jan. 2012.

[5] P. Edder, D. Ortelli, and C. Corvi, "Survey of Antibiotics Residues in Honey on the Swiss Market," p. 2200.

[6] "Statement on the findings in recent studies investigating sub-lethal effects in bees of some neonicotinoids in consideration of the uses currently authorised in Europe," *EFSA J.*, vol. 10, no. 6, Jun. 2012.

[7] "Scientific Opinion on the science behind the development of a risk assessment of Plant Protection Products on bees (Apis mellifera , Bombus spp. and solitary bees)," *EFSA J.*, vol. 10, no. 5, p. 2668, May 2012.

[8] J. D. van Klaveren and P. E. Boon, "Probabilistic risk assessment of dietary exposure to single and multiple pesticide residues or contaminants: Summary of the work performed within the SAFE FOODS project," *Food Chem. Toxicol.*, vol. 47, no. 12, pp. 2879–2882, Dec. 2009.

[9] V. Gaudin, "Advances in biosensor development for the screening of antibiotic residues in food products of animal origin – A comprehensive review," *Biosens. Bioelectron.*, vol. 90, no. September 2016, pp. 363–377, 2017.

[10] B. E. Hawkins, M. Cooper, and I. Campbell, "Acoustic Detection Technology in the Analysis of Biomolecular Interactions," pp. 30–33, 2006.

[11] E. Mauriz *et al.*, "Determination of carbaryl in natural water samples by a surface plasmon resonance flow-through immunosensor," *Biosens. Bioelectron.*, vol. 21, no. 11, pp. 2129–2136, May 2006.

[12] F. and agriculture organization of the united nations and world health Organization, "A 'missing' family of classical orthogonal polynomials," *J. Phys. A Math. Theor.*, vol. 44, no. 8, p. 085201, Feb. 2011.

[13] C. Alimentarius, "Maximum Residue Limits (MRLs)." [Online]. Available: http://www.fao.org/fao-who-codexalimentarius/codex-texts/maximum-residue-limits/en/.

[14] F. Paredes and J. J. Roca, *Offarm*, vol. 23, no. 3. Doyma, 2004.

[15] J. C. Keller, Roy A; Giddings, "chromatography," *Encyclopedia Britannica*. [Online]. Available: https://www.britannica.com/science/chromatography.

[16] D. Debayle, G. Dessalces, and M. F. Grenier-Loustalot, "Multi-residue analysis of traces of pesticides and antibiotics in honey by HPLC-MS-MS," *Anal. Bioanal. Chem.*, vol. 391, no. 3, pp. 1011–1020, Jun. 2008.

[17] M. B. Albero-Romano, "Determinación de residuos de contaminantes orgánicos en miel y zumos.," 2009.

[18] C. Blasco, M. Fernández, Y. Picó, and G. Font, "Comparison of solid-phase microextraction and stir bar sorptive extraction for determining six organophosphorus insecticides in honey by liquid chromatography-mass spectrometry," in *Journal of Chromatography A*, 2004, vol. 1030, no. 1–2, pp. 77–85.

[19] C. Pirard *et al.*, "Development and validation of a multi-residue method for pesticide determination in honey using on-column liquid-liquid extraction and liquid chromatography-tandem mass spectrometry," *J. Chromatogr. A*, vol. 1152, no. 1–2, pp. 116–123, 2007.

[20] P. A. Souza Tette, L. R. Guidi, M. B. De Abreu Glória, and C. Fernandes, "Pesticides in honey: A review on chromatographic analytical methods," *Talanta*, vol. 149, pp. 124–141, 2016.

[21] I. Rezić, A. J. M. Horvat, S. Babić, and M. Kaštelan-Macan, "Determination of pesticides in honey by ultrasonic solvent extraction and thin-layer chromatography," *Ultrason. Sonochem.*, vol. 12, no. 6, pp. 477–481, 2005.

[22] J. Atienza, J. J. Jiménez, J. L. Bernal, and M. T. Martín, "Supercritical fluid extraction of fluvalinate residues in honey. Determination by high-performance liquid chromatography," *J. Chromatogr. A*, vol. 655, no. 1, pp. 95–99, 1993.

[23] J. J. Jiménez, J. Atienza, and J. L. Bernal, "Characterization of fluvalinate residues in honey by gas chromatography–atomic emission detection and gas chromatography–mass spectrometry," *J. High Resolut. Chromatogr.*, vol. 18, no. 6, pp. 367–372, 1995.

[24] C. Blasco *et al.*, "Assessment of Pesticide Residues in Honey Samples from Portugal and Spain," *J. Agric. Food Chem.*, vol. 51, no. 27, pp. 8132–8138, 2003.

[25] S. R. Rissato, M. S. Galhiane, F. R. N. Knoll, and B. M. Apon, "Supercritical fluid extraction for pesticide multiresidue analysis in honey: Determination by gas chromatography with electron-capture and mass spectrometry detection," *J. Chromatogr. A*, vol. 1048, no. 2, pp. 153–159, 2004.

[26] M. García-Chao, M. J. Agruña, G. F. Calvete, V. Sakkas, M. Llompart, and T. Dagnac, "Validation of an off line solid phase extraction liquid chromatography-tandem mass spectrometry method for the determination of systemic insecticide residues in honey and pollen samples collected in apiaries from NW Spain," *Anal. Chim. Acta*, vol. 672, no. 1–2, pp. 107–113, 2010.

[27] G. Amendola, P. Pelosi, and R. Dommarco, "Solid-phase extraction for multi-residue analysis of pesticides in honey," *J. Environ. Sci. Heal. - Part B Pestic. Food Contam. Agric. Wastes*, vol. 46, no. 1, pp. 24–34, 2010.

[28] S. Bonzini, P. Tremolada, I. Bernardinelli, M. Colombo, and M. Vighi, "Predicting pesticide fate in the hive (part 1): Experimentally determined τ-Fluvalinate residues in bees, honey and wax," *Apidologie*, vol. 42, no. 3, pp. 378–390, 2011.

[29] M. Juan-Borrás, A. Periche, E. Domenech, and I. Escriche, "Routine quality control in honey packaging companies as a key to guarantee consumer safety. The case of the presence of sulfonamides analyzed with LC-MS-MS," *Food Control*, vol. 50, no. July 2014, pp. 243–249, 2015.

[30] B. Albero, C. Sánchez-Brunete, and J. L. Tadeo, "Multiresidue determination of pesticides in honey by matrix solid-phase dispersion and gas chromatography with electron-capture detection," *J. AOAC Int.*, vol. 84, no. 4, pp. 1165–1171, 2001.

[31] C. Sánchez-Brunete, B. Albero, E. Miguel, and J. L. Tadeo, "Determination of insecticides in honey by matrix solid-phase dispersion and gas chromatography with nitrogen-phosphorus detection and mass spectrometric confirmation," *J. AOAC Int.*, vol. 85, no. 1, pp. 128–133, 2002.

[32] J. J. Jiménez, J. L. Bernal, M. J. Del Nozal, M. T. Martín, and A. L. Mayorga, "Solid-phase microextraction applied to the analysis of pesticide residues in honey using gas chromatography with electron-capture detection," *J. Chromatogr. A*, vol. 829, no. 1–2, pp. 269–277, 1998.

[33] M. Volante *et al.*, "A SPME-GC-MS approach for antivarroa and pesticide residues analysis in honey," *Chromatographia*, vol. 54, no. 3–4, pp. 241–246, 2001.

[34] J. Yu, C. Wu, and J. Xing, "Development of new solid-phase microextraction fibers by sol-gel technology for the determination of organophosphorus pesticide multiresidues in food," *J. Chromatogr. A*, vol. 1036, no. 2, pp. 101–111, May 2004.

[35] N. G. Tsiropoulos and E. G. Amvrazi, "Determination of pesticide residues in honey by single-drop microextraction and gas chromatography," *J. AOAC Int.*, 2011.

[36] A. Kamel, "Refined methodology for the determination of neonicotinoid pesticides and their metabolites in honey bees and bee products by liquid chromatography-tandem mass spectrometry (LC-MS/MS)," *J. Agric. Food Chem.*, vol. 58, no. 10, pp. 5926–5931, 2010.

[37] M. R. F. Sampaio, D. Tomasini, L. V. Cardoso, S. S. Caldas, and E. G. Primel, "Determination of pesticide residues in sugarcane honey by QuEChERS and liquid chromatography," *J. Braz. Chem. Soc.*, vol. 23, no. 2, pp. 197–205, 2012.

[38] M. Proietto Galeano *et al.*, "UHPLC/MS-MS analysis of six neonicotinoids in honey by modified QuEChERS: Method development, validation, and uncertainty measurement," *Int. J. Food Sci.*, vol. 2013, pp. 1–7, 2013.

[39] M. W. Kujawski *et al.*, "Determining pesticide contamination in honey by LC-ESI-MS/MS - Comparison of pesticide recoveries of two liquid-liquid extraction based approaches," *LWT - Food Sci. Technol.*, vol. 56, no. 2, pp. 517–523, 2014.

[40] P. Calatayud-Vernich, F. Calatayud, E. Simó, and Y. Picó, "Efficiency of QuEChERS approach for determining 52 pesticide residues in honey and honey bees," *MethodsX*, vol. 3, pp. 452–458, Jan. 2016.

[41] A. Gillet *et al.*, "Chemical and microbiological analysis of neomycin," *J. Pharm. Belg.*, vol. 27, no. 4, pp. 381–401, 1972.

[42] R. Bogaerts and F. Wolf, "A standardized method for the detection of residues of antibacterial substances in meat.," *Fleischwirtschaft*, vol. 60, no. 4, pp. 672–673, 1980.

[43] R. Bogaerts, J. M. Degroodt, and D. De Vos, "[The microbiological assay of chloramphenicol hemisuccinate and application of the method with pyrrolidinomethyltetracycline (rolitetracycline) (author's transl)].," *Ann. Pharm. Fr.*, vol. 40, no. 1, pp. 37–41, Apr. 1982.

[44] L. Cervera-Chiner, "Aplicación y validación de la tecnología de inmunosensores piezoeléctricos de alta frecuencia (HFF-QCM) para la detección de pesticidas y antibióticos en miel," 2020.

[45] S. Zhang, A. Garcia-D'Angeli, J. P. Brennan, and Q. Huo, "Predicting detection limits of enzyme-linked immunosorbent assay (ELISA) and bioanalytical techniques in general," *Analyst*, vol. 139, no. 2, pp. 439–445, 2014.

[46] Thermo Fisher Scientific Inc., "Overview of Elisa," 2019. [Online]. Available: https://www.thermofisher.com/nl/en/home/life-science/protein-biology/protein-biology-learning-center/protein-biology-resource-library/pierce-protein-methods/overview-elisa.html#4.

[47] L. C. Clark and C. Lyons, "Electrode systems for continuous monitoring in

cardiovascular surgery," *Ann. N. Y. Acad. Sci.*, vol. 102, no. 1, pp. 29–45, Dec. 2006.

[48] Y. Montagut, J. Garcia, Y. Jimenez, C. March, A. Montoya, and A. Arnau, "QCM Technology in Biosensors," in *Biosensors - Emerging Materials and Applications*, InTech, 2011.

[49] L. Cervera-chiner, C. March, and A. Arnau, "Detection of DDT and carbaryl pesticides in honey by means of immunosensors based on high fundamental frequency quartz crystal microbalance (HFF-QCM)," no. February, 2020.

[50] A. Montoya, A. Ocampo, and C. March, "Fundamentals of Piezoelectric Immunosensors," in *Piezoelectric Transducers and Applications*, Berlin, Heidelberg: Springer Berlin Heidelberg, pp. 289–306.

[51] M. Nirschl, F. Reuter, and J. Vörös, "Review of Transducer Principles for Label-Free Biomolecular Interaction Analysis," *Biosensors*, vol. 1, no. 3, pp. 70–92, Jul. 2011.

[52] M. Hussain, F. Rupp, H. P. Wendel, and F. K. Gehring, "Bioapplications of acoustic crystals, a review," *TrAC Trends Anal. Chem.*, vol. 102, pp. 194–209, 2018.

[53] P. Fernando, G. F.; Webb, D. J.; Ferdinand, "Optical-Fiber Sensors," *MRS Bull.*, vol. 27, pp. 359–364, 2002.

[54] A. A. Fernández, Román;Calero, María; Jiménez, Yolanda ; Arnau, "A Real-Time Method for Improving Stability of Monolithic Quartz Crystal Microbalance Operating under Harsh Environmental Conditions," *Sensors*, 2021.

[55] A. Alassi, M. Benammar, and D. Brett, "Quartz Crystal Microbalance Electronic Interfacing Systems: A Review," *Sensors*, vol. 17, no. 12, p. 2799, Dec. 2017.

[56] J. Rickert, W. Göpel, G. L. Hayward, B. A. Cavic, and M. Thompson, "Biosensors Based on Acoustic Wave Devices," *Sensors Updat.*, vol. 5, no. 1, pp. 105–139, Apr. 1999.

[57] N. G. Durmuş, R. L. Lin, M. Kozberg, D. Dermici, A. Khademhosseini, and U. Demirci, "Acoustic-Based Biosensors," in *Encyclopedia of Microfluidics and Nanofluidics*, Boston, MA: Springer US, 2014, pp. 1–15.

[58] J. W. S. Rayleigh, "The Theory of Sound," *Dover Publ. New York*, 1945.

[59] G. Sauerbrey, "Verwendung von Schwingquarzen zur Wägung dünner Schichten und zur Mikrowägung," *Zeitschrift für Phys.*, vol. 155, no. 2, pp. 206–222, 1959.

[60] D. Johannsmann, *The Quartz Crystal Microbalance in Soft Matter Research*. Cham: Springer International Publishing, 2015.

[61] P. L. Konash and G. J. Bastiaans, "Piezoelectric crystals as detectors in liquid chromatography," *Anal. Chem.*, vol. 52, no. 12, pp. 1929–1931, Oct. 1980.

[62] V. E. Granstaff and S. J. Martin, "Characterization of a thickness-shear mode quartz resonator with multiple nonpiezoelectric layers," *J. Appl. Phys.*, vol. 75, no. 3, pp. 1319–1329, Feb. 1994.

[63] A. Arnau, "Models for Resonant Sensors.," in *Piezoelectric Transducers and Applications*, 2nd ed., Springer Berlin Heidelberg.

[64] Y. Jiménez, M. Otero, and A. Arnau, "QCM Data Analysis and Interpretation," in *Piezoelectric Transducers and Applications*, Berlin, Heidelberg: Springer Berlin Heidelberg, 2008, pp. 331–398.

[65] A. Arnau, Y. Jiménez, and T. Sogorb, "An extended Butterworth-Van Dyke model for quartz crystal microbalance applications in viscoelastic fluid media," *IEEE*

Trans. Ultrason. Ferroelectr. Freq. Control, vol. 48, no. 5, pp. 1367–1382, Sep. 2001.

[66] R. Lucklum, D. Soares, and K. Kanazawa, *Piezoelectric Transducers and Applications*, Second Edi. Berlin, Heidelberg: Springer Berlin Heidelberg, 2008.

[67] A. Arnau, "El crital de cuarzo como sensor microgravimétrico en medios amortiguados (Tomos 1 y 2)," 1999.

[68] A. A. Vives, Ed., *Piezoelectric Transducers and Applications*. Berlin, Heidelberg: Springer Berlin Heidelberg, 2008.

[69] D. S. Ralf Lucklum, Kay Kanazawa, *Piezoelectric Transducers and Applications*. Berlin, Heidelberg, Heidelberg: Springer Berlin Heidelberg, 2008.

[70] M. Minunni, M. Mascini, and S. Tombelli, "Analytical Applications of QCM-based Nucleic Acid Biosensors," in *Piezoelectric Sensors*, Springer Berlin Heidelberg, 2007, pp. 211–235.

[71] F. Höök and B. Kasemo, "The QCM-D Technique for Probing Biomacromolecular Recognition Reactions," in *Piezoelectric Sensors*, Springer Berlin Heidelberg, 2007, pp. 425–447.

[72] F. L. Dickert and P. A. Lieberzeit, "Imprinted Polymers in Chemical Recognition for Mass-Sensitive Devices," in *Piezoelectric Sensors*, Springer Berlin Heidelberg, 2007, pp. 173–210.

[73] R. Fernández, P. García, M. García, J. García, Y. Jiménez, and A. Arnau, "Design and Validation of a 150 MHz HFFQCM Sensor for Bio-Sensing Applications," *Sensors*, vol. 17, no. 9, p. 2057, Sep. 2017.

[74] L. Rodriguez-Pardo, J. Fariña, C. Gabrielli, H. Perrot, and R. Brendel, "Resolution in quartz crystal oscillator circuits for high sensitivity microbalance sensors in damping media," *Sensors Actuators B Chem.*, vol. 103, no. 1–2, pp. 318–324, Sep. 2004.

[75] E. Uttenthaler, M. Schräml, J. Mandel, and S. Drost, "Ultrasensitive quartz crystal microbalance sensors for detection of M13-Phages in liquids," *Biosens. Bioelectron.*, vol. 16, no. 9–12, pp. 735–743, 2001.

[76] J. V. García *et al.*, "Love Mode surface acoustic wave and high fundamental frequency quartz crystal microbalance immunosensors for the detection of carbaryl pesticide," in *Procedia Engineering*, 2014, vol. 87.

[77] C. March *et al.*, "High-frequency phase shift measurement greatly enhances the sensitivity of QCM immunosensors," *Biosens. Bioelectron.*, vol. 65, pp. 1–8, Mar. 2015.

[78] A. Montoya *et al.*, "A high fundamental frequency (HFF)-based QCM immunosensor for tuberculosis detection," *Curr. Top. Med. Chem.*, vol. 17, no. 14, 2017.

[79] R. Fernández, P. García, M. García, J. V. García, Y. Jiménez, and A. Arnau, "Design and validation of a 150 MHz HFFQCM sensor for bio-sensing applications," *Sensors (Switzerland)*, vol. 17, no. 9, pp. 1–13, 2017.

[80] L. Cervera-Chiner *et al.*, "High Fundamental Frequency Quartz Crystal Microbalance (HFF-QCM) immunosensor for pesticide detection in honey," *Food Control*, vol. 92, pp. 1–6, 2018.

[81] L. Cervera-Chiner, C. March, A. Arnau, Y. Jiménez, and Á. Montoya, "Detection of DDT and carbaryl pesticides in honey by means of immunosensors based on high fundamental frequency quartz crystal microbalance (HFF-QCM)," *J. Sci. Food Agric.*, vol. 100, no. 6, pp. 2468–2472, Apr. 2020.

[82] L. Cervera-Chiner *et al.*, "High Fundamental Frequency Quartz Crystal Microbalance (HFF-QCMD) Immunosensor for detection of sulfathiazole in honey," *Food Control*, vol. 115, no. February, p. 107296, 2020.

[83] T. Tatsuma, Y. Watanabe, N. Oyama, K. Kitakizaki, and M. Haba, "Multichannel quartz crystal microbalance," *Anal. Chem.*, vol. 71, no. 17, pp. 3632–3636, 1999.

[84] W. Tao, P. Lin, Y. Ai, H. Wang, S. Ke, and X. Zeng, "Multichannel quartz crystal microbalance array: Fabrication, evaluation, application in biomarker detection," *Anal. Biochem.*, vol. 494, pp. 85–92, Feb. 2016.

[85] J. Rabe, V. Seidemann, and S. Buettgenbach, "Monolithic fabrication of wireless miniaturized quartz crystal microbalance (QCM-R) array for biochemical sensing," in *TRANSDUCERS '03. 12th International Conference on Solid-State Sensors, Actuators and Microsystems. Digest of Technical Papers (Cat. No.03TH8664)*, 2003, vol. 2, no. 7, pp. 1875–1876.

[86] J. Rabe, S. Büttgenbach, B. Zimmermann, and P. Hauptmann, "Design, manufacturing, and characterization of high-frequency thickness-shear mode resonators," *Proc. Annu. IEEE Int. Freq. Control Symp.*, pp. 106–112, 2000.

[87] T. Leblois, C. R. Tellier, and T. Messaoudi, "Chemical etching of Y-rotated quartz plates: Experiments and theoretical approach," *Sensors Actuators, A Phys.*, vol. 61, no. 1–3, pp. 405–414, 1997.

[88] Y.-Y. Chen *et al.*, "Acoustic interference suppression of quartz crystal microbalance sensor arrays utilizing phononic crystals," *Appl. Phys. Lett.*, vol. 102, no. 15, p. 153514, Apr. 2013.

[89] J. R. Vig, R. L. Filler, and Y. Kim, "Uncooled IR imaging array based on quartz microresonators," *J. Microelectromechanical Syst.*, vol. 5, no. 2, pp. 131–137, 1996.

[90] T. Abe and M. Esashi, "One-chip multichannel quartz crystal microbalance (QCM) fabricated by Deep RIE," *Sensors Actuators A Phys.*, vol. 82, no. 1, pp. 139–143, 2000.

[91] P. Kao, S. Doerner, T. Schneider, D. Allara, P. Hauptmann, and S. Tadigadapa, "A micromachined quartz resonator array for biosensing applications," *J. Microelectromechanical Syst.*, vol. 18, no. 3, pp. 522–530, 2009.

[92] V. N. Hung, T. Abe, P. N. Minh, and M. Esashi, "Miniaturized, highly sensitive single-chip multichannel quartz-crystal microbalance," *Appl. Phys. Lett.*, vol. 81, no. 26, pp. 5069–5071, 2002.

[93] K. Seidler, M. Polreichová, P. A. Lieberzeit, and F. L. Dickert, "Biomimetic yeast cell typing - Application of QCMs," *Sensors*, vol. 9, no. 10, pp. 8146–8157, 2009.

[94] S. Guan and R. B. Nielsen, "Rapid scan Fourier transform detection of a frequency encoded quartz crystal microbalance array," *Rev. Sci. Instrum.*, vol. 74, no. 12, pp. 5241–5248, Dec. 2003.

[95] M. M. A. François, E. Ergezen, J. Desa, K. Pourrezaei, and R. Lec, "Multi-layer interfacial property analysis using a Multi-frequency Thickness Shear Mode (MFTSM) device built on a single-chip," *Proc. - IEEE Ultrason. Symp.*, pp. 256–259, 2007.

[96] A. Tuantranont, A. Wisitsora-at, P. Sritongkham, and K. Jaruwongrungsee, "A review of monolithic multichannel quartz crystal microbalance: A review," *Anal. Chim. Acta*, vol. 687, no. 2, pp. 114–128, 2011.

[97] J. P. Lafleur, A. Jönsson, S. Senkbeil, and J. P. Kutter, "Recent advances in lab-on-a-chip for biosensing applications," *Biosens. Bioelectron.*, vol. 76, pp. 213–233, 2016.

[98] L. El Fissi *et al.*, "OSTEMER polymer as a rapid packaging of electronics and microfluidic system on PCB," *Sensors Actuators, A Phys.*, vol. 285, pp. 511–518, 2019.

[99] G. Papadakis, J. M. Friedt, M. Eck, D. Rabus, G. Jobst, and E. Gizeli, "Optimized acoustic biochip integrated with microfluidics for biomarkers detection in molecular diagnostics," *Biomed. Microdevices*, vol. 19, no. 3, pp. 1–11, 2017.

[100] B. Nasseri, N. Soleimani, N. Rabiee, A. Kalbasi, M. Karimi, and M. R. Hamblin, "Point-of-care microfluidic devices for pathogen detection," *Biosens. Bioelectron.*, vol. 117, no. May, pp. 112–128, 2018.

[101] G. Huang *et al.*, "A rapid, low-cost, and microfluidic chip-based system for parallel identification of multiple pathogens related to clinical pneumonia," *Sci. Rep.*, vol. 7, no. 1, pp. 1–10, 2017.

[102] D. Croux *et al.*, "Development of multichannel quartz crystal microbalances for MIP-based biosensing," *Phys. Status Solidi Appl. Mater. Sci.*, vol. 209, no. 5, pp. 892–899, 2012.

[103] K. Jaruwongrungsee, U. Waiwijit, A. Wisitsoraat, M. Sangworasil, C. Pintavirooj, and A. Tuantranont, "Real-time multianalyte biosensors based on interference-free multichannel monolithic quartz crystal microbalance," *Biosens. Bioelectron.*, vol. 67, pp. 576–581, 2015.

[104] M. A. Amer, A. Turo, J. Salazar, L. Berlanga-Herrera, M. J. Garcia-Hernandez, and J. A. Chavez, "Multichannel QCM-based system for continuous monitoring of bacterial biofilm growth," *IEEE Trans. Instrum. Meas.*, vol. 69, no. 6, pp. 2982–2995, 2020.

[105] J. Rabe, S. Büttgenbach, J. Schröder, and P. Hauptmann, "Monolithic miniaturized quartz microbalance array and its application to chemical sensor systems for liquids," *IEEE Sens. J.*, vol. 3, no. 4, pp. 361–368, 2003.

[106] P. Kao, D. Allara, and S. Tadigadapa, "Fabrication and performance characteristics of high-frequency micromachined bulk acoustic wave quartz resonator arrays," *Meas. Sci. Technol.*, vol. 20, no. 12, p. 124007, Dec. 2009.

[107] H. Ogi, H. Naga, Y. Fukunishi, M. Hirao, and M. Nishiyama, "170-MHz Electrodeless Quartz Crystal Microbalance Biosensor: Capability and Limitation of Higher Frequency Measurement," *Anal. Chem.*, vol. 81, no. 19, pp. 8068–8073, Oct. 2009.

[108] H. Becker and C. Gärtner, "Polymer microfabrication technologies for microfluidic systems," *Anal. Bioanal. Chem.*, vol. 390, no. 1, pp. 89–111, 2008.

[109] H. Min *et al.*, "Modified Random Sequential Adsorption Model for Understanding Kinetics of Proteins Adsorption at a Liquid–Solid Interface," *Langmuir*, vol. 33, no. 29, pp. 7215–7224, Jul. 2017.

[110] J. R. Vig and F. L. Walls, "A review of sensor sensitivity and stability," *Proc. Annu. IEEE Int. Freq. Control Symp.*, pp. 30–33, 2000.

[111] E. S. Muckley, C. Anazagasty, C. B. Jacobs, T. Hianik, and I. N. Ivanov, "Low-cost scalable quartz crystal microbalance array for environmental sensing," in *Organic Sensors and Bioelectronics IX*, 2016, vol. 9944.

[112] E. Corradi *et al.*, "An objective, principal-component-analysis (PCA) based, method which improves the quartz-crystal-microbalance (QCM) sensing performance," *Sensors Actuators, A Phys.*, vol. 315, 2020.

[113] B. Mumyakmaz, A. Özmen, M. A. Ebeoğlu, C. Taşaltin, and I. Gürol, "A study on the development of a compensation method for humidity effect in QCM sensor responses," *Sensors Actuators, B Chem.*, vol. 147, no. 1, pp. 277–282, 2010.

[114] Y. Montagut, C. March, A. Arnau, P. W. Group, and H. C. Technology, “Validation of a Phase-Mass Characterization Concept and Interface for Acoustic Biosensors,” pp. 4702–4720, 2011.

2. Thesis objectives

The **main objective** of this thesis is the design and development of a new generation of monolithic high-resolution quartz crystal microbalance sensors (MHFF-QCM), which combined with immunoassays, allow for the simultaneous detection of chemical residues with very different chemical composition. This technology will set the foundation of a new high-throughput screening method to be used as an alternative and/or complementary analysis technique to the classical ones. The novel analytical method should meet the requirements demanded from honey packing industry, which mainly are low cost, fast and automated operation and easy handling.

In this context, the objectives of this doctoral thesis are the following:

1. Design and development of a High Fundamental Frequency Quartz Crystal Microbalance Array for high-throughput screening and low-volume sensing applications in liquid. This objective comprises the following sub-objectives:
   1.1. Optimization of the resonator and electrode dimensions to ensure independent operation of individual sensor elements. This implies to minimize crosstalk and to separate spurious modes from the fundamental.
   1.2. Physical evaluation of the array including MESA region characterization and surface roughness.
   1.3. Electrical characterization of the array, which includes evaluation of the resonance frequency, quality factor, spurious mode suppression and interactions between array elements (crosstalk).
2. Development of a fast operation method for measuring Δf_r and $\Delta\Gamma$ (ΔD) resonator parameters at multiple overtones with the capability of characterizing each resonator of the array with high-resolution time and high precision. The method should account for the electrical parasitic effects to make the measurement more robust against electrical artefacts. This objective comprises the following sub-objectives:
   2.1. Implementation of the firmware over the hardware previously developed in the group for the characterization system [114].
   2.2. Evaluation of the method performance with single sensors for two types of real experiments: (I) Applications that involve great changes in both Δf_r and $\Delta\Gamma$; and (II) applications where changes in Δf_r are larger than in $\Delta\Gamma$.
   2.3. Evaluation of the method in the readout of multiple sensors integrated in the array in the adsorption of a model bioanalyte experiment.

3. Design and development of a microfluidic cartridge housing the HFF-QCM monolithic sensor array for its operation in flow and for its functionalization. This objective comprises the following sub-objectives:
   3.1. Development of a low-volume in-batch cell that allows performing immobilization processes on the sensing surfaces of the resonators in the array.
   3.2. Design of a microfluidic flow cell with low volume channels for parallel measurements and with a sealing mechanism to ensure liquid confinement while maintaining good stability. The device must provide an electrical, mechanical and thermal interface between the array and the electronic characterization system. Low cost and easy manufacturing and assembly are other key requirements. The device comprises developing a Printed Circuit Board, that allows connection to the characterization system, and a microfluidic structure based on biocompatible materials.
   3.3. Validation of the developed cartridge, which should be based in obtaining reproducible measurements of Δf_r and ΔD in both types of experiments: Air-to-liquid transition and the adsorption of a model bioanalyte.
4. Implementation of a signal processing method to improve the stability of Δf_r and ΔD measurements in real time. The method should overcome instabilities and LoD degradation due to unwanted environmental factors, such as pressure and temperature changes, as well as perturbations intrinsic to the sensor setup (mechanical stress exerted by the microfluidic cartridge and noise of the characterization system). This objective comprises the following sub-objectives:
   4.1. Development and implementation of the algorithm.
   4.2. Validation of the method capability to reduce frequency instability caused by intrinsic factors.
   4.3. Validation of the method in an adsorption of a model bioanalyte under external controlled factors consisting of temperature and flow rate gradients.
5. Validation of the technological developments resulting from the achievement of the previous objectives. The goal is to perform a proof of concept in which the novel developed technology could be used for the simultaneous detection of two chemical residues with very different chemical composition in honey. This objective comprises the following sub-objectives:

5.1. Development of a fast and simple competitive immunosensor for the simultaneous detection of the fungicide thiabendazole and the antibiotic sulfathiazole in honey samples.

5.2. Comparison of the results in terms or Limit of Detection, Limit of Quantification accuracy and precision with LC MS/MS chromatography as reference technique.

3. Results

3.1. High Fundamental Frequency (HFF) Monolithic Resonator Arrays for Biosensing Applications: Design, Simulations, Experimental Characterization.

Román Fernández, María Calero, Ilya Reiviakine, José Vicente García, María Isabel Rocha-Gaso, Antonio Arnau and Yolanda Jiménez

IEEE Sensors Journal, Volume 2, 1 January 2021, Pages 284 -295

Abstract

Miniaturized, high-throughput, cost-effective sensing devices are needed to advance lab-on-a-chip technologies for healthcare, security, environmental monitoring, food safety, and research application. Quartz crystal microbalance with dissipation (QCMD) is a promising technology for the design of such sensing devices, but its applications have been limited, until now, by low throughput and significant costs. In this work, we present the design and characterization of 24-element monolithic QCMD arrays for high-throughput and low-volume sensing applications in liquid. Physical properties such as geometry and roughness, and electrical properties such as resonance frequency, quality factor, spurious mode suppression, and interactions between array elements (crosstalk), are investigated in detail. In particular, we show that the scattering parameter, S_{21}, commonly measured experimentally to investigate crosstalk, contains contributions from the parasitic grounding effects associated with the acquisition circuitry. Finite element method simulations do not take grounding effects into account explicitly. However, these effects can be effectively modelled with appropriate equivalent circuit models, providing clear physical interpretation of the different contributions. We show that our array design avoids unwanted interactions between elements and discuss in detail aspects of measuring these interactions that are often-overlooked.

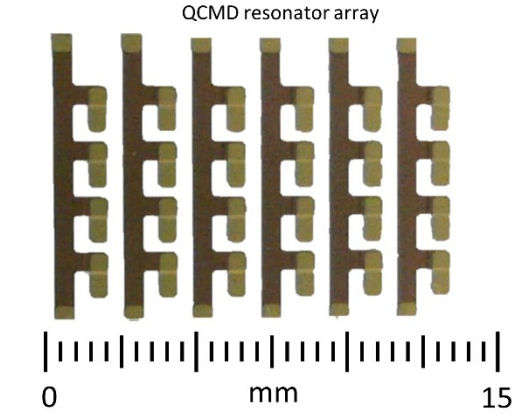

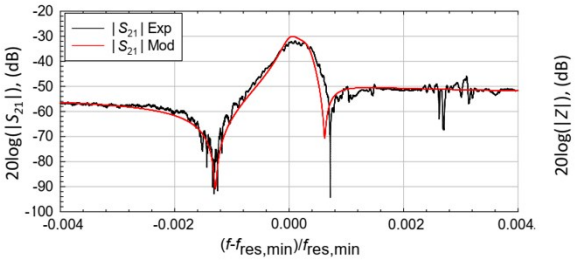

Keywords

Biosensors, crosstalk, finite element modelling simulation, food safety, monolithic arrays, nanotechnology, pathogen detection, piezoelectricity, point-of-care, QCMD, quartz crystal microbalance, quartz resonators.

3.1.1. Introduction

A wide range of bioanalytical applications requires robust and compart detectors (sensors) for rapid and reliable quantification of multiple analytes in small sample volume lab-on-a-chip (LoC) devices. Applications range from Point-of-Care (PoC) devices for disease diagnostics, health monitoring, and treatment monitoring in personalized medicine [1], [2] to devices for analysis of active substances and pathogens in food and environmental safety [3]. It is foreseen that LoC devices will replace costly conventional analytical methods that require trained personnel, centralized laboratories, relatively large sample volumes, and complex sample preparation protocols.

Critical requirements for the design of the sensors for LoC devices include simplicity and low cost, high sensitivity and specificity, low volume, portability and high-throughput. These sensors should be able to reliably detect specific analytes present at very low concentrations against a strong non-specific background;[4] allow deployment “in the field” (non-centralized laboratories, food processing plants, supermarkets, hospitals, patients’ homes); have low sample/reagent consumption; and enable simultaneous monitoring of multiple analytes at high speed to improve throughput [1], [2], [5]–[7]. Quartz Crystal Microbalance with Dissipation (QCMD) [8], [9] technology is emerging as a feasible candidate for their design, because it has the capability to satisfy all of those requirements.

QCMD is a sensing technique based on piezoelectric resonators, typically a quartz plate that is electrically excited to oscillate in a thickness-shear mode at its resonance frequency. Interactions between the resonator and its environment are sensed as changes in its resonance frequency and bandwidth (dissipation) [8], [10], [11]. In its simplest form, QCMD senses mass of the material absorbed at the resonator surface [12]. Specificity is conferred by modifying resonator surfaces with antibodies or antigens for performing direct-, sandwich-, or competitive immunoassays, [13] while surface modification with DNA probes allows for DNA-based detection; this works even in complex samples without further purification [14]. The sensitivity of QCMD-based immunoassays is, in the clinically relevant range, comparable to that of ELISA [13], and be further improved using the so-called high fundamental frequency (HFF) resonators, [15], [16] with frequencies in the 50MHz – 150MHz range [17]–[19]. HFF resonators offer an improvement in sensitivity because the frequency shift due to a given load scales with the square of the resonance frequency according to Sauerbrey relationship [12]. In practice,

the improvement has so far been more modest than predicted by theory [20], but HFF resonators offer a unique approach to miniaturizing and parallelizing QCMD-based assays through the design of the monolithic resonator arrays with low-volume elements, thus also improving the throughput and reducing reagent consumption. Design and testing of such monolithic HFF QCMD resonators arrays are the focus of the current contribution.

Our array design is shown in Figure 3.1.1. Arrays consist of 6 columns of 4 resonator elements each. The design of each of the array elements is based on that of the individual 150 MHz HFF resonators we reported previously [21]. Individual resonators had a one-sided inverted MESA geometry and were optimized in terms of size, electrode geometry, and inverted MESA region thickness for spurious mode suppression, operation in liquids, as well as constraints imposed by the manufacturing and integration with fluidics and electronics. [18], [19], [22]. Here, we characterize physical and electrical properties of these arrays (surface topography and roughness; resonance and inharmonic responses; interactions between array elements) and include a preliminary testing operation of the arrays in liquid.

Monolithic QCMD arrays designs have been presented previously. The initial focus was on gas sensing applications [23]–[25]. Sensing applications in liquids started appearing more recently [24]–[32]. These designs demonstrated the potential of monolithic sensor arrays for improving the throughput of the detection of biological samples in liquid environments with QCMD, but they also illustrated some of the problems associated with their design and implementation. In particular, the field of HFF resonator arrays remains in its infancy, and much remains to be done in terms of optimizing their design for practical applications. In this work, we investigate interactions (interference, crosstalk) between array elements, and how these interactions are measured and modelled. We compare experimental measurements of the crosstalk between array elements with the results of the finite element method (FEM) simulations. Our analysis reveals that the FEM simulations do not reproduce experimental results unless the parasitic grounding phenomena arising from the interface to the readout systems are explicitly taken into account; these have not previously received attention in the literature. We propose a lumped element equivalent circuit model that is much simpler than the FEM simulations. This simple model is able to provide a reliable representation of the experimental measurements. Moreover, it also allows a direct identification of the physical

contributions to the experimentally measured crosstalk between the array elements. This has practical implications for the design of monolithic HFF QCMD arrays because it allows a quick estimation of the inter-element interference and a means to identify its causes.

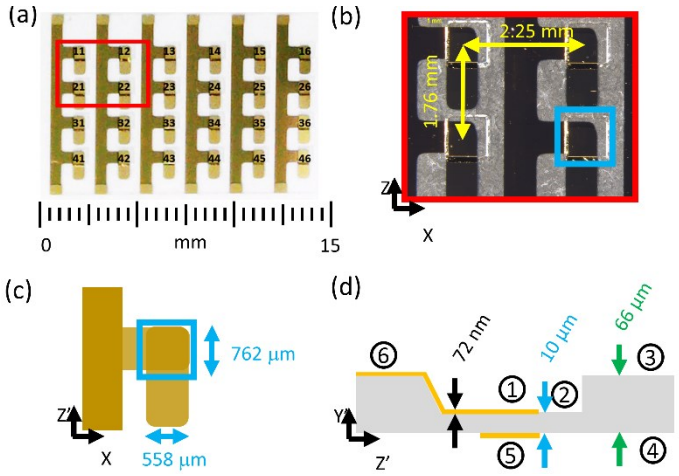

Figure 3.1.1. The main result of this work is the 24-element monolithic QCMD resonator array. A photograph is shown in (a). Numbers indicate the row and the column of each element. (b) An optical micrograph of four of the array elements (outlined with a red box in (a)). The image is taken in transmission, and therefore, the gold appears black, while quartz appears light-grey. Center-to-center distances between the individual array elements along the X and the Z' directions are indicated. (c) and (d): top view and side view of the individual array elements, respectively. The dimensions of the square MESA region, 762 µm × 762 µm, and the width of the gold electrode, 558 µm, are indicated in (c), while thicknesses of the substrate region, the MESA region, and the electrodes (gold with a Cr adhesion layer), are indicated in (d). Quartz crystallographic axes indicated in (b) also apply to (a). Note, that the working surface of the array is the one with the common electrodes, which in this figure is facing down. The "back" surface is the one with the MESA region.

3.1.2. Materials and Methods

3.1.2.1. Materials

Nanopure water used in this study was either analytical grade water (Panreac Química SLU, Barcelona, Spain), or produced with a Smart2Pure UVUF water purification system (Thermo Fisher Scientific, Barcelona, Spain). Distilled water was purchased at the local supermarket. 99.5% pure ethanol was from Panreac Química SLU. Ultra-pure nitrogen was from Al Air Liquide España, S.A. (Valencia, Spain), distributed with a gas filter pistol equipped with a 1 µm pore diameter PTFE filter (Skan AG, Allschwil, Switzerland). Acetone was of technical grade (Panreac Química SLU).

3.1.2.2. Array Manufacturing

Resonator arrays based on the one-sided inverted MESA technology were manufactured from 66μm thick AT-cut quartz wafers using photolithographic, wet etching, and thermal evaporation/filament plating technologies [18]. A photo of one of such arrays is shown in Figure 3.1.1, where the dimensions are also indicated. These arrays are designated AWS-Array2-24-150.0M (Advanced Wave Sensors S. L., Valencia, Spain) for future reference.

3.1.2.3. Array Preparation, Cleaning

Prior to use, the arrays were treated for 10 min in UV/ozone cleaner (BioForce Nanosciences Inc., Chicago, IL, USA), rinsed with ethanol, distilled water, dried with a stream of filtered nitrogen, and again treated with UV/ozone for another 10 min.

3.1.2.4. Array Characterization

3.1.2.4.1. Physical Characterization

The arrays were examined optically with an MZ APO Stereomicroscope from Leica Microsystems (Leica Microsistemas S.L.U, Barcelona, Spain). Surface morphology, topography & roughness, as well as presence of contamination, electrode alignment and presence of the etching channels in the quartz, were investigated with atomic force microscopy (AFM), scanning electron microscopy (SEM) and optical profilometry (OP).

SEM was performed with a Field Emission Scanning Electron Microscope (Ultra 55 FEGSEM, Zeiss, Oberkochen, Germany) at a working distance of 3.8mm with an accelerating voltage of 2kV and a vacuum level of 8×10^{-7}mbar at the chamber. The sample was mounted using a colloidal silver adhesive (SPI Supplies, West Chester, PA, USA).

AFM was performed with a Multimode 8 Atomic Force Microscope (Bruker, Billerica, MA, USA) equipped with a JV vertical engage scanner and a silicon tip with a spring constant of 26N/m and a resonance frequency of 300kHz (OTESTA-R3, Bruker, Billerica, MA, USA). For imaging, the arrays were attached to metal pucks with double-sided tape and imaged in tapping mode at scanning rates of 0.5Hz–1Hz (depending on the scan size) at optimal gain. Images were acquired in air. To acquire some of the images, arrays had to be cut.

The profile of the MESA surface of the array was analyzed with a Surftest SJ-410 profilometer (Mitutoyo, Kanagawa, Japan) with a 2µm radius and 60º angle 12AAC731 tip. The surface was scanned with a rate of 0.5mm/s.

3.1.2.4.2. Electrical Characterization

Complex admittance spectra of the array elements, as well as the scattering parameter S_{21} used to evaluate crosstalk between array elements, were measured with a DG8SAQ VNWA 3 Vector Network Analyzer (SDR-Kits, Melksham, Wiltshire, UK).

In order to connect the arrays to the network analyzer, we adapted a benchtop robot (F4300N.1, Fisnar Inc., Germantown, Wisconsin, USA, Figure 3.1.4a) to house two custom-designed printed circuit boards (PCBs): one mounted on the base of the robot, and the other one on its moving arm (Figure 3.1.4b, c). The array studied was effectively sandwiched between the two PCBs, mounted with the MESA region facing up. In this configuration, an electrical contact is established between the common electrode of the array (bottom in Figure 3.1.1a) and the bottom PCB, which is grounded, on one hand, and the individual electrodes of the different array elements and the top PCB through 0.6mm diameter spring contacts (Peak Test, Chester-Le-Street, County Durham, UK), on the other hand. The top PCB has five spring contacts, four of which are connected to four array elements, while the fifth one connects the bottom PCB to ground. The spring contacts assure an electrical connection without generating an uncontrolled pressure that could break the array. With this setup, we measured the admittance of each of the array elements, and cross-talk between pairs of elements (S_{ij}, $S_{i+1,j}$); (S_{ij},$S_{i,j+1}$); (S_{ij},$S_{i+1,j+1}$) with i=1··6 and j=1··4 along the X direction, Z' direction, and the diagonal. The setup was calibrated by placing the calibration components at the PCB level. The surfaces of the PCBs were degreased with acetone immediately prior to measurements.

Complex admittance spectra were used to visualize spurious modes and quantify the separation between the fundamental and the first spurious mode for each of the array elements. Around the resonance frequency, the complex admittance spectra were fit to a phase-shifted Lorentzian model proposed by Petri and co-workers [33], to obtain maximum conductance, G_{max}; resonance frequencies, f_{res}; and bandwidths, Γ, of the array elements. Quality factors, Q, were calculated from f_{res} and Γ as $Q = f_{res}/2\Gamma$. The phase-shifted Lorentzian provides a robust fit to the data that is relatively insensitive to the residual calibration imperfections.

Measurements of the S_{21} parameter for characterizing the cross-talk between the elements were performed by exciting one array element with an incident power of 1mW (0dBm) and recording the power at the neighbouring array element, on each of the array element pairs for the three directions (X, Z', diagonal).

3.1.2.5. Modelling and Simulations

3.1.2.5.1. Equivalent Circuit Model

An equivalent circuit model was developed to analyze the cross-talk between array elements based on the monolithic crystal filter topology (MCF, Figure 3.1.10a) [34], [35].

The equivalent circuit consists of two resonators. Each resonator is represented by a Butterworth-van Dyke (BvD) circuit containing the standard resistor R_i, inductor L_i, and a capacitor C_i connected in series representing the motional, or acoustic, branch, and a capacitor C_{0i}, connected in parallel, representing the electrical branch that describes the static and parasitic capacitances; i=1 or 2 is one of the two coupled resonators. The two resonators shared a common electrode, grounded via parasitic elements consisting of an inductor L_p and a resistor R_p as shown in Figure 3.1.10b.

The coupling between the two resonators is represented by a parallel network of a resistor R_e and a capacitor C_e, and an inductor L_a. R_e and C_e, represent electrical coupling, and L_a acoustic coupling, respectively. Further details are provided in Section S3 of the Supporting Information (Appendix A). Such modified BvD circuit models of coupled resonators have been introduced in the literature previously [34]–[36].

3.1.2.5.2. FEM Simulations

3D FEM simulations of the coupled resonators were used to further understand crosstalk between the array elements. They were implemented in the commercial software package ANSYS version 19 (ANSYS, Canonsburg, PA, USA) running on a high-performance workstation (C50000 Pro workstation, Orbital Computers LLC, WA, USA). As a starting point for the simulations, we took the numerical model of a single 150MHz HFF-QCM resonator we have previously developed [21], since this individual resonator served as the basis for the design of the array elements.

Material properties were assigned based on the 'SOLID226' coupled-field element of the ANSYS libraries that captures the coupling between displacements and electrical

potentials in piezoelectric materials. Values for the physical properties of AT-cut quartz used in the calculations are listed elsewhere [21], [37], [38]. To model the detuning, the density of the quartz was slightly modified for one of the resonators. The damping factor was set to $5 \cdot 10^{-5}$. The structure was meshed according to the procedure described in ref. [21], which also describes the electrode effects. The mesh is also shown in Figure 3.1.9a and 9b. More details about FEM modelling can be found in Section S2 of the Supporting Information (Appendix A).

3.1.3. Results and Discussion

3.1.3.1. The Geometry of the Monolithic HFF-QCMD Arrays

The key result of this work is the 24-element array design shown in the optical micrographs in Figure 3.1.1a, b. The elements are organized into 6 columns of 4 elements each. The columns are defined by the six long electrodes running the size of the array in the Z' direction, with four short rectangular finger-like electrodes extending away from each column along the X direction. The column electrodes are grounded, thus effectively forming one electrode common to all 24 array elements. This common electrode constitutes the "working" side of the array. It faces the sample.

On the other side of the array, the short rectangular electrodes are oriented with their long axes along the Z' direction and are connected to the driving circuitry individually. Array elements (numbered with a row and a column index in Figure 3.1.1a) consist of square one-sided inverted MESA structures (visible in Figure 3.1.1b) sandwiched between the two sets of the short rectangular electrodes that are oriented orthogonally to each other. One such individual element is depicted schematically in Figure 3.1.1c. Element design is based on the individual 150 MHz HFF resonators we reported previously [21].

The side view of the MESA region, with dimensions, is shown in Figure 3.1.1d, where various numbers refer to the different zones of the array element surfaces. In particular, zones 1 and 6 correspond to the surface of the rectangular electrode on the etched side of the array, while zone 5 corresponds to the surface of the rectangular electrode on the flat side of the array (grounded, working surface). Zones 2 and 3 refer to the bare quartz on the etched side of the array, and zone 4 on the flat side. The flat side of the MESA corresponds to the working side of the array.

3.1.3.2. Physical Characterization of the Arrays

The arrays were fabricated by a combination of photolithography and wet etching processes. These methods have previously been used by us [21] and others [18], [24], [39]–[41] to successfully fabricate high-quality HFF-QCMD resonators and monolithic resonator arrays based on the inverted MESA geometry. The process is cost-effective, robust, and yields low-roughness resonator surfaces, but it can result in etch channels and etch pits that are detrimental to the resonator performance [41]–[44]. We investigated the morphology and roughness of the resonator surfaces and reproducibility of the individual features across the array elements by optical microscopy, FEGSEM, profilometry, and AFM. The results are presented in Table 3.1.1, Figure 3.1.2 and Figure 3.1.3.

A FEGSEM image of a typical array element is shown in Figure 3.1.2a. The square inverted MESA region is readily visible, and the rectangular gold electrode extending from the surrounding buffer to the MESA region itself (zones 1 and 6) can be identified. Note, that the inverted MESA is bound by the edges with different slopes due to the anisotropy of the etching process [43]–[45]. The electrode is seen to closely follow the slanted edge of the inverted MESA (on the left in Figure 3.1.2a), insuring proper conductivity across the electrode [44]. The two electrodes are perpendicular to each other. This makes our design robust to mask misalignments.

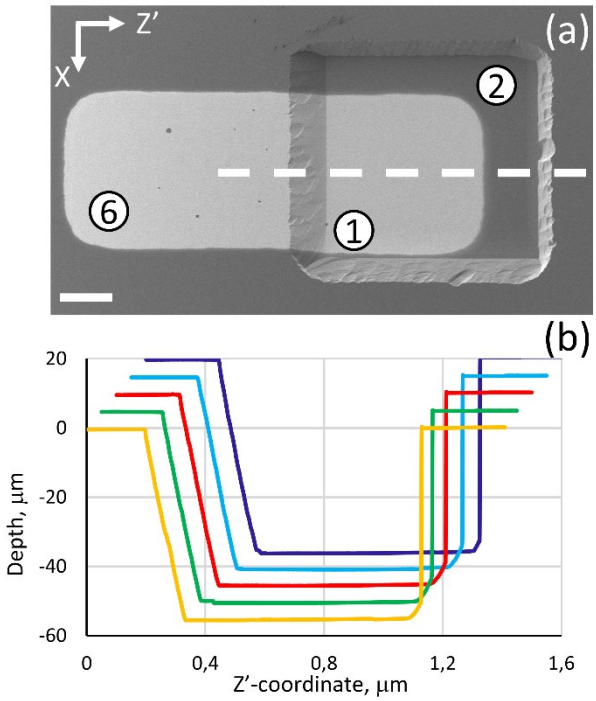

Figure 3.1.2 Physical Characterization of the Arrays (a) A FEGSEM image of one of the array elements showing the inverted-MESA region (zone 2) and the gold electrode (zones 1 and 6). Zone numbers refer to Figure 3.1.1d. White

dashed line indicates where the surface profiles, shown in (b), were taken. Axes indicate the crystallographic orientation of the AT-cut quartz. Scale bar is 200 μm. (b) Surface profiles measured with a profilometer along the direction indicated with the dashed white line in (a). Profiles are offset by 0.05 μm along the abscissa and by 5 μm along the ordinate relative to each other. Note the characteristic difference in slopes between the two sides of the inverted MESA region that arises from the anisotropy of the etching process.

The reproducibility of the depth and size of the inverted MESA region can be evaluated from the profilometry traces shown in Figure 3.1.2b. Here, each color represents a different array element from two different arrays. The fabrication process was extremely reproducible, with the etching depth of 55.9 μm ± 0.5 μm, which is convenient for reliable operation in automated data acquisition systems.

Table 3.1.1 Values of roughness

Zone (see Figure 3.1.1d)	R_a (nm) 2.5 μm x 2.5 μm
1 (Gold, etched, MESA)	0.67 ± 0.01
2 (Quartz, etched, MESA)	0.72 ± 0.06
3 (Quartz, etched, buffer)	0.9 ± 0.1
4 (Quartz, flat, buffer)	0.34 ± 0.04
5 (Gold, flat, MESA)	0.79 ± 0.2
6 (Gold, etched, buffer)	1.02 ± 0.08

Calculated from the AFM images of the different regions (zones) of the resonator elements of an array, such as those shown in Figure 3.1.3. Zone numbers are specified in Figure 3.1.1d. “Etched” and “flat” refer to two sides of the array.

FEGSEM images reflect the uniformity of the surface finish of the array elements after the etching process. This is further investigated on a smaller length scale in Figure 3.1.3, where the AFM images of zones 1, 2, 4, and 5 of one of the array elements are shown. Apart from a few spikes caused, most likely, by contamination of the samples during the cutting and mounting of the array on the stage of the AFM, the images appear devoid of any large-scale features. This is consistent with the SEM results presented above. The values of the roughness calculated from these images for the different zones are summarized in Table 3.1.1. In all of the zones, the roughness is ~ 1 nm or less, (Table 3.1.1). Note, that on the flat side, the gold deposition increases the roughness (c.f. zones 4 and 5 in Table 3.1.1), while on the etched side, it decreases the roughness (c.f. zones 1 and 2 in Table 3.1.1). This arises from the finite size of the gold grains, which are larger

than the features of the polished quartz face but smaller than the features of the etched quartz face.

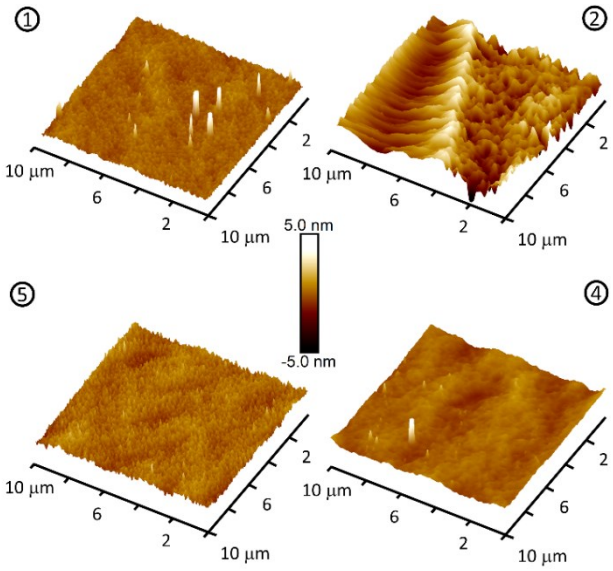

Figure 3.1.3 High-resolution Surface Characterization of the Array Elements AFM images of the different regions of one element of an array. Encircled numbers refer to the zones defined in Figure 3.1.1d; 1) Surface of the gold electrode in the MESA region, 2) MESA region without the electrode, 4) Bottom surface of the resonator without the electrode and 5) Surface of the gold electrode on the bottom face. A few white regions (spikes) are seen in the images of zone 1 and zone 4.

The roughness of the resonator surfaces is important for acoustic sensor performance in liquids: gas bubbles can be trapped in the roughness during the wetting of the sensors; new energy dissipations channels arise from the hydrodynamic effects at the oscillating sensor surface; finally, roughness affects adsorption behaviour of biomolecules. These effects are minimized in our case by etching the blanks from one side only. This leaves the working side of the array polished and untouched, exhibiting sub-nm roughness (Table 3.1.1) that is, in fact, better than that of the state-of-the-art resonators (~ 1 nm [46]). These values are of the same order as those reported in the literature (see Table 3.1.2). Indeed, the only currently available method of improving the surface roughness of the resonators beyond this range is through the ultra-flat technology that has not yet been generalized to the HFF resonators [46], [47].

In summary, the physical characterization of the arrays revealed array elements with highly reproducible lateral dimensions and depths, devoid of large-scale surface features that would impede their operation, with surfaces roughness of the order of ~ 1 nm.

Table 3.1.2 Comparison of Quality Factor Q and Roughness Ra reported by different manufacturing techniques

Reference	Frequency (MHz)	R_a (nm)	Q (in air)	Fabrication process
Values in this work	150	1	12000	Wet etching
Abe et al. [48]	94	2	30000	Deep RIE
Liang et al. [40]	84	--	25000	Wet etching
Hung et al. [49]	83	4-8	12000	Deep RIE
Liang et al. [40]	73	--	24000	Wet etching
Kao et al. [25],[27]	60-70	2	22100	Deep RIE
Liang et al. [40]	60	--	27000	Wet etching
Buettgenbach et al. [44]	48	10	50000	Wet etching
Liang et al. [40]	47	--	25000	Wet etching
Zhang et al. [50]	45	--	13200	Wet etching
Zimmermann et al. [18]	30	--	37.000	Wet etching
Abe et al. [51]	20	2	2000	Deep RIE

RIE: Reactive Ion Etching

3.1.3.3. Electrical Characterization of the arrays

3.1.3.3.1. Resonance parameters

To characterize resonance behavior of the array elements, their complex admittance spectra were measured using a vector network analyzer. To this end, the arrays were mounted in a home-made device adapted from a bench-top robot shown in Figure 3.1.4. Resonance frequencies and quality factors are shown in Figure 3.1.5 and Figure 3.1.6, respectively. The data reveal compact distributions of frequencies and quality factors from 26 different arrays, with averages of 149 MHz± 0.2MHz and (1.2±0.1)·104 for the resonance frequency and quality factor, respectively (measured in air).

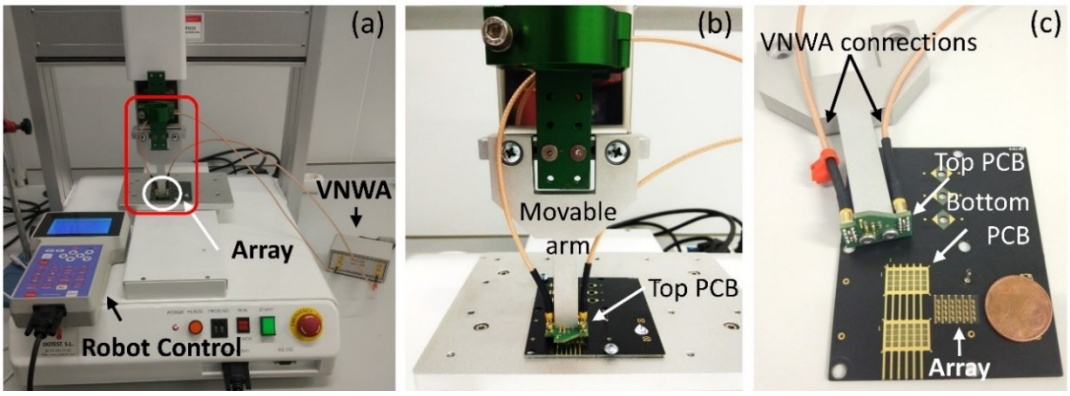

Figure 3.1.4 Home-made robotic setup for the electrical characterization of the arrays. (a) Overview of the base with the movable arm and the network analyzer (VNWA). Location of the array, under the movable arm, is indicated with a white circle, while the red outline defines the region shown in (b). (b) Enlarged view of the movable arm, with the top PCB, and VNWA connection cables visible. In this configuration, the array is not visible as it is sandwiched between the two PCBs. They are shown in (c) in the open configuration. (c) The PCB assembly: bottom PCB with an array and a 5¢ euro coin to give the idea of the scale; Movable arm, detached from the robot, with the top PCB and the VNWA connection cables.

The variation in the values of the resonance frequency between array elements is similar to that we reported for the single sensors previously [21]. There is a slight systematic trend visible in Figure 3.1.5 with the resonance frequencies decreasing across the columns, most likely due to uneven etching that will be fixed in the subsequent batches. The detuning between sensors caused by the manufacturing deviations, even though unintended, is beneficious for crosstalk reduction [38].

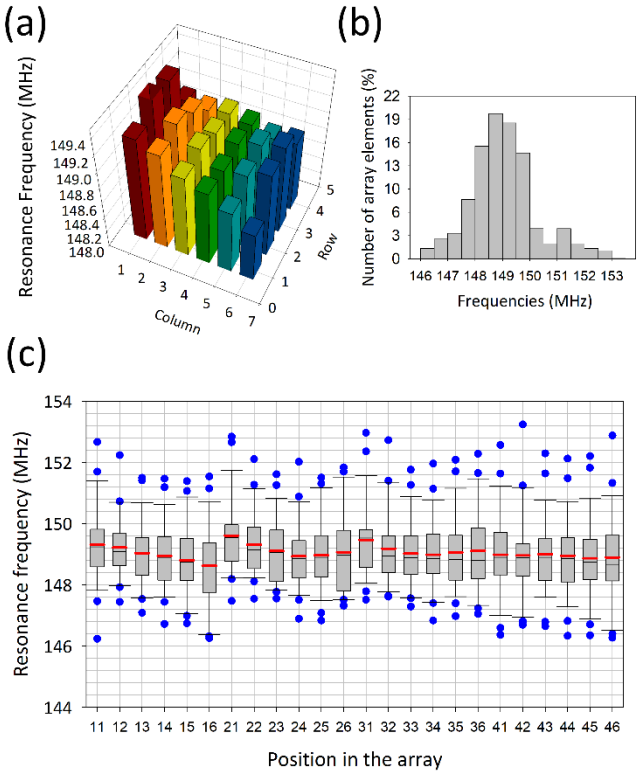

Figure 3.1.5 Resonance Frequencies of the Array Elements The results from 26 arrays are shown. Measurements were performed in air. (a) A 3D bar plot of the average resonance frequencies of the array elements as a function of their position in the arrays. (b) A histogram of the resonance frequencies of the array elements depicting their overall distribution. (c) A box plot of the resonance frequencies of the array elements as a function of position in the array. Red lines: means; black lines: medians; the box defines 25th and 75th percentiles, while the error bars define 10th and 90th percentiles, while blue filled circles show outliers.

The observed quality factors of the array elements can also be compared with the theoretical limit estimated according to the relationship $Q \cdot f_{res} = 1.6 \cdot 10^3$Hz [20]. For the resonance frequency of 150MHz, this relationship yields the expected value of ~1.1x10^5 for the maximal attainable quality factor. The experimentally observed values are within an order of magnitude lower than of this theoretical limit. They are close to what we have previously reported for the individual 150MHz resonators of the same design ($9.5 \cdot 10^3$ [21]). Furthermore, we have previously obtained quality factors of $(4.4 \pm 0.4) \cdot 10^4$ for the 50 MHz resonators and $(2.5 \pm 1.0) \cdot 10^4$ for 100 MHz resonators; the measurements were performed with the same setup as shown in Figure 3.1.4. The theoretical limits for these resonators are $3.2 \cdot 10^5$ and $1.6 \cdot 10^5$, respectively. The measured values are also similar to the ones reported in the literature (see Table 3.1.2). This comparison with our own and literature values for various HFF resonators reveals that the quality factors of HFF resonators are typically 1 – 2 orders of magnitude lower than

expected theoretical limits. According to some authors, some surface features (such as etch pits, etching channels or large-scale roughness) or departures from parallelism tend to reduce the quality factor of the resonators [42]–[44], [52].

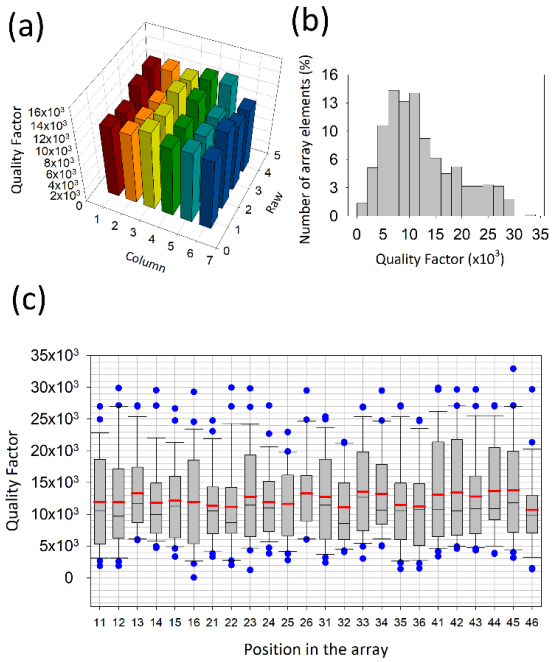

Figure 3.1.6 Quality Factors parameters of the Array Elements. Results from 26 arrays are shown. (a), (b), and (c) are the same as in Figure 3.1.5, but for the quality factor.

3.1.3.3.2. Analysis of Inharmonic Sidebands

Spurious modes may be an issue for sensing applications because coupling between them and the harmonic mode takes energy from the latter [18], [22]. This effect is more dramatic in liquid-media applications [18], [53] and the problem is more acute with the HFF resonators because for higher fundamental frequencies, inharmonics are relatively closer to the harmonic mode than in the case of lower fundamental frequencies [22].

Suppression of inharmonic modes is achieved by optimizing electrode geometry (electrode surface area and thickness) relative to the geometry of the inverted-MESA region based on the energy trapping principle developed for the classical QCMD resonators. The so-called plate-back equation is used to estimate the necessary electrode thickness [22], [54], and a compromise is then found between spurious mode suppression, conductivity, and the resonator quality factor [21], [27], [38], [55]. We have optimized electrode geometry for the individual 150MHz resonators, as described in our previous work [21]. Here, we study the effect of their integration into the array on the inharmonic

behavior by comparing experimentally measured conductance of the array elements as a function of frequency (Figure 3.1.7a, b) with the results of the FEM simulations of the individual resonators (Figure 3.1.7c). Heatmaps of conductance as a function of frequency show the detuning between the array elements (Figure 3.1.7a). For an easier quantification of inharmonic separation, the same heatmaps are shown in Figure 3.1.7b as a function of normalized frequency, f/f_{res}, where f_{res} is the resonance frequency of each array element.

For most of the array elements, the intense fundamental mode <111> appears at $f/f_{res} = 1$, followed by the inharmonic modes at higher frequencies. Significantly, the harmonic analysis performed by FEM simulations of the individual resonators accurately predicts the localization of the inharmonic modes found in the array elements experimentally (dashed lines in Figure 3.1.7b). In particular, the odd modes <113>, <131> and <133> (black dashed lines in Figure 3.1.7b) appear in all of the array elements as expected on theoretical grounds at frequencies that fit very well with the predictions of the FEM simulations for the individual resonators [21]. The separation between the fundamental <111> and the first of the odd inharmonic modes <113> is ~300kHz or 0.003 in terms of f/f_{res} , which agrees well with the results presented by Buettgenbach et al. for a 50MHz HFF resonator [44]. This separation is enough for measurements in aqueous media, but it should be made as wider as possible within the limits set by manufacturing restrictions.

The main difference between the predictions of the FEM simulations for the individual resonators and experimental results obtained with the arrays is that even modes (<112>,<121>,<122>,<132>,<114>,<132> and <124>) are also visible in some elements of the arrays, as a consequence of the slight asymmetries existing in the real resonators (white dashed lines in Figure 3.1.7b) [22]. On the other hand, the misalignment during the array fabrication process, apparent in the FEGSEM images (Figure 3.1.2a), lead to the asymmetries in the electrode configuration and different electrode thickness/effective surface areas for the different array elements, translating into differences in the spectra. These effects are minor, however. Apart from these two aspects, the modal behavior of the array elements is well-predicted by the FEM simulations of the individual resonators and is unaffected by their being part of a monolithic array.

3.1.3.3.3. Analysis of the interactions between array elements (crosstalk)

The purpose of the resonator arrays is to enable parallel measurements with each of its elements functioning independently of each other. Therefore, the extent of the interactions between the elements is an important consideration.

Experimentally, interactions between array elements are measured through the scattering parameter S_{21} shown in Figure 3.1.8. It is immediately clear that the cross-talk between array elements in each of the three directions is, for all intents and purposes, negligible and our design is appropriate for parallel individual measurements: the experimental maximum value in $|S_{21}|$, that is ~ –32dB at the most with averages values of less than –50dB (Figure 3.1.8a – c). These values agree well with those reported by other authors: ~-30dB for the 3×3 66 MHz array [25], [27]; ~-50dB for the 4×4 43 MHz array [24], and < -40dB for the 2×2 10MHz array (with average values smaller than - 60dB) [56].

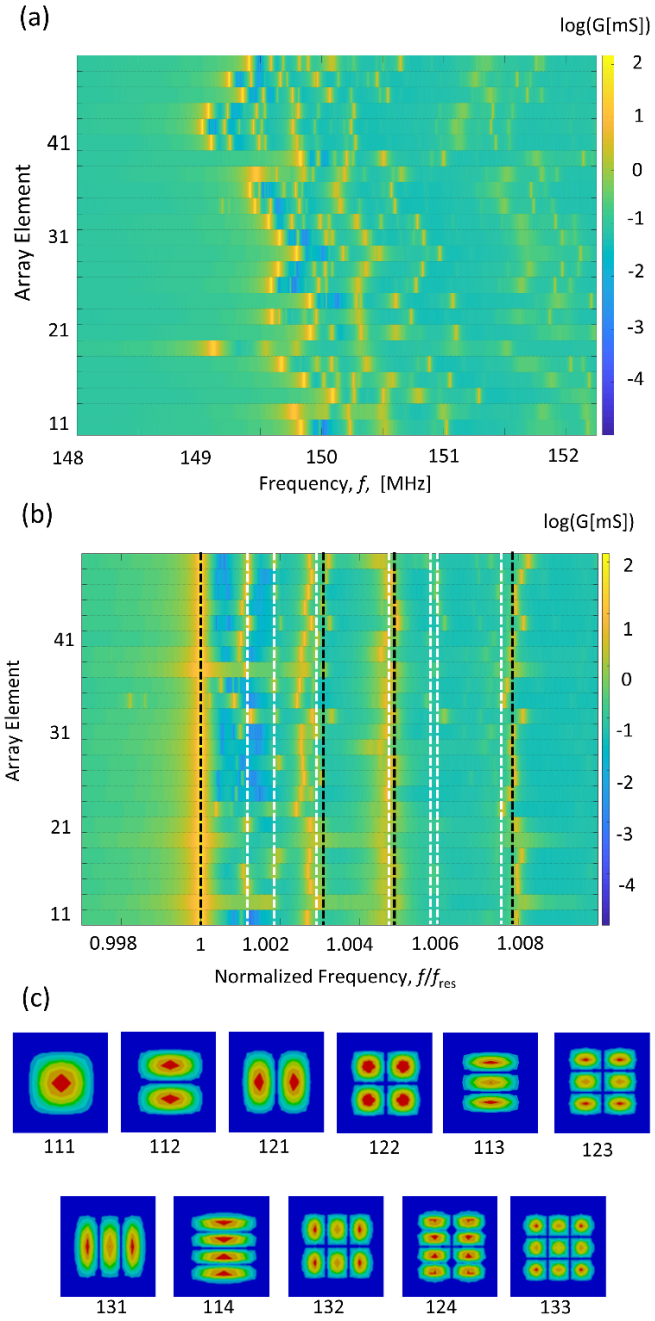

Figure 3.1.7 Inharmonic Analysis of the Array Elements. Heatmaps of conductance as a function of frequency, f, (a), and as a function of normalized frequency, f/f_{res}, where, f_{res} is the resonance frequency of the array element, (b), for different array elements. Representative results for one array are shown. The most intense (highest conductance) mode is the fundamental, <111> mode that appears at $f/f_{res} = 1$. Dashed lines in (b) refer to the different inharmonic modes, black for odd, and white for even. The frequencies of the modes, and their displacement patterns that are shown in (c), were calculated with modal analysis simulations of individual resonators [18].

The experimental observation of negligible cross-talk is supported by the results of the FEM simulations (Figure 3.1.9) that show lack of acoustic interactions between array

elements ($|S_{21}|$ below -50dB) and lack of displacement in the passive resonator when the active neighbour is excited (see Figure 3.1.9d).

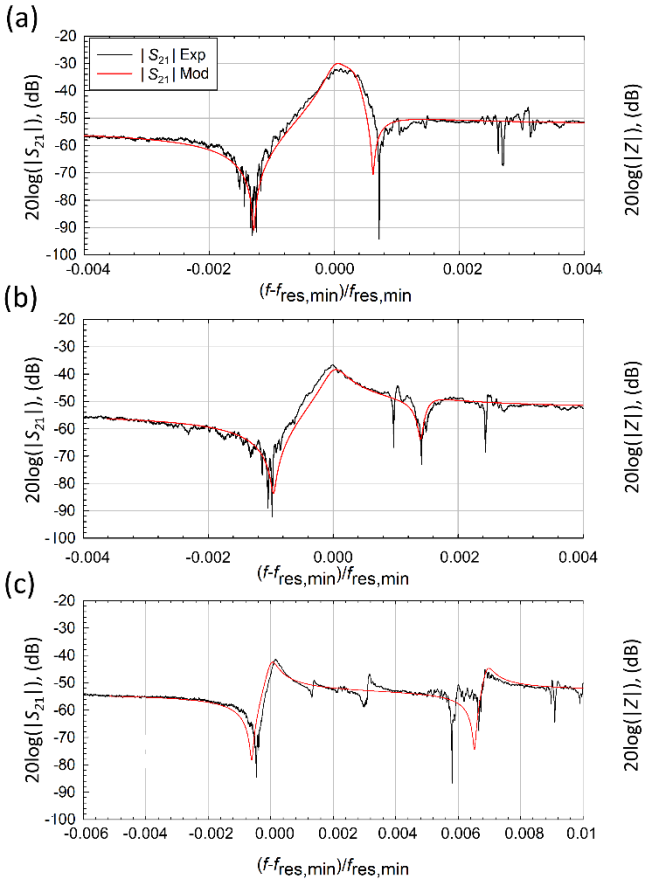

Figure 3.1.8 Cross-talk analysis: results. Plots of the scattering parameter, $|S_{21}|$, as a function of frequency normalized to the resonance frequency of the element with the lower resonance frequency, $f_{res,min}$, for three different values of detuning $\Delta f_{ij} = f_i - f_j$, where i^{th} element is the active one and j^{th} element is the passive one. For $|S_{21}|$, the experimental results are shown in black, and equivalent circuit model calculation results—in red. Equivalent circuit model parameters were: $C_1 = C_2 = 5.73$ fF, $C_e = 32$ fF, $R_e = \infty$ Ω, $L_a = 0$ H, $C_{01} = C_{02} = 2.29$ pF, $L_p = 2$ nH and $R_p = 0$ Ω, $f_{res,\,j} = f_{res,\,i} + \Delta f_{ij}$. Furthermore, in (a), $f_{res,1} = 148.1$ MHz, $\Delta f = 49$ kHz, $R_1 = 7$ Ω, and $R_2 = 4$ Ω; in (b), $f_{res,1} = 147.5$ MHz, $\Delta f = 212$ kHz, $R_1 = 12$ Ω, $R_2 = 11.4$ Ω; in (c), $f_{res,1} = 147.3$ MHz, $\Delta f = -1009$ kHz, $R_1 = 13$ Ω, and $R_2 = 15$ Ω.

Similarly, analytical calculations based on MCF filters design also predict that acoustic coupling should be minimal. Indeed, the coupling strength K can be easily estimated from the geometry of the array and the properties of quartz according to the following expression [34]: $K = \frac{3c_{11}}{8\rho f_{res}^2 \phi_x^2} e^{-\xi d}$. Here $c_{11}=8.674\cdot10^{10}$ N m^2 is the elastic coefficient of AT quartz in the X direction, f_{res} is the resonance frequency of the uncoupled resonators (assumed to be the same in this case; no detuning), ρ is the density of quartz, and d is the distance between the resonators along the X direction (2.25 mm). ξ is the propagation

constant for the shear-thickness mode, defined as $\xi = \frac{2.298}{t}\Delta^{1/2}$, where t is the thickness of the resonator and Δ is the so-called plate-back, $\Delta = \frac{f_s - f_{res}}{f_s}$, where fs is the resonance frequency of the quartz plate without the electrodes. In our case, $f_s \approx 165$ MHz, $f_{res} \approx 150$ MHz, giving $\Delta \sim 0.0909$ and $\xi \sim 69287.3$. $\phi_x = d + 2r + \frac{0.418t}{\Delta^{1/2}}$ is the effective length of the vibration volume along the X axis, where r is the electrode dimension in the X direction; in our case, this is taken for the individual electrodes on the etched side of the array, or 550 μm, giving $3 \cdot 10^{-3}$ for ϕ_x. Plugging the numbers into the expression for K, one arrives at a value of $\sim 10^{-74}$. In other words, in our arrays, the elements are not expected to interact acoustically.

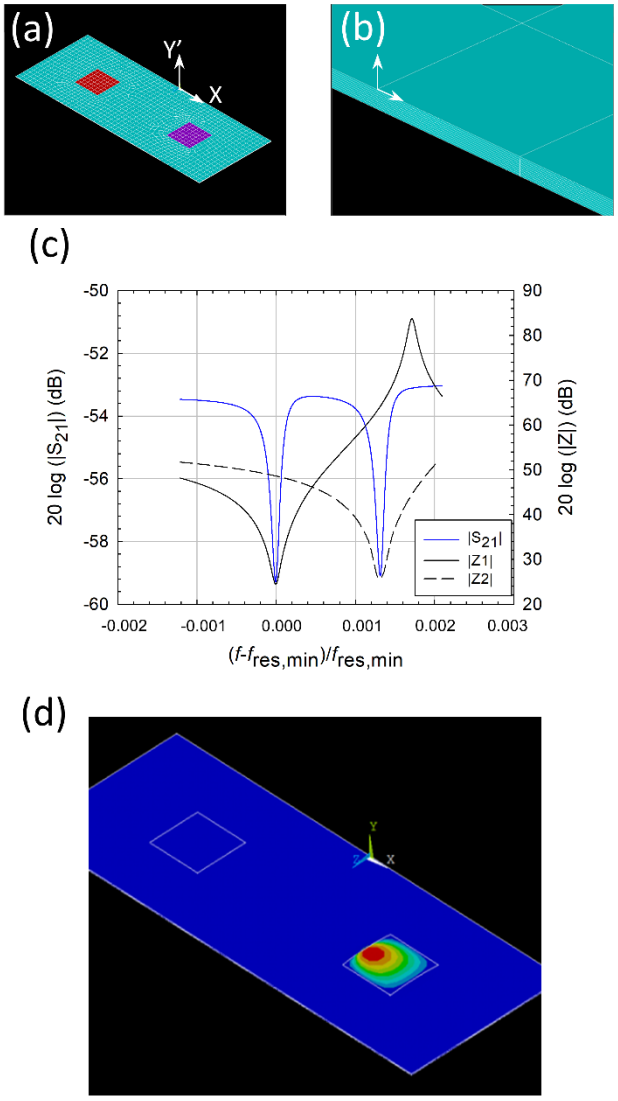

Figure 3.1.9 Cross-talk analysis: FEM simulations. Simulation geometry and meshing. (a) Two resonators on the same AT quartz substrate are shown, with the mesh indicated. Mesh size was 50 μm × 50 μm. The distance between

the two resonators was 2.25 mm (element-element distance in X direction of the manufactured array). (b) View of one of the mesh elements illustrating the meshing in the thickness direction. The substrate thickness was 10 μm, meshed into 10 slabs. Axes in (a) and (b) indicate crystallographic directions. (c) A plot of $|S_{21}|$ extracted from the simulations as a function of the normalized frequency and the corresponding impedances Z. Detuning was $\Delta f = 200$ kHz. To bring the values of $|S_{21}|$ away from resonance in the FEM simulations into register with the experimental ones, a capacitor with a value of ~ 23 fF, had to be explicitly introduced into the FEM simulations. (d) Patterns of instantaneous displacement in the active (right) and passive (left) resonators. There is no evidence of displacements in the passive resonator when the active one is excited with 0.5 V.

Interestingly, however, the FEM simulations do actually not reproduce the experimentally observed dependence of S_{21} on frequency: the peak in S_{21} visible in Figure 3.1.8a – c is absent in Figure 3.1.9c. To understand this discrepancy, we constructed an equivalent circuit model based on the classical MCF topology [34], [35]. The model proposed here, shown in Figure 3.1.10b, adds new elements L_p and R_p to the well-known model used in MCF theory to account for the parasitic electrical grounding effects in the experimental setup.

The correspondence between the predictions of the model and the experimental data, visible in Figure 3.1.9a-c, is excellent when acoustic coupling was neglected (L_a=0), but the electrical component of the coupling (C_e) and a poor grounding L_p were considered. S_{21} in Figure 3.1.9a-c is measured at three different values of detuning between the two elements. Note, that in this model, L_p is the only adjustable parameter, and its value was the same for all three values of the detuning. A more detailed explanation about the effects of the individual circuit elements on the crosstalk can be found in section S3 of the Supporting Information (Appendix A).

The authors wish to point out that, although the modeled parasitic effects are, in this case, negligible, and would not affect the characterization of the designed array, this does not invalidate the model itself. The model proposed faithfully represents those mentioned effects and allows its identification in a simple and sufficiently precise way. Therefore, it may be applicable in other cases where such effect could be not negligible.

Note, that while our discussion of the cross-talk is based on the results of the X-crystallographic direction only, all of the above arguments apply equally to the other crystallographic directions up to the substitution of the appropriate values for the geometric, elastic, and piezoelectric parameters.

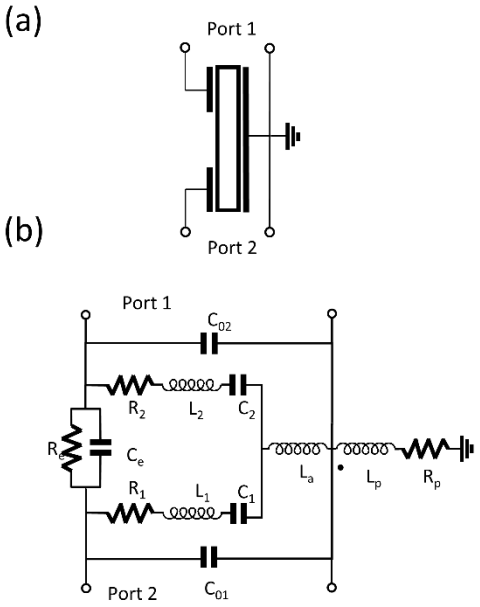

Figure 3.1.10 Cross-talk analysis: the equivalent circuit model. Array element topology (a), and its equivalent circuit representation (b), used to analyze crosstalk between the adjacent array elements. The topology corresponds to two resonators sharing a common electrode that is grounded. R_1, L_1, C_1 and R_2, L_2, C_2 comprise the motional branches of the BvD circuits used to represent each of the two quartz resonators (array elements). C_{01} and C_{02} account for the static capacitances between the electrodes of each of the two resonators. Coupling between the resonators is modeled with a combination of a capacitor C_e, inductor L_a, and a resistor R_e; the latter accounts for the losses. Parasitic elements L_p and R_p model the ground path. Further details can be found in the text.

3.1.3.4. Behavior of the Arrays in Liquid

As a final step, we checked whether the arrays functioned in liquids. These results are merely illustrative; details of the microfluidic cell and the detailed validation of array performance in fluids will be presented in a future publication.

The change in the resonance frequency and bandwidth upon transfer from air to water is expected to satisfy the Kanazawa-Gordon-Mason (KGM) relation [8], [57], [58], $\Delta f + i\Delta\Gamma = -\frac{(1-i)\sqrt{2f_{res}^3 \rho_{liq} \eta_{liq}}}{Z_q \sqrt{2\pi}}$, where Z_q is the acoustic impedance of AT quartz ($8.84 \cdot 10^6$ kg m^{-2} s^{-1}), f_{res} is the fundamental resonance frequency of the array element, ρ_{liq} is the density of the liquid, and η_{liq} its viscosity. The results are shown in Table 3.1.3, where the theoretically expected values and experimentally obtained values for the arrays and various individual resonators are shown.

Table 3.1.3 Air-to-water frequency and bandwidth

Condition	Δf kHz	ΔΓ kHz	Accuracy	
			rms (Δf) kHz	rms (ΔΓ) kHz
150 MHz (n = 1)				
Theory	-113 ± 0.6	113 ± 0.6		
Experiment (arrays)	-103 ± 16	116 ± 12	19 (16%)	13 (11%)
35 MHz (f_0 = 5 MHz, n = 7)				
Theory	-1.78	1.78		
Experiment	-1.83 ± 0.05	1.67 ± 0.009	0.05 (3%)	0.12 (7%)
150 MHz (f_0 = 50 MHz, n = 3)				
Theory	-37	37		
Experiment	-40 ± 2	38 ± 2	3 (8%)	2 (5%)
100 MHz (n = 1)				
Theory	-60	60		
Experiment	-62 ± 2	53.0 ±0.5	2.4 (4%)	7.3 (12%)

Data shifts for the arrays prepared in this study compared with those for the individual sensors. Theoretical values were calculated using the KGM relationship. For the arrays, the resonance frequencies, fres, of the individual elements (Figure 3.1.5) were used in the calculations. Errors are standard deviations, accuracy values are rms deviations between the measured and the theoretical values. Water density and viscosity at 22ºC were used in the calculations.

The values presented in Table 3.1.3 show that the air-to-water shifts can be measured with these arrays with the accuracy comparable to that observed with the individual HFF resonators. We also note that the frequency shift due to the change from air to water, ~ – 113 kHz, is much smaller than the separation between the fundamental and the first inharmonic modes, which is ~ 300 kHz (see section III.C.2).

3.1.4. Conclusion

The main result of this work is the 24-element monolithic, high fundamental frequency (HFF) QCMD array design and the physical and electrical characterization of the arrays manufactured according to this design. Special emphasis in characterizing the arrays was placed on surface roughness, inharmonic sidebands, and analysis of the interactions between the elements of the array, as these aspects will detrimentally affect array performance and may limit its biosensing functionality.

Reproducibility of array manufacturing has been demonstrated. The roughness of the working surface of the array was ~ 1 nm, that is to say, comparable with that of other commercially available QCMD resonators. Resonance frequencies of the array elements of 149 MHz ± 0.2 MHz and quality factors of $(1.2 \pm 0.1) \cdot 10^4$, averaged over 26 different arrays, have been obtained. Inharmonic modes do not disturb operation with liquids, since a separation between the fundamental and the first observed inharmonic of ~ 300 kHz was achieved. This value significantly exceeds the change in frequency and bandwidth due to the immersion of the arrays in aqueous media. The behavior of the array elements fits very well with that of the individual resonators of the same design and predictions of the FEM simulations. Finally, we demonstrate that the performance of the arrays in liquid is comparable to that of the individual HFF resonators.

A significant part of our work deals with the interactions between the array elements. We show that there are no detectable acoustic interactions between the array elements for our array geometry. This conclusion is consistent with the theoretical predictions and is supported by the results of the geometry-specific FEM simulations. We also observed differences between the experimental S_{21} shape and FEM simulations results. Using an equivalent circuit model based on the MCF topology, we show that these differences are explained entirely by parasitic impedances from the grounding of the resonators. This model can be useful for the general design of monolithic HFF QCMD arrays; since it provides a simple tool that allows a fast simulation of the interferences between array elements and a mean to identify the causes and try to avoid them.

We expect our arrays to be useful for biosensing applications and our results to investigators wishing to design their own high-performance monolithic HFF QCMD arrays.

Acknowledgment

The authors would also like to thank Jorge Martínez from the Laboratory of High Frequency Circuits (LCAF) of the Universitat Politècnica de València (UPV) for assistance with profilometry, and Manuel Planes, José Luis Moya, Mercedes Tabernero, Alicia Nuez and Joaquin Fayos from the Electron Microscopy Services of the UPV for helping with the AFM, and SEM measurements. M.Calero is the recipient of the doctoral fellowship BES-2017-080246 from the Spanish Ministry of Economy, Industry and Competitiveness (Madrid, Spain).

This research was funded by Spanish Ministry of Economy and Competitiveness with FEDER funds (AGL 2016-77702-R) and European Commission Horizon 2020 Programme (Grant Agreement number H2020-FETOPEN-2016-2017/737212-CATCH-U-DNA - Capturing non-Amplified Tumor Circulating DNA with Ultrasound Hydrodynamics) for which the authors are grateful.

Román Fernández is with the Center for Research and Innovation in Bioengineering (Ci2B), Universitat Politècnica de València, València, Spain and with Advanced Wave Sensors S.L., Paterna, València, Spain. (e-mail: rfernandez@awsensors.com); Yolanda Jiménez, Antonio Arnau and María Calero are with the Center for Research and Innovation in Bioengineering (Ci2B), Universitat Politècnica de València, València, Spain; Ilya Reiviakine is with Advanced Wave Sensors S.L., Paterna, Valencia, Spain and with the Department of Bioengineering, University of Washington, Seattle, WA, 98150 USA; María Isabel Rocha-Gaso and José Vicente García are with Advanced Wave Sensors S.L., Paterna, València, Spain.

References

[1] M. U. Ahmed, I. Saaem, P. C. Wu, and A. S. Brown, “Personalized diagnostics and biosensors: a review of the biology and technology needed for personalized medicine,” Crit. Rev. Biotechnol., vol. 34, no. 2, pp. 180–196, 2014.

[2] V. Gubala, L. F. Harris, A. J. Ricco, M. X. Tan, and D. E. Williams, “Point of Care Diagnostics: Status and Future,” Anal. Chem., vol. 84, no. 2, pp. 487–515, 2012.

[3] J. L. C. M. Dorne, J. L. C. M. Dorne, L. R. Bordajandi, B. Amzal, P. Ferrari, and P. Verger, “Combining analytical techniques, exposure assessment and biological effects for risk assessment of chemicals in food,” TrAC Trends Anal. Chem., vol. 28, no. 6, pp. 695–707, Jun. 2009.

[4] N. L. Anderson and N. G. Anderson, “The Human Plasma Proteome,” Mol. Cell. Proteomics, vol. 1, no. 11, pp. 845–867, Nov. 2002.

[5] J. Kirsch, C. Siltanen, Q. Zhou, A. Revzin, and A. Simonian, “Biosensor technology: recent advances in threat agent detection and medicine,” Chem. Soc. Rev., vol. 42, no. 22, p. 8733, 2013.

[6] P. Arora, A. Sindhu, N. Dilbaghi, and A. Chaudhury, “Biosensors as innovative tools for the detection of food borne pathogens,” Biosens. Bioelectron., vol. 28, no. 1, pp. 1–12, 2011.

[7] P. . Patel, “(Bio)sensors for measurement of analytes implicated in food safety: a review,” TrAC Trends Anal. Chem., vol. 21, no. 2, pp. 96–115, Feb. 2002.

[8] D. Johannsmann, The Quartz Crystal Microbalance in Soft Matter Research. Cham: Springer International Publishing, 2015.

[9] Y. Montagut, J. Garcia, Y. Jimenez, C. March, A. Montoya, and A. Arnau, “QCM Technology in Biosensors,” in Biosensors - Emerging Materials and Applications, InTech, 2011.

[10] M. D. Ward and D. A. Buttry, “In Situ Interfacial Mass Detection with Piezoelectric Transducers,” Science (80-.)., vol. 249, no. 4972, pp. 1000–1007, Aug. 1990.

[11] I. Reviakine, D. Johannsmann, and R. P. Richter, “Hearing What You Cannot See and Visualizing What You Hear: Interpreting Quartz Crystal Microbalance Data from Solvated Interfaces,” Anal. Chem., vol. 83, no. 23, pp. 8838–8848, Dec. 2011.

[12] G. Sauerbrey, “Use of vibrating quartz for thin film weighing and microweighing,” Z. Phys., vol. 155, pp. 206–222, 1959.

[13] A. Grammoustianou and E. Gizeli, “Acoustic Wave–Based Immunoassays,” in Handbook of Immunoassay Technologies, J. H. T. L. Sandeep K. Vashist, Ed. Elsevier, 2018, pp. 203–239.

[14] G. Papadakis, P. Palladino, D. Chronaki, A. Tsortos, and E. Gizeli, “Sample-to-answer acoustic detection of DNA in complex samples,” Chem. Commun., vol. 53, no. 57, pp. 8058–8061, 2017.

[15] C. March-Iborra, “High-Frequency phase shift measurement greatly enhances the sensitivity of QCM immunosensors,” Biosens. Bioelectron., vol. 65, pp. 1–8, 2015.

[16] L. Cervera-Chiner et al., “High Fundamental Frequency Quartz Crystal Microbalance (HFF-QCM) immunosensor for pesticide detection in honey,” Food Control, vol. 92, pp. 1–6, Oct. 2018.

[17] Gunter K. Guttwein, Arthur D. Ballato, and Theodore J. Lukaszek, "VHF-UHF Piezoelectric Resonators," 3,694,677, 1972.

[18] B. Zimmermann, R. Lucklum, P. Hauptmann, J. Rabe, and S. Büttgenbach, "Electrical characterisation of high-frequency thickness-shear-mode resonators by impedance analysis," Sensors Actuators B Chem., vol. 76, no. 1–3, pp. 47–57, Jun. 2001.

[19] J. Rabe, S. Büttgenbach, B. Zimmermann, and P. Hauptmann, "Design, manufacturing, and characterization of high-frequency thickness-shear mode resonators," Proc. Annu. IEEE Int. Freq. Control Symp., pp. 106–112, 2000.

[20] L. Rodriguez-Pardo, J. Fariña, C. Gabrielli, H. Perrot, and R. Brendel, "Resolution in quartz crystal oscillator circuits for high sensitivity microbalance sensors in damping media," Sensors Actuators B Chem., vol. 103, no. 1–2, pp. 318–324, Sep. 2004.

[21] R. Fernández, P. García, M. García, J. García, Y. Jiménez, and A. Arnau, "Design and Validation of a 150 MHz HFFQCM Sensor for Bio-Sensing Applications," Sensors, vol. 17, no. 9, p. 2057, Sep. 2017.

[22] Virgil E. Bottom, Introduction to quartz crystal unit design. New York: Van Nostrand Reinhold, 1982.

[23] C. Kreutz et al., "High frequency quartz micro balances: A promising path to enhanced sensitivity of gravimetric sensors," Sensors, vol. 6, no. 4, pp. 335–340, 2006.

[24] J. Rabe, S. Büttgenbach, J. Schröder, and P. Hauptmann, "Monolithic miniaturized quartz microbalance array and its application to chemical sensor systems for liquids," IEEE Sens. J., vol. 3, no. 4, pp. 361–368, 2003.

[25] P. Kao, S. Doerner, T. Schneider, D. Allara, P. Hauptmann, and S. Tadigadapa, "A micromachined quartz resonator array for biosensing applications," J. Microelectromechanical Syst., vol. 18, no. 3, pp. 522–530, 2009.

[26] A. Tuantranont, A. Wisitsora-at, P. Sritongkham, and K. Jaruwongrungsee, "A review of monolithic multichannel quartz crystal microbalance: A review," Anal. Chim. Acta, vol. 687, no. 2, pp. 114–128, 2011.

[27] P. Kao, D. Allara, and S. Tadigadapa, "Fabrication and performance characteristics of high-frequency micromachined bulk acoustic wave quartz resonator arrays," Meas. Sci. Technol., vol. 20, no. 12, p. 124007, Dec. 2009.

[28] D. Croux et al., “Development of multichannel quartz crystal microbalances for MIP-based biosensing,” Phys. Status Solidi Appl. Mater. Sci., vol. 209, no. 5, pp. 892–899, 2012.

[29] T. Tatsuma, Y. Watanabe, N. Oyama, K. Kitakizaki, and M. Haba, “Multichannel quartz crystal microbalance,” Anal. Chem., vol. 71, no. 17, pp. 3632–3636, 1999.

[30] K. Jaruwongrungsee, U. Waiwijit, A. Wisitsoraat, M. Sangworasil, C. Pintavirooj, and A. Tuantranont, “Real-time multianalyte biosensors based on interference-free multichannel monolithic quartz crystal microbalance,” Biosens. Bioelectron., vol. 67, pp. 576–581, 2015.

[31] W. Tao, P. Lin, Y. Ai, H. Wang, S. Ke, and X. Zeng, “Multichannel quartz crystal microbalance array: Fabrication, evaluation, application in biomarker detection,” Anal. Biochem., vol. 494, pp. 85–92, Feb. 2016.

[32] M. Nirschl et al., “CMOS-integrated film bulk acoustic resonators for label-free biosensing,” Sensors, vol. 10, no. 5, pp. 4180–4193, 2010.

[33] J. Petri, S. Hochstädt, T. Nentwig, A. Pausch, A. Langhoff, and D. Johannsmann, “A Fast Electrochemical Quartz Crystal Microbalance,which Acquires Frequency and Bandwidth on Multiple Overtones,” Electroanalysis, vol. 29, no. 3, pp. 806–813, Mar. 2017.

[34] R. A. Sykes and W. D. Beaver, “High Frequency Monolithlc Crystal Filters with Posslble Application to Single Frequency and Single Side Band Use,” in 20th Annual Symposium on Frequency Control, 1966, pp. 288–308.

[35] A. A. Vives, J. M. F. y D. L. Osorio, T. S. Devesa, and Y. J. Jiménez, SISTEMAS ELECTRÓNICOS DE COMUNICACIONES I. Valencia: Universitat Politècnica de València, 2000.

[36] S. Berg and D. Johannsmann, “Laterally coupled quartz resonators,” Anal. Chem., vol. 73, no. 6, pp. 1140–1145, 2001.

[37] W. D. Beaver, “Analysis of Elastically Coupled Piezoelectric Resonators,” J. Acoust. Soc. Am., vol. 43, no. 5, pp. 972–981, 1968.

[38] F. Lu, H. P. Lee, P. Lu, and S. P. Lim, “Finite element analysis of interference for the laterally coupled quartz crystal microbalances,” Sensors Actuators, A Phys., vol. 119, no. 1, pp. 90–99, 2005.

[39] H. Iwata, “Multistage chemical etching for high-precision frequency adjustment in ultrahigh-frequency fundamental quartz resonators,” IEEE Trans. Ultrason. Ferroelectr. Freq. Control, vol. 52, no. 9, pp. 1435–1442, 2005.

[40] J. Liang, J. Huang, T. Zhang, J. Zhang, X. Li, and T. Ueda, “An experimental study on fabricating an inverted mesa-type quartz crystal resonator using a cheap wet etching process,” Sensors (Switzerland), vol. 13, no. 9, pp. 12140–12148, 2013.

[41] Y. Nagaura, K. Kinoshita, and S. Yokomizo, “High-frequency, plano-convex quartz oscillators made by a dual-face lapping machine,” in Proceedings of the 2000 IEEE/EIA International Frequency Control Symposium and Exhibition (Cat. No.00CH37052), 2000, pp. 255–259.

[42] J. R. Vig, “Chemically Polished Quartz,” in 31st Annual Symposium on Frequency Control, 1977, pp. 131–143.

[43] J. R. Hunt and R. C. Smythe, “Chemically Milled VHF and UHF AT-Cut Resonators,” in 39th Annual Symposium on Frequency Control, 1985, pp. 292–300.

[44] S. Buettgenbach, J. Rabe, B. Zimmermann, and P. R. Hauptmann, “High-frequency thickness-shear mode resonators for sensor application in liquids,” in Advanced Environmental and Chemical Sensing Technology, 2001, vol. 4205, no. February 2001, p. 207.

[45] W. P. Hanson, “Chemically polished high frequency resonators,” Proc. 37th AFCS, pp. 261–234, 1983.

[46] J. A. Rubio Lara, F. Bergler, S. J. Attwood, J. M. Edwardson, and M. E. Welland, “Ultra-flat Gold QCM Electrodes Fabricated with Pressure Forming Template Stripping for Protein Studies at the Nanoscale,” Langmuir, 2019.

[47] R. P. Richter and A. Brisson, “QCM-D on mica for parallel QCM-D - AFM studies,” Langmuir, vol. 20, no. 11, pp. 4609–4613, 2004.

[48] T. Abe, V. Hung, and M. Esashi, “Inverted mesa-type quartz crystal resonators fabricated by deep-reactive ion etching,” IEEE Trans. Ultrason. Ferroelectr. Freq. Control, vol. 53, no. 7, pp. 1234–1236, Jul. 2006.

[49] V. N. Hung, T. Abe, P. N. Minh, and M. Esashi, “Miniaturized, highly sensitive single-chip multichannel quartz-crystal microbalance,” Appl. Phys. Lett., vol. 81, no. 26, pp. 5069–5071, 2002.

[50] J. Zhang, J. Liang, and T. Ueda, “Design and evaluation of a dual channel high frequency Quartz crystal Microbalance,” Proc. Int. Conf. Sens. Technol. ICST, 2016.

[51] T. Abe and M. Esashi, “One-chip multichannel quartz crystal microbalance (QCM) fabricated by Deep RIE,” Sensors Actuators A Phys., vol. 82, no. 1, pp. 139–143, 2000.

[52] J. R. Vig, “Etching Estudies on Singly and Double Rotated Quartz Plates,” Proc. 33rd Annu. Symp. Freq. Contr., pp. 351–358, 1979.

[53] L. Li, T. Abe, and M. Esashi, “Microfabricated smerical bi-convex quartz crystal microbalance array,” 18th IEEE Int. Conf. Micro Electro Mech. Syst. 2005. MEMS 2005., pp. 327–330, 2005.

[54] W. Shockley, D. R. Curran, and D. J. Koneval, “Trapped-Energy Modes in Quartz Filter Crystals,” J. Acoust. Soc. Am., vol. 41, no. 4B, pp. 981–993, 1967.

[55] H. Jiang, “Finite element analysis on electrode structure of QCM,” 2009 Chinese Control Decis. Conf. CCDC 2009, pp. 3618–3621, 2009.

[56] E. Zampetti, S. Pantalei, A. Macagnano, E. Proietti, C. Di Natale, and A. D’Amico, “Use of a multiplexed oscillator in a miniaturized electronic nose based on a multichannel quartz crystal microbalance,” Sensors Actuators, B Chem., vol. 131, no. 1, pp. 159–166, 2008.

[57] K. K. Kanazawa and J. G. Gordon, “Frequency of a quartz microbalance in contact with liquid,” Anal. Chem., vol. 57, no. 8, pp. 1770–1771, 1985.

[58] W. P. Mason, Piezoelectric crystals and their application to ultrasonics. New York: Van Nostrand, 1950.

3.2. A Fast Method for Monitoring the Shifts in Resonance Frequency and Dissipation of the QCM Sensors of a Monolithic Array in Biosensing Applications

Román Fernández, María Calero, José Vicente García, Ilya Reiviakine, Antonio Arnau and Yolanda Jiménez

IEEE Sensors Journal, Volume 21, Issue 5, December 2020, 6643-6651

Abstract

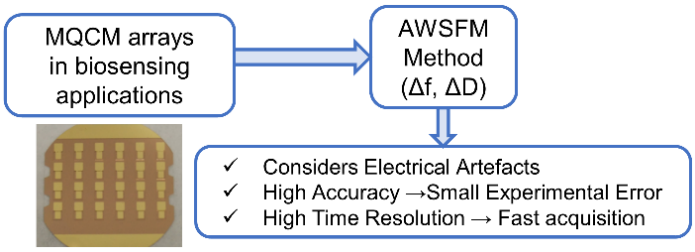

Improvement of data acquisition rate remains as an important challenge in applications with Quartz Crystal Microbalance (QCM) technology where high throughput is required. To address this challenge, we developed a fast method capable of measuring the response of a large number of sensors and/or overtones, with a high time resolution. Our method, which can be implemented in a low-cost readout electronic circuit, is based on the estimation of Δf_r (frequency shift) and ΔD (dissipation shift) from measurements of the sensor response obtained at a single driving frequency. By replacing slow fitting procedures with a direct calculation, the time resolution is only limited by the physical characteristics of the sensor (resonance frequency and quality factor), but not by the method itself. Capabilities of the method are demonstrated by monitoring multiple overtones with a single 5 MHz sensor and a Monolithic QCM array comprising 24 50MHz-sensors. Accuracy of the method is validated and compared with the state-of-the-art, as well as with a reference method based on impedance analysis.

Keywords

Biosensor, Fast acquisition, Monolithic Quartz Crystal Microbalance (MQCM), Multiple overtones, Sensor array devices.

3.2.1. Introduction

Analytical techniques based on Quartz Crystal Microbalance (QCM) have been steadily growing mainly driven by advantageous features such as: 1) direct label-free detection; 2) real-time non-invasive approach; 3) low cost and 4) ability to detect mass, viscoelastic and conformational changes occurring on the sensor surface. Point-of-care diagnosis [1], [2], security, environmental and food safety monitoring [3], are key application fields for QCM technology. In these fields, novel technical developments such as the use of highly sensitive sensor designs for multi-analyte detection and the improvement of the physical interpretation of the different phenomena occurring on the sensor surface will contribute to strengthen QCM technology [4], [5]. Recently, a highly sensitive QCM immunosensor has been successfully developed and tested for its use in pesticide determinations in food. An improvement of two orders of magnitude in Limit of Detection (LOD), when comparing with that reported for traditional 9 MHz QCM, has been achieved by combining a low-noise interface readout circuit with 100 MHz High Fundamental Frequency (HFF) QCM sensors [6]–[9]. The increment in the frequency, originated from the reduction of the sensor thickness [10], provides more sensitive resonators with a reduced surface area [11]. Size reduction allows for their integration in an array configuration, giving rise to the Monolithic QCM (MQCM) technology [12]–[20]. MQCM offers a unique approach to miniaturizing and parallelizing QCM-based assays, thus improving the throughput and reducing reagent consumption. MQCM places stringent requirements on the readout circuit. Most importantly, a high acquisition rate is required for rapidly characterizing all of the array elements. This is particularly important when probing the resonators at multiple overtones. Multiple overtone measurements are increasingly recognized as an important extension of the QCM technique. They are needed for enhancing physical interpretation of the different phenomena occurring on the sensor surface [21].

In a typical QCM experiment, the magnitudes acquired are the shifts in the resonance frequency, Δf_r, and the dissipation, ΔD (equivalent to the half-bandwidth $\Delta \Gamma$), at one or more overtones. These relevant electric parameters of the resonant sensors are related with the physical and/or biochemical properties of the layers deposited over them through various models. These models can be found in references [22], [23]. In other words, a high resolution and fast operation readout system that provides Δf_r and ΔD is required to match the capabilities of MQCM and drive the development of QCM technology. While

the classical impedance spectrometry has been routinely used for sensor characterization, mainly in very high frequency applications, the readout systems based on this method are costly and not fast enough to access many sensors in MQCM arrays, because it is difficult to lower the time per sweep below 0.5 s [24]. The time limitations of the impedance spectrometry method become even more severe when the measurements need to be done on multiple overtones [25]. Ring-down methods also provide measurements at multiple overtones, but their operation frequency is limited up to 70 MHz, thus limiting the sensibility [10], [26], [27]. Moreover, they require a high processing time (~ 1s per overtone [24]), thus preventing its use for a fast tracking of the processes occurring on multiple resonators in MQCM technology. Oscillators are faster than the previously mentioned systems. Their main drawbacks have been pointed out when working in-liquid applications and with high frequency resonators [28]–[32].

Arnau and coworkers [32], [33] proposed an alternative readout circuit based on the tracking of the sensor phase at a fixed excitation frequency. This characterization circuit can work with HFF-QCM sensors with limited phase and frequency noises, thus improving the LOD [31]. The approach allows for a low-cost implementation of the electronics and high integration capability, which, together with its high operation speed, opens the possibility of combining sequential acquisition with multichannel parallel detection in MQCM, even when probing them on multiple overtones. The circuit directly measures the phase and amplitude response of the resonator at a fixed frequency. A direct relationship between the measured phase shift and the mass variation of the layer over the resonator is provided. This relationship is only valid when, along the experiment, the resonator works in gravimetric regime (variations on the resonator amplitude are negligible) and the frequency changes are extremely small. Moreover, neither Δf_r and ΔD are provided. These aspects limit the applicability of the approach proposed in references [32], [33] for bioanalytical applications. Recently, other authors [34], [35] have proposed a method based on the measurement of the sensor impedance at a single fixed driving frequency that assumes that the sensor characteristic impedance zq remains invariant during the experiment. The method, named Fixed Frequency Drive (FFD), provides Δf_r and ΔD, but it does not take into account the electrical parasitic effects. The non-consideration of these parasitic effects could lead to errors in the sensor characterization.

This paper introduces a single-frequency-based QCM characterization method named Acoustic Wave Single Frequency Measurement (AWSFM) for measuring Δf_r and ΔD at multiple overtones. The method uses the hardware introduced by Arnau and co-workers in references [32], [33] with a new approach to provide Δf_r and ΔD. AWSFM fast method considers, not only the motional properties of the resonator (directly related to the biochemical and physical properties of the layers), but also the electrical parasitic effects [24]. Impedance spectrometry analysis accounts for these parasitic effects through the fitting of resonance models to entire frequency sweeps. This makes the measurement more robust against the electrical artefacts at the cost of slowing down the operation speed. Instead, AWSFM method performs an initial fitting of the sensor admittance spectrum, followed by a calculation of the frequency and dissipation shifts from a measurement at a single testing frequency. Therefore, our method combines the speed of a readout interface circuit working at a single frequency with the advantages of impedance analysis that allows electrical parasitic effects to be taken into account.

Two different versions of AWSFM method are presented in this work. The only meaningful difference between the two implementations is the testing frequency selection procedure. While AWSFM-Fixed Frequency (AWSFM-FF) keeps the sensor testing frequency fixed during the whole experiment (represented in Figure 3.2.1 in green color), AWSFM-Tracking (AWSFM-T) updates the testing frequency continuously by adjusting its value to the current sensor resonance frequency (represented in Figure 3.2.1 in blue color).

To evaluate the performance and accuracy of AWSFM method, we first carry out a parametric study based on the offline post-processing of real experimental data, which lets us test the influence of the different parameters affecting the method accuracy separately. Then, both versions are implemented and tested in real-time experiments for two significant applications: characterization of 1) multiple overtones in an individual sensor for two different experiments: water to water-glycerol mixture medium exchange and electrochemical deposition of copper; and 2) multiple sensors integrated in a Monolithic QCM array for direct adsorption of Neutravidin.

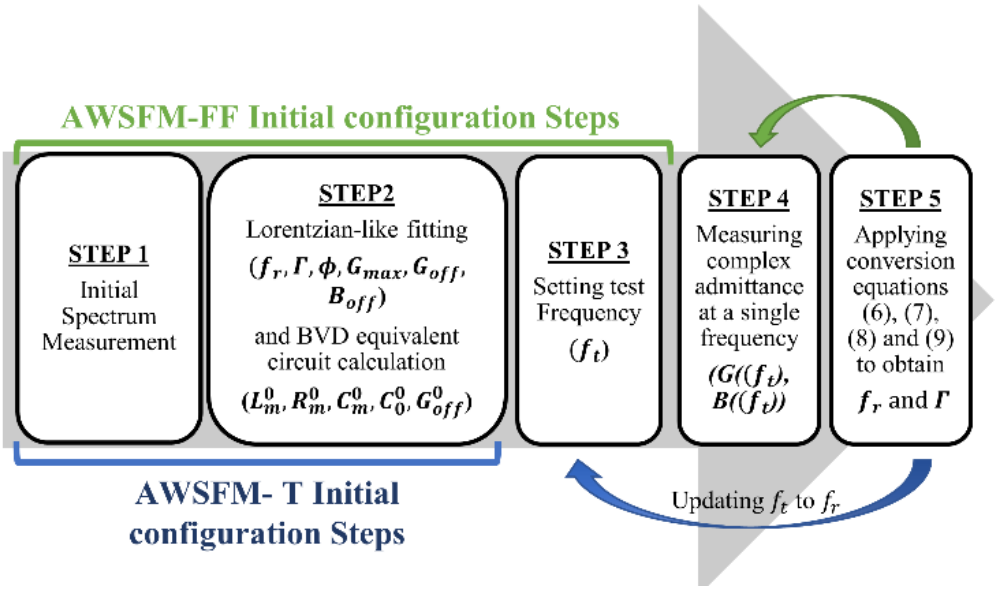

Figure 3.2.1 Flow diagrams describing the different steps of both approaches AWSFM-FF (Green) and AWSFM-T (blue) to estimate the values of f_r and D (or Γ).

3.2.2. Materials and Methods

3.2.2.1. Description of the novel characterization method

Our QCM characterization method is based on the application of the well-known Butterworth-van-Dyke (BVD) model. The BVD equivalent circuit models the response of the uncoated QCM sensor close to its resonance frequencies [36]. The model has two branches: the first one is known as "static branch" that is formed by a capacitor C_0, which is associated with the electrical capacitance of the dielectric material of the quartz resonator. The second branch is the so-called "motional branch" and it is formed by an LCR series circuit (R_m, L_m and C_m). A third branch containing a frequency dependent conductance (G_{off}) can be added to consider the experimental increment of the conductance baseline with the frequency [24], [37], [38]. Each one of the electrical elements of the motional branch is related to the mechanical properties of the resonator.

The AWSFM method yields the changes in the resonance frequency and in the dissipation of the sensor (Δf_r and ΔD) from the real and imaginary parts of the electrical sensor admittance measured at a single testing frequency. Next, the equations that define AWSFM are introduced. (It is important to mention that the applicability of the method requires an initial estimation of the whole set of the BVD circuit parameters R_m^0, L_m^0, C_m^0,

G_{off} and C_0^0-, and to assume that no changes will occur in C_m and C_0 during the experiment).

The complex admittance of the sensor predicted by the BVD equivalent circuit is:

$$Y_X = G(\omega_t) + jB(\omega_t) = [R_m/(R_m^2 + X_m^2)] + j\omega_t C_0 - j[X_m/(R_m^2 + X_m^2)] \quad (1)$$

where ω_t is the angular frequency at which the admittance is measured ($\omega_t = 2\pi f_t$ where f_t is the testing frequency), G is the conductance after subtracting G_{off} value, B is the susceptance, and X_m is defined as:

$$X_m = L_m\omega_t - [1/(C_m\omega_t)] \quad (2)$$

Separating real and imaginary parts in (1) and rearranging the terms, Equations (3) and (4) are obtained:

$$G(\omega_t) = 1/\left[R_m\left(1 + (X_m^2/R_m^2)\right)\right] \quad (3)$$

$$B(\omega_t) = \omega_t C_0 - \left[(X_m/R_m)/\left[R_m\left(1 + (X_m^2/R_m^2)\right)\right]\right] \quad (4)$$

Operating with (3) and (4), it is possible to obtain the relation (5):

$$(X_m/R_m) = \left(\omega_t C_0 - B(\omega_t)\right)/G(\omega_t) \quad (5)$$

Substitution of (5) into (3) leads to Equation (6) that allows the changes in the resistance associated to the losses in the sensor from the measurement of the admittance at the angular frequency ω_t to be estimated:

$$R_m = 1/\left[G(\omega_t)\left[1 + \left(\omega_t C_0 - B(\omega_t)\right)^2/G(\omega_t)^2\right]\right] \quad (6)$$

Combining Equations (2) and (5) and solving for Lm, Equation (7) is obtained.

$$L_m = (R_m/\omega_t)\left[\left(\omega_t C_0 - B(\omega_t)\right)/G(\omega_t)\right] + 1/(\omega_t^2 C_m) \quad (7)$$

Finally, the motional series resonant frequency f_r can be calculated directly from the well-known Equation (8). L_m is obtained from Equation (7), and $C_m = C_m^0$ is calculated in the initial fitting of the admittance spectrum of the sensor and kept constant.

$$f_r = 1/\left(2\pi\sqrt{L_m C_m}\right) \quad (8)$$

The dissipation factor D and the half-bandwidth Γ are then obtained from L_m and $R_m$values by applying the BVD relation for the quality factor [36]:

$$D = 1/Q = 2\Gamma/f_r = R_m/(2\pi f_r L_m) \tag{9}$$

Equations (6) and (8) can be applied to estimate, respectively, the value of the resistance and the resonance frequency of a QCM sensor in real time from the complex admittance of the sensor monitored at a single frequency. Equation (9) can be alternatively used instead of Equation (6) to estimate losses in the sensor through the dissipation or the half-bandwidth parameters. It is worthwhile mentioning that changes in C_m and C_0 lead to errors in Δf_r and ΔD estimated with the method; we discuss this in the section III.

Practical implementation of AWSFM method is described next. Most of the steps are identical in AWSM-FF and AWSM-T approaches; the only meaningful difference lies on whether the testing frequency is updated or not (see Figure 3.2.1):

STEP 1: Electrical artefacts affecting the sensor response are considered by performing an initial sweep of the complex electrical admittance spectrum in the 3dB bandwidth around the resonance.

STEP 2: Nelder-Mead Simplex algorithm [39] is used to fit the measured spectrum ($G(f)$ and $B(f)$) to a "phase-shifted-Lorentzian" function described in [24].

$$G(f) = G_{max}\left(\frac{f^2(2\Gamma)^2}{(f_r^2 - f^2)^2 + f^2(2\Gamma)^2}\cos\phi - \frac{f(2\Gamma)(f_r^2 - f^2)}{(f_r^2 - f^2)^2 + f^2(2\Gamma)^2}\sin\phi\right) + G_{off} \tag{10}$$

$$B(f) = G_{max}\left(\frac{f^2(2\Gamma)^2}{(f_r^2 - f^2)^2 + f^2(2\Gamma)^2}\sin\phi + \frac{f(2\Gamma)(f_r^2 - f^2)}{(f_r^2 - f^2)^2 + f^2(2\Gamma)^2}\cos\phi\right) + B_{off} \tag{11}$$

where f_r is the resonance frequency, G_{max} is the maximum conductance, G_{off} is the conductance offset, B_{off} is the susceptance offset, Γ is resonance half-bandwidth that is directly related to dissipation and ϕ is a shift angle accounting for a slight tilt of the resonance curve in the complex plane, which is often found. From these parameters, the values of the BVD elements can be directly obtained [36]:

$$\mathrm{R}_m^0 = 1/G_{max} \tag{12}$$
$$\mathrm{L}_m^0 = R_m/(4\pi\Gamma) \tag{13}$$
$$\mathrm{C}_m^0 = 1/(4\pi^2 f_r^2 L_m) \tag{14}$$
$$\mathrm{C}_0^0 = B_{off}/2\pi f_r \tag{15}$$

This procedure results in the values of the parameters G_{off}^0, R_m^0, L_m^0, C_m^0, and C_0^0 that best represent the initial response of the sensor.

STEP3: The testing frequency, f_t, is set to the value of f_r obtained in step 2. This step is just called once in AWSFM-FF implementation of the method, while it is called continuously in AWSFM-T implementation to keep the testing frequency updated to the f_r value throughout the experiment.

STEP 4: Values of G and B are monitored at the testing frequency f_t during the experiment ($G(\omega_t)$ and $B(\omega_t)$).

STEP 5: Equations (6), (7), (8) and (9) are used to calculate the values of f_r and losses (R_m, D or Γ) from $G(\omega_t)$ and $B(\omega_t)$measured in step 4 and from the initial values of C_m and C_0 extracted in step 2 (($C_m^0$and C_0^0). The resonance frequency f_r obtained in this step is used to update the testing frequency in step 3 of AWSFM-T method.

3.2.2.2. Instrument and devices

3.2.2.2.1. Sensors

Individual, circular, 14 mm 5 MHz QCM sensors (AWSensors S.L., Valencia, Spain), that were used in this study, are AT-cut bevelled plano-plano quartz crystals coated with circular wrapped gold electrodes. MQCM arrays (AWSensors S.L.) comprised 24 HFF-QCM sensors integrated in a 1-inch circular AT-cut quartz wafer. The fundamental frequency of the resonators in these arrays is 50 MHz, and their surfaces are flat and polished. The working side of the array is a grounded common electrode to avoid capacitive coupling through the liquid (see Section SI in the supporting information, Appendix B).

To clean the sensors, they were exposed to UV radiation for 10 min in a UV/ozone cleaner (BioForce Nanosciences Inc., Chicago, IL, USA), rinsed with 99% pure ethanol, rinsed with bi-distilled water, dried with ultra-pure nitrogen gas (Al Air Liquide España, S.A.) using a gas filter pistol equipped with a 1 μm pore diameter PTFE filter (Skan AG, Allschwil, Switzerland), and treated again with UV/ozone for 10 min.

3.2.2.2.2. Sensor electrical characterization

AWS X1 platform (AWSensors S.L.) was used to characterize individual 5 MHz sensor response. This Quartz Crystal Microbalance with Dissipation (QCMD) instrument is based on the fixed-frequency phase-shift measurement technique described elsewhere [33]. AWS X1 incorporates several operation modes including a characterization method based on classical impedance spectroscopy that provides both frequency and dissipation information. This operation mode was used as a reference method in this work. AWS X24 platform (AWSensors S.L.) was used to characterize MQCM array response. This device is based on the same core technology as AWS X1 system and is capable of measuring simultaneously the acoustic response of up to 24 HFF-QCMD sensors. AWSuite software package (AWSensors S.L.) has been used to control both instruments and to register and process the acquired data.

3.2.2.3. Experimental

3.2.2.3.1. Water to water-glycerol mixture medium exchange measurement protocol

Double distilled water-Glycerol mixtures (25%) were prepared. Their theoretical viscosities and densities are 1.386 Pa·s and 1061.15 kg/m^3, respectively [40]. 5 MHz QCM sensors were mounted into a measurement flow-cell (AWSensors S.L.). AWS Flow Control Unit, (AWSensors S.L.) was used to generate a uniform flow through the sensor cell. A flow rate of 50µL/min was set. Temperature, controlled with the integrated Peltier elements, was set to 23°C. Assay procedure was as follows: 1) Sensor stabilization under flow of bi-distilled water until stable baselines for frequency and dissipation are achieved. 2) Glycerol injection for 12.5 min. 3) Bi-distilled water flow through the sensor. Steps 2) and 3) are repeated 3 times.

3.2.2.3.2. Electrochemical deposition of copper

Copper sulphate ($CuSO_4$) dissolution 10 mM was prepared using double distilled water. Electrochemical quartz crystal microbalance experiments were carried out with a SP-200 potentiostat/galvanostat (Biologic, Grenoble, France). A cyclic voltammetry was carried out using a conventional three-electrode in-batch cell (AWSensors S.L.). Top surface of a 5 MHz QCM sensor was used as the working electrode. The reference electrode was Ag|AgCl with a 3 M NaCl internal solution (RE-1B, ALS Co., Ltd, Tokyo, Japan) and

the counter electrode was a platinum partially coiled wire (ALS Co., Ltd). Cyclic voltammograms were registered at a sweep rate of 20 mV s^{-1}. Maximum and minimum vertex potentials were set to 0.5 V and -0.22 V, respectively. Three cycles were measured with each method to check the repeatability of the experiment.

3.2.2.3.3. Neutravidin adsorption over MQCM array

Neutravidin adsorption was measured using three different characterization methods: reference impedance spectrometry method, AWSFM-T and AWSFM-FF. 8 sensors of the same array were monitored in each experiment. A MQCM custom flow measurement cell (Jobst Technologies, Freiburg, Germany) was used. Fluidic channels were filled with PBS at a flow rate of 20 µL/min. Baseline signals were acquired for ~ 5 – 10 min, followed by the injection of neutravidin (at a concentration of 100 µg/mL in PBS). See Supplementary information SI for further details (Appendix B).

3.2.2.4. Chemicals

Nanopure water used in this study was either analytical grade water (Panreac Química SLU, Barcelona, Spain), or produced with a Smart2Pure UVUF water purification system (Thermo Fisher Scientific, Barcelona, Spain). Pure ethanol was purchased from Panreac Química SLU (Barcelona, Spain) and Glycerol was purchased from Scharlab (Barcelona, Spain) with 99.5% reagent grade. Phosphate buffered saline (PBS) tablets for preparing 0.01 M phosphate buffer containing 0.0027 M potassium chloride and 0.137 M sodium chloride, pH 7.4, at 25 °C were purchased from Sigma Aldrich Química, S.L.U. (Madrid, Spain). NeutrAvidin and Sodium Dodecyl Sulfate (SDS) 20% solution were purchased from Fisher Scientific S.L. (Madrid, Spain). COBAS Cleaner was purchased from Sanilabo S.L. (Valencia, Spain).

3.2.3. Results and Discussion

3.2.3.1. Parametric Study of the characterization methods

A parametric study based on the offline processing of real QCMD experiments was performed to deepen our understanding of the AWSFM method. In this study, we developed a custom software code to simulate the admittance spectrum of the sensor at

any driving frequency starting from the six parameters of the "phase-shifted-Lorentzian" model described in Eq. 10 and 11. These parameters (f_r, G_{max}, G_{off}, B_{off}, Γ and ϕ) were gathered from real experiments monitored along the time by using classical impedance spectrometry. We have used real data as starting point, instead of ideal ones, in order to obtain a more accurate evaluation of the method. Our software code also implements AWSFM method to calculate the expected resonance frequency and dissipation shifts from the simulated admittance spectrum (See Supplementary information SII for further details, Appendix B). We have also included FFD method proposed by Guha and co-workers [34] in our analysis for comparison. Two representative cases were chosen to test the proposed method: 1) a rigid layer contacting a Newtonian medium and 2) a semi-infinite Newtonian medium exchange.

In the first case, AWSFM-FF and AWSFM-T results agree well with the experimental frequency data (see Figure 3.2.2(a)). FFD method underestimates the frequency shift for $|\Delta f_r|$ values higher than 500 Hz. However, it behaves well for small frequency shifts. We attribute the limited operating range of FFD method to the assumption that the sensor characteristic impedance ($z_q = \sqrt{L_m/C_m}$), i.e., L_m to C_m ratio, does not change during the experiment. Unlike the FFD method, AWSFM-FF and AWSFM-T methods consider L_m variations (C_m is kept constant throughout the experiment). From our point of view, the latter assumption fits better with the nature of QCM experiments, where mass transfer processes at the sensor surface are studied, since theoretical physical meaning of L_m parameter is indeed directly related to mass changes [36].

AWSFM-T is the only scheme that provides an accurate estimation of the half-bandwidth shift (see Figure 3.2.2(b)). Methods based on the fixed testing frequency that is not updated during the experiment (AWSFM-FF and FFD) fail to reproduce the experimentally observed changes in the half-bandwidth when the $|\Delta f_r|$ is greater than 500Hz.

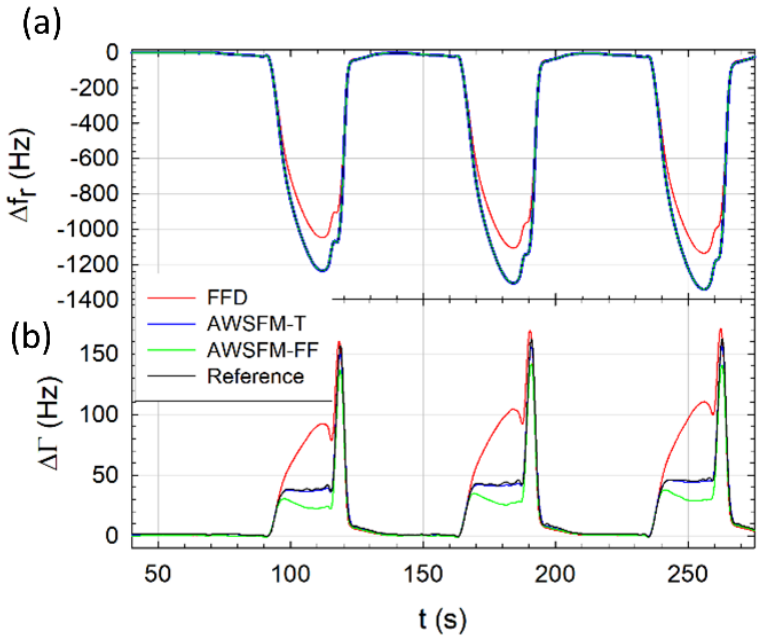

Figure 3.2.2 Resonance frequency (a) and half-bandwidth (b) shifts versus time for a rigid layer contacting a Newtonian medium obtained experimentally (black) and with the simulated methods: AWSFM-T (blue), AWSFM-FF (green) and FFD (red).

Simulation was extended to all the overtones acquired (from 1st to 13th) for the two representative experimental conditions. A general trend that was observed for all three methods is that the errors are considerably larger in half-bandwidth dissipation than in the frequency determination. This is shown in Figure 3.2.3, where it can be seen that the errors in the half-bandwidth are especially significant in the case of a rigid layer contacting a Newtonian medium for the fixed-frequency methods (AWSFM-FF and FFD). Furthermore, the errors in the case of the FFD method are always larger than in the case of the other two methods, both for the frequency, and for the half-bandwidth. On the other hand, the AWSFM-FF achieves a good accuracy in f_r, but exhibit higher errors in Γ than the AWSFM-T method, which is the most accurate of all three for both f_r and Γ. AWSFM-T errors do not exceed 2.02 ppm for f_r and 4482 ppm for Γ for both experimental conditions.

Since the methods are based on the estimation of sensor admittance at a single testing frequency while assuming constant C_0 and C_m parameters, we hypothesize that validity ranges and accuracies of fixed frequency methods could be affected by the nature of the changes in the admittance spectrum "shape". If f_r variations are larger than Γ, then f_r starts to move away from ft. When the gap between f_r and f_t becomes of the same order of magnitude as the sensor resonance 3 dB span, error increases in those fixed frequency

methods. A detailed discussion about this point can be found in SIII of Supplementary Information (Appendix B).

After comparing the accuracy of the methods, we studied their sensitivity to the initial value selection of f_t and C_0. Since AWSFM-T is directly based on the continuous update of the testing frequency, we just studied the influence of f_t selection for AWSFM-FF and FFD methods. Although the influence of this parameter is not very significant in f_r measurements, which is in agreement with other author results [34], our calculations show a strong dependence in the determination of Γ on the testing frequency for both methods. This behavior is consistent for the two experimental conditions considered (see Supplementary Information SIV for further details, Appendix B).

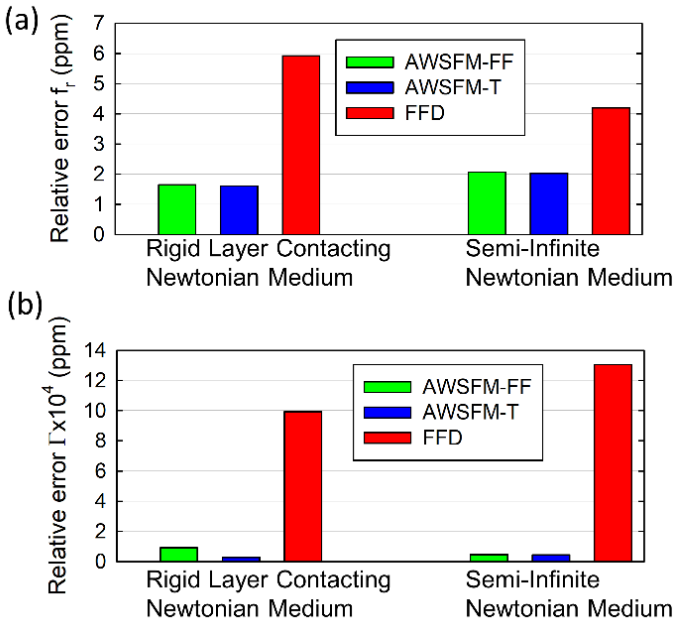

Figure 3.2.3 Simulated resonance frequency (a) and half-bandwidth (b) absolute relative error (in parts per million) with respect to experimental data for a semi-infinite Newtonian medium exchange and a rigid layer contacting a Newtonian medium for AWSFM-T (blue bar), AWSFM-FF (green bar) and FFD method (red bar).

We also considered the influence of the initial value of C_0 on the results obtained with the different methods. Since this parameter is especially sensitive to the parasitic capacitances produced by wires, connectors, and electrical contacts in the measurement cells, it is normally responsible of most of the electrical artefacts affecting the sensor response. A calculation of the influence of a small variation in C_0 on the accuracy for the three characterization methods reveals that the error is not negligible in the determination of the half bandwidth (see further details in Supplementary Information SV, Appendix B).

3.2.3.2. Real time measurements in multiple overtone experiments

To show the capabilities of AWSFM method in real applications, AWSFM-T and AWSFM-FF were implemented in the AWS X1 platform by developing a custom firmware code. Two experiments were monitored in real time: a water to water-glycerol (25%) mixture and a copper electrodeposition over the sensor top electrode surface.

The results of the measurements performed with the water-glycerol mixtures are shown in Figure 3.2.4. It can be seen that Δf_r and ΔΓ measurements obtained with both methods exhibit a good linearity with respect the square root of the overtone order n predicted by the Kanazawa-Gordon-Mason equation [41], with R-squared larger than 0.993. AWSFM-FF average relative error is 7.04% for Δf_r and 2.76% for ΔΓ. AWSFM-T average relative error is 5% for Δf_r and 1.7% for ΔΓ. An explanation for why the errors are close in this case is provided in the SIII of the supplementary information (Appendix B).

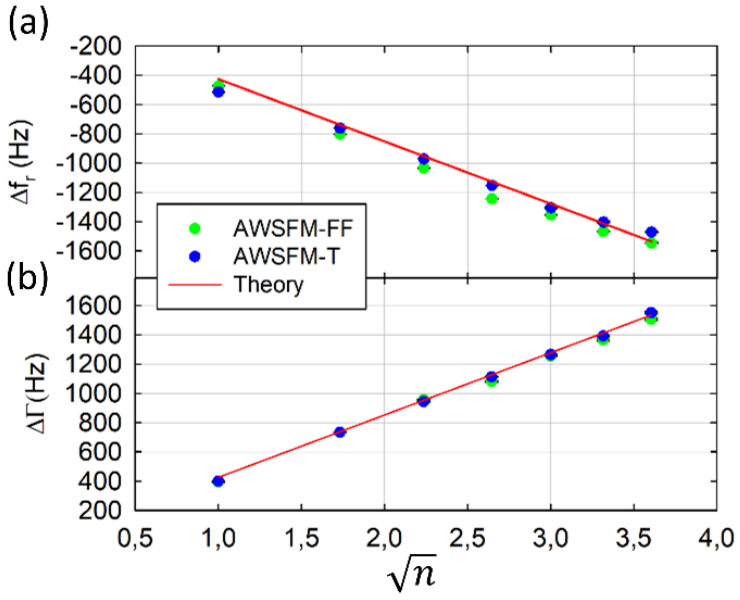

Figure 3.2.4 Shifts in frequency (a) and half-bandwidth (b) registered after the injection of water-glycerol mixture (25% in concentration). Both, AWSFM-FF (green circles) and AWSFM-T (blue circles) methods are depicted with the theoretical value predicted by Kanazawa-Gordon-Mason equation (red line).

Figure 3.2.5 shows the results of the copper electrodeposition experiments. AWSFM-T results, both for Δf_r/n and ΔΓ/n, are in good agreement with the reference method (impedance analysis). Larger errors are observed with the AWSFM-FF method than with the AWSFM-T method, which concurs with the simulation results presented above. AWSFM-FF method underestimates Δf_r/n values at higher frequencies (with the increasing overtone order n), while the measured ΔΓ/n values are underestimated or

overestimated for different n. Considering all overtones in the calculation, the average relative error in Δf_r/n is 7.11% and 151.38% in ΔΓ/n for the AWSFM-FF method, and 0.89% and 2.73% for the AWSFM-T method.

3.2.3.3. Real time measurements in Neutravidin direct adsorption over a MQCM device

Finally, direct adsorption of neutravidin (NAV) over the gold surface was monitored using a MQCM device comprising 24 HFF-QCM sensors operating at a fundamental frequency of 50 MHz. Average crosstalk between neighbor sensors was measured to be around -65 dB. This value assures the independence of the sensor response and it is better than -50 dB, recently reported for 150 MHz HFF-QCM arrays [42]. Neutravidin is commonly used in biosensing applications to prepare the sensor surface for further chemical modification [43]–[47].

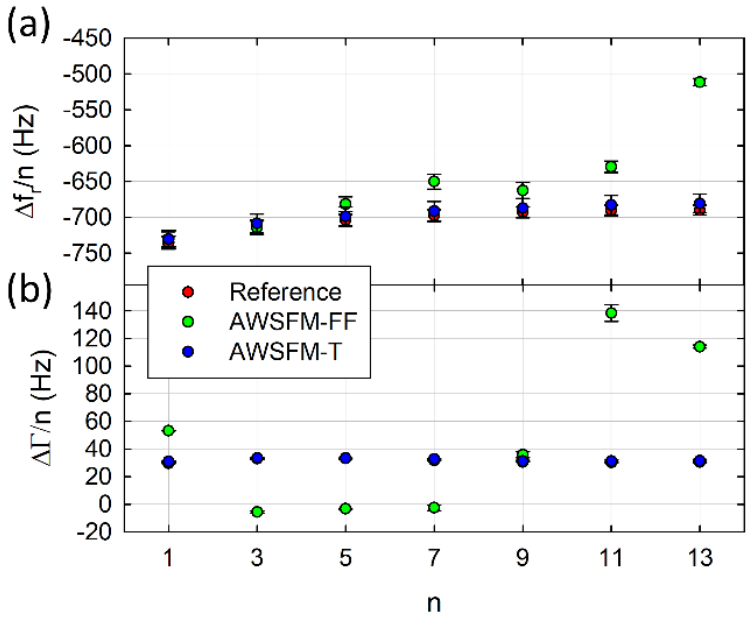

Figure 3.2.5 Normalized shifts in resonance frequency (a) and half-bandwidth (b) versus overtone order. Values were taken at the value of minimum frequency shift of the voltammetry cycle for 3 consecutive cycles. AWSFM-FF (green circles) and AWSFM-T (blue circles) methods are compared with the reference impedance spectroscopic method (red circles). Error bars are included in the graphs to show the measurement variance.

Figure 3.2.6 shows the average resonance frequency and dissipation shifts measured over the 8 sensors tested by each method. ΔD is used in this section instead of ΔΓ for easier comparison with the literature. Impedance analysis, which is used here as a reference, provides an average Δf_r value of -6075 ± 155 Hz. Considering a Sauerbrey coefficient of -0.1765 ng·cm^{-2} Hz^{-1} for 50 MHz sensors, an average areal mass density of 1072 ± 27

ng·cm^{-2} can be estimated. This value is in good agreement with the literature. Wolny et al. reported a mass density of 1081 ng·cm^{-2}, working with 4.95 MHz sensors [45]. Hays et al. reported 920 ng·cm^{-2} at 5 MHz as a first step to build a gold QCM haemoglobin immunosensors [46]. Boujday et al. reported 980 ng·cm^{-2} working at 3rd overtone of a 5MHz QCM to study the adsorption on Neutravidin and its relation to the efficiency of biosensors [47]. Tsortos and coworkers have reported mass densities from 908 to 1261 ng·cm^{-2} at the seventh overtone of a 5 MHz QCM in their works using Neutravidin to study DNA conformation [43], [44].

The absolute value of the dissipation is somewhat more difficult to discuss: it is frequency-dependent, because the rate at which energy is dissipated at the oscillating solid/liquid interface depends on the frequency. This limits the ability to compare our results, obtained with the 50 MHz sensors, with the literature, where low frequency sensors are normally used. A useful qualitative argument can, however, be made. A near-zero dissipation shift is expected for a Sauerbrey-like protein layer, but Neutravidin adsorption typically results in non-Sauerbrey behaviour. Therefore, we take our impedance analysis results at face value, as they are consistent with the literature in this qualitative sense. The important consideration for the purposes of this work is whether the AWSFM-T and -FF methods accurately reproduce the results of the impedance analysis.

For future reference, we quote a value of 0.0045·10^{-6}/Hz for the so-called acoustic ratio, $\Delta D/\ \Delta f_r$. Acoustic ratio is a parameter that depends on molecular geometry and the geometry of binding of the molecule to the surface [48], but not on other details of the experiment. It is also frequency-dependent. We note that our observed value is close to that reported by Tsortos and co-workers (0.0046·10^{-6}/Hz at 35 MHz, the seventh overtone of a 5 MHz sensor) [43]. Both these values are smaller than that of Wolny et al. (0.03·10^{-6}/Hz at 4.95 MHz) [45], or Boujday et al. (0.018·10^{-6}/Hz at 15 MHz) [47], confirming the expected trend that acoustic ratio should decrease with the resonance frequency.

Comparing the ability of the AWSFM approaches to reproduce the results of the impedance analysis (Figure 3.2.6), we can see that both AWSFM-FF and AWSFM-T agree well with reference method in Δf_r measurements. AWSFM-FF provides a frequency shift of -6115 ± 373 Hz while AWSFM-T gives -6069 ± 181 Hz. Dissipation results provided by AWSFM-T are also in very good agreement with the reference method, but this is not the case for the AWSFM-FF method: the average ΔD measured

with the AWSFM-T method is $26.4 \pm 2.9 \cdot 10^{-6}$, compared to the reference value of $27.3 \pm 3.2 \cdot 10^{-6}$. However, as it was expected from the preliminary parametric study and the real time electrodeposition experiments, fixed-frequency algorithms like AWSFM-FF fail to estimate properly the losses of the sensor unless the widening in the sensor response is of the same order as the frequency shift (see a qualitative explanation in SIII of Supplementary information, Appendix B).

3.2.3.4. Timing considerations

It is interesting to discuss the benefits of the different methods from the data acquisition rate point of view. As it has been previously mentioned, AWS X1 platform hardware was used to implement both AWSFM-T and AWSFM-FF schemes. Without loss of generality, instrument acquisition rate has been set to 10 ksps and a 10-samples direct averaging has been configured to improve the signal to noise ratio. Thus, AWSFM-FF implementation effective sampling rate is 1000 sps. On the other hand, AWSFM-T effective acquisition rate used in the measures presented in this paper is 250 sps. This rate depends on factors such as the calculation time required to compute the new testing frequency after each acquisition (400 μs in our case), the time required to modify the testing frequency in AWS X1 signal generator (hundreds of ns) and the settling time necessary to assure that steady-state has been reached in the sensor response after changing the testing frequency. Usually, the settling time is defined as a multiple of the relaxation time τ, defined as the time needed by an oscillator to adapt to changing external conditions.

$$\tau = Q/2\pi f_r \tag{16}$$

As it can be inferred from Equation 16, τ will depend not only on the sensor frequency but on the operating conditions through Q. For instance, in the case of a 5 MHz sensor operating at 1st overtone in air τ = 3.9 ms, for a 5 MHz sensor operating at 1st overtone in bi-distilled water τ = 180 μs, for a 50 MHz sensor operating at 1st overtone in air τ = 180 μs and for a 150 MHz HFF-QCM sensor operating at 1st overtone in air τ = 3.9 μs. Our current AWSFM-T and AWSFM-FF implementations allow for settling time configuration. All multiple overtone experiments described in this paper have been carried out with a 5 ms settling time.

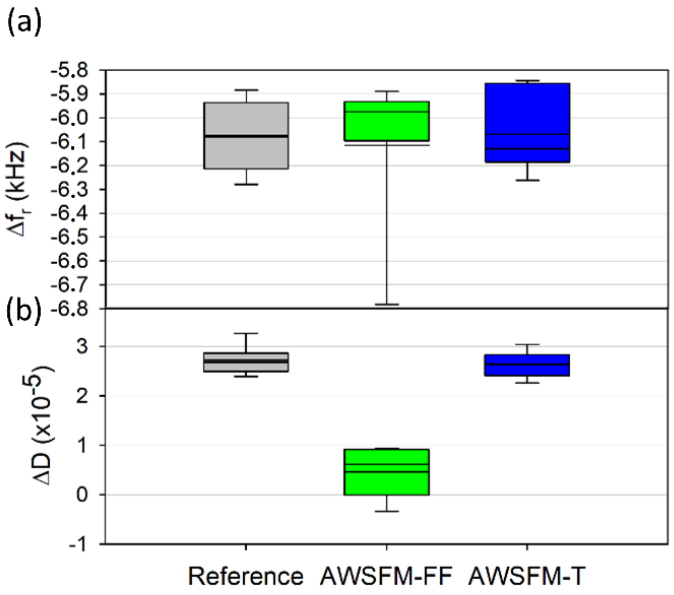

Figure 3.2.6 (a) Average resonance frequency shift (a) and average dissipation shift (b) measured for 8 sensors of the same array using AWSFM-FF (green bar), AWSFM-T (blue bar) and reference method (grey bar) during NAV adsorption.

It is worth mentioning that it takes the reference method 12 s to characterize the 24 HFF-QCM sensors integrated in the array while AWSFM method just needs less than 300 ms. Of course, acquisition rates of the AWSFM implementations described in this paper cannot be considered as the maximum ones achievable. It is possible to modify the current instrument setup or it is even possible to use another hardware platform to obtain a higher data rate. But, leaving aside hardware considerations, the only factor that really impacts on the method throughput rate is τ. At this point, AWSFM-FF could offer an advantage over AWSFM-T since it does not require to wait for the resonance settling time because, unlike AWSFM-T, AWSFM-FF testing frequency is kept constant during the whole experiment. However, in most real applications, multiple overtone approach or sensor arrays are used. In those cases, it is necessary to change the operation frequency to characterize the next overtone/sensor in a multiplexed configuration. Thus, settling time must be respected anyway and time resolution advantages of fixed-frequency methods (AWSFM-FF and FFD) disappear. In those cases, AWSFM-T is clearly the most accurate single-frequency characterization method providing Δf_r, and ΔD (or ΔΓ).

3.2.4. Conclusion

A novel characterization method (AWSFM) capable of determining the resonance frequency and dissipation through electric admittance measured at a single driving frequency has been presented in this work. Two different versions of the method have

been implemented. Main difference between them lies in the selection of the testing frequency. While the first scheme, named AWSFM-FF, operates at a fixed frequency, the second scheme, named AWSFM-T, updates continuously the testing frequency tracking the resonance frequency of the resonator. A parametric study has been carried out to study the influence of the testing frequency and the parasitic capacitances on the accuracy of the method. According to our results, a bad estimation of the values of f_t and C_0 during the initial experiment setup could lead to a significant error increase in $\Delta\Gamma$.

Both schemes have been implemented and tested in real time experiments for two representative applications. While AWSFM-FF has provided good results in Δf_r, it has shown errors in $\Delta\Gamma$. AWSFM-T has shown to be accurate both in Δf_r and $\Delta\Gamma$ and it is especially suitable for applications where a large number of sensors/overtones must be monitored simultaneously.

To the best knowledge of the authors, no other single-frequency-based characterization method has been previously used to monitor biosensing experiments simultaneously in 24 HFF-QCM sensors integrated in the same quartz substrate.

Funding sources

This research was funded by Spanish Ministry of Economy and Competitiveness with FEDER funds (AGL 2016-77702-R) and European Commission Horizon 2020 Programme (Grant Agreement number H2020-FETOPEN-2016-2017/737212-CATCH-U-DNA-Capturing non-Amplified Tumor Circulating DNA with Ultrasound Hydrodynamics) for which the authors are grateful. M. Calero is the recipient of the doctoral fellowship BES-2017-080246 from the Spanish Ministry of Economy, Industry and Competitiveness (Madrid, Spain).

References

[1] M. U. Ahmed, I. Saaem, P. C. Wu, and A. S. Brown, “Personalized diagnostics and biosensors: a review of the biology and technology needed for personalized medicine,” Crit. Rev. Biotechnol., vol. 34, no. 2, pp. 180–196, Jun. 2014.

[2] V. Gubala, L. F. Harris, A. J. Ricco, M. X. Tan, and D. E. Williams, “Point of Care Diagnostics: Status and Future,” Anal. Chem., vol. 84, no. 2, pp. 487–515, 2012.

[3] J. L. C. M. Dorne, J. L. C. M. Dorne, L. R. Bordajandi, B. Amzal, P. Ferrari, and P. Verger, “Combining analytical techniques, exposure assessment and biological effects

for risk assessment of chemicals in food," TrAC Trends Anal. Chem., vol. 28, no. 6, pp. 695–707, Jun. 2009.

[4] R. E. Speight and M. A. Cooper, "A Survey of the 2010 Quartz Crystal Microbalance Literature," J. Mol. Recognit., vol. 25, no. 9, pp. 451–473, 2012.

[5] J. P. Lafleur, A. Jönsson, S. Senkbeil, and J. P. Kutter, "Recent advances in lab-on-a-chip for biosensing applications," Biosens. Bioelectron., vol. 76, pp. 213–233, 2016.

[6] C. March et al., "High-frequency phase shift measurement greatly enhances the sensitivity of QCM immunosensors," Biosens. Bioelectron., vol. 65, pp. 1–8, Mar. 2015.

[7] L. Cervera-Chiner et al., "High Fundamental Frequency Quartz Crystal Microbalance (HFF-QCM) immunosensor for pesticide detection in honey," Food Control, vol. 92, pp. 1–6, Oct. 2018.

[8] L. Cervera-Chiner, C. March, A. Arnau, Y. Jiménez, and Á. Montoya, "Detection of DDT and carbaryl pesticides in honey by means of immunosensors based on high fundamental frequency quartz crystal microbalance (HFF-QCM)," J. Sci. Food Agric., vol. 100, no. 6, pp. 2468–2472, Apr. 2020.

[9] L. Cervera-Chiner et al., "High Fundamental Frequency Quartz Crystal Microbalance (HFF-QCMD) Immunosensor for detection of sulfathiazole in honey," Food Control, vol. 115, no. september, p. 107296, Sep. 2020.

[10] G. Sauerbrey, "Verwendung von Schwingquarzen zur Wägung dünner Schichten und zur Mikrowägung," Zeitschrift für Phys., vol. 155, no. 2, pp. 206–222, 1959.

[11] R. Fernández, P. García, M. García, J. García, Y. Jiménez, and A. Arnau, "Design and Validation of a 150 MHz HFFQCM Sensor for Bio-Sensing Applications," Sensors, vol. 17, no. 9, p. 2057, Sep. 2017.

[12] P. Kao, D. Allara, and S. Tadigadapa, "Fabrication and performance characteristics of high-frequency micromachined bulk acoustic wave quartz resonator arrays," Meas. Sci. Technol., vol. 20, no. 12, p. 124007, Dec. 2009.

[13] T. Tatsuma, Y. Watanabe, N. Oyama, K. Kitakizaki, and M. Haba, "Multichannel quartz crystal microbalance," Anal. Chem., vol. 71, no. 17, pp. 3632–3636, 1999.

[14] W. Tao, P. Lin, Y. Ai, H. Wang, S. Ke, and X. Zeng, "Multichannel quartz crystal microbalance array: Fabrication, evaluation, application in biomarker detection," Anal. Biochem., vol. 494, pp. 85–92, Feb. 2016.

[15] J. Rabe, S. Büttgenbach, J. Schröder, and P. Hauptmann, "Monolithic miniaturized quartz microbalance array and its application to chemical sensor systems for liquids," IEEE Sens. J., vol. 3, no. 4, pp. 361–368, 2003.

[16] J. R. Vig, R. L. Filler, and Y. Kim, "Uncooled IR imaging array based on quartz microresonators," J. Microelectromechanical Syst., vol. 5, no. 2, pp. 131–137, 1996.

[17] T. Abe and M. Esashi, "One-chip multuchannel quartz crystal microbalance fabricated by deep RIE," Sensors Actuators A Phys., vol. 82, pp. 139–143, 2000.

[18] V. N. Hung, T. Abe, P. N. Minh, and M. Esashi, "Miniaturized, highly sensitive single-chip multichannel quartz-crystal microbalance," Appl. Phys. Lett., vol. 81, no. 26, pp. 5069–5071, 2002.

[19] A. Tuantranont, A. Wisitsora-at, P. Sritongkham, and K. Jaruwongrungsee, "A review of monolithic multichannel quartz crystal microbalance: A review," Anal. Chim. Acta, vol. 687, no. 2, pp. 114–128, 2011.

[20] R. Fernandez et al., "High Fundamental Frequency (HFF) Monolithic Resonator Arrays for Biosensing Applications: Design, Simulations, Experimental Characterization," IEEE Sens. J., vol. Accepted, pp. 1–1, 2020.

[21] G. A. McCubbin et al., "QCM-D fingerprinting of membrane-active peptides," Eur. Biophys. J., vol. 40, no. 4, pp. 437–446, 2011.

[22] D. Johannsmann, The Quartz Crystal Microbalance in Soft Matter Research. Cham: Springer International Publishing, 2015.

[23] R. Lucklum, D. Soares, and K. Kanazawa, "Models for resonant sensors," in Piezoelectric Transducers and Applications, Second Edi., A. Arnau, Ed. Springer Berlin Heidelberg, 2008, pp. 63–96.

[24] J. Petri, S. Hochstädt, T. Nentwig, A. Pausch, A. Langhoff, and D. Johannsmann, "A Fast Electrochemical Quartz Crystal Microbalance, which Acquires Frequency and Bandwidth on Multiple Overtones," Electroanalysis, vol. 29, no. 3, pp. 806–813, Mar. 2017.

[25] M. Ferrari, V. Ferrari, and D. Marioli, “Interface circuit for multiple-harmonic analysis on quartz resonator sensors to investigate on liquid solution microdroplets,” Sensors Actuators, B Chem., vol. 146, no. 2, pp. 489–494, 2010.

[26] H. Ogi, H. Naga, Y. Fukunishi, M. Hirao, and M. Nishiyama, “170-MHz Electrodeless Quartz Crystal Microbalance Biosensor: Capability and Limitation of Higher Frequency Measurement,” Anal. Chem., vol. 81, no. 19, pp. 8068–8073, Oct. 2009.

[27] Y. Montagut, J. V. García, Y. Jiménez, C. March, Á. Montoya, and A. Arnau, “Validation of a Phase-Mass Characterization Concept and Interface for Acoustic Biosensors,” Sensors, vol. 11, no. 5, pp. 4702–4720, Apr. 2011.

[28] A. Arnau, “A Review of Interface Electronic Systems for AT-cut Quartz Crystal Microbalance Applications in Liquids,” Sensors, vol. 8, no. 1, pp. 370–411, Jan. 2008.

[29] E. Uttenthaler, M. Schräml, J. Mandel, and S. Drost, “Ultrasensitive quartz crystal microbalance sensors for detection of M13-Phages in liquids,” Biosens. Bioelectron., vol. 16, no. 9–12, pp. 735–743, 2001.

[30] B. Zimmermann, R. Lucklum, P. Hauptmann, J. Rabe, and S. Büttgenbach, “Electrical characterisation of high-frequency thickness-shear-mode resonators by impedance analysis,” Sensors Actuators B Chem., vol. 76, no. 1–3, pp. 47–57, Jun. 2001.

[31] A. Arnau, Y. Montagut, J. V García, and Y. Jiménez, “A different point of view on the sensitivity of quartz crystal microbalance sensors,” Meas. Sci. Technol., vol. 20, no. 12, p. 124004, Dec. 2009.

[32] Y. Montagut, J. Garcia, Y. Jimenez, C. March, A. Montoya, and A. Arnau, “QCM Technology in Biosensors,” in Biosensors - Emerging Materials and Applications, InTech, 2011.

[33] Y. J. Montagut, J. V. García, Y. Jiménez, C. March, A. Montoya, and A. Arnau, “Frequency-shift vs phase-shift characterization of in-liquid quartz crystal microbalance applications,” Rev. Sci. Instrum., vol. 82, no. 6, p. 064702, Jun. 2011.

[34] A. Guha, N. Sandström, V. P. Ostanin, W. van der Wijngaart, D. Klenerman, and S. K. Ghosh, “Simple and ultrafast resonance frequency and dissipation shift measurements using a fixed frequency drive,” Sensors Actuators B Chem., vol. 281, pp. 960–970, Feb. 2019.

[35] A. Guha et al., “Direct detection of small molecules using a nano-molecular imprinted polymer receptor and a quartz crystal resonator driven at a fixed frequency and amplitude,” Biosens. Bioelectron., vol. 158, no. January, 2020.

[36] D. S. Ralf Lucklum, Kay Kanazawa, Piezoelectric Transducers and Applications. Berlin, Heidelberg, Heidelberg: Springer Berlin Heidelberg, 2008.

[37] K. Kanazawa, S. M. Yoon, and N. J. Cho, “Analyzing spur-distorted impedance spectra for the QCM,” J. Sensors, vol. 2009, pp. 1–8, 2009.

[38] R. Lucklum, C. Behling, R. W. Cernosek, and S. J. Martin, “Determination of complex shear modulus with thickness shear mode resonators,” J. Phys. D. Appl. Phys., vol. 30, no. 3, pp. 346–356, Feb. 1997.

[39] J. A. Nelder and R. Mead, “A Simplex Method for Function Minimization,” Comput. J., vol. 7, no. 4, pp. 308–313, Jan. 1965.

[40] M. L. sheely, “Glycerol Viscosity Tables,” Ind. Eng. Chem., vol. 24, no. 9, pp. 1060–1064, Sep. 1932.

[41] K. K. Kanazawa and J. G. Gordon, “Frequency of a quartz microbalance in contact with liquid,” Anal. Chem., vol. 57, no. 8, pp. 1770–1771, Jul. 1985.

[42] R. Fernández et al., “High Fundamental Frequency (HFF) Monolithic Resonator Arrays for Biosensing Applications: Design, Simulations, Experimental Characterization,” IEEE Sens. J., vol. Accepted, 2020.

[43] A. Tsortos, G. Papadakis, and E. Gizeli, “Acoustic wave biosensor for detecting DNA conformation; A study with QCM-D,” in 2008 IEEE International Frequency Control Symposium, 2008, vol. 24, no. 4, pp. 346–349.

[44] A. Tsortos, G. Papadakis, and E. Gizeli, “Shear acoustic wave biosensor for detecting DNA intrinsic viscosity and conformation: A study with QCM-D,” Biosens. Bioelectron., vol. 24, no. 4, pp. 836–841, Dec. 2008.

[45] P. M. Wolny, J. P. Spatz, and R. P. Richter, “On the Adsorption Behavior of Biotin-Binding Proteins on Gold and Silica,” Langmuir, vol. 26, no. 2, pp. 1029–1034, Jan. 2010.

[46] H. C. W. Hays, P. A. Millner, and M. I. Prodromidis, “Development of capacitance based immunosensors on mixed self-assembled monolayers,” Sensors Actuators B Chem., vol. 114, no. 2, pp. 1064–1070, Apr. 2006.

[47] S. Boujday, A. Bantegnie, E. Briand, P. G. Marnet, M. Salmain, and C. M. Pradier, “In-depth investigation of protein adsorption on gold surfaces: Correlating the structure and density to the efficiency of the sensing layer,” J. Phys. Chem. B, vol. 112, no. 21, pp. 6708–6715, 2008.

[48] D. Johannsmann, I. Reviakine, and R. P. Richter, “Dissipation in films of adsorbed nanospheres studied by quartz crystal microbalance (QCM),” Anal. Chem., vol. 81, no. 19, pp. 8167–8176, Oct. 2009.

3.3. A Multichannel Microfluidic Sensing Cartridge for Bioanalytical Applications of Monolithic Quartz Crystal Microbalance.

María Calero, Román Fernández, Pablo García, José Vicente García, María García, Esther Gamero-Sandemetrio, Ilya Reviakine, Antonio Arnau and Yolanda Jiménez

Biosensors 10(12), 189, November 2020

Abstract

Integrating acoustic wave sensors into lab-on-a-chip (LoC) devices is a well-known challenge. We address this challenge by designing a microfluidic device housing a monolithic array of 24 high-fundamental frequency quartz crystal microbalance with dissipation (HFF-QCMD) sensors. The device features six 6-µL channels of four sensors each for low-volume parallel measurements, a sealing mechanism that provides appropriate pressure control while assuring liquid confinement and maintaining good stability, and provides a mechanical, electrical, and thermal interface with the characterization electronics. We validate the device by measuring the response of the HFF-QCMD sensors to the air-to-liquid transition, for which the robust Kanazawa–Gordon–Mason theory exists, and then by studying the adsorption of model bioanalytes (neutravidin and biotinylated albumin). With these experiments, we show how the effects of the protein–surface interactions propagate within adsorbed protein multilayers, offering essentially new insight into the design of affinity-based bioanalytical sensors.

Keywords

HFF-QCM (high fundamental frequency quartz crystal microbalance); mass transport; flow cell; biosensor; food safety; PoC (point of care); MQCM (monolithic quartz crystal microbalance)

3.3.1. Introduction

Inexpensive, fast, parallel, small-volume sensors for detecting minute amounts of analytes in complex samples are required for wide-spread application of lab-on-a-chip (LoC) devices in research-, industrial-, and health-related areas [1], [2]. Equipped with such sensors, LoC devices can overcome the drawbacks of the conventional bulk analytical approaches that rely on expensive centralized facilities and play their singular role in the individualization of health care promised by personalized medicine [3].

Quartz crystal microbalance with dissipation, or QCMD, offers the technology needed for developing and mass-producing sensors for LoC applications. QCMD is known for its thin film monitoring [4] and biomolecular interaction measurement capabilities [5]. Digital, label-free, and very simple—its basic principle is based on electrically measuring resonance properties (frequency and dissipation) of a quartz crystal resonator [6]—QCMD can be easily automated. Key challenges for integrating QCMD technology into LoC-based applications are low throughput, high cost per sensor and per assay (related to sample/reagents volume), and lack of versatile and effective microfluidic/mechanical interfaces that can assure reliable field operation. Further improvements in sensitivity would also be beneficial for rapidly detecting small amounts of analytes in dilute samples.

To address these challenges, we introduce a microfluidic cartridge housing a monolithic high fundamental frequency (HFF) QCMD sensor array. We picked HFF-QCMD sensors because they are more sensitive than their low fundamental frequency counterparts, and can be used with low sample volumes (a few μL), and because they offer the possibility of integration into monolithic arrays [7]–[9]. Higher sensitivity is due to the smaller thickness of the HFF resonators [4], [10], which in turn leads to a reduced surface area and therefore, to smaller sample volume [11]. Integration overcomes two major impediments for developing QCMD-based sensors for LoC applications: low throughput and relatively high individual sensor cost. QCMD and HFF-QCMD sensors have already been used to develop immunoassays [12]–[17] and DNA hybridization assays with the limit of detection (LoD) in the tens of femtomoles [18] and in complex samples (blood, saliva) [19], [20], but currently, advanced commercial systems offer measurements with at most four sensors at a time, each of which has to be operated individually. This negates other advantages of QCMD technology in high-volume LoC applications. To this end, we have recently reported our design of monolithic 150 MHz HFF-QCMD sensor arrays and characterized their performance [7]. Here, we present the design of an integrated

microfluidic cartridge for housing the arrays (Figure 3.3.1) and evaluate its performance for measuring biomolecular interactions in a biotin/neutravidin based system. Our work advances the state-of-the-art by integrating sensing and microfluidic analyte delivery compatible with LoC applications.

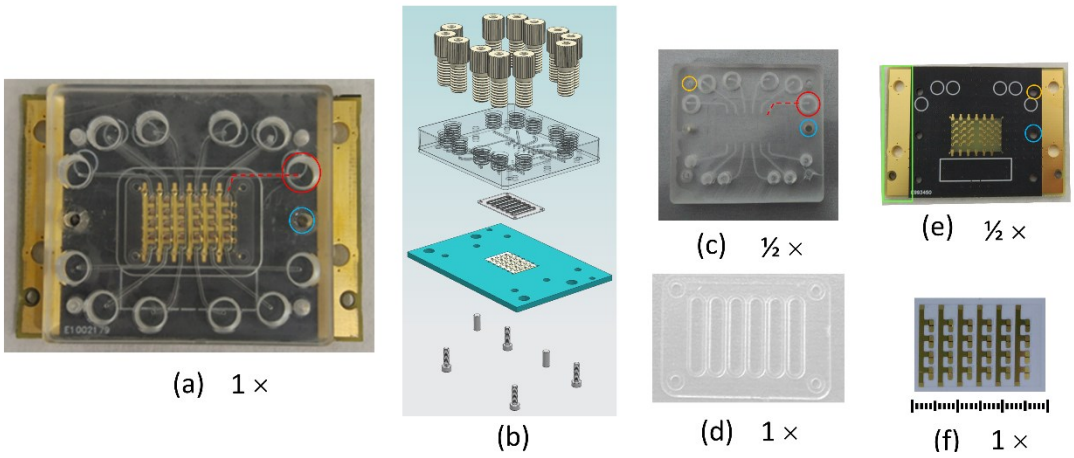

Figure 3.3.1 Multichannel Microfluidic Sensor Cartridge. Assembled cartridge (a). Schematic of cartridge assembly (b) from components (from top to bottom): microfluidic connectors, Poly(methyl methacrylate) (PMMA) cell, Poly(dimethylsiloxane) (PDMS) gasket, Printed Circuit Board (PCB) with the array, assembly screws and alignment pins. Photos of its components: PMMA cell (c), PDMS gasket with six channels (d), PCB (e), and the 24-element HFF-QCMD array (f), (see Fig. S1 in the Supporting Information for an enlarged view (Appendix C)). Note the difference in scale: (c) and (e) are shown at half the size relative to (a), (d), and (f), which are drawn to scale. Array dimensions are 14.25 mm × 9.05 mm.

The development of robust and simple HFF-QCMD detection systems for LoC applications is very much in its infancy [2]. Integration of the fluidic circuitry with the array of quartz sensors faces a number of challenges [21], [22], the key of which is insuring independent operation of the individual sensor elements that is free of the interaction between them. Interactions between sensors can be mediated electrically, mechanically, or via the fluidic path affecting analyte transport to the surface. Therefore, our evaluation of the cartridge and array performance focused as much on the reproducible measurements of frequency and dissipation shifts in response to the introduction of bioanalytes as on the independent operation of the individual array elements, as evidenced by the absence of artifacts originating from the interaction between them through any of the three pathways (electrical, mechanical, fluidic). Our experimental results were consistent with the literature and with the results of numerical calculations of molecular transport rates based on the channel and array geometry, molecular diffusion coefficients, and fluid flow rates.

3.3.2. Materials and Methods

3.3.2.1. Materials

Nanopure water used in this study was either analytical grade water (Panreac Química SLU, Barcelona, Spain), or produced with a Smart2Pure UVUF water purification system (Thermo Fisher Scientific, Barcelona, Spain). Nitrogen was from Air Liquide España S.A. (Valencia, Spain). Phosphate buffered saline (PBS) tablets for preparing 0.01 M phosphate buffer containing 0.0027 M potassium chloride and 0.137 M sodium chloride, pH 7.4, at 25 °C, and Bovine Serum Albumin (BSA) were purchased from Sigma Aldrich Química, S.L.U. (Madrid, Spain). NeutrAvidin (Nav), biotinylated BSA (bBSA), and Sodium Dodecyl Sulfate (SDS) 20% solution were purchased from Fisher Scientific S.L. (Madrid, Spain). COBAS Cleaner was purchased from Sanilabo S.L. (Valencia, Spain).

Poly(methyl methacrylate), PMMA, was from Monje Hermanos S.L. (Valencia, Spain); poly(dimethylsiloxane), PDMS, was from Ellsworth Adhesives Iberica, (Madrid, Spain). Single-component conductive epoxy AA-DUCT 900 was from Atom Adhesives (Providence, RI, USA). DuPont™ Teflon® FEP film with a thickness of 76 μm was from Dupont (Wilmington, DE, USA).

3.3.2.2. Multichannel Microfluidic Sensing Cartridge Design

The multichannel sensor cartridge consists of an array, a custom-made Printed Circuit Board (PCB) for mounting the array, and a microfluidic cell consisting of a gasket and the body. These components are shown in Figure 3.3.1 while their design and manufacturing are described below.

3.3.2.3. Arrays and PCBs

Monolithic HFF-QCMD sensor arrays (AWS-Array2-24-150.0M, Advanced Wave Sensors (AWSensors) S. L., Valencia, Spain) were manufactured as described previously [7]. They were mounted on rectangular 52.02 mm × 36.02 mm × 1.55 mm PCBs custom-designed using the ALTIUM Designer 18 software package (Altium, San Diego, CA, USA) following high-frequency signal routing and crosstalk prevention considerations and manufactured from FR4-type material by Eurocircuits (Mechelen, Belgium). The mounting was done with a single-component conductive epoxy that was deposited by

stencil printing technology (eC-stencil-mate, Eurocircuits). The stencil was configured to leave a tiny quantity (≈ 0.16 mg) of epoxy on each contact area, sufficient for making electrical contact, but not in excess in order not to affect the resonant behavior of the sensors. Before the deposition of the epoxy, the PCBs were degreased with acetone and dried at 50 °C for 5 min. Once the conducting epoxy was deposited, the arrays were placed on the PCBs manually with the assistance of a USB Microscope (Shenzhen Andonstar Tech Co. Ltd., Shenzhen, China) and a manual pick and place machine (eC-placer, Eurocircuits). The epoxy was cured at 150 °C for 1 h in an oven (eC-reflow-mate v4, Eurocircuits, Mechelen, Belgium). During the curing process, a 70 g weight was placed over the array to ensure a good contact between the array and the PCB. The array surface was protected with the transparent Fluorinated Ethylene Propylene (FEP) film.

3.3.2.4. Microfluidic Cell

The microfluidic cell consisted of two parts: a flexible gasket containing six independent flow channels, one for each column of the array, and the body of the cell for housing the gasket that contained inlet and outlet fluidic channels, the opening for the mounting screws, and the alignment pins (Figure 3.3.1b).

The gaskets were fabricated from PDMS using a mold, 9 gaskets at a time. To this end, the required volume of the PDMS curing agent and PDMS monomer was mixed at the 1:10 ratio. Vacuum was applied to the mixture for 45 min to remove air. The mold was dried at 60 °C and the freshly degassed PDMS mixture was cast onto the mold. Curing took place in an oven at 60 °C for 80 min. The height of the channels is determined by the thickness of the gasket being 480 μm while the width is 1.46 mm. Consequently, the total volume of each fluidic channel was less than 6 μL. (See Section S3 of the Supporting Information, Appendix C).

The body of the microfluidic cell consisted of two parts: the top that contained the openings for standard microfluidic connectors (VacuTight Ferrule Tefzel Red P-840 (ETFE) 1/16, Fitting P-844, IDEX Health & Science, Rohnert Park, CA, USA) for connecting the cell to the external flow control device, and the bottom, that contained inlet and outlet microchannels, 12 in total, connecting those openings to the fluidic channels in the gasket.

The mold for manufacturing PDMS gaskets, and the two parts of the microfluidic cell, were manufactured from PMMA in the vertical CNC (Computer Numerical Control)

machining center (Chevalier 1418VMC-Plus, Falcon Machine Tools Co. Ltd., Chang Hua, Taiwan). The two pieces of the microfluidic cell were joined by first softening their surfaces with ethanol, and then pressing them against each other over a period of 1 min at 70 °C, as described in ref. [23]. In this manner, a one-piece microfluidic cell was obtained. The PDMS gasket was mounted on the cell, and the cell with the gasket was placed on top of the PCB-mounted array. The assembly was guided by the alignment pins and held together with screws, as shown in Figure 3.3.1b.

3.3.2.5. Evaluation of Cartridge Performance

The performance of the array-based sensor cartridge was evaluated by monitoring resonance frequency and dissipation in situ and in real time as the arrays were exposed to liquid flow and as proteins were adsorbed to the surfaces of the arrays (in separate experiments). The results of the protein adsorption experiments were further compared with those obtained with the commercially available, individual 50 MHz HFF-QCMD sensors (AWsensors S.L., Valencia, Spain).

Resonance frequency and bandwidth (or dissipation) of the arrays and individual HFF sensors were measured as a function of time with the AWSensors X24 and A20+ platforms, respectively, running the AWSuite software package. Individual sensors were mounted in the standard, commercially available QuickLock® measurement cells (AWSensors S.L., Valencia, Spain). Fluid flow and sample injection were controlled with the AWSensors multichannel F20+ fluidics controller connected to the inlets of the sensing cartridge (for the arrays) or the inlets of the QuickLock® measurement cells.

For the measurements of the air-to-liquid transition, baseline frequency and bandwidth signals were acquired in air for ~15 min, followed by flowing PBS buffer, at a flow rate of 20 μL/min.

For the protein adsorption experiments, baseline frequency and dissipation signals were acquired in buffer flowing at a rate of 14.5–20 μL/min, depending on the experiment, for ~ 5–10 min, followed by the injection of the proteins, Nav (at a concentration of 100–200 μg/mL in PBS) or bBSA (at a concentration of 100 μg/mL). Each injection was always repeated twice, 100 μL each time, to ensure that adsorption reached saturation.

3.3.2.6. Array, Cell and Sensor Cleaning and Preparation

Prior to the experiments, PCB-mounted arrays and individual sensors were immersed in freshly filtered 2% SDS solution for 30 min. They were rinsed with Nanopure water and dried under a stream of nitrogen directed at the array and sensor surfaces through a 0.45 μm pore diameter filter housed in hand-held filter gun assembly (Skan AG, Allschwil, Switzerland) and then cleaned for 30 min in a UV/Ozone Cleaner (BioForce Nanosciences, Salt Lake City, UT, USA) that was preheated for 30 min prior to use. After cleaning, array and sensor surfaces were rinsed with ethanol to reduce the oxide that forms as a result of the UV-Ozone treatment [24] and once again dried with a stream of filtered nitrogen.

The PDMS gasket and the PMMA cell were immersed in COBAS cleaner for 30 min, rinsed with, and then sonicated in Nanopure water for 15 min to remove traces of the detergent, and dried with a stream of filtered nitrogen.

Individual sensors were mounted in the QuickLock™ measurement cells cleaned with the COBAS cleaning solution for 30 min, followed by repeated rinsing with water and ethanol, and drying with a stream of filtered nitrogen.

3.3.3. Results and Discussion

3.3.3.1. Multichannel Microfluidic Sensing Cartridge Design and Assembly

A microfluidic cartridge holding a 24 HFF-QCM sensor array operating at 150 MHz [7] was designed and implemented (Figure 3.3.1a). It consists of a microfluidic cell that delivers fluid to the sensing elements arranged in six channels of four elements each (Figure 3.3.1c), a soft PDMS gasket forming the six microfluidic channels (Figure 3.3.1d) that seals the PMMA fluid cell to the array, and the array mounted on the PCB that served as the bottom of the cell (Figure 3.3.1e,f). PMMA is a low-cost, transparent material with good thermal insulating capacity that is suitable for disposable cartridges and is used routinely in biomedical applications (e.g., bone cement [25], [26]). It has been selected because of its adequate rigidity to confer robustness to the microfluidic assembly design and its mass fabrication potential [23]. The PDMS gasket is fixed in the PMMA cell with the help of four guides (Figure 3.3.1d). The PMMA cell contains sockets for the fluidic

connectors on the top (outlined in red in Figure 3.3.1a,c), as well as sockets for the guiding pins (blue in Figure 3.3.1a,c,e) used to align the array, and mounting screws (yellow in Figure 3.3.1c,e) used to fix it. The assembly process is very simple and results in a rectangular chamber design which avoids non-uniform sample distribution [27], [28]. The PCB offers mechanical protection, ease of handling, improves the thermal stability of the array during measurements, and forms the contacts between the array and the acquisition electronics. To this end, we integrated into the PCB design two gold sidebands (highlighted in a green rectangle in Figure 3.3.1e) that are connected to the Peltier elements of the temperature control system, providing a direct thermal path. Our design allows simultaneous measurements with six different solutions. Furthermore, within each of these six measurements, it is possible to have four replicas with identically treated array element surfaces. Alternatively, each array element could be used to immobilize a different biomolecule, allowing four independent measurements with each of the six solutions at the expense of statistics.

3.3.3.2. Cartridge Performance

The performance of the cartridge was evaluated in two separated sets of experiments: the responses of the sensors to changing the media from air to liquid were measured in a first set of experiments, and sequential adsorption of proteins neutravidin and biotinylated BSA (bBSA) on the sensor surface was followed in the second set. Cartridge and array performance were evaluated by comparing our experimental results with theoretical predictions and with other experimental data, either obtained in this study with individual HFF-QCMD sensors or reported in the literature with the classical low-fundamental frequency QCMD sensors. The distribution of sensor responses was analyzed as a function of sensor position in the array to assure independent operation of the individual sensors. Finally, biomolecular transport in the cartridge has also been studied to evaluate possible limitations of the microfluidic cartridge design.

3.3.3.2.1. Air-to-Liquid Transition

Changes in the frequency and bandwidth of a quartz resonator upon exposure to a Newtonian liquid are well-understood as a result of the classical works by Mason [29] and Kanazawa [30]. When discussing the air-liquid shifts, it is more convenient to use bandwidth than dissipation, because the frequency and bandwidth changes are expected

to be equal and opposite: $\Delta f = -\Delta\Gamma = -f_{res}^{3/2}\left(\eta_l\rho_l/\pi\rho_q\mu_q\right)^{1/2}$; this is the so-called Kanazawa–Gordon–Mason equation, where f_{res} is the fundamental resonance frequency of the resonator, η_l and ρ_l are the liquid viscosity and density, respectively, ρ_q is the density of quartz, and μ_q is its shear elastic modulus. Experimental results are shown in Figure 3.3.2, where the shifts in both signals upon the transition from air to buffer are plotted as a function of the array element (Supplementary Fig. S1, Appendix C). We find no systematic trends in the shifts of either of the two signals as a function of the array element position, as is expected for the normal functioning of the array, the flow system, and the electronics. It is interesting to note the increase in Δf and $-\Delta\Gamma$ in sensors 20 to 24. Although it seems a systematic trend, this effect was not observed in other measurements, confirming its coincidental nature.

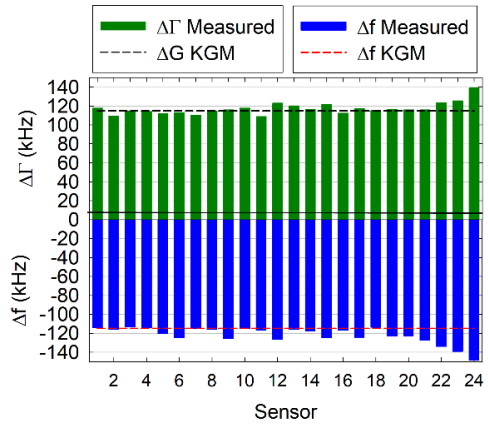

Figure 3.3.2 Air-buffer measurements. A plot of the typical set of air-to-buffer shifts for all the elements of one array (bars) with the expected values calculated based on the Kanazawa-Gordon-Mason equation (dashed lines).

On average, we observed shifts of −120 ± 15 kHz for Δf and 115 ± 9 kHz for $\Delta\Gamma$, averaged over 110 individual air-to-buffer measurements. The theoretical values for the arrays used in these measurements are ± (115 ± 2) kHz, where the negative and the positive signs refer to the frequency and the dissipation shifts, respectively, and the error arises from the variation of the elements' resonance frequencies [7]. The larger experimentally observed value of Δf is expected, because finite roughness typically masquerades as an additional Sauerbrey shift that does not affect the bandwidth [31], [32]; a 5 kHz difference in frequency would correspond to a Sauerbrey film of ~9.9 Å with a density of 1 g/cm^3, which is reasonable given the roughness values of ~1 nm we reported previously for the surfaces of these arrays [7].

3.3.3.2.2. Protein Adsorption and Interaction Studies

The functionality of the multichannel cartridges for sensing biomolecular interactions was evaluated using neutravidin (Nav) and biotinylated BSA (bBSA) as a model system that is widely used in biotechnology and bioanalytics [33], [34].

Proteins were allowed to adsorb in sequence, starting with Nav in one set of experiments, and starting with bBSA in another set. Each sequence consisted of three sets of (Nav + bBSA) pairs, with non-biotinylated BSA injected between each step to test for non-specific adsorption. The purpose of the two different sequences was to establish a protocol for subsequent applications of these arrays in bioanalytical sensing. One such sequence is shown in Figure 3.3.3a.

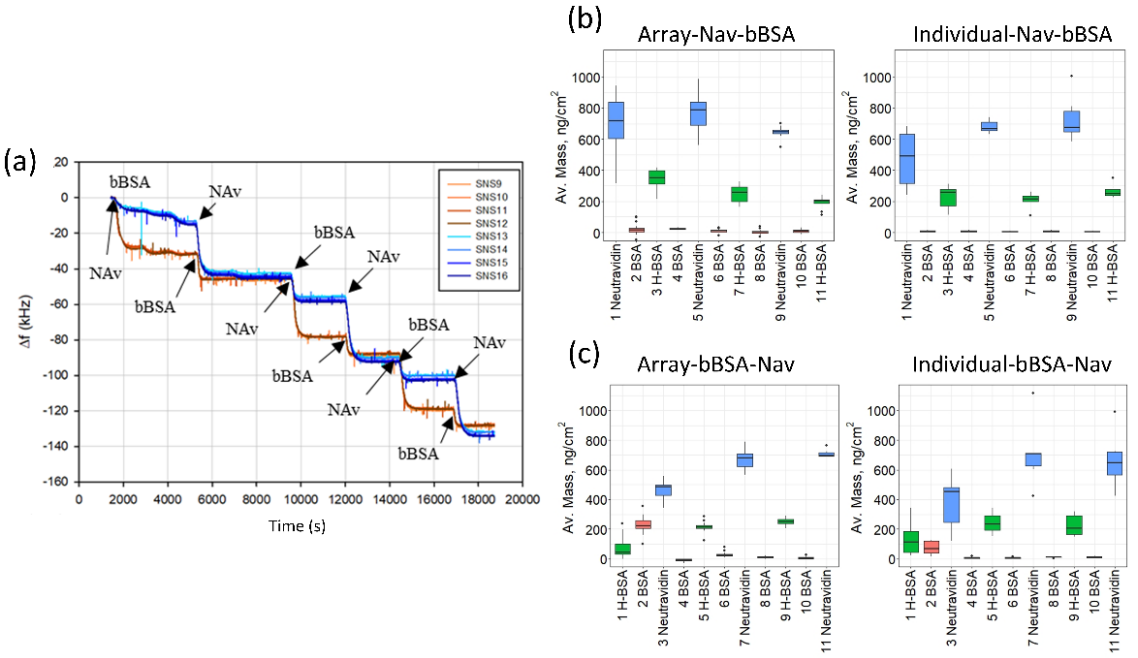

Figure 3.3.3 Protein adsorption measurements. (a) Frequency changes due to the sequential adsorption of proteins for two columns of the array relative to a baseline in buffer. In one of the two columns (SNS13 to SNS16), proteins were adsorbed in sequence bBSA-Nav- bBSA-Nav- bBSA-Nav, in the other (SNS9 to SNS12) Nav-bBSA-Nav-bBSA-Nav-bBSA. SNSi with i = 9 to 16 refers to the element position on the array according to Fig. S1 in the Supporting Information. (b,c) (Apendix C) Mass changes observed in the experiments performed with arrays (left) and individual 50 MHz resonators at the 3rd overtone (right) for the two adsorption sequences, respectively. Error bars are standard deviations.

Average results from multiple arrays and individual HFF sensors are shown in Figure 3.3.3b (for the Nav–BSA sequence) and in Figure 3.3.3c (for the bBSA–Nav) sequence. The adsorbed layer masses, calculated from the frequency shifts using the Sauerbrey

relationship [4], are summarized in Table S1 in the Supporting Information (Appendix C). The masses expected on the basis of the sizes of the molecules and the corresponding literature values are presented in Supplementary Table S2 (Appendix C). The adsorption processes are depicted schematically in Figure 3.3.4.

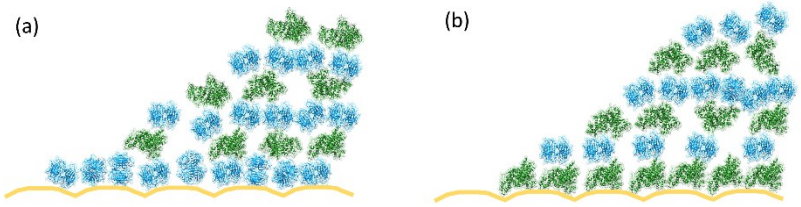

Figure 3.3.4 Schematic representation of the surface architecture achieved in the adsorption experiments. (a) Shows the adsorption sequence starting with Nav, and (b)—starting with bBSA. The gold is shown in yellow, Nav in light blue, and BSA in green. No distinction is made between the biotinylated and non-biotinylated BSA. The vertical dimension of the roughness of the gold is to scale with the sizes of the proteins; similarly, the protein dimensions are also drawn to scale relative to each other, but Nav aggregation is ignored for simplicity. On average, there is ~ one bBSA molecule for every two Nav molecules adsorbed on gold. Away from the surface, there are ~ three Nav molecules per every bBSA molecule. See Section S2 in the Supporting Information for further discussion (Appendix C). This figure was prepared using USCF Chimera version 1.14 [35].

Several trends can be noted in the experimental data. First and foremost, there is a good agreement between the results obtained with the arrays and with the individual HFF resonators (Figure 3.3.3, Supplementary Table S1, Appendix C). Second, the amounts of protein adsorbed observed with both systems (arrays and the individual resonators) are in good agreement with the literature. Focusing on the adsorption of Nav on gold (Figure 3.3.3b), we find 700 ± 180 ng/cm^2 for the array and 590 ± 200 ng/cm^2 for the individual sensors (Supplementary Table S1, Appendix C). The limiting value of the adsorbed Nav mass is also ~ 700 ng/cm^2 ("limiting" here refers to the apparent saturation of the values of the adsorbed mass as a function of the adsorption step in Figure 3.3.3b,c). This is in good agreement with the literature values for Nav adsorption on gold that range between ~ 700 and ~ 1300 ng/cm^2 (Supplementary Table S2, Appendix C). The variability here is due to the tendency of this protein to aggregate and corresponds to the age and treatment of the neutravidin solution. The aggregation tendency also explains the difference between the observed masses and their expected values based on the protein dimensions and between Nav and a very similar protein, streptavidin (Sav) (Supplementary Table S2, Appendix C) [36].

The amount of Nav adsorbed onto gold pre-coated with bBSA is significantly smaller, than directly onto gold (~400 ng/cm^2, nearly identical for the arrays and the individual

sensors; Figure 3.3.3c and Supplementary Table S1, Appendix C). Also, the variation in the mass of Nav adsorbed, expressed as a standard error, is 15 ng/cm^2 when it is adsorbed on the bBSA layer, but 38 ng/cm2 when it is adsorbed onto gold directly, indicating that orienting Nav on a biotinylated substrate results in a more homogeneous layer. The value of the adsorbed mass of Nav on bBSA is in good agreement with that adsorbed on the biotinylated SLBs [36] (566 ng/cm2, Supplementary Table S2, Appendix C). One of the factors that contribute to the observed difference in the adsorbed mass is the difference in protein orientation: it is quasi-random when Nav is adsorbed on gold but fixed by the underlying bBSA layer when Nav adsorbs on bBSA. Such an effect has already been reported for Sav (Supplementary Table S2, Appendix C): a larger amount of this protein adsorbs on the mercaptounadecanoic acid (MUA) SAM or on gold than on a layer of biotinylated molecules (lipids or alkane thiols).

With Nav, there is the additional effect of aggregation of this protein, an effect that is absent in the case of Sav. Indeed, the difference between Nav adsorbed on gold and Nav adsorbed on bBSA or bSLB is much greater, than between streptavidin adsorbed on gold vs. bSLB or bSAM (Supplementary Table S2, Appendix C).

Notably, the tendency of neutravidin to aggregate appears to be reduced, when it is adsorbed in a fixed orientation on the biotinylated substrates (bBSA, Table S1, or bSLB, Supplementary Table S2, Appendix C), compared to when it is adsorbed on gold. This could also be due to the increased stability of this protein in the biotin-bound conformation [37], or to the steric limitations arising from the number of accessible biotins presented by the biotinylated surfaces. This effect is gradually lost in the subsequent adsorption steps (steps 2 and 3 in Supplementary Table S1, Appendix C and Figure 3.3.4) since the limiting values of the adsorbed amounts of Nav are independent of the direction of the adsorption.

The value of the limiting mass of bBSA (~ 230 ng/cm^2, steps 2 and 3 in Supplementary Table S1, Appendix C) nearly identical for the arrays and the individual sensors, is independent of the direction of adsorption, and is consistent with what has been reported by others for bBSA on Nav on gold or on Nav on SLBs (Table S2, Appendix C). It is worth noting that there is a significant difference in the behavior of the biotinylated and non-biotinylated versions of BSA on bare gold (c.f. our results quoted above with Table S2 in the supporting information, Appendix C). This has been noted before by Kim et al. when adsorbing BSA/bBSA mixtures on gold [38]. The effect has not been investigated

further, but probably originates from the effect of biotinylation on the adsorbed protein orientation, conformation, or both.

We would like to underscore the importance of the comparison between the array and the individual sensors: since we [11]–[16] and others [17], [39]–[41] have previously demonstrated the robustness and reproducibility of HFF resonators, the observed correspondence shows (1) that integration into an array does not affect their performance, and (2), demonstrates the functionality of the microfluidic cartridge. The comparison with the published results obtained with the same bioanalytical systems using classical, low-frequency individual sensors confirms that our array-based cartridge is capable quantitatively and accurately assaying bioanalytical systems based on specific binding.

3.3.3.2.3. Biomolecular Transport in the Microfluidic Cartridge

One concern with an integrated array of sensing elements and the corresponding fluidics is the presence of systematic artifacts arising from transport limitations in the fluidic channels. Here, we first analyze the variation in the adsorbed protein layer masses detected by the different array elements (Figure 3.3.5) and then compare transport kinetics of the analytes in the fluidic cartridge with theoretical predictions based on molecular diffusion coefficients and the geometry of the fluidic channels and the arrays (Figure 3.3.6). We demonstrate lack of such systematic errors.

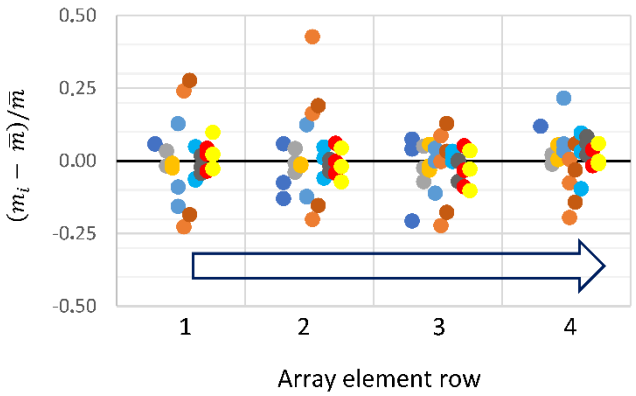

Figure 3.3.5 Variation in the adsorbed mass as a function of the sensor position. The absolute deviation of the adsorbed mass, normalized by the mean, is plotted against the row of the array element. m_i is the adsorbed mass detected by the i-th element of the array (see Fig. S1). $\bar{m}$ is the average mass in a given column. Different colors represent different experiments. Results of each individual experiment are offset from each other for visibility. Blue open arrow indicates the direction of the fluidic flow up the column.

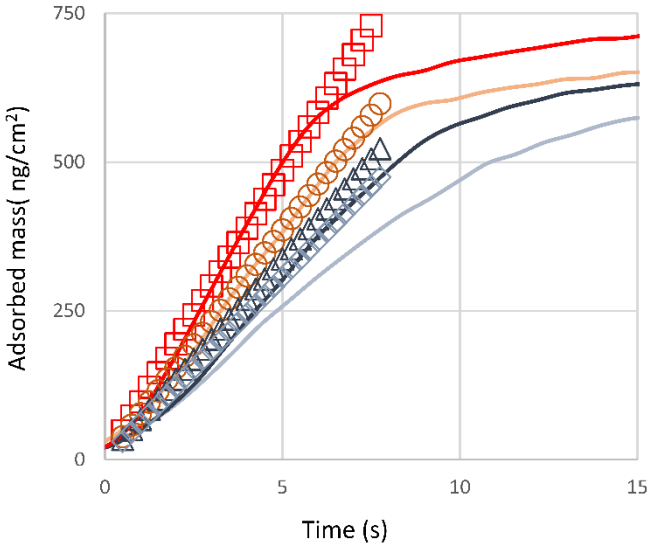

Figure 3.3.6 Comparison of the experimental and theoretical molecular transport rates at the array elements. Solid lines: experimental results for one array column obtained with Nav adsorbing on gold. Open symbols: calculated Γ(x,t), where x specifies the distance between the inlet and the array element.

Indeed, it can be seen in Figure 3.3.5 that the distribution of the adsorbed masses of Nav as a function of the array element location is random. For most of the experiments, the variation is <15%, in terms of the absolute deviation. The data shown in Figure 3.3.5 also illustrate the robustness of the cartridge and array system to repeated cleaning and assembly cycles; arrays survive up to 30 such cycles without loss of performance.

Finally, we show that the experimentally observed transport rates can be compared semi-quantitatively with the predictions of simple calculations based on the channel geometry and molecular diffusion coefficient.

In the case of a flow through a rectangular channel with the width 2W and height 2R at a flow rate Q, the evolution of the surface coverage as a function of time and position along the channel, x, is described by $\Gamma(x,t) = 0.49\, D^{2/3} \frac{Q^{1/3}}{R^{2/3} W^{1/3}} \frac{1}{x^{1/3}} C_b\, t$, where $\Gamma(x,t)$is the adsorbed mass at location x and time t, D is the diffusion coefficient (60 μm^2/s), and Cb is the bulk analyte concentration [42], [43]. This equation describes transport to a surface by a combination of flow and diffusion. The results are plotted in Figure 3.3.6 for our channel dimensions, Q = 4 μL/min, C_b = 0.195 mg/mL and three different locations x, such that the first sensor is 1.8 mm from the inlet and the distance between the sensors is 1.8 mm. In the example shown in Figure 3.3.6, only the last of the four sensor elements displays significant deviation. The leveling off of the adsorption curves at longer times is

due to surface saturation that is not taken into account by this equation, which only considers the transport of the molecules to the surface.

This equation applies to situations where surfaces act as “perfect sinks” (adsorption kinetics is transport-limited, or, equivalently, the rate, at which the molecule binds to the surface >> than the transport rate), and when the flow-mediated transport is much faster, than the diffusion-mediated transport so that the bulk concentration profile in the x-direction is uniform in time. The first of the two conditions is met in cases of quasi-irreversible adsorption of protein molecules at bare surfaces in the initial stages of the adsorption [44], [45]. The second needs to be evaluated by comparing transport and diffusive timescales in our geometry. This can be formally done in terms of a pair of Peclet numbers, one comparing transport and diffusive timescales along the channel normal ($Pe_H = \frac{Q}{2DW}$.), and the other—along the channel length ($Pe_S = 6\lambda^2 Pe_H$, where $\lambda = L_s/2R$is the ratio of sensor length to the channel height, and other variables are as defined above) [46]. For our geometry, for all relevant flow rates, both $Pe_H \gg 1$ and $Pe_S \gg 1$, indicating that indeed, the flow mediated transport along the channel is much faster, than the diffusion across the channel, and substantiating the validity of the above equation for $\Gamma(x, t)$. A more detailed analysis of the Peclet numbers for different analyte species can be found in Supplementary Section S3 (Appendix C).

The differences between experiment and calculation, such as the one visible in Figure 3.3.6 for the last sensor in a column, must originate from the deviations of the channel geometry from that of a straight rectangular channel (inlet and outlet at 90° to the channel axis) and variation of the surface properties (advantageous contamination) between the sensor elements.

One further important assumption underpins the above analysis: that the material of the fluid cell is essentially non-adsorbing. This is because the well, where the analyte is placed (Figure 3.3.1, red circle), is located some 11 mm from the first sensor. However, it is impossible to fit the data for all four sensors if x for the first sensor is set to 11 mm, because the differences between sensor locations (1.8 mm apart) become irrelevant in comparison with the long inlet tube. The observed differences in the adsorption rates for the four sensors shown in Figure 3.3.6 therefore indicate that there is a minimal loss of the analyte on the inlet tube itself.

3.3.4. Conclusions

A microfluidic cartridge designed to host an array of 24 HFF-QCM resonators in bioanalytical applications was implemented. It works as a mechanical, electrical and thermal interface between the QCMD sensing array, the characterization instrument, and the fluid analyte. Currently, the assembly is aimed at research laboratories that reuse the array and allows fast and easy assembly and disassembly of the cartridge. Re-use of 30+ times with repeated surface cleaning is demonstrated. Use of low cost of the materials (PMMA, PDMS, custom PCB) makes the design appropriate for disposable applications. The functionality of the array + cartridge combination is evaluated using air-liquid shifts and adsorption of biomacromolecules (biotinylated albumin and neutravidin). Experimental results on the adsorbed masses and adsorption rates demonstrate quantitative agreement with the literature and theoretical considerations (protein geometry, transport conditions). Systematic errors arising from flow geometry are ruled out. The array + cartridge combination is used to show that the first adsorption step is critical in defining the molecular properties of the sensing interface: adsorbing neutravidin onto biotinylated BSA pre-adsorbed on the gold results in a more controlled layer of biotin sites for the subsequent sensing application than adsorbing neutravidin directly on the gold. In summary, the device is shown to be robust and function reliably in complex biosensing applications. In the future, it will be used to test human DNA samples for single base mutations in the colorectal cancer liquid biopsy samples and extended to immunoassays for pesticide and antibiotic detection in honey samples.

References

[1] S. A. Soper et al., “Point-of-care biosensor systems for cancer diagnostics/prognostics,” Biosens. Bioelectron., vol. 21, no. 10, pp. 1932–1942, 2006.

[2] J. P. Lafleur, A. Jönsson, S. Senkbeil, and J. P. Kutter, “Recent advances in lab-on-a-chip for biosensing applications,” Biosens. Bioelectron., vol. 76, pp. 213–233, 2016.

[3] B. Nasseri, N. Soleimani, N. Rabiee, A. Kalbasi, M. Karimi, and M. R. Hamblin, “Point-of-care microfluidic devices for pathogen detection,” Biosens. Bioelectron., vol. 117, no. May, pp. 112–128, 2018.

[4] G. Sauerbrey, “Verwendung von Schwingquarzen zur Wägung dünner Schichten und zur Mikrowägung,” Zeitschrift für Phys., vol. 155, no. 2, pp. 206–222, 1959.

[5] I. Reviakine, D. Johannsmann, and R. P. Richter, “Hearing What You Cannot See and Visualizing What You Hear: Interpreting Quartz Crystal Microbalance Data from Solvated Interfaces,” Anal. Chem., vol. 83, no. 23, pp. 8838–8848, Dec. 2011.

[6] D. Johannsmann, The Quartz Crystal Microbalance in Soft Matter Research. Cham: Springer International Publishing, 2015.

[7] R. Fernández et al., “High Fundamental Frequency (HFF) Monolithic Resonator Arrays for Biosensing Applications: Design, Simulations, Experimental Characterization,” IEEE Sens. J., vol. Accepted, 2020.

[8] A. Tuantranont, A. Wisitsora-at, P. Sritongkham, and K. Jaruwongrungsee, “A review of monolithic multichannel quartz crystal microbalance: A review,” Anal. Chim. Acta, vol. 687, no. 2, pp. 114–128, 2011.

[9] P. Kao, D. Allara, and S. Tadigadapa, “Fabrication and performance characteristics of high-frequency micromachined bulk acoustic wave quartz resonator arrays,” Meas. Sci. Technol., vol. 20, no. 12, p. 124007, Dec. 2009.

[10] B. Zimmermann, R. Lucklum, P. Hauptmann, J. Rabe, and S. Büttgenbach, “Electrical characterisation of high-frequency thickness-shear-mode resonators by impedance analysis,” Sensors Actuators B Chem., vol. 76, no. 1–3, pp. 47–57, Jun. 2001.

[11] R. Fernández, P. García, M. García, J. García, Y. Jiménez, and A. Arnau, “Design and Validation of a 150 MHz HFFQCM Sensor for Bio-Sensing Applications,” Sensors, vol. 17, no. 9, p. 2057, Sep. 2017.

[12] C. March et al., “High-frequency phase shift measurement greatly enhances the sensitivity of QCM immunosensors,” Biosens. Bioelectron., vol. 65, pp. 1–8, Mar. 2015.

[13] L. Cervera-Chiner et al., “High Fundamental Frequency Quartz Crystal Microbalance (HFF-QCM) immunosensor for pesticide detection in honey,” Food Control, vol. 92, pp. 1–6, Oct. 2018.

[14] L. Cervera-Chiner, C. March, A. Arnau, Y. Jiménez, and Á. Montoya, “Detection of DDT and carbaryl pesticides in honey by means of immunosensors based on high fundamental frequency quartz crystal microbalance (HFF-QCM),” J. Sci. Food Agric., vol. 100, no. 6, pp. 2468–2472, Apr. 2020.

[15] L. Cervera-Chiner et al., “High Fundamental Frequency Quartz Crystal Microbalance (HFF-QCMD) Immunosensor for detection of sulfathiazole in honey,” Food Control, vol. 115, no. september, p. 107296, Sep. 2020.

[16] A. Montoya et al., “A High Fundamental Frequency (HFF)-based QCM Immunosensor for Tuberculosis Detection,” Curr. Top. Med. Chem., vol. 17, pp. 1623–1630, 2017.

[17] A. Grammoustianou and E. Gizeli, “Acoustic Wave–Based Immunoassays,” in Handbook of Immunoassay Technologies, J. H. T. L. Sandeep K. Vashist, Ed. Elsevier, 2018, pp. 203–239.

[18] D. Milioni, P. Mateos-Gil, G. Papadakis, A. Tsortos, O. Sarlidou, and E. Gizeli, “Acoustic Methodology for Selecting Highly Dissipative Probes for Ultrasensitive DNA Detection,” Anal. Chem., vol. 92, no. 12, pp. 8186–8193, Jun. 2020.

[19] G. Papadakis, P. Palladino, D. Chronaki, A. Tsortos, and E. Gizeli, “Sample-to-answer acoustic detection of DNA in complex samples,” Chem. Commun., vol. 53, no. 57, pp. 8058–8061, 2017.

[20] G. Papadakis et al., “Micro-nano-bio acoustic system for the detection of foodborne pathogens in real samples,” Biosens. Bioelectron., vol. 111, pp. 52–58, Jul. 2018.

[21] L. El Fissi et al., “OSTEMER polymer as a rapid packaging of electronics and microfluidic system on PCB,” Sensors Actuators, A Phys., vol. 285, pp. 511–518, 2019.

[22] G. Papadakis, J. M. Friedt, M. Eck, D. Rabus, G. Jobst, and E. Gizeli, “Optimized acoustic biochip integrated with microfluidics for biomarkers detection in molecular diagnostics,” Biomed. Microdevices, vol. 19, no. 3, pp. 1–11, 2017.

[23] A. M. D. Wan, T. A. Moore, and E. W. K. Young, “Solvent Bonding for Fabrication of PMMA and COP Microfluidic Devices,” J. Vis. Exp., vol. 2017, no. 119, Jan. 2017.

[24] H. Ron, S. Matlis, and I. Rubinstein, “Self-assembled monolayers on oxidized metals. 2. Gold surface oxidative pretreatment, monolayer properties, and depression formation,” Langmuir, vol. 14, no. 5, pp. 1116–1121, 1998.

[25] J. Charnley, “The Classic: The Bonding of Prostheses to Bone by Cement,” Clin. Orthop. Relat. Res., vol. 468, no. 12, pp. 3149–3159, Dec. 2010.

[26] T. Jaeblon, “Polymethylmethacrylate: Properties and Contemporary Uses in Orthopaedics,” Am. Acad. Orthop. Surg., vol. 18, no. 5, pp. 297–305, May 2010.

[27] M. Jönsson, H. Anderson, U. Lindberg, and T. Aastrup, “Quartz crystal microbalance biosensor designII. Simulation of sample transport,” Sensors Actuators B Chem., vol. 123, no. 1, pp. 21–26, Apr. 2007.

[28] K. Jaruwongrungsee and T. Maturos, “Analysis of Quartz Crystal Microbalance Sensor Array with Circular Flow Chamber,” … J. Appl., pp. 50–54, 2009.

[29] W. P. Mason, Piezoelectric crystals and their application to ultrasonics. New York: Van Nostrand, 1950.

[30] K. K. Kanazawa and J. G. Gordon, “Frequency of a quartz microbalance in contact with liquid,” Anal. Chem., vol. 57, no. 8, pp. 1770–1771, 1985.

[31] L. Daikhin and Michael Urbakh, “Influence of surface roughness on the quartz crystal microbalance response in a solution New configuration for QCM studies,” Faraday Discuss., vol. 107, no. 0, pp. 27–38, 1997.

[32] S. J. Martin, V. E. Granstaff, and G. C. Frye, “Characterization of a quartz crystal microbalance with simultaneous mass and liquid loading,” Anal. Chem., vol. 63, no. 20, pp. 2272–2281, Oct. 1991.

[33] M. Wilchek and E. A. Bayer, “The Avidin-Biotin Complex in Bioanalytical Applications,” Anal. Biochem., vol. 1, no. 32, pp. 1–32, 1988.

[34] E. P. Diamandis and T. K. Christopoulos, “The Biotin-(Strept)Avidin System: Principles and Applicationsin Biotechnology,” Clin. Chem., vol. 37, no. 5, pp. 625–636, 1991.

[35] E. F. Pettersen et al., “UCSF Chimera - A visualization system for exploratory research and analysis,” J. Comput. Chem., vol. 25, no. 13, pp. 1605–1612, 2004.

[36] P. M. Wolny, J. P. Spatz, and R. P. Richter, “On the Adsorption Behavior of Biotin-Binding Proteins on Gold and Silica,” Langmuir, vol. 26, no. 2, pp. 1029–1034, Jan. 2010.

[37] A. T. Marttila et al., "Recombinant NeutraLite Avidin: a non-glycosylated, acidic mutant of chicken avidin that exhibits high affinity for biotin and low non-specific binding properties," FEBS Lett., vol. 467, no. 1, pp. 31–36, 2000.

[38] N. H. Kim, T. J. Baek, H. G. Park, and G. H. Seong, "Highly sensitive biomolecule detection on a quartz crystal microbalance using gold nanoparticles as signal amplification probes.," Anal. Sci. Int. J. Japan Soc. Anal. Chem., vol. 23, no. 2, pp. 177–181, Feb. 2007.

[39] H. Ogi, H. Naga, Y. Fukunishi, M. Hirao, and M. Nishiyama, "170-MHz Electrodeless Quartz Crystal Microbalance Biosensor: Capability and Limitation of Higher Frequency Measurement," Anal. Chem., vol. 81, no. 19, pp. 8068–8073, Oct. 2009.

[40] B. P. Sagmeister, I. M. Graz, R. Schwödiauer, H. Gruber, and S. Bauer, "User-friendly, miniature biosensor flow cell for fragile high fundamental frequency quartz crystal resonators," Biosens. Bioelectron., vol. 24, no. 8, pp. 2643–2648, Apr. 2009.

[41] E. Uttenthaler, M. Schräml, J. Mandel, and S. Drost, "Ultrasensitive quartz crystal microbalance sensors for detection of M13-Phages in liquids," Biosens. Bioelectron., vol. 16, no. 9–12, pp. 735–743, 2001.

[42] W. T. Hermens, M. Beneš, R. Richter, and H. Speijer, "Effects of flow on solute exchange between fluids and supported biosurfaces," Biotechnol. Appl. Biochem., vol. 39, no. 3, pp. 277–284, 2004.

[43] A. B. Dahlin, Plasmonic Biosensors. An integrated view of Refractometric Detection, vol. 4. Amsterdam: Ios Press, 2012.

[44] N. GREEN, "AVIDIN. 1. THE USE OF [14C]BIOTIN FOR KINETIC STUDIES AND FOR ASSAY," Biochem. J., vol. 89, no. 3, pp. 585–591, Dec. 1963.

[45] J. R. Wayment and J. M. Harris, "Biotin−Avidin Binding Kinetics Measured by Single-Molecule Imaging," Anal. Chem., vol. 81, no. 1, pp. 336–342, Jan. 2009.

[46] T. M. Squires, R. J. Messinger, and S. R. Manalis, "Making it stick: convection, reaction and diffusion in surface-based biosensors," Nat. Biotechnol., vol. 26, no. 4, pp. 417–426, 2008.

3.4. A Real-Time Method for Improving Stability of Monolithic Quartz Crystal Microbalance Operating under Harsh Environmental Conditions

Román Fernández, María Calero, Yolanda Jiménez and Antonio Arnau

Sensors, June 2021

Abstract

Monolithic quartz crystal microbalance (MQCM) has recently emerged as a very promising technology suitable for biosensing applications. These devices consist of an array of miniaturized QCM sensors integrated within the same quartz substrate capable of detecting multiple target analytes simultaneously. Their relevant benefits include high throughput, low cost per sensor unit, low sample/reagent consumption and fast sensing response. Despite the great potential of MQCM, unwanted environmental factors (e.g., temperature, humidity, vibrations, or pressure) and perturbations intrinsic to the sensor setup (e.g., mechanical stress exerted by the measurement cell or electronic noise of the characterization system) can affect sensor stability, masking the signal of interest and degrading the limit of detection (LoD). Here, we present a method based on the discrete wavelet transform (DWT) to improve the stability of the resonance frequency and dissipation signals in real time. The method takes advantage of the similarity among the noise patterns of the resonators integrated in an MQCM device to mitigate disturbing factors that impact on sensor response. Performance of the method is validated by studying the adsorption of proteins (neutravidin and biotinylated albumin) under external controlled factors (temperature and pressure/flow rate) that simulate unwanted disturbances.

Keywords

Monolithic quartz crystal microbalance; Biosensor; Discrete wavelet transform

3.4.1. Introduction

Conventional analytical methods currently employed as a "gold standard" require trained personnel in centralized laboratories to perform time-consuming experiments with costly, large, and bulky devices. Owing to their simplicity, reduced size, good sensitivity and low cost, novel biosensors may play a fundamental role in the very near future, becoming an alternative analytical tool in health care, food security and environmental monitoring applications.

Biosensors can be classified by their transduction mechanism. Nirsch et al. provided a comprehensive overview about sensor transducer principles for label-free biomolecular interaction analysis [1]. Although novel transducers are continuously emerging, electrochemical, optical and acoustic transducers are the most popular ones. These three approaches are well-established technologies with their advantages and drawbacks (see references [1,2] for more information).

Among acoustic biosensor technologies, quartz crystal microbalance (QCM) stands out as a direct label-free detection tool suitable for real-time monitoring. QCM operation is based on the so-called gravimetric technique [3], which relates mass changes on the sensor surface to resonance frequency shifts, Δf_r. This approach has been widely applied in biochemical sensing: immunoassays, protein adsorption, DNA hybridization, etc. [4–7]. If the dissipation parameter, ΔD, is also monitored (QCMD), viscoelastic and conformational properties of the sample can be studied as well [8].

Recently, an enhancement in the limit of detection (LoD) of around two orders of magnitude has been reported for high fundamental frequency QCMD (HFF-QCMD) sensors with resonance frequencies of up to 150 MHz [9–14]. The HFF-QCMD principle of operation relies on the reduction of the quartz plate thickness of a classical QCMD [14], resulting in a sensitivity increase and a surface reduction [15]. Thanks to their small footprint, it is possible to integrate dozens of HFF-QCMD sensors within the same substrate through the design of Monolithic QCM arrays (MQCM) [16]. Miniaturized and parallelized elements in the array lead to relevant benefits including high throughput, lower cost per sensor unit, less sample/reagent consumption and faster sensing response [17–19].

Although MQCM technology is well-suited for biosensing, there are still remaining challenges that hamper its adoption for portable applications. Some effects intrinsic to the

sensor setup (such as mechanical stress exerted by the measurement cell or electronic noise of the characterization system) and external factors (such as temperature, humidity, vibrations, or pressure) can strongly affect sensor stability [20], masking the signal of interest and degrading LoD. Isolating the sensor response from those factors is not trivial and increases the complexity and cost of the testing equipment, often preventing the development of lightweight and portable instruments appropriate for real-time applications.

Changes in pressure can be a consequence of the pumping system (i.e., typical "peaks" with syringe-pumped fluidic systems [15]), or of a change in flow rate of the fluidic system, i.e., when regenerating the sensor surface in an immunoassay [9,12]. Changes in room temperature also have a significant influence on the HFF-QCMD resonators response. In the case of temperature regulation, active thermal control systems, usually based on Peltier thermoelectric modules, are common. There have been attempts to find alternative solutions to the use of bulky, expensive and complex control systems. Mecea et al. proposed the use of two QCM resonators simultaneously, one of which is used as a reference [21]. The effect of temperature fluctuations in the resonance frequency is cancelled by directly subtracting the signals from both sensors. The Mecea method significantly reduces temperature disturbances when two conditions are met: (1) the temperature is equal at both resonators, and 2) the response of both resonators versus temperature matches. Rahtu et al. [22] compared the aforementioned method with a numerical correction of the temperature effect based on a third-degree polynomial model. Rahtu's method provided similar performance with-out the necessity of a reference QCM resonator. However, it only proved to be valid for monotonous temperature variations and showed convergence issues. Furthermore, this scheme requires an additional temperature sensor. Pierce designed an insensitive quartz microbalance based on stress-compensated (SC) crystals [23]. By simultaneously measuring the resonance frequency of two overtones at a single resonator and assuming a gravimetric regime, it was possible to calibrate the crystal response to temperature without the need for an external thermometer. The main disadvantage of SC-cut resonators is their higher cost due to the complex double rotation process re-quired for their manufacturing.

In a real portable biosensing device, not only the temperature but also many other factors can concurrently undermine the sensor stability, leading to a lack of reliability in the measurements. In this case, a more complex signal conditioning stage, combining

different strategies, is required. At some point, selective filtering can be applied [24]. It tends to work well to reduce high-frequency fluctuations (noise) but fails in removing low-frequency disturbances (drift), whose spectrum often overlaps with the signal components of interest. Advanced statistical methods, such as principal com-ponent analysis (PCA), can also be used. PCA is based on the dimensional reduction of a large dataset to highlight its most statistically significant components, which ideally are related to the signals of interest, while removing the less significant components, which could be associated with frequency instability. Lately, Corradi et al. applied the PCA method to improve the detection limit of a QCM sensor operating in multiple overtones [25]. Mumyakmaz et al. combined PCA with neural networks to compensate for the effect of humidity in toluene gas monitoring [26]. However, due to their relatively high computational cost, PCA-based approaches are not generally used for signal correction in real time, but for pattern recognition purposes in post-processing stages.

It is important to mention at this point that although dissipation is a very valuable QCM parameter that provides information about viscoelastic and conformational characteristics of the sample, all methods we found in the literature are focused exclusively on improving the quality of the resonance frequency.

Here, we present a method based on the discrete wavelet transform (DWT) to improve the stability and reliability of resonance frequency and dissipation signals of QCMD sensors. DWT is the discretely sampled version of the continuous wavelet transform. Wavelets are mathematical functions widely used for time-frequency analysis of transient, non-stationary and time-varying phenomena [27]. Wavelet analysis is based, as with Fourier theory, on the concept of signal approximation using superposition. A general way of looking at wavelet functions is as families of functions with an excellent resolution in both frequency and time. This feature makes wavelet analysis a powerful tool in signal processing applications. The algorithm introduced in this paper takes advantage of the high similarity found among the noise patterns of the resonators integrated in an MQCM device to mitigate both intrinsic and environment factors that impact on the sensor response, thus effectively improving LoD in portable applications. This approach is suitable for real-time signal correction because of its low computational cost.

To validate the performance of the method, we first investigated its capability to reduce frequency instability caused by sensor intrinsic factors. For that, we simulated a basal

state of the setup by making a system to work under controlled and static external conditions of temperature and pressure. Then, we extended our investigation to evaluate the method under a harsh environment, simulated by high temperature and flow rate gradients. Under these conditions, we monitored a protein adsorption experiment. Label-free detection of protein–ligand interactions is one of the paramount applications of QCM [28]. In particular, we selected neutravidin (NAv) and biotinylated bovine serum albumin (bBSA) as a relevant model system since these proteins are commonly used in biotechnology and bioanalytics to prepare the sensor surface for further chemical modification [29–33].

3.4.2. Principles of the Method

Generally, DWT is calculated through the so-called Mallat tree decomposition scheme [27], which is based on a quadrature mirror filter that splits the signal into two sub-bands. After a decimation by 2, the high-frequency sub-band is termed as the detail coefficients and the low-frequency sub-band as the approximation coefficients. This process can be repeated sequentially, generating several decomposition levels (see Section S1 of the Supporting Information, Appendix D). DWT is a reversible process and after the transformation, the original signal can be recovered from the whole set of detail and approximation coefficients.

When DWT is applied to frequency and dissipation signals measured at a pair of resonators integrated in an MQCM device, an interesting effect is observed in the approximation coefficient series that it is not clearly apparent from raw data. A high linear correlation level is found in the time derivative of the approximation coefficient between neighbor resonators if they are subjected to similar environmental conditions (see green inset in Figure 3.4.1a and its detailed view in Figure 3.4.1b). In contrast, when a sample is injected only through the sensor but not through the *reference* (black inset in Figure 3.4.1a), time derivatives differ significantly, as can be seen in the detailed view of Figure 3.4.1c. It is important to note that although the sensors are very close to each other (<2 mm) and they are integrated in the same quartz substrate, their absolute response to those external factors differ to some extent. Based on the above observations, we assume that linearly correlated variations in DWT time derivatives of neighbor resonators are caused by unwanted external effects. Hence, we propose a method that combines DWT analysis

with an algorithm that extracts and cancels out these correlated factors to improve both resonance frequency and dissipation stability.

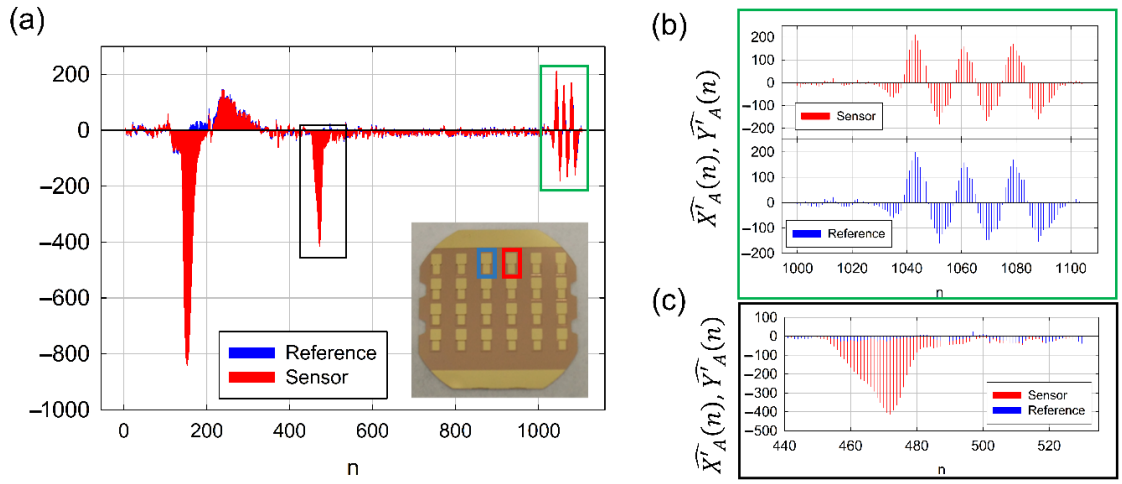

Figure 3.4.1 (a) Time derivative of the frequency shift approximation coefficients for the sensor (red) and the reference (blue); n refers to the sample index (b). Detailed view of the green inset in figure (a). (c) Detailed view of the black inset in figure (a).

3.4.3. Materials and Methods

3.4.3.1. Description of the Method

To introduce the method, let us consider two resonators as the ones depicted in Figure 3.4.1a. One of the resonators, which we call sensor, is exposed to the sample, while the other, which we call *reference*, is kept isolated from it. We call *x(n)* the sampled signal in time domain (either resonance frequency or dissipation) measured at the *sensor* and *y(n)* the same sampled signal measured at the *reference* resonator. The method provides a corrected output signal called *z(n)*. *n* refers to the sample index.

Practical implementation is depicted schematically in Figure 3.4.2 and described next:

STEP 1: We calculate the DWT of *x(n)* and *y(n)*. Without loss of generality, we apply the Daubechies wavelet transform with three vanishing moments (db3) and four decomposition levels [34]. This transform will generate five series of coefficients: we use $X_K(n)$ and $Y_K(n)$ to refer to the whole set of wavelet coefficients of the sensor and the *reference* respectively; *k*= A, D1, D2, …, Dq. (see Equation (1)).

$$x(n) \xrightarrow{DWT} X_A(n), X_{D1}(n), X_{D2}(n), X_{D3}(n), X_{D4}(n)$$
$$y(n) \xrightarrow{DWT} Y_A(n), Y_{D1}(n), Y_{D2}(n), Y_{D3}(n), Y_{D4}(n) \quad (1)$$

where $X_A(n)$ and $Y_A(n)$ refer to the approximation coefficients expansion; $X_{Dq}(n)$ and $Y_{Dq}(n)$ represent the detail coefficients expansions of the different decomposition levels q (q = 1 to 4) (see Figure S1 of the Supporting Information, Appendix D). Each one of these coefficient series captures the behavior of the signal in a certain frequency sub-band.

STEP 2: We use the so-called wavelet shrinkage technique [27] to eliminate all those detail wavelet coefficients that do not make a significant contribution to the total energy of the signal (see Supporting Information Section S2, Appendix D). To that end, hard-thresholding is applied [27]. The threshold components are named $\hat{X}_K(n)$ for the *sensor* and $\hat{Y}_K(n)$ for the *reference*.

STEP 3: Numerical time derivatives of the threshold components are calculated for the *sensor* ($\widehat{X'}_K(n)$) and the *reference* ($\widehat{Y'}_K(n)$).

STEP 4: Pearson product-moment correlation coefficient, *R*, is calculated between $\widehat{X'}_K(n)$ and $\widehat{Y'}_K(n)$. A window of *w* samples around each sample *n* is considered for the calculation. The correlation coefficient is determined by dividing the covariance of $\widehat{X'}_K(n)$ and $\widehat{Y'}_K(n)$ by the product of the two variables' standard deviations according to Equation (2).

$$R(n) = \frac{Cov(\widehat{X'}_K(n), \widehat{Y'}_K(n))}{\sigma_{\widehat{X'}_K}\sigma_{\widehat{Y'}_K}} \quad (2)$$

Then, the *p*-value *P(n)* is obtained from *R* to determine whether or not the correlation between the *sensor* and *reference* is statistically significant. The *p*-value is computed by transforming the correlation to create a t statistic having *w*-2 degrees of freedom. The confidence bounds are based on an asymptotic normal distribution of 0.5 × log ((1 + R)/(1 − R)).

STEP 5: We use $\widehat{X'}_K(n)$ and $\widehat{Y'}_K(n)$ to calculate the derivatives of the wavelet coefficients of the new corrected signal $Z'_K(n)$. If the $\widehat{X'}_K(n)$ and $\widehat{Y'}_K(n)$ components are statistically related in a significant way (*P(n)* < 5%), the derivative of the corrected coefficient is calculated as a linear projection of the reference space into the sensor space:

$$Z'_K(n) = \hat{X}'_K(n) - a - b\hat{Y}'_K(n) \quad (3)$$

where *a*, *b* are the coefficients that minimize the linear fit between $\widehat{X'}_K(n)$ and $\widehat{Y'}_K(n)$ in the window of *w* samples centered on sample n. If *P(n)* does not indicate a high degree of correlation (*P(n)* > 5%), $Z'_K(n)$ is directly calculated as:

$$Z'_K(n) = \widehat{X'}_K(n) - \widehat{Y'}_K(n) \quad (4)$$

STEP 6: Once the derivatives of the wavelet components of the corrected signal have been determined, numerical integration is applied to obtain $Z_A(n)$, $Z_{D1}(n)$, $Z_{D2}(n)$,…, $Z_{Dq}(n)$.

STEP 7: Finally, the inverse wavelet transform will be performed to obtain the corrected signal in the time domain *z(t)* (see Figure S1b of the Supporting Information, Appendix D).

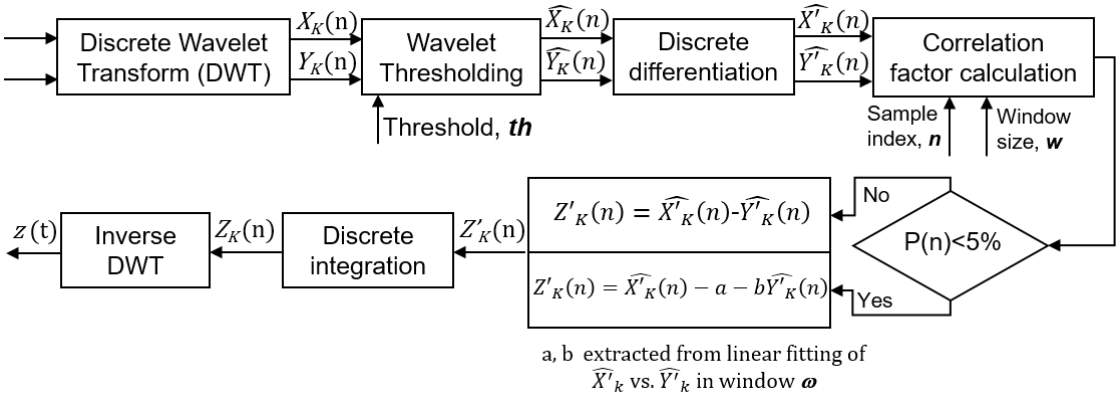

Figure 3.4.2 Flow diagram describing the different steps of the method.

3.4.3.2. Chemicals

Nanopure water and pure ethanol were purchased from Panreac Química SLU (Barcelona, Spain). Phosphate-buffered saline (PBS) tablets for preparing 0.01 M phosphate buffer containing 0.0027 M potassium chloride and 0.137 M sodium chloride, pH 7.4, at 25 °C were purchased from Sigma Aldrich Química, S.L.U. (Madrid, Spain). NeutrAvidin (NAv), biotinylated BSA (bBSA), and sodium dodecyl sulfate (SDS) 20% solution were purchased from Fisher Scientific S.L. (Madrid, Spain). COBAS Cleaner was purchased from Sanilabo S.L. (Valencia, Spain).

3.4.3.3. Instrument and Devices

3.4.3.3.1. Sensors

MQCM arrays (AWSensors S. L.) comprised 24 HFF-QCM sensors integrated in a 1-inch circular AT-cut quartz wafer. The fundamental frequency of the resonators in these arrays is 50 MHz, and their surfaces are flat and polished (See Figure S2 in the Supporting Information, Appendix D). To clean the sensors, they were exposed to UV radiation for 10 min in a UV/ozone cleaner (BioForce Nanosciences Inc., Chicago, IL, USA), rinsed with 99% pure ethanol, rinsed with bi-distilled water, dried with ultra-pure nitrogen gas (Al Air Liquide España, S.A.) and treated with UV/ozone for 10 min again.

3.4.3.3.2. Sensor Electrical Characterization

AWS X24 platform (AWSensors S. L.) was used to characterize the MQCM array response. This QCMD instrument is based on a fixed-frequency phase-shift measurement technique described elsewhere [35,36]. AWS X24 is capable of simultaneously measuring the acoustic response of up to 24 HFF-QCMD sensors with a sampling rate of three samples per second per sensor, providing both resonance frequency and dissipation data. A thermal management module is embedded into the AWS X24 system to control the temperature of the MQCM array. Temperature range can be set between 20 °C and 40 °C. A flow control module (FCUPro, AWSensors S. L.) was used to generate a stable flow through the sensor channels. AWSuite software package (AWSensors S. L.) was used to control the instrument and to register the acquired data.

3.4.3.4. Experimental

Protein adsorption experiments were performed over the MQCM array. For that, first, the MQCM device was mounted in a custom flow measurement cell (Jobst Technologies, Freiburg, Germany) previously cleaned with COBAS cleaning solution for 30 min, followed by repeated rinsing with HCl 0.1 M and water and dried with a stream of filtered nitrogen. Flow tubing was connected to the cell to create two separate flow regions (named *S* and *R*) with 12 sensors each (see Section S3 in the Supporting Information, Appendix D). Resonance frequency and dissipation of every sensor in the array was monitored in real-time during the experiment. Fluidic channels were filled with PBS at a flow rate of 20μL/min. Baseline signals were acquired for ~5 to 10 min, followed by the sample injections only in the flow region *S* but not in region *R*, which acts as reference.

The first injection consisted of neutravidin (NAv) at a high concentration (100 µg/mL). The second injection consisted of biotinylated bovine serum albumin (biotinylated BSA), at a concentration of 100 µg/mL.

3.4.4. Results and Discussion

We applied the algorithm presented in Section 3.4.3.1 to improve the stability and reliability of an MQCM device comprising 24 HFF-QCM sensors operating at a fundamental frequency of 50 MHz. The method provides a corrected output signal *z(n)*, with improved stability with respect to the raw sensor signal *x(n)*, by removing the signal fraction common to the time derivative of the DWT components of the sensor and the reference. Unlike Mecea's approach, here, we consider the different resonator absolute responses by performing a linear projection of the reference space into the sensor space, which contributes to effectively cancelling the combined effect of all external interferences, even if the absolute resonator responses to those effects do not match perfectly (Equation (3) in step 5 of the method).

In the study, we worked with pairs of resonators (see Figure 3.4.1a). The first resonator worked as a *sensor* while we considered the second one as a *reference*. Both resonators, although very close to each other (distance < 2 mm), were located in independent flow channels in such a way that we could inject sample solely over the resonator operating as a *sensor* (see Figure S2 in the Supporting Information, Appendix D).

We studied the performance of the algorithm under different experimental conditions.

3.4.4.1. Improvement of the Frequency Stability

In a first experiment, the sensor and reference fluidic channels were filled with PBS at a flow rate of 20 µL/min and then the flow was stopped. No sample was injected in the *sensor* channel. MQCM resonance frequency was monitored for one hour under controlled temperature (23 ± 0.05 °C) conditions. In this scenario, only effects intrinsic to the sensor setup such as the mechanical stress exerted by the measurement cell, electronic noise of the characterization system, or compressional waves due to the presence of a liquid over the sensor surface, among others, affect the frequency stability.

The monitored resonance frequency shift is shown in Figure 3.4.3a. The algorithm (black trace) greatly reduced the noise level when compared with the raw sensor signal (red trace). Sensor baseline drift also improved, from 200 Hz/hour to less than 20 Hz/hour.

Furthermore, we compared our results with a modification of Mecea's traditional approach [21] (green trace), which consists of applying a 16-sample length sliding averaging window to the result of the direct subtraction of the resonance frequency signals measured at the reference and at the sensor (hereinafter called the "filtered Mecea compensation method"). Averaging was applied to reduce the high-frequency noise level of the original method. Even after the additional averaging stage, our algorithm provided a better performance than the filtered Mecea compensation method both in noise rejection and drift compensation (150 Hz/hour).

In order to study the stability improvement in more detail, we calculated the so-called Allan deviation (ADEV) defined in Equation (5). Allan deviation is a useful tool commonly applied to analyze the frequency stability of resonators, oscillators and clocks [20].

$$\sigma_y(\tau) = \sqrt{\frac{1}{2}\langle(\bar{y}_{n+1} - \bar{y}_n)^2\rangle} \tag{5}$$

In Equation (5), τ is the time between samples n + 1 and n, also called integration time, and $\bar{y}_n = \Delta f / f_0$ is the nth fractional frequency average over the integration time. The lower the ADEV value, the higher the resonator stability. As can be observed in Figure 3.4.3b, our algorithm offers better frequency stability for the whole τ range. Specifically, in the case of short integration times (corresponding to high frequency events in the signal), the stability enhancement is higher than two orders of magnitude when compared with the ADEV corresponding to the raw sensor signal and one order of magnitude better than the ADEV of the filtered Mecea compensation method. This improved performance relies on the high-frequency denoising capabilities of the wavelet thresholding scheme implemented (step 2 of the algorithm described in Section 3.4.3.1). When long integration times are considered (corresponding to low frequency variations in the signal), a three-fold enhancement with respect to the filtered Mecea compensation method and an improvement of up to one order of magnitude if compared with raw resonance frequency are achieved. We attribute such a good performance at reducing low frequency noise to the capability of the algorithm to suppress DWT components linearly correlated in both resonators (step 5 of the algorithm described in Section 3.4.3.1). This is achieved by performing a subtraction of the derivatives of the wavelet coefficients after a linear projection of the reference space into the sensor space, which has demonstrated to be

more effective for the cancelation of this type of low frequency noise than a direct subtraction.

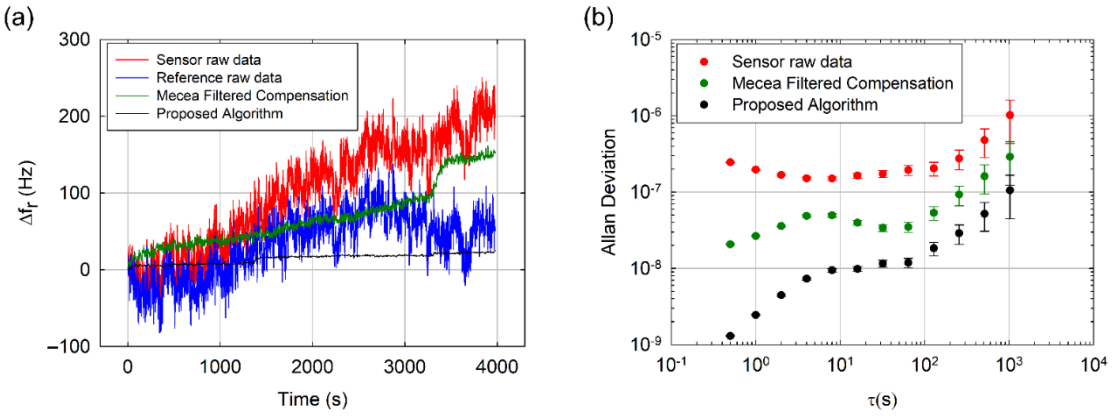

Figure 3.4.3 (a) Time evolution of the resonance frequency shifts measured at the sensor (red trace) and reference (blue trace) resonators. Corrected resonance frequency shift provided by our algorithm (black line) and by the filtered Mecea compensation method (green trace) are depicted as well. (b) Allan deviation vs. integration time calculated for the raw sensor resonance frequency (red dots), for the corrected resonance frequency using our algorithm (black dots) and for the corrected resonance using filtered Mecea compensation method (green dots). Error bars are included.

3.4.4.2. Instrument Detection Limit

The International Union of Pure and Applied Chemistry (IUPAC) states LoD as the lowest concentration of an analyte that an analytical process can reliably detect [37]. This definition considers the influence of intrinsic sensor parameters such as sensitivity, baseline stability and signal to noise ratio but also other factors such as the sensitivity and specificity of the sensor coating. Since the contribution of sensor surface functionalization to LoD depends on the application, an alternative definition is required to assess the sensor performance. Here, we use the instrument detection limit (IDL). For a gravimetric sensor, IDL is defined as the minimum surface mass that can be detected. IDL is defined as 3σ/S in ng/cm^2, where σ is the system noise in Hz, and S is the sensitivity in Hz cm^2/ng. QCM sensitivity is directly related to the sensor resonance frequency through the Sauerbrey equation [3]:

$$S = \frac{\Delta f_r}{\Delta m} = -\frac{2f_0^2}{\sqrt{\eta_q \rho_q}} \tag{6}$$

where ρ_q is the quartz density, η_q is the AT-cut quartz shear modulus, Δm is the surface mass density in ng/cm^2, f_0 is the sensor fundamental resonance frequency and Δf is the frequency shift measured at the sensor. In the case of an HFF-QCM sensor with a

fundamental resonance frequency of 50 MHz, S = −5.657 Hz cm^2/ng. As shown in Figure 4, IDL obtained by processing the raw sensor data with our algorithm is ~0.2 ng/cm^2, which is more than one order of magnitude better than IDL obtained directly from the raw sensor data (~8.38 ng/cm^2), and almost one order of magnitude better than the one provided by the filtered Mecea compensation method (~1.56 ng/cm^2).

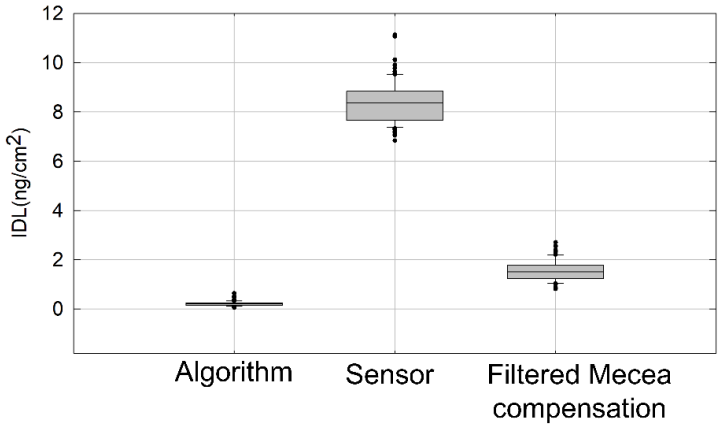

Figure 3.4.4 Instrument detection limit (IDL) calculated from raw sensor data, the filtered Mecea compensation method and the algorithm presented in this paper. IDL has been calculated as 3σ/S in ng/cm^2, where σ is the system noise in Hz, and S is the sensitivity in Hz cm^2/ng. A total of 100 intervals of the acquired baseline have been used in the calculation. Error bars are included in the figure.

3.4.4.3. Removal of External Environmental Factors

We also tested the capability of the method to cancel the influence of unwanted external factors in resonance frequency and dissipation signals, such as temperature and flow rate gradients. PBS saline buffer was continuously flown through the *reference* and *sensor* channels (*R* and *S* regions, respectively, in Figure S2b in the Supporting Information, Appendix D), and only NAv and bBSA were injected sequentially in the *sensor* channel (*S* region). Both NAv and bBSA were prepared at high concentration (100 µg/mL) to ensure that adsorption reached saturation, avoiding possible differences among sensors caused by the uneven distribution of the sample in the flow measurement cell [33]. The response of one pair of resonators (*sensor–reference*) integrated in the MQCM device is depicted in Figure 3.4.5. To emulate a harsh environment with changing conditions, temperature control was configured to increase from 23 °C to 34 °C and to decrease back to 23 °C during the experiment (see Figure 3.4.5c). Both raw resonance frequency (Figure 3.4.5b) and dissipation (Figure 3.4.5a) shifts measured at the *reference* resonator (blue traces) were heavily distorted by the temperature effect. *Sensor* response (red traces), in

turn, was affected both by the temperature shift and by the biomolecular interactions taking place on its surface.

In the case of the NAv sample injection, raw resonance frequency shift registered at the sensor is far from the typical smooth monotonically decreasing curve expected. The raw dissipation shift also shows strange behavior. If we consider that the NAv adsorption process reaches a plateau at 2500 s, the frequency shift is −3681 Hz, corresponding to a mass density of 650 ng/cm^2, and a dissipation shift of $-43 \cdot 10^{-6}$. These results do not match well with the literature, where typical values reported for mass density are greater than 750 ng/cm^2 and negative ΔD values have not been described [29–32]. These results do not match either with control experiments carried out at 23 °C (see Table 3.4.1).

Regarding bBSA injection, although baseline stabilization is not complete because of the temperature influence, we considered that a plateau was reached at 5500 s, where raw Δf_r is −2818 Hz (498 ng/cm^2) and ΔD is $52 \cdot 10^{-6}$. Theoretically, bBSA should be adsorbed over NAv as a monolayer, giving an approximate mass value of 250 ng/cm^2 [33]. Furthermore, there is a significant mismatch with control experiments shown in Table 3.4.1.

At this point, we applied our algorithm to disentangle contributions arising from temperature and from protein adsorption. Corrected resonance frequency and dissipation shifts are depicted as black traces in Figure 3.4.5 a,b, respectively. Both corrected signals show a typical behavior characteristic of a protein adsorption experiment carried out under constant temperature conditions (see Figure S3 in the Supporting Information, Appendix D). After the correction, NAv and bBSA resonance frequency and dissipation shifts are in good agreement with the literature data [29–32] and control experiments. We conjecture that small deviations between control and validation experiments showed in Table 3.4.1 are related to sample preparation and to the temperature shift effect on the protein adsorption process.

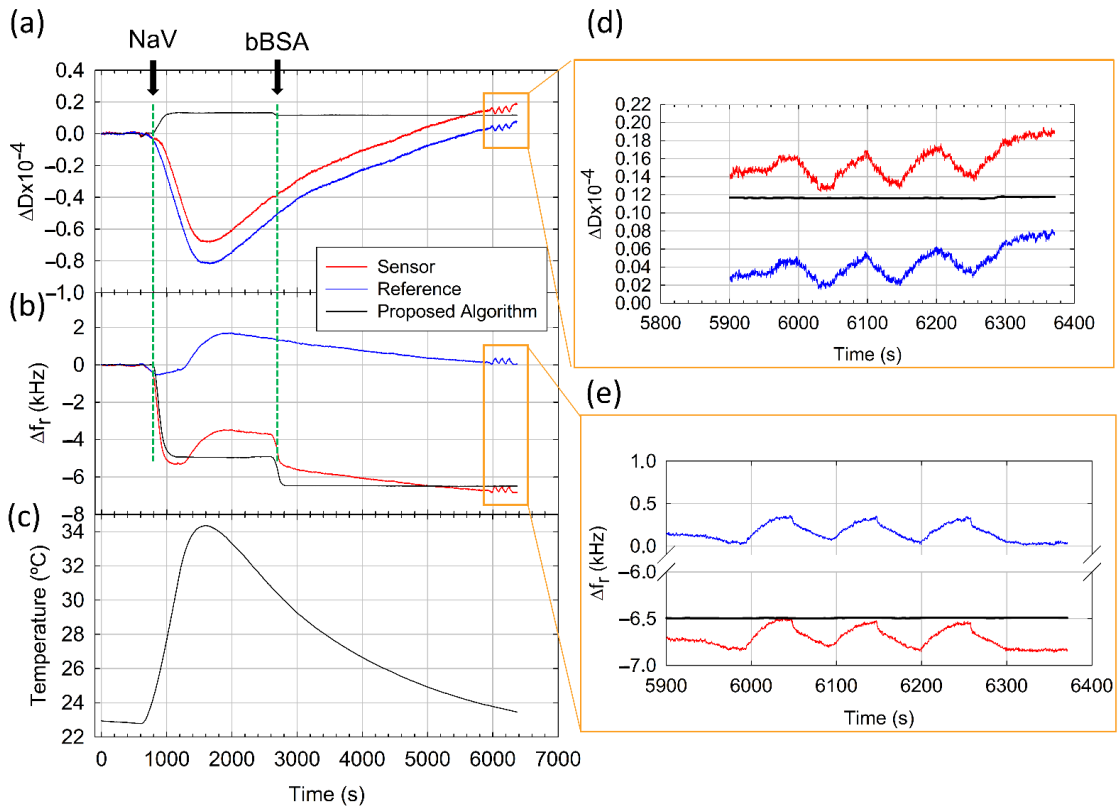

Figure 3.4.5 Dissipation (a) and resonance frequency (b) shifts monitored for sensor (red trace), reference (blue trace) and the algorithm result (black trace) under conditions of changing temperature and flow rate. (c) Temperature time evolution configured to increase from 23 °C to 34 °C and back to 23 °C. Detail of the effect of flow rate variation in dissipation (d) and resonance frequency (e) shifts.

Table 3.4.1 Comparison of resonance frequency and dissipation shifts measured during a control experiment (see S4 in the Supporting Information, Appendix D) and the results provided by the algorithm in the experiment showed in Figure 3.4.5 under strong influence of external factors. Control experiment was carried out under stable temperature (23 °C) and flow rate (20 µL/min). Data shown in the table represent average and standard deviation calculated from 4 HFF-QCMD sensors integrated in a column of the MQCM device.

	NAv		**bBSA**	
	Control Experiment	**Algorithm Result**	**Control Experiment**	**Algorithm Result**
Δf_r (Hz)	−5454 ± 193	−5002 ± 125	−1335 ± 121	−1558 ± 63
ΔD (10^{-6})	13.7 ± 3.5	16 ± 6.5	1.8 ± 3.6	−0.8 ± 0.2

Finally, we evaluated the capability of the method to correct additional flow rate gradients. To investigate this point, we modified the flow rate between 15 and 35 µL/min from 6000 to 6300 s (see Figure 3.4.5). This periodic variation resulted in a saw-tooth-shaped interference that affects both resonators. Since the *sensor* and *reference* are

located in different flow channels, interference is highly correlated but not identical in both resonators. Nevertheless, the proposed method adequately removed the effects of the flow rate variation both in resonance frequency and dissipation shifts, as is shown on insets (e) and (d) in Figure 3.4.5, respectively. We consider it important to underscore that temperature was not yet stable at 6000 s (see Figure 3.4.5c). Thus, our method effectively cancelled the combined effect of both factors, e.g., temperature and flow rate variation.

3.4.5. Conclusions

We presented a method that exploits the high level of correlation found in the response of the acoustic wave sensors integrated in an MQCM device to minimize the impact of unwanted disturbances on the stability and reliability of the measurement. The method is based on the hypothesis that interferences caused by harsh environmental conditions (such as temperature or pressure) or factors intrinsic to the sensor setup (such as electronic noise or stress caused by the measurement cell) can be effectively removed from resonance frequency and dissipation by combining DWT with an algorithm to cancel signal components common to two resonators, i.e., sensor and reference. The method is robust against variations in the absolute sensor responses to those external or internal factors.

When tested under static flow conditions and controlled temperature (23 ± 0.05 °C) the method showed an IDL enhancement of almost two orders of magnitude with respect to the original sensor data. Furthermore, the method successfully minimized the effect of changing temperature (between 23 °C and 34 °C) and flow rate (between 15 and 35 μL/min) in protein adsorption experiments.

To the best of the authors' knowledge, no other method has been previously proposed in the literature to correct both dissipation and resonance frequency against external and internal disturbances in QCMD. In the near future, we plan to apply these results to develop a portable immunosensor system for on-site monitoring of pesticides and antibiotics in honey samples.

Funding

This work was supported by the European Commission Horizon 2020 Programme, Capturing non-Amplified Tumor Circulating DA with Ultrasound Hydrodynamics, under

Grant H2020-FETOPEN-2016-2017/737212-CATCH-U-DNA. M. Calero is the recipient of the doctoral fellowship BES-2017-080246 from the Ministerio de Economía, Industria y Competitividad de España.

References

[1] Nirschl, M.; Reuter, F.; Vörös, J. Review of transducer principles for label-free biomolecular interaction analysis. Biosensors 2011, 1, 70–92.

[2] Gaudin, V. Advances in biosensor development for the screening of antibiotic residues in food products of animal origin—A comprehensive review. Biosens. Bioelectron. 2017, 90, 363–377.

[3] Sauerbrey, G. Verwendung von Schwingquarzen zur Wägung dünner Schichten und zur Mikrowägung. Z. Phys. 1959, 155, 206–222.

[4] Lucklum, R.; Kanazawa, K.; Soares, D. Piezoelectric Transducers and Applications; Vives, A.A., Ed.; Springer: Berlin/Heidelberg, Germany, 2008; ISBN 978-3-540-77507-2.

[5] Minunni, M.; Mascini, M.; Tombelli, S. Analytical Applications of QCM-based Nucleic Acid Biosensors. In Piezoelectric Sensors; Springer: Berlin/Heidelberg, Germany, 2007; pp. 211–235.

[6] Höök, F.; Kasemo, B. The QCM-D Technique for Probing Biomacromolecular Recognition Reactions. In Piezoelectric Sensors; Springer: Berlin/Heidelberg, Germany, 2007; pp. 425–447.

[7] Dickert, F.L.; Lieberzeit, P.A. Imprinted Polymers in Chemical Recognition for Mass-Sensitive Devices. In Piezoelectric Sensors; Springer: Berlin/Heidelberg, Germany, 2007; pp. 173–210.

[8] Johannsmann, D. Studies of Viscoelasticity with the QCM. In Piezoelectric Sensors; Springer: Berlin/Heidelberg, Germany, 2007; pp. 49–109.

[9] March, C.; García, J.V.; Sánchez, Á.; Arnau, A.; Jiménez, Y.; García, P.; Manclús, J.J.; Montoya, Á. High-frequency phase shift measurement greatly enhances the sensitivity of QCM immunosensors. Biosens. Bioelectron. 2015, 65, 1–8.

[10] Montoya, A.; March, C.; Montagut, Y.; Moreno, M.J.; Manclús, J.J.; Arnau, A.; Jimenez, Y.; Jaramillo, M.; Marin, P.; Torres, R.A. A High Fundamental Frequency

(HFF)-based QCM Immunosensor for Tuberculosis Detection. Curr. Top. Med. Chem. 2017, 17, 1623–1630.

[11] Cervera-Chiner, L.; March, C.; Arnau, A.; Jiménez, Y.; Montoya, Á. Detection of DDT and carbaryl pesticides in honey by means of immunosensors based on high fundamental frequency quartz crystal microbalance (HFF-QCM). J. Sci. Food Agric. 2020, 100, 2468–2472.

[12] Cervera-Chiner, L.; Juan-Borrás, M.; March, C.; Arnau, A.; Escriche, I.; Montoya, Á.; Jiménez, Y. High Fundamental Frequency Quartz Crystal Microbalance (HFF-QCM) immunosensor for pesticide detection in honey. Food Control 2018, 92, 1–6.

[13] Cervera-Chiner, L.; Jiménez, Y.; Montoya, Á.; Juan-Borrás, M.; Pascual, N.; Arnau, A.; Escriche, I. High Fundamental Frequency Quartz Crystal Microbalance (HFF-QCMD) Immunosensor for detection of sulfathiazole in honey. Food Control 2020, 115, 107296.

[14] Zimmermann, B.; Lucklum, R.; Hauptmann, P.; Rabe, J.; Büttgenbach, S. Electrical characterisation of high-frequency thickness-shear-mode resonators by impedance analysis. Sens. Actuators B Chem. 2001, 76, 47–57.

[15] Fernández, R.; García, P.; García, M.; García, J.; Jiménez, Y.; Arnau, A. Design and Validation of a 150 MHz HFFQCM Sensor for Bio-Sensing Applications. Sensors 2017, 17, 2057.

[16] Fernandez, R.; Calero, M.; Reiviakine, I.; Garcia, J.V.; Rocha-Gaso, M.I.; Arnau, A.; Jimenez, Y. High Fundamental Frequency (HFF) Monolithic Resonator Arrays for Biosensing Applications: Design, Simulations, Experimental Characterization. IEEE Sens. J. 2020, 21, 284–295.

[17] Tuantranont, A.; Wisitsora-at, A.; Sritongkham, P.; Jaruwongrungsee, K. A review of monolithic multichannel quartz crystal microbalance: A review. Anal. Chim. Acta 2011, 687, 114–128.

[18] Hung, V.N.; Abe, T.; Minh, P.N.; Esashi, M. Miniaturized, highly sensitive single-chip multichannel quartz-crystal microbalance. Appl. Phys. Lett. 2002, 81, 5069–5071.

[19] Abe, T.; Esashi, M. One-chip multuchannel quartz crystal microbalance fabricated by deep RIE. Sens. Actuators A Phys. 2000, 82, 139–143.

[20] Vig, J.R.; Walls, F.L. A review of sensor sensitivity and stability. In Proceedings of the 2000 IEEE/EIA International Frequency Control Symposium and Exhibition (Cat. No.00CH37052), Kansas City, MO, USA, 9 June 2000; pp. 30–33.

[21] Mecea, V.M.; Carlsson, J.O.; Heszler, P.; Bârtan, M. Development and testing of a high temperature quartz crystal microbalance. Vacuum 1995, 46, 691–694.

[22] Rahtu, A.; Ritala, M. Compensation of temperature effects in quartz crystal microbalance measurements. Appl. Phys. Lett. 2002, 80, 521–523.

[23] Pierce, D.E. A temperature insensitive quartz microbalance. IEEE Trans. Ultrason. Ferroelectr. Freq. Control 1998, 45, 1238–1245.

[24] Muckley, E.S.; Anazagasty, C.; Jacobs, C.B.; Hianik, T.; Ivanov, I.N. Low-cost scalable quartz crystal microbalance array for environmental sensing. In Organic Sensors and Bioelectronics IX; International Society for Optics and Photonics: Bellingham, WA, USA, 2016; p. 99440Y.

[25] Corradi, E.; Agostini, M.; Greco, G.; Massidda, D.; Santi, M.; Calderisi, M.; Signore, G.; Cecchini, M. An objective, principal-component-analysis (PCA) based, method which improves the quartz-crystal-microbalance (QCM) sensing performance. Sens. Actuators, A Phys. 2020, 315, 112323.

[26] Mumyakmaz, B.; Özmen, A.; Ebeoğlu, M.A.; Taşaltin, C.; Gürol, I. A study on the development of a compensation method for humidity effect in QCM sensor responses. Sens. Actuators, B Chem. 2010, 147, 277–282.

[27] Mallat, S. A Wavelet Tour of Signal Processing; Elsevier: Amsterdam, The Netherlands, 2008.

[28] Janshoff, A.; Steinem, C. Label-free detection of protein-ligand interactions by the quartz crystal microbalance. Methods Mol. Biol. 2005, 305, 47–64.

[29] Wolny, P.M.; Spatz, J.P.; Richter, R.P. On the Adsorption Behavior of Biotin-Binding Proteins on Gold and Silica. Langmuir 2010, 26, 1029–1034.

[30] Boujday, S.; Bantegnie, A.; Briand, E.; Marnet, P.G.; Salmain, M.; Pradier, C.M. In-depth investigation of protein adsorption on gold surfaces: Correlating the structure

and density to the efficiency of the sensing layer. J. Phys. Chem. B 2008, 112, 6708–6715.

[31] Tsortos, A.; Papadakis, G.; Gizeli, E. Acoustic wave biosensor for detecting DNA conformation; A study with QCM-D. In Proceedings of the 2008 IEEE International Frequency Control Symposium, Honolulu, HI, USA, 19–21 May 2008; Volume 24, pp. 346–349.

[32] Tsortos, A.; Papadakis, G.; Gizeli, E. Shear acoustic wave biosensor for detecting DNA intrinsic viscosity and conformation: A study with QCM-D. Biosens. Bioelectron. 2008, 24, 836–841.

[33] Calero, M.; Fernández, R.; García, P.; García, J.V.; García, M.; Gamero-Sandemetrio, E.; Reviakine, I.; Arnau, A.; Jiménez, Y. A Multichannel Microfluidic Sensing Cartridge for Bioanalytical Applications of Monolithic Quartz Crystal Microbalance. Biosensors 2020, 10, 189.

[34] Griffel, D.H.; Daubechies, I. Ten Lectures on Wavelets. Math. Gaz. 1995, 79, 224.

[35] Montagut, Y.J.; García, J.V.; Jiménez, Y.; March, C.; Montoya, A.; Arnau, A. Frequency-shift vs phase-shift characterization of in-liquid quartz crystal microbalance applications. Rev. Sci. Instrum. 2011, 82, 064702.

[36] Fernandez, R.; Calero, M.; Garcia-Narbon, J.V.; Reiviakine, I.; Arnau, A.; Jimenez, Y. A Fast Method for Monitoring the Shifts in Resonance Frequency and Dissipation of the QCM Sensors of a Monolithic Array in Biosensing Applications. IEEE Sens. J. 2021, 21, 6643–6651.

[37] Nic, M.; Znamenacek, J. IUPAC. Compendium of Chemical Terminology 2nd ed.(the “Gold Book”); International Union of Pure and Applied Chemistry: 2005; Volume 1670.

3.5. High Fundamental Frequency (HFF) Monolithic Resonator Array for the simultaneous detection of pesticides and antibiotics in complex food

Under revision process. Sensors and Actuators B: Chemical

Abstract

As in the case of food industry in general, there is a global concern about safety and quality in complex food matrix such as honey, which is driving the demand for fast, sensitive, and affordable analytical techniques across the honey-packaging industry. Although excellent techniques like liquid chromatography-tandem mass spectrometry (LC-MS/MS) are available, these are still lacking in speed, portability, simplicity and cost-effectiveness. Here, a new approach is presented where a competitive immunoassay is combined with a novel High Fundamental Frequency Quartz Crystal Microbalance (HFF-QCMD) array biosensor for the simultaneous detection of antibiotics and pesticides in honey. For the proof of concept, thiabendazole and sulfathiazole residues were monitored in spiked honey samples. Results revealed that HFF-QCMD arrays provide a complementary and reliable tool to LC-MS/MS for the analysis of contaminants in this kind of complex matrices, while avoiding elaborate sample pre-treatment. The good sensitivity achieved (I_{50} values in the 1-10 ug/L range) and the short analysis time (60 minutes for 24 individual assays), together with the ability for multiple analyte detection (24 sensor array) and its cost-effectiveness, pave the way for the implementation of a fast on-line, in situ routine control of potentially hazardous chemical residues in honey.

Keywords

Immunosensor, HFF-QCMD array, honey, LC-MS/MS, antibiotic, pesticide

3.5.1. Introduction

The analysis of contaminants in complex food matrices by current analytical techniques presents some difficulties, such as the need of an elaborate sample pre-treatment. Honey is an example of complex food that has attracted a great interest in the last years. As a consequence of primary agricultural and livestock activities, potentially hazardous chemical residues can come into contact with bees, contaminating the beehive products and reaching the end consumer. This is a public health problem of enormous interest to the authorities, the beekeeping sector and the scientific community [1–3]. The origin of those chemicals is two-fold: on the one hand, veterinary treatments with acaricides, sulfa drugs, antibiotics, etc., necessary to deal with diseases and parasites in bees [4,5]; on the other hand, agricultural treatments with pesticides, mainly neonicotinoids [6–9], with which bees come into contact when collecting nectar in crops close to hives. A report by the EFSA (European Food Safety Agency) has confirmed this reality, highlighting the impact of these residues on the health of bees, and on that of honey and pollen consumers [9,10]. Therefore, controlling the presence of chemicals that could pose a risk to human health is essential in the marketing of honey. Current regulations are increasingly restrictive, limiting or even prohibiting the presence of these chemicals [10]. The 'gold standard' technique for quantifying these residues is the liquid chromatography-tandem mass spectrometry (LC-MS/MS) methodology [11–13]. LC-MS/MS provides the lowest limits of detection (LOD) both for pesticides and antibiotics [13]. However, chromatographic technics are expensive, time-consuming and require highly qualified personnel. These techniques do not allow for the simultaneous analysis of several residues with different chemical properties (i.e. pesticides and antibiotics) in a single assay, since the pre-treatment of the sample and even the chromatographic setup are very different when high resolution is demanded. Moreover, this analytical method is only available in centralized laboratories, consequently it is not adequate as an on-line control tool implanted in situ in a honey packaging industry, which needs automated, simpler, cheaper and faster screening methods that provide LODs as close as possible to those required.

In this scenario, biosensors emerge as complementary and/or alternative methods to the classical ones. Although there is a myriad of biosensing mechanisms and novel ones are continuously emerging [14,15], biosensors based on acoustic wave sensors and, particularly quartz crystal microbalance (QCMD), stand out as a real-time and label-free detection tool suitable for the analysis of contaminants in complex matrices, such as

honey. During the last years, the LOD of QCMD technology has been improved by around two orders of magnitude through the development of high fundamental frequency QCMD (HFF-QCMD) sensors with resonance frequencies of up to 150 MHz [16,17]. The HFF-QCMD principle of operation relies on the reduction of the quartz plate thickness of a classical QCMD [18], resulting in a sensitivity increase and a surface reduction [19]. Recently, individual HFF-QCMD sensors have been combined with a competitive immunoassay and used for pesticide (DDT [20] and carbaryl [21]) and antibiotic (sulfathiazole [22]) detection in honey samples with satisfactory results. However, the use of individual sensors is not feasible for the routine control of chemical residues in honey, since a list of several analytes must be monitored in the same sample. Thanks to their small footprint, it is possible to integrate dozens of HFF-QCMD sensors within the same substrate through the design of monolithic QCMD arrays [23]. Miniaturized and parallelized elements in the array lead to relevant benefits including high throughput, lower cost per sensor unit, less sample/reagent consumption and faster sensing response [24–26].

In the present work we apply, for the first time, a novel 24 sensor HFF-QCMD array to the development of a fast and simple competitive immunosensor for the simultaneous detection of two compounds belonging to very different chemical families: the fungicide thiabendazole (TBZ) and the antibiotic sulfathiazole (SFZ) in honey samples. The analytical performance of the proposed method in terms of LOD, Limit of Quantification (LOQ), accuracy and precision, was compared to LC-MS/MS as reference technique.

3.5.2. Material and Methods

3.5.2.1. Honey samples, chemicals and immunoreagents

Thiabendazole- and sulfathiazole-free honey (supplied by “Beemiel”, Valencia, Spain and checked by chromatographic analysis) was used as “blank honey”. Honey samples were spiked with TBZ (Riedel-de Häen, Seelze, Germany) or SFZ (Sigma Aldrich, Steinheim, Germany) when required.

The reagents used for covalent immobilization of the sensor array were: thiol compounds 11-mercapto-1-undecanol 97% (MUOH) and 16-mercaptohexadecanoic acid 90% (MHDA), 1-ethyl-3-(-3-dimethyl-amino-propyl) carbodiimide hydrochloride (EDC), n-hydroxysuccinimide (NHS) (all of them provided by Sigma-Aldrich Chemie, Steinheim,

Germany), and ethalonamine blocking agent (from Sigma, St. Louis, MO, USA). Bovine Serum albumin (BSA) fraction V (Sigma-Aldrich Chemie, Steinheim, Germany) was used to prevent non-specific antibody adsorption to the functionalized surface.

The immunoreagents for SFZ assay (provided by Custom Antibody Service, U2-ICTS-NANBIOSIS; Nb4D group-IQAC-CSIS/CIBER-BBN; Barcelona, Spain) were the following: SA2-BSA AE1 B28 protein-hapten conjugate and 6C11 (batch 8678) purified monoclonal antibody (MAb) against sulfathiazole. The immunoreagents for TBZ assay, BSA–TN3C protein–hapten conjugate and LIB–TN3C13 MAb were previously prepared as described [27].

Nanopure water and pure ethanol were purchased from Panreac Química SLU (Barcelona, Spain). Phosphate buffered saline (PBS) tablets for preparing 0.01 M phosphate buffer containing 0.0027 M potassium chloride and 0.137 M sodium chloride, pH 7.4, at 25 °C were from Sigma Aldrich Química, S.L.U. (Madrid, Spain) and was used as mobile phase in experiments. For cleaning the arrays and some pieces of the microfluidic system we used: a 20% solution of sodium dodecyl sulfate (SDS) (from Fisher Scientific S.L., Madrid, Spain), COBAS Cleaner (provided by Sanilabo S.L. Valencia, Spain), and piranha solution obtained by a mixture of hydrogen peroxide (H2O2, 50% purity) and sulphuric acid (H2SO4, 95%) in a 1:3 (v/v) ratio (both from Merck Life Science S. L. U., Madrid, Spain).

For the regeneration of the HFF-QCMD array we used sodium hydroxide prepared from pellets (98% NaOH) from Sigma Aldrich Chemie (Steinheim, Germany) and 1 M hydrochloric acid from Acros Organics purchased from Fisher Scientific S.L. (Madrid, Spain).

HPLC-grade acetonitrile and methanol solvents were from Prolabo (VWR International, France). The formic acid (purity 99%), analytical grade sodium chloride (NaCl), anhydrous magnesium sulphate, disodium hydrogen citrate sesquihydrate, trisodium citrate dihydrate and Bondesil Primary-Secondary Amine (PSA) were provided by Sigma Aldrich (Saint Quentin Fallavier, France). Cartridges for SPME extraction (Strata X–CW, 100 mg/3 mL) were supplied by Phenomenex (California, USA).

3.5.2.2. HFF-QCMD array methodology

3.5.2.2.1. HFF-QCMD array immunosensor setup

Arrays of 24 HFF-QCMD sensors organized in 6 columns of 4 resonator elements each were supplied by AWSensors (AWSensors S.L., Valencia, Spain). Arrays are based on a 50 MHz one-sided inverted MESA geometry and are optimized in terms of size and electrode geometry to facilitate manufacturing and integration with fluidics and electronics, spurious mode suppression, and operation in liquids [19,23].

Figures 3.5.1 (a) and (b) show top and bottom surfaces of the array device, respectively. Figure 3.5.1 (c) shows the array mounted in the flow measurement cell (Jobst Technologies, Freiburg, Germany). Measurement cell is divided into 6 independent flow channels covering 4 sensors each. Each channel has an inlet and an outlet that can be connected to flow tubing through steel cannulas. Flow connections of the array sensor measurement cell were configured to create two independent flow regions A and P (with 3 columns each) represented in Figure 3.5.1 (c) with blue and red dashed lines, respectively.

The arrays were immersed in piranha solution for 3 min and, before surface functionalization, were cleaned following the previously described protocol [28].

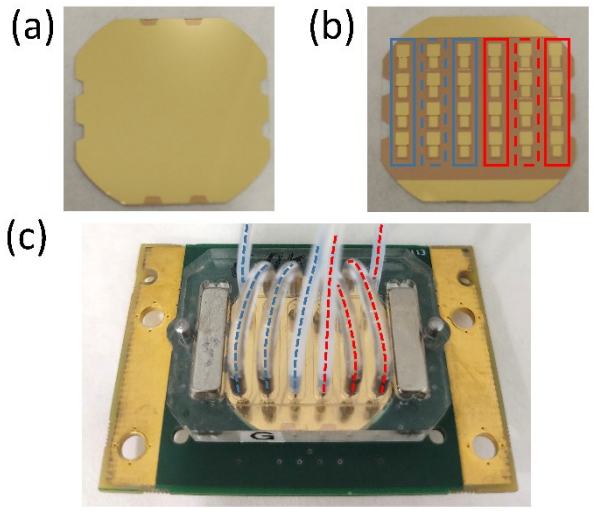

Figure 3.5.1 (a) Top and (b) bottom surfaces of the 24 HFF-QCMD array. (c) Array mounted in the flow cell. Blue and red dashed lines in (c) indicate the three columns of region A and P, respectively, that share the flow.

AWS X24 platform (AWSensors) was used for the simultaneous characterization of the 24 elements of the array. This QCMD instrument is based on a fixed-frequency phase-

shift measurement technique described elsewhere [29]. Both, the resonance frequency f_s and energy dissipation D were measured in real time [30]. AWS F20 platform (AWSensors) was used to generate a uniform flow through the array surface. Prior to use, all tubing (including those of the flow cell) were cleaned with COBAS cleaning solution for 30 min at a flow rate of 100 µL/min. Then, 0.1M HCl and nanopure water were pumped for 30 min each one. The sample was injected through an injection valve containing a 250 µL loop. Temperature was continually controlled by these platforms and kept at 25ºC. Moreover, a degasser was used to prevent signal distortion caused by bubbles. AWS Suite software package (AWSensors) was used to control both platforms and to register and process the acquired data.

3.5.2.2.2. Detection format and array sensor functionalization

The indirect competitive immunoassays developed to determine TBZ and SFZ were binding inhibition tests based on the conjugate-coated format [16]. Hapten-conjugates were immobilized on the gold sensing area of the array through the formation of mixed self-assembled monolayers (mSAM) of alkane thiols as intermediate layers. For the surface functionalization, the array was placed in a specially designed immobilization cell (provided by AWSensors), where the active area of the sensors was exposed to functionalization reagents. The cell divided the array into six columns containing four sensors each. The first and last column in each region (continuous line rectangles in Figure 3.5.1 (b)) contained sensors functionalized for the detection of pesticide TBZ (in Region P) and of antibiotic SFZ (in Region A). The middle column in both regions contained reference resonators (dashed line rectangles in Figure 3.5.1 (b)). Reference sensor columns are imbricated with functionalized sensor columns to achieve a configuration in which each sensor has a reference one aside.

The immobilization protocols were based on those previously reported in references [21,22,31], with the following volumes and concentrations adapted to the array immobilization cell: a) 100 µL of a 2.5 mM solution of compounds MUOH and MHDA in ethanol (50:1 M ratio); b) 100 µL of an ethanolic solution of EDC/NHS was incubated for 3.5 h.

3.5.2.2.3. Immunoassay optimization: Selection of the immunoreagent concentrations

The optimal combination of hapten-conjugate and monoclonal antibody concentrations was obtained to accomplish the trade-off of having a good signal-to-noise ratio (resonance frequency shift signal of around 1000 Hz) for the lowest analyte concentration, with the minimum immunoreagent consumption [21,22]. For this purpose, conjugates SA2-BSA for SFZ and BSA–TN3C for TBZ were immobilized onto two different arrays at the following concentrations (one different per column of the array): 0, 1, 5, 10, 20 and 50 µg/mL. Each functionalized array was tested with three different concentrations of the corresponding monoclonal antibody: 0.5, 1 and 2 µg/mL. The combination that met the trade-off established was selected as the optimum one: for SFZ 10 µg/mL of SA2-BSA AE1 B28 conjugate with 2 µg/mL of 6C11 MAb and for TBZ 5 µg/mL of BSA–TN3C conjugate with 1 µg/mL of LIB–TN3C13 MAb. A comparison with the values obtained for the individual HFF-QCMD technology has been included in section S1 of the supporting information (Appendix E).

3.5.2.2.4. Immunoassay protocol

The inhibition assay protocols were based on those previously reported [16,22]. Briefly, in a first step, a mixture of a fixed concentration of the corresponding MAb with standard solutions of the analyte (4×10^{3} to 4×10^{-3} µg/mL) or with the spiked honey samples was preincubated for 10 min at 25 ºC. A 20 µl/min continuous flow rate of working buffer (PBS) was pumped through sensors. When a nearly constant baseline was reached (5-10 min), 250 µL of the preincubated mixture were injected over the functionalized immunosensors surface. As the binding between the free antibody and the immobilized conjugate took place, the shifts in f_s and D were monitored in real time. Binding equilibrium was reached after around 30 min. The regeneration of the reactive surface to break the active antibody-hapten conjugate binding was carried out by pumping 0.1 M HCl for SFZ and 0.1 M NaOH for TBZ at a flow rate of 125 µl/min.

All diluted standards were tested at least three times. Moreover, injections corresponding to the maximum signal (absence of analyte in the dilution) were run every two standard solution injections for signal normalization and for evaluate the functionalization quality.

Standard curves for SFZ and TBZ were obtained in PBS-diluted honey by plotting normalized frequency shifts against the analyte concentration as previously described [22].

3.5.2.2.5. Honey samples pre-treatment for HFF-QCMD array

The only required sample pre-treatment was dilution in PBS. Different dilutions of honey in PBS (1/50, 1/100, 1/150 and 1/200 (w/v)) were tested to check the matrix effect of honey, as well as the occurrence of obstruction phenomena in fluidic microchannels. For this purpose, a limiting MAb concentration for each analyte (see section 3.5.2.2.3) was mixed with honey dilutions. Then, each mixture was injected over the corresponding array region (see Figure 3.5.1 (c)). To quantify matrix effects, the resonance frequency and dissipation changes due to the specific binding of the MAb to the immobilized conjugate were registered.

3.5.2.3. Chromatographic methodology

Stock solutions of STZ and TBZ were prepared at 1000 μg mL^{-1} by dissolving 10 mg of each compound in 25 mL of methanol and stored at -20 ˚C. The working standard solutions were prepared by successive dilution of each stock solution with nanopure water. All of the standard solutions were stored in amber glass bottles at −18 °C for a maximum of one year.

The extraction and subsequently chromatography procedure for SFZ was carried out as described [22]. For TBZ analysis, the QuEChERS procedure was followed: honey sample (5.0 g) was weighed into a polypropylene centrifuge tube (50 mL), and spiked when proceeded, with proper amounts of working standard solution of TBZ. Next, 10 mL nanopure water were added and shaken until a complete honey homogenization, then 10 mL of acetonitrile, 4 g magnesium sulfate anhydrous (MgSO4), 1 g sodium chloride (NaCl), 1 g sodium citrate dihydrate and 0.5 g disodium hydrogen citrate sesquihydrate were added and vigorously hand shaken for 1 min followed for a 1 min on a vortex mixer. The tube was centrifuged at 4000 rpm for 5 min at 4 ºC. After centrifugation, in order to clean up the solution, 4 mL of the supernatant was transferred to another tube (10 mL) containing 1.5 g of magnesium sulfate and 150 mg primary secondary amine (PSA). In the same way as before, a subsequent shaking and centrifugation step were performed.

Finally, 1000 µL of the upper solution was filtered (nylon 0.22 mm) prior to being analysed by high-performance liquid chromatography-tandem mass spectrometry (HPLC-MS/MS). The column used was an Atlantis T3 (2.1 × 100 mm, Waters). The mobile phase consisted in 0.1% formic acid in nanopure water as phase [A] and methanol as phase [B] with a flow rate of 0.3 mL/min. The gradient elution program was as follows: 0–1 min, 95%-50% A; 1–3 min, 95% A; 3–4.2 min, 30%–10% A; 4.2–4.3 min, 10%-90% A; 4.3–6 min, 90% A. The instruments conditions were as follows: the capillary voltage was set at 4000 V, whereas the drying gas temperature and sheath gas temperature were both 350 °C, with a drying gas flow of 12 L/min, the nebulizer pressure was set at 35 psi. The ions monitored by multiple reactions monitoring (MRM) were 321→194 and 321→152.

3.5.3. Results and Discussion

3.5.3.1. Standard calibration curves: Immunoassay sensitivity and matrix effect

One of the advantages of the proposed analytical technique is the simplicity of the pre-treatment required to work with honey. Figure 3.5.2 shows Δf_S and ΔD records acquired to select the optimum honey dilution ratio. Before the interaction takes place, only PBS flowed through the array sensors (T_1 in Figure 3.5.2). During the interaction interval (T_2 in Figure 3.5.2), mixtures containing antibodies and diluted honey came into contact with the array. In this interval, differences in the records corresponded both to immunoreagent interactions over the functionalized sensors surface and to honey viscoelasticity. As expected, the lower the dilution ratio the higher the sample viscoelasticity and hence the differences between PBS and honey dilutions records. Once honey dilution was replaced by PBS (T_3 in Figure 3.5.2), only the effect of the immunoreagent interactions remained and, as expected in a gravimetric regime, dissipation barely changed. Only a small deviation ~4×10^{-6} persisted around 25 min after the beginning of the interaction. This deviation tended to vanish with a PBS flow running over the time. Unlike dissipation response, a meaningful decrease in frequency resulted due to the antibodies mass attached to the immobilized conjugate. In this case, all the records stabilized in a frequency ~1000Hz±200Hz (T_3 interval). This 20% of variability remained even after regeneration, which allows us to conclude that the differences were neither caused by the dilution ratio nor by the persistence of honey. We attribute these deviations to the small physical

differences (i.e. Mesa region thickness and roughness) existing among the different resonators of the array [23], but also to the variability of the immobilization and regeneration processes applied over each sensor. To deal with this variability, it is very common to work with normalized signals [16,21,22]. In order not to increase the limit of detection of the technique, lower dilution ratios are desirable. However, the main challenge we faced with low dilution ratios was the obstruction of channels in the microfluidic system by honey matrix. To avoid this difficulty, we found that a 1/100 (w/v) ratio was the optimum dilution, which is in the same order of magnitude as those used with individual HFF-QCMD resonators [20–22].

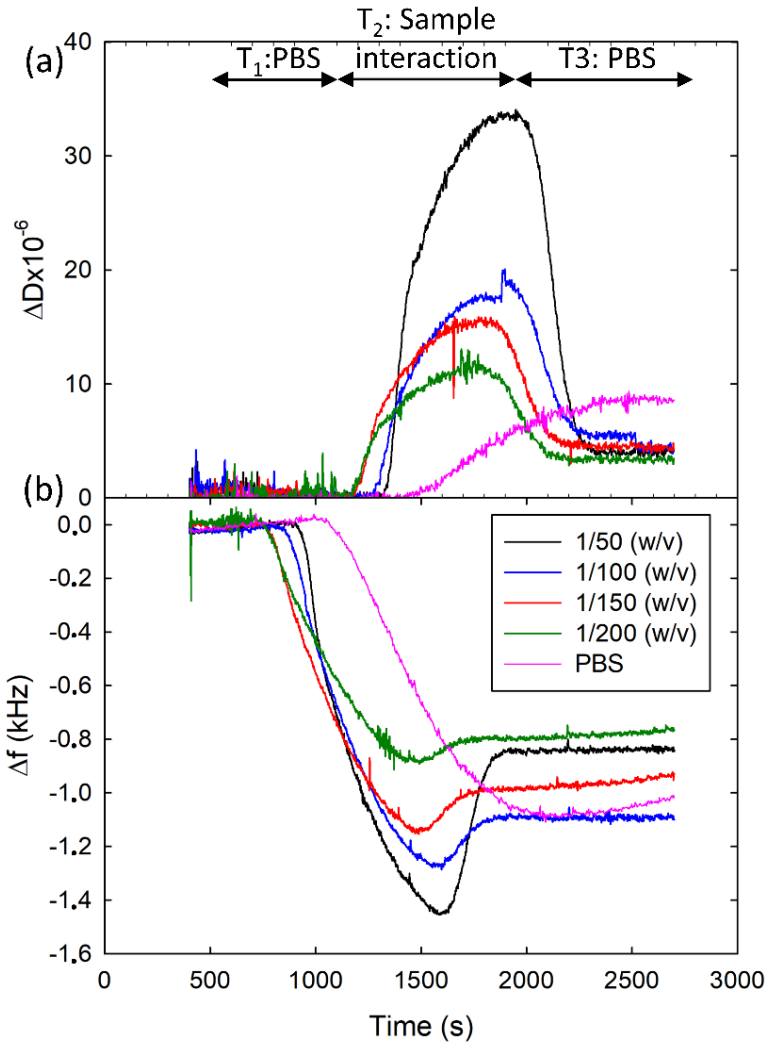

Figure 3.5.2 Records of Δf_s (b) and ΔD (a) acquired to select the honey dilution ratio. Different curves correspond to PBS and different dilution ratios.

Standard calibration curves were obtained for both SFZ and TBZ in 1/100 (w/v) diluted honey (see Figure 3.5.3 (a) and (b), respectively). Experimental dots and error bars in the figure correspond to the average of eight determinations of the same sample provided by

eight sensors of the array, with their respective standard deviations. From these curves, the immunosensor analytical parameters of interest were determined (Table 3.5.1): Working Range (WR), LOD, LOQ and I50 value [22].

Table 3.5.1 Immunosensor analytical parameters for the HFF-QCMD array standard curves of SFZ and TBZ in 1/100 (w/v) diluted honey.

	SFZ (µg/L)	TBZ (µg/L)
I_{50}	7.8	1.5
LOD	0.7	0.4
LOQ	1.7	0.7
WR	1.7 a 34.9	0.7 a 3.1

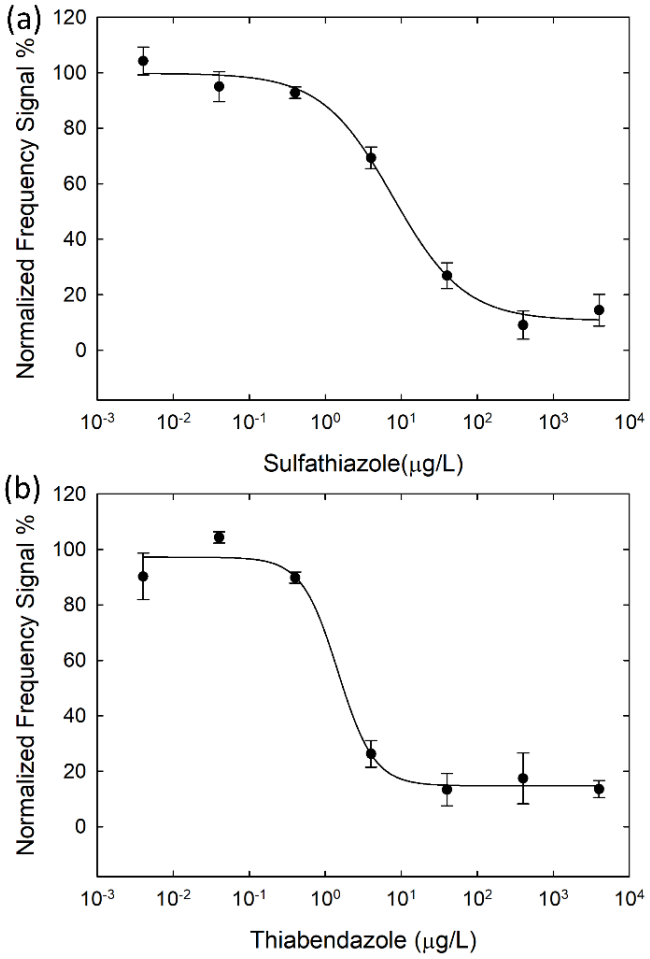

Figure 3.5.3 HFF-QCMD array standard calibration curves in honey diluted 1/100 (w/v) in PBS for SFZ (a) and TBZ (b). Each point is the average of eight determinations. Vertical bars represent standard deviations.

By using HFF-QCMD array technology, it is possible to use of 8 sensors simultaneously with similar immunoreagent volumes than those used with individual HFF-QCMD sensors, which drastically reduces costs and improves throughput. Immunosensor analytical parameters are in the same order of magnitude than those obtained with individual HFF-QCMD technology. Only small deviations were observed for SFZ immunosensors and attributed to two causes: (1) the reduction in the resonance frequency of the sensors (50 MHz in HFF-QCMD array vs. 100 MHz in individual HFF-QCMD), which contributes to a slight increase of LOD; and (2) the increase in the concentration of the immobilized conjugate (10 µg/µL in HFF-QCMD array *vs.* 5 µg/µL in individual HFF-QCMD), which produces a shifting of the calibration curve to the right and, consequently, an increase of the I_{50} value. For TBZ, there are not previous results reported in honey but a similar behavior was found in PBS (see Section S2 in the Supporting Information, Appendix E).

3.5.3.2. HFF-QCMD array validation with HPLC LC-MS/MS

To evaluate the performance of HFF-QCMD array technology as an analytical tool, several samples of blank honey spiked at 5 levels (53, 105, 264, 529 and 1059 µg/kg) for SFZ and at 4 levels (31, 62, 156 and 313 µg/kg) for TBZ were analyzed by HFF-QCMD array and HPLC LC-MS/MS in terms of precision (Coefficient of Variation - CV %) and accuracy (recovery %).

Figure 3.5.4 (a) and (b) depicts the superposition of the calibration curve (dashed blue line) with the experimental normalized frequency shift measured for each honey sample spiked with a fixed concentration of the analyte (red dots). Each red point with its error bar corresponds to the average of eight determinations of the same spiked honey sample.

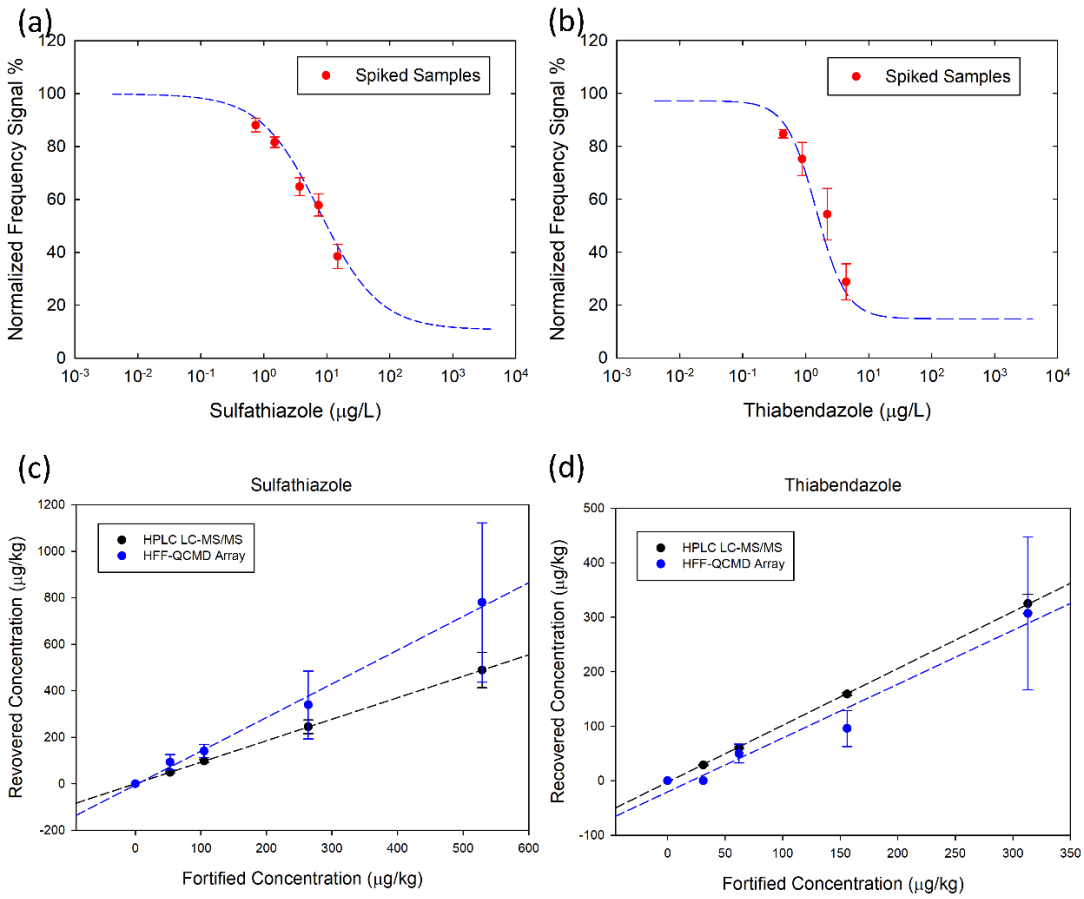

Figure 3.5.4 Superposition of the calibration curves (blue dashed lines) and the normalized frequency shifts registered with spiked honey samples at several fixed concentration levels, for SFZ (a) and TBZ (b). Recovered concentration vs. fortified known concentration for SFZ (c) and TBZ (d).

To compare the accuracy of HFF-QCMD array technique with that of LC-MS/MS, we depicted in Figure 3.5.4 (c) and (d) the recovered concentration versus the fortified known one for both techniques and SFZ and TBZ respectively. Linear regressions performed provide correlation coefficients above 0.95 for both techniques and analytes. For TBZ, slopes of 0.876 and 1.044 were obtained for HFF-QCMD array and LC-MS/MS, respectively. Regarding SFZ, slopes of 0.955 and 0.924 for HFF-QCMD array and LC-MS/MS were obtained, respectively.

Tables 3.5.2 and 3.5.3 show the comparison of the recovery and CVs obtained with both techniques for TBZ and SFZ, respectively. No false positives were detected in any case. Recovery percentages ranged from 73% to 130% and for 94% to 137% for TBZ and SFZ, respectively. In general, the precision and accuracy results for both analytes remained close to those established by the GC SANCO 12571/2013 guidelines [32], with an overall overestimation in the concentration values recovered for SFZ and an underestimation for

TBZ. Nevertheless, the proof of concept performed indicates that an effort is still needed in order to comply with the margins established by the standard, both for the recovery percentage (between 80% and 120%) and for CV (values lower than 20%).

Table 3.5.2 Analysis of TBZ-spiked honey samples. Comparison of HFF-QCMD array technology with LC-MS/MS.

Spiked level (µg/kg)	Recovered (µg/kg)	Recovery (%)	CV (%)	Detected (µg/kg)	Recovery (%)	CV (%)
	HFF-QCMD array[1]			**LC-MS/MS[2]**		
0	<LOD	No false positives		<LOD	No false positives	
31	40±3	130	8	29±1.2	94	4
62	60±13	97	21	60±1.6	97	2.6
156	114±34	73	30	159±2.4	102	1.5
313	285±134	91	33	325±17.2	104	5.3

*Average of 8 and 6 independent determinations for HFF-QCMD array and LC-MS/MS, respectively.
[1] Sample dilution factor 1/100 (v/w)
[2]Sample dilution factor 1/2 (v/w)

Table 3.5.3 Analysis of SFZ-spiked honey samples. Comparison of HFF-QCMD array technology with LC-MS/MS.

Spiked level (µg/kg)	Recovered (µg/kg)	Recovery (%)	CV (%)	Detected (µg/kg)	Recovery (%)	CV (%)
	HFF-QCMD array[1]			**LC-MS/MS[2]**		
0	<LOD	No false positives		<LOD	No false positives	
53	72±19	137	27	49±4	94	8.2
105	128±19	122	15	98±6,4	93	6.5
264	351±60	133	16	245±29,4	93	12
529	500±101	94	20	489±76,3	92	15.6

*Average of 8 and 6 independent determinations for HFF-QCMD array and LC-MS/MS, respectively.
[1] Sample dilution factor 1/100 (v/w)
[2]Sample dilution factor 1/2 (v/w)

One of the advantages of the new analytical technique introduced in this work deals with its capability to provide the simultaneous detection of analytes of different chemical

nature (i.e. pesticides and antibiotics) present in the same honey sample, which is not possible with LC-MS/MS techniques. To explore this ability, we simulated a real situation by fortifying honey with both types of chemical residues (TBZ and SFZ) at the same time.

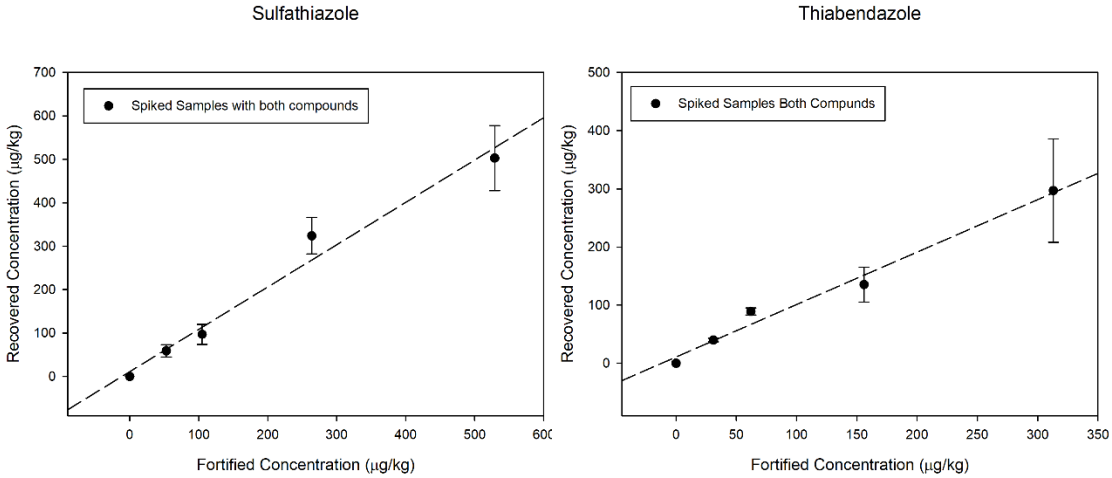

Figure 3.5.5 Recovered concentration versus the fortified known concentration for both SFZ (a) and TBZ (b).

No significant differences were observed with respect to the case in which honey was spiked with a single analyte. Recovery percentages were between 92% and 122% for SFZ and between 87% and 143% for TBZ with CVs in both cases below 25% (see Section S3 in the supporting information, Appendix E). Slopes in the linear regression of recovered concentration versus the fortified one were 0.973 for SFZ and 0,905 the TBZ (Figure 3.5.5). These results reveal the validity of the technique to detect chemical residues of very different origin in a single test and with a single pre-treatment of the sample. This reduces the complexity of the technique and the analysis time.

3.5.4. Conclusion

In this work, we report the successful application of a novel 24 sensor HFF-QCMD biosensing array for the simultaneous detection of TBZ and SFZ chemical residues in honey. The assay protocol, based on a competitive immunoassay, is completely automated so no trained personnel is required. LOD and LOQ are adequate for preliminary honey screening purposes. Analysis time (60-90 min) is of the same order of magnitude as in current reference techniques, i.e. LC-MS/MS. Unlike chromatographic methods, complex sample pre-treatment is not necessary, just a sample dilution (1/100 (w/v)) is required. This allows the simultaneous detection of compounds with very

different chemical properties (i.e. pesticides and antibiotics), thus reducing the complexity, size and cost of the analysis.

All these characteristics hold promise for the fast adoption of this technology as an unattended on-line screening tool complementary to chromatographic analysis in food packaging industry.

In the next future, method optimization is envisaged by improving the microfluidic channel design to allow the injection of less diluted honey samples. A new HFF-QCMD array design will also be considered to work at higher resonance frequencies (200 MHz). Both strategies are expected to improve (decrease) LOD. Finally, higher accuracy and precision should be achieved by optimizing immobilization and regeneration processes.

Funding

This work was supported by Ministerio de Economía, Industria y Competitividad de España– Agencia Estatal de Investigación with FEDER (Fondo Europeo de Desarrollo Regional) funds under Grants AGL2016-77702-R and AGL2013-48646-R). M. Calero is the recipient of the doctoral fellowship BES-2017-080246 from the Ministerio de Economía, Industria y Competitividad de España.

Acknwoledgements

The authors would also like to thank Lourdes Cervera for her advice in the practical tasks of this work.

References

[1] J.D. van Klaveren, P.E. Boon, Probabilistic risk assessment of dietary exposure to single and multiple pesticide residues or contaminants: Summary of the work performed within the SAFE FOODS project, Food Chem. Toxicol. 47 (2009) 2879–2882. doi:10.1016/j.fct.2009.10.047.

[2] J.C. Larsen, Risk assessment of chemicals in European traditional foods, Trends Food Sci. Technol. 17 (2006) 471–481. doi:10.1016/J.TIFS.2006.04.007.

[3] J.L.C.M. Dorne, J.L.C.M. Dorne, L.R. Bordajandi, B. Amzal, P. Ferrari, P. Verger, Combining analytical techniques, exposure assessment and biological effects for risk assessment of chemicals in food, TrAC Trends Anal. Chem. 28 (2009) 695–707. doi:10.1016/j.trac.2009.03.008.

[4] H. Boncristiani, R. Underwood, R. Schwarz, J.D. Evans, J. Pettis, D. Vanengelsdorp, Direct effect of acaricides on pathogen loads and gene expression levels in honey bees Apis mellifera, J. Insect Physiol. 58 (2012) 613–620. doi:10.1016/J.JINSPHYS.2011.12.011.

[5] B.A. Daisley, J.A. Chmiel, A.P. Pitek, G.J. Thompson, G. Reid, Missing Microbes in Bees: How Systematic Depletion of Key Symbionts Erodes Immunity, Trends Microbiol. 28 (2020) 1010–1021. doi:10.1016/J.TIM.2020.06.006.

[6] P.R. Whitehorn, S. O'Connor, F.L. Wackers, D. Goulson, Neonicotinoid Pesticide Reduces Bumble Bee Colony Growth and Queen Production, Science (80-.). 336 (2012) 351–352. doi:10.1126/SCIENCE.1215025.

[7] M. Henry, M. Béguin, F. Requier, O. Rollin, J.-F. Odoux, P. Aupinel, J. Aptel, S. Tchamitchian, A. Decourtye, A Common Pesticide Decreases Foraging Success and Survival in Honey Bees, Science (80-.). 336 (2012) 348–350. doi:10.1126/SCIENCE.1215039.

[8] C.H. Krupke, G.J. Hunt, B.D. Eitzer, G. Andino, K. Given, Multiple Routes of Pesticide Exposure for Honey Bees Living Near Agricultural Fields, PLoS One. 7 (2012) e29268. doi:10.1371/journal.pone.0029268.

[9] D. vanEngelsdorp, M.D. Meixner, A historical review of managed honey bee populations in Europe and the United States and the factors that may affect them, J. Invertebr. Pathol. 103 (2010) S80–S95. doi:10.1016/j.jip.2009.06.011.

[10] Regulation (EC) No 396/2005 of the European Parliament and of the Council of 23 February 2005 on maximum residue levels of pesticides in or on food and feed of plant and animal origin and amending Council Directive 91/414/EEC Text with EEA relevance., (n.d.). https://eur-lex.europa.eu/legal-content/EN/ALL/?uri=celex%3A32005R0396.

[11] M. Juan-Borrás, E. Domenech, I. Escriche, Mixture-risk-assessment of pesticide residues in retail polyfloral honey, Food Control. 67 (2016) 127–134. doi:10.1016/J.FOODCONT.2016.02.051.

[12] P.A. Souza Tette, L.R. Guidi, M.B. De Abreu Glória, C. Fernandes, Pesticides in honey: A review on chromatographic analytical methods, Talanta. 149 (2016) 124–141. doi:10.1016/j.talanta.2015.11.045.

[13] A. Masiá, M.M. Suarez-Varela, A. Llopis-Gonzalez, Y. Picó, Determination of pesticides and veterinary drug residues in food by liquid chromatography-mass spectrometry: A review, Anal. Chim. Acta. 936 (2016) 40–61. doi:10.1016/J.ACA.2016.07.023.

[14] M. Nirschl, F. Reuter, J. Vörös, Review of Transducer Principles for Label-Free Biomolecular Interaction Analysis, Biosensors. 1 (2011) 70–92. doi:10.3390/bios1030070.

[15] V. Gaudin, Advances in biosensor development for the screening of antibiotic residues in food products of animal origin – A comprehensive review, Biosens. Bioelectron. 90 (2017) 363–377. doi:10.1016/j.bios.2016.12.005.

[16] C. March, J. V. García, Á. Sánchez, A. Arnau, Y. Jiménez, P. García, J.J. Manclús, Á. Montoya, High-frequency phase shift measurement greatly enhances the sensitivity of QCM immunosensors, Biosens. Bioelectron. 65 (2015) 1–8. doi:10.1016/j.bios.2014.10.001.

[17] A. Montoya, C. March, Y. Montagut, M.J. Moreno, J.J. Manclús, A. Arnau, Y. Jimenez, M. Jaramillo, P. Marin, R.A. Torres, A High Fundamental Frequency (HFF)-based QCM Immunosensor for Tuberculosis Detection, Curr. Top. Med. Chem. 17 (2017) 1623–1630. doi:10.1386/ctl.9.1.5.

[18] B. Zimmermann, R. Lucklum, P. Hauptmann, J. Rabe, S. Büttgenbach, Electrical characterisation of high-frequency thickness-shear-mode resonators by impedance analysis, Sensors Actuators B Chem. 76 (2001) 47–57. doi:10.1016/S0925-4005(01)00567-6.

[19] R. Fernández, P. García, M. García, J. García, Y. Jiménez, A. Arnau, Design and Validation of a 150 MHz HFFQCM Sensor for Bio-Sensing Applications, Sensors. 17 (2017) 2057. doi:10.3390/s17092057.

[20] L. Cervera-Chiner, C. March, A. Arnau, Y. Jiménez, Á. Montoya, Detection of DDT and carbaryl pesticides in honey by means of immunosensors based on high fundamental frequency quartz crystal microbalance (HFF-QCM), J. Sci. Food Agric. 100 (2020) 2468–2472. doi:10.1002/jsfa.10267.

[21] L. Cervera-Chiner, M. Juan-Borrás, C. March, A. Arnau, I. Escriche, Á. Montoya, Y. Jiménez, High Fundamental Frequency Quartz Crystal Microbalance (HFF-QCM)

immunosensor for pesticide detection in honey, Food Control. 92 (2018) 1–6. doi:10.1016/j.foodcont.2018.04.026.

[22] L. Cervera-Chiner, Y. Jiménez, Á. Montoya, M. Juan-Borrás, N. Pascual, A. Arnau, I. Escriche, High Fundamental Frequency Quartz Crystal Microbalance (HFF-QCMD) Immunosensor for detection of sulfathiazole in honey, Food Control. 115 (2020) 107296. doi:10.1016/j.foodcont.2020.107296.

[23] R. Fernandez, M. Calero, I. Reiviakine, J.V. Garcia, M.I. Rocha-Gaso, A. Arnau, Y. Jimenez, High Fundamental Frequency (HFF) Monolithic Resonator Arrays for Biosensing Applications: Design, Simulations, Experimental Characterization, IEEE Sens. J. 21 (2020) 284–295. doi:10.1109/JSEN.2020.3015011.

[24] A. Tuantranont, A. Wisitsora-at, P. Sritongkham, K. Jaruwongrungsee, A review of monolithic multichannel quartz crystal microbalance: A review, Anal. Chim. Acta. 687 (2011) 114–128. doi:10.1016/j.aca.2010.12.022.

[25] V.N. Hung, T. Abe, P.N. Minh, M. Esashi, Miniaturized, highly sensitive single-chip multichannel quartz-crystal microbalance, Appl. Phys. Lett. 81 (2002) 5069–5071. doi:10.1063/1.1532750.

[26] T. Abe, M. Esashi, One-chip multuchannel quartz crystal microbalance fabricated by deep RIE, Sensors Actuators A Phys. 82 (2000) 139–143. doi:10.1016/S0924-4247(99)00330-1.

[27] A. Abad, J.J. Manclús, M.J. Moreno, A. Montoya, Determination of Thiabendazole in Fruit Juices by a New Monoclonal Enzyme Immunoassay, J. AOAC Int. 84 (2001) 156–161. doi:10.1093/jaoac/84.1.156.

[28] M. Calero, R. Fernández, P. García, J.V. García, M. García, E. Gamero-Sandemetrio, I. Reviakine, A. Arnau, Y. Jiménez, A Multichannel Microfluidic Sensing Cartridge for Bioanalytical Applications of Monolithic Quartz Crystal Microbalance, Biosensors. 10 (2020) 189. doi:10.3390/bios10120189.

[29] Y.J. Montagut, J. V. García, Y. Jiménez, C. March, A. Montoya, A. Arnau, Frequency-shift vs phase-shift characterization of in-liquid quartz crystal microbalance applications, Rev. Sci. Instrum. 82 (2011) 064702. doi:10.1063/1.3598340.

[30] R. Fernández, M. Calero, J. V García, I. Reviakine, A. Arnau, Y. Jiménez, A fast method for monitoring the shifts in resonance frequency and dissipation of the QCM

sensors of a Monolithic array in biosensing applications, IEEE Sens. J. (2020) 1. doi:10.1109/JSEN.2020.3042653.

[31] C. March, J. V. García, Á. Sánchez, A. Arnau, Y. Jiménez, P. García, J.J. Manclús, Á. Montoya, High-frequency phase shift measurement greatly enhances the sensitivity of QCM immunosensors, Biosens. Bioelectron. 65 (2015) 1–8. doi:10.1016/j.bios.2014.10.001.

[32] E.C.& C.P. DIRECTORATE-GENERAL, Guidance document on analytical quality control and validation procedures for pesticide residues analysis in food and feed, n.d. https://www.eurl-pesticides.eu/library/docs/allcrl/AqcGuidance_Sanco_2013_12571.pdf.

4. Final Conclusions and Future Research Lines

A novel technology based on a monolithic high-resolution quartz crystal array has been developed in this thesis. This new generation of QCMD resonators, conveniently functionalized to constitute an immunosensor, allows for the simultaneous detection of chemical residues with very different chemical composition, such as pesticides and antibiotics, in real samples of honey. This novel technology contributes to solve the challenges identified in chapter 1.5.1, thus providing an alternative screening analysis method to the classical ones that meets the requirements demanded from honey packaging industry, namely, low cost, fast and automated operation and easy to handle. To accomplish this main result, several multidisciplinary research lines have been undertaken.

The purpose of the first research line was to design a high throughput and cost-effective sensor device to be used in biological applications that entail the contact of the device with a fluid medium. To this end, an array of High Fundamental Frequency QCMD resonators has been designed, manufactured and evaluated. Its high-fundamental frequency feature leads to the miniaturization of the resonator elements, which results in the integration of 24 HFF-QCMD 150 MHz sensors on a same wafer with dimensions 14.25 mm×9.05 mm. Resonator elements are based on one-sided inverted MESA technology. In the proposed design, the sensor elements are arranged in 6 columns of 4 resonators each. The designed array has been evaluated both, at a physical and electrical level. Roughness of the resonator elements surfaces has been determined to be smaller than 1 nm, this ensures a good acoustic performance of the array elements, particularly in fluid media operation (diluted honey for the application that concern us). It has been verified that the manufacturing process of the MESA region is extremely reproducible, which is reflected in the low dispersion of both, the frequency and quality factor values, being very similar to those previously reported for single HFF-QCMD resonators. Related to this, although having reproducible resonance frequencies for the resonator elements was a goal, small variation observed in frequency values were beneficial to reduce crosstalk. Optimization of the geometry undertaken for both, resonators and electrodes, provided a sufficient separation between the fundamental and the first spurious modes for its use in biosensing applications in fluid media. Finally, special attention has been paid to the study of the interference between resonators. In this context, it can be ensured the independent operation of individual sensor elements, since a negligible crosstalk value of S_{21}~-32dB was measured for a batch of several manufactured arrays.

Keeping in mind the goal of developing a novel technology able to operate as a screening analysis technique, a fast operation method for measuring two representative resonator parameters, Δf_r and ΔD, with high-resolution time and high precision has been developed. This development was framed in the second research line addressed in this thesis. The method has the capability of providing a real time response of each resonator element of the array at several overtones. The experiments performed showed that, while the reference method used (impedance spectrometry) needs 12 s to characterize the 24 array elements, the novel method proposed just needs less than 300 ms. Nevertheless, these values cannot be considered as the minimum ones achievable since it is possible to modify the hardware to obtain a higher data rate. Thus, leaving aside hardware considerations, the key factor that really affects the method throughput rate is the relaxation time of the resonator (τ), which depends on the resonator frequency and on the operating conditions. For a 150 MHz HFF-QCM resonator operating in air $\tau \sim \mu s$, which makes the method very suitable to accomplish the goal of achieving a fast-screening analysis technique. The method comprises an initial fitting that accounts for the electrical parasitic effects, which makes the measurement more robust against electrical artefacts. Once that initial fitting is performed, the method operates at a single frequency, continuously updated during the experiment, which makes possible the fast operation of the method. Two key features of this novel method are that the readout electronic circuit necessary to operate with the method is low-cost and only the instrument setup and resonator settling time limit the measurements resolution.

Housing of the array is necessary for connecting it to the characterization system and, also for its operation with diluted honey (fluid medium). With this purpose, a third research line was conducted with the main goal of designing, manufacturing and evaluating a microfluidic cartridge. The cartridge defines six 6-µL channels of four sensors each for low-volume parallel measurements, ensuring the liquid confinement in each channel. It was manufactured with biochemically compatible materials (PDMS and PMMA) and can be either reusable or disposable. To evaluate its performance, an experiment for measuring biomolecular interactions in a biotin/neutravidin based system was conducted. The evaluation consisted of checking that reproducible measurements of Δf_r and ΔD were obtained in response to the subsequent adsorption of several biotin/neutravidin layers. The measurements showed an independent operation of the individual array elements, as well as a random distribution of the adsorbed masses as a

function of the array element location. This revealed that microfluidics of the cartridge allows for a uniform distribution of the reagents over the whole array. Arrays survived up to 30 cleaning and assembly cycles without loss of performance, which brings to light robustness of the cartridge and array system. This is a key feature for food control analysis, since working with reusable cartridges will drastically reduce the cost of the analysis.

HFF-QCMD technology used in the array provides better LoDs when compared with traditional QCMD, but also a higher sensitivity to disturbances. On the one hand, the influence of external factors, such as temperature or pressure gradients, can mask the signal and, therefore worsen LoD provided by this technology. On the other hand, intrinsic disturbances, such as mechanical stress exerted by the cartridge or characterization system noise, can generate instabilities in the measurements. To make the novel technique to be suitable for the main goal of the thesis, these two types of disturbances should be minimized. With this goal, the fourth research line of the thesis was started up. In this line, a signal processing based on the discrete wavelet transform (DWT) has been proposed, seeking to cancel those noise patterns that are similar in all of the resonators integrated in the array. The processing method developed was validated by using the same adsorption experiment of several biotin/neutravidin layers. Results showed an improvement of two orders of magnitude in the detection limit of the instrument under conditions of static flow and controlled temperature. This is a very valuable improvement of the novel technology developed in this thesis, since MRLs in honey are increasingly restrictive, in particular in antibiotic detection, where “absence” of this chemical residue is required.

Fifth research line addressed in the thesis consisted of the design of a proof of concept suitable to validate the novel developments accomplished in previous research lines for the analysis of chemical residues in honey. A competitive immunoassay was developed for the simultaneous detection of two very different chemical composition residues, namely, the fungicide thiabendazole and the antibiotic sulfathiazole. Results revealed that the developed technology can be used as a complementary screening and reliable tool to LC-MS/MS for the analysis of contaminants in complex food matrices. This novel analytical technique provided a good sensitivity (I_{50} values in the 1-10 ug/L range), a cost-effective analysis and a short analysis time (60 minutes for 24 individual assays). Moreover, it has the capability for multiple analyte detection (24 sensor array), which

makes it possible to detect simultaneously antibiotics and pesticides in the same analysis. Unlike chromatographic methods, complex sample pre-treatment is not necessary, just a sample dilution of the sample is required to avoid micro-channels obstruction. This is a key advantage of this novel technique versus the classical, which require complex pre-treatments, often with very contaminant reagents.

Based on the different issues experienced during the development of this thesis, the future works proposed to be explored are the following:

1) Re-design of the monolithic array to increase its sensitivity by exploring three possibilities:
    - Increasing the fundamental resonance frequency to reach frequency values ~200MHz.
    - Measuring the resonators response at its overtones.
    - Exploring a new paradigm based on acoustic coupling between adjacent resonators.
2) Optimization of the readout hardware:
    - To overcome the limitation imposed by current hardware in AWSFM-T method throughput rate.
    - To increase bandwidth and operation frequency.
3) Re-design of the cartridge by working in two features:
    - Optimization of the micro-channels layout to minimize channel obstruction. This will allow working with lower ratio dilutions, which, in turn, will enhance LoD of the analysis technique.
    - Improvement of the cartridge assembly by replacing the screws by other type of fasteners.
4) Optimization of the immobilization and regeneration processes to reduce the variability of the analysis technique.

5. Annexes

Appendix A

Supporting Information

SI. BvD circuit parameters of the fabricated arrays

TABLE SI
SUMMARY OF THE BVD CIRCUIT PARAMETERS

Parameter	Array 1	Array 2	Array 3
C_0 (pF)	2.39 ± 0.07	2.28 ± 0.06	2.33 ±0.08
C_m (fF)	5.7 ± 0.8	5.4 ± 0.5	5.4 ± 0.7
L_m (mH)	0.20 ± 0.03	0.22 ± 0.03	0.22 ± 0.04
R_m (Ω)	16.2 ± 12.9	9.1 ± 2.8	20.7 ± 12.9
f_{res} (MHz)	149.6 ± 29.1	149.1 ± 68.7	147.9 ± 43.7
C_0/C_m	424 ± 59	430 ± 43	437.3 ± 57

Values of three fabricated arrays selected at random. They were obtained from fitting the measured resonance curves. The resistor, R_m, capacitor, C_m, and inductor, L_m, comprise motional or acoustic branch, and C_0—the static or electrical branch.

Values of C_0/C_m agree well with those reported by other authors for 50MHz [1] and 66MHz [2] sensors.

SII. FEM Simulations

Here, we give some additional details concerning the finite element method (FEM) simulations of the arrays. As already mentioned in the main text, the starting point for the simulations was our previous FEM model of the individual 150 MHz resonators.[3] There were several essential differences between that work and the current model that allowed us to investigate resonance properties of the array elements and the cross-talk between the elements in the array.

Firstly, in order to model the array, geometrical transformations (reflection and gluing) were applied to generate a two-resonator array that is shown in Figure 3.1.9 in the main text.

Secondly, to model the effect of detuning, the two elements were assigned slightly different density so that their resonance frequencies differed by the appropriate amounts.

Third, a capacitor of ~ 23 fF, was introduced between the elements to match experimental behavior of S_{21} away from resonance. This value matches with the sum of the two capacitances that model the effects not considered by FEM simulations: the dielectric

effects of air (modeled by C_{fa}) and of the circuit board (PCB) on which the array was mounted (modeled by C_{ep}). Their values are estimated to be C_{fa} = 8 fF and C_{ep} = 4–13 fF from calculations based on the microstrip coupling theory described in [4].

Forth, S_{21} was calculated from the output of the FEM simulations, which comprises displacement patterns and charges generated at the electrodes, as well as the voltage on the passive element, as a function of frequency. Current, I, was calculated from the charges on the electrodes of both elements. Currents and voltages were used to calculate the 2x2 impedance matrixes of the two-element network, Z, where V = ZI, and V and I are the 2-element voltage and current vectors, respectively. $Z_{ij} = V_i/I_j$, where i and j are element indexes, with the active element that was excited with 0.5 V assigned and index of 1, and the passive element and index of 2. The impedance matrix Z was converted into the scattering matrix S using appropriate transformations [5]. Note, that in the case of the detuned array, the simulations had to be run twice with active and passive elements interchanged for calculating the impedance matrix.

The results of the simulations are shown in Figure 3.1.9 in the main text.

SIII. Equivalent Circuit Model

Here, we investigate the effects of the individual circuit elements in the equivalent circuit (Fig. S1) on the crosstalk between the resonators as represented by the scattering parameter S_{21}.

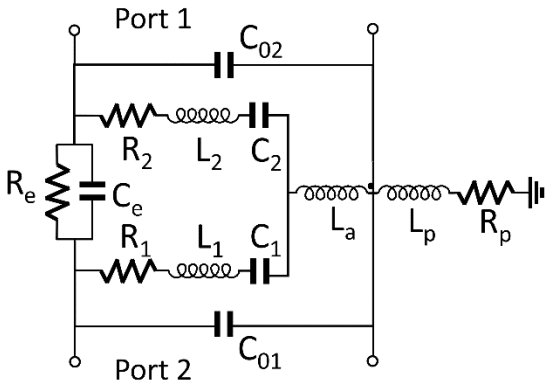

Fig. S1. Monolithic crystal filter equivalent circuit used to model coupled array elements. Same as Figure 3.1.10b in the main text of the paper. Elements are defined in the text.

The equivalent circuit of the coupled array elements consists of two BvD circuits with elements C_i, L_i, R_i, C_{0i} representing the two resonators, where I = 1, 2, sharing a common electrode (grounded) and coupled through a set of elements C_e, R_e, and L_a, and the parasitic elements between the common electrode and the ground L_p and R_p (Fig. S1).

When the parasitic elements are not considered, the common electrode is connected directly to ground.

Numerical values for the elements of the two BvD circuits (R_i, C_i, C_{0i}), obtained from fitting the measured resonance curves (Table SI in Supporting Information), were as follows: $C_1 = C_2 = 5.73$ fF, $C_{01} = C_{02} = 2.29$ pF and $R_1 = R_2 = 16$ **Ω**, for the figures in this Supporting Information (values considered in Figure 3.1.8 are detailed in the figure caption). $L_i = \frac{1}{C_i(2\pi f_{res,i})^2}$ was used to set the values of L_i, where $f_{res,i}$ are the series resonance frequencies of the two elements to be used in the calculations to mimic experimentally observed detuning between. For the figures in this Supporting Information $f_{res,1} = 150$ MHz, $f_{res,2} = 150$ MHz + Δf, and Δf is indicated in each figure (values in Figure 3.1.8 are detailed in the figure caption). Capacitance value of C_e was determined from the experimental value of $|S_{21}|$ away from resonance to be 32 fF. This value is in good agreement with the range of values estimated by the microstrip coupling theory [4]. L_a is related with the parameter that quantifies the coupling strength, K, through $L_a = L_i \times K$.[6], [7] K in the figures is obtained from fitting the measured maximum crosstalk. Losses, either represented by R_e or by R_p, included in the model to make it more general, were found to slightly alter the shape of the S_{21} curves, but did not contribute significantly to the outcome of the equivalent circuit model calculations. Thus, R_e is considered infinite and R_p null, unless otherwise indicated. Values for the other elements are indicated in the figure captions.

Fig. S2 shows the crosstalk between the two resonators when only the electric coupling is considered, that is, when L_a and L_p are set to zero and only the capacitor, C_e, was assigned a value based on the experimental measurements of S_{21} away from resonance. The behavior of S_{21} exhibits two dips (transmission zeros), located at the series resonance frequencies of the two resonators. This occurs because at the resonance frequencies, the resistances of the resonators are small, and there is a low impedance electrical path from the input port to the ground via one of the two resonators. In this way, the electrical signal from the source leaks to ground through the resonators instead of arriving at the output (Port 2 in Fig. S1).

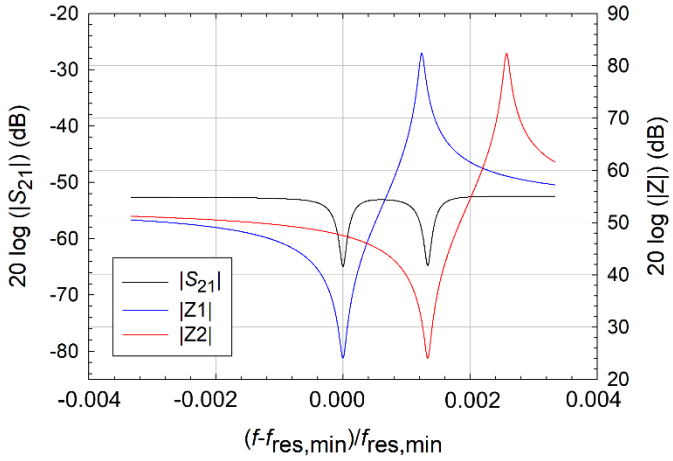

Fig. S2. Crosstalk between the two elements and their impedances for the case of L_a = 0 H, C_e = 32 fF, L_p=0 H and Δf=200 kHz. Note, that the locations of the two dips in $|S_{21}|$ coincide with the resonance frequencies of the two elements.

Fig. S3 shows the crosstalk between the two resonators when only the acoustic coupling is considered, that is, when C_e and L_p are set to zero, and only the effect of the inductance L_a is taken into account. S_{21} exhibits a maximum that takes the shape of a plateau bound by the series resonance frequencies of the two resonators. No transmission zeros are observed, because the direct path to ground at the resonance frequencies of the resonators is blocked by the inductor. The transmission between the two ports is at the maximum at frequencies that are between the resonance frequencies of the two resonators, where their resistance is smaller than that of the inductor, and a low-impedance path is generated between the two ports. This works when the two resonance frequencies are close to each other (small detuning); if the detuning is increased, a dip appears midway between the two resonance frequencies (not shown). Mathematically, S_{21} has poles at the series resonance frequencies of the two resonators.

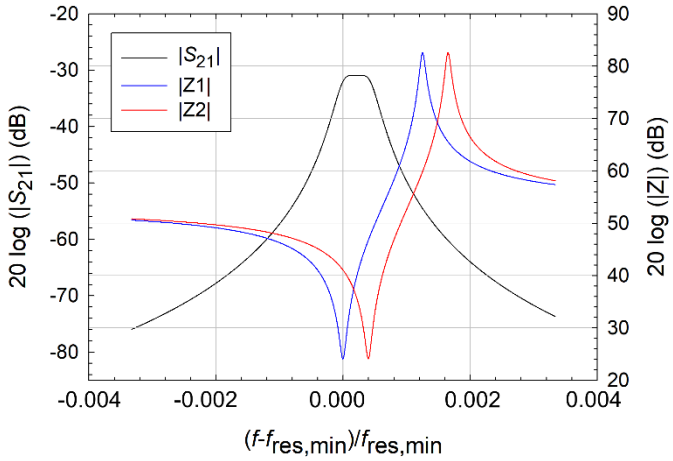

Fig. S3. Crosstalk between the two elements and their impedances for the case of $L_a = L_1 \times K$ H, $K = 1 \times 10^{-5}$, C_e = 0 fF, L_p=0 H and Δf = 60 kHz. Note, how the locations of the two resonance frequencies relate to the transmission maximum in the S_{21}.

An interesting feature of S_{21} behavior observed experimentally is the difference between frequencies at which the transmission zeros occur and the series resonance frequencies of the resonators. This feature, not observed when the equivalent circuit model only considers the electric coupling through C_e (see Fig. S2), is captured by the equivalent circuit model when considering the capacitor Ce together with an inductor.

The origin of this feature is in the interference phenomena. When the circuit contains both a capacitor C_e and an inductor, either L_a (see Fig. S4) or L_p (see Fig. S5), the electrical signal has two paths to travel from Port 1 to Port 2 (Fig. S1): one through C_e, and the other through the resonators, with their respective frequency-dependent behavior. When the two signals arrive at Port 2 out of phase, they cancel each other out, producing the transmission zero. The reason why the first transmission zero always occurs at a frequency $f < f_{res,min}$ is that the phase of the signal travelling through the resonator is inverted at the series resonance frequency. Further, the frequency at which the first transmission zero occurs depends on the impedance of the coil, and on the detuning: the higher the impedance and the smaller the detuning, the greater will be the difference between the frequency of the first transmission zero and the series resonance frequency (the lower will be the frequency of the first transmission zero). The inverse relationship between the frequency of the first transmission zero and the detuning is easy to understand since detuning, as we have seen, diminishes the influence of one resonator on the other. These interference phenomena are considered in more detail in ref [8].

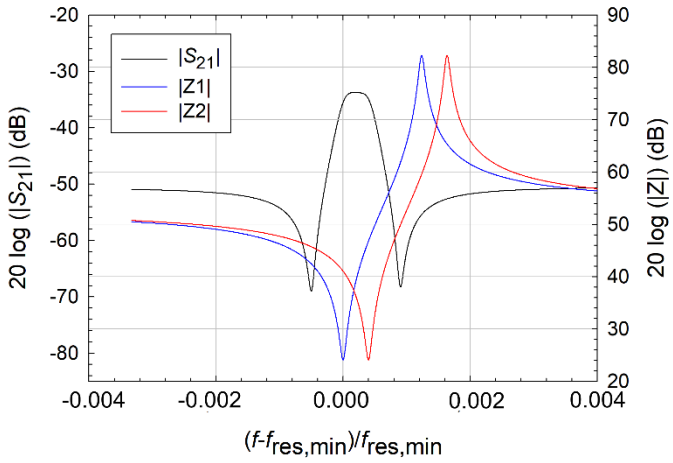

Fig. S4. Cross-talk between the two elements and their impedances for the case of $L_a = L_1 \times K$ H, $K = 1 \times 10^{-5}$, $C_e = 32$ fF, $L_p = 0$ H and $\Delta f = 60$ kHz. Note, how the locations of the two transmission zeros in $|S_{21}|$ are shifted from the resonance frequencies of the resonators.

The equivalent circuit model that was ultimately found to quantitatively agree with the experiments was the one that disregards the acoustic coupling (L_a) but considers a poor

electrical grounding through the parasitic inductance, L_p = 2 nH (Fig. S5). Value of inductance L_p is on the range between 1 and 9 nH estimated from the electrode geometry according to the following references [4], [9].

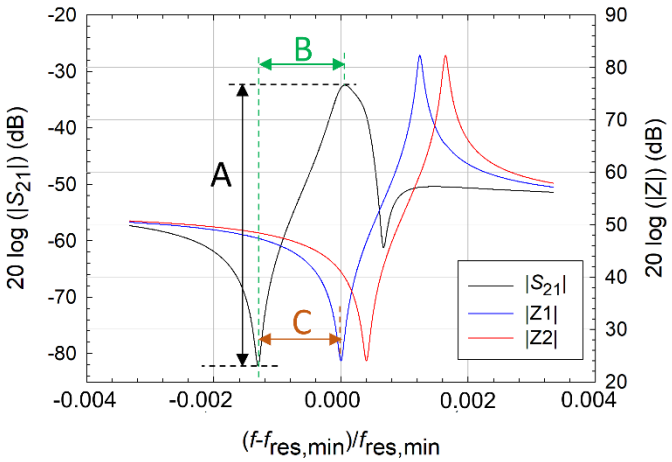

Fig. S5. Crosstalk between the two elements and their impedances for the case of L_a = 0 H, C_e = 32 fF, L_p = 2 nH, and Δf=60 kHz.

The effect of detuning on the behavior of S_{21} predicted by the model with L_p is further explored in Fig. S6. To effectively study this effect, three salient characteristics of S_{21} (parameters A, B and C) were defined (see Fig. S5). A is the amplitude of the peak in $|S_{21}|$ measured from the first transmission zero, B is the difference in frequency between the first transmission zero and the maximum in $|S_{21}|$, and C is the difference between the first transmission zero and the resonance frequency of the element with the lower resonance frequency. Fig. S6 represents the evolution of these parameters with detuning. Experimental results from three different arrays are shown by using different colors. Black dots represent the results from model calculations. Note, in particular, how the dependence of the parameters A, B, and C on detuning are captured by the model. Increased detuning diminishes the amplitude of the maximum in S_{21} and shifts the location of the transmission zeros relative to the resonance frequencies of the resonators. This behavior was found on the experimental measurements.

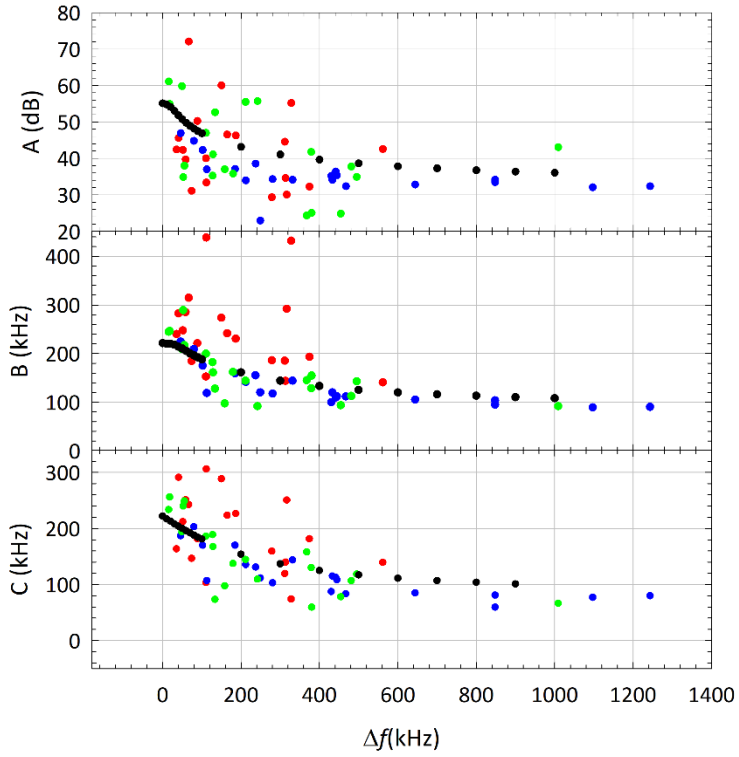

Fig. S6. Dependence of the parameters A, B, and C, defined in Fig. S5, on the detuning. Experimental results from three different arrays are shown in color, model calculations—in black. La = 0 H, C_e = 32 fF, and L_p =2 nH.

References

[1] B. Zimmermann, R. Lucklum, P. Hauptmann, J. Rabe, and S. Büttgenbach, "Electrical characterisation of high-frequency thickness-shear-mode resonators by impedance analysis," Sensors Actuators B Chem., vol. 76, no. 1, pp. 47–57, 2001.

[2] P. Kao, S. Doerner, T. Schneider, D. Allara, P. Hauptmann, and S. Tadigadapa, "A micromachined quartz resonator array for biosensing applications," J. Microelectromechanical Syst., vol. 18, no. 3, pp. 522–530, 2009.

[3] R. Fernández, P. García, M. García, J. V. García, Y. Jiménez, and A. Arnau, "Design and validation of a 150 MHz HFFQCM sensor for bio-sensing applications," Sensors (Switzerland), vol. 17, no. 9, pp. 1–13, 2017.

[4] J. Hong and M. J. Lancaster, Microstrip Filters for RF/Microwave Applications. John Wiley & Sons, Inc., 2001.

[5] D. A. Frickey, "Conversions between S, Z, Y, H, ABCD, and T parameters which are valid for complex source and load impedances," IEEE Trans. Microw. Theory Tech., vol. 42, no. 2, pp. 205–2011, 1994.

[6] R. A. Sykes and W. D. Beaver, “High Frequency Monolithlc Crystal Filters with Posslble Application to Single Frequency and Single Side Band Use,” Proc. IEEE Ultrason. Symp., pp. 288–308, 1966.

[7] A. A. Vives, J. M. F. y D. L. Osorio, T. S. Devesa, and Y. J. Jiménez, SISTEMAS ELECTRÓNICOS DE COMUNICACIONES I. Valencia: Universitat Politècnica de València, 2000.

[8] J. Brian Thomas, “Cross-coupling in coaxial cavity filters - A tutorial overview,” IEEE Trans. Microw. Theory Tech., vol. 51, no. 4 II, pp. 1368–1376, 2003.

[9] R. Garg and I. J. Bahl, “Characteristics of Coupled Microstriplines,” IEEE Trans. Microw. Theory Tech., vol. 27, no. 7, pp. 700–705, 1979.

Appendix B

Supporting Information

S1. DESCRIPTION OF THE MONOLITHIC QCM SETUP

This section details the Monolithic QCM setup used in the real time monitoring of the neutravidin adsorption experiment. Figure S1 (a) and (b) show top and bottom surfaces of the MQCM device, respectively. Array consists of 6 columns of 4 HFF-QCM resonator elements each. Array elements are based on a 50 MHz one-sided inverted MESA geometry and are optimized in terms of size and electrode geometry to facilitate manufacturing and integration with fluidics and electronics, spurious mode suppression, and operation in liquids. The top electrode is grounded, and it is common to all 24 array elements. This common electrode constitutes the "working" side of the array. It faces the sample. On the other side of the array, the short rectangular electrodes are connected to the driving circuitry individually.

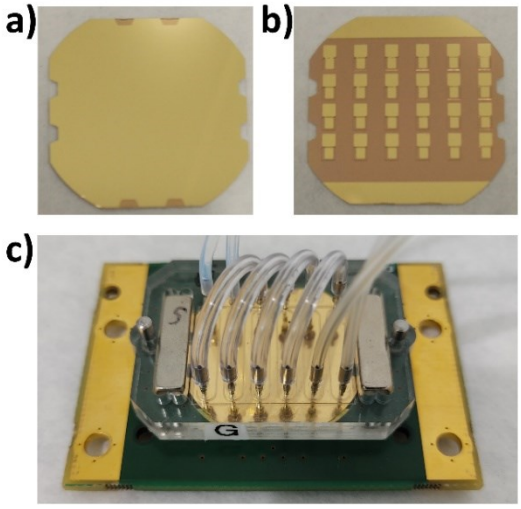

Fig S1. (a) Top and (b) bottom surfaces of the Monolithic QCM device. (c) MQCM device mounted in the flow cell.

Fig. S1 (c) shows the array mounted in the flow measurement cell. Measurement cell is divided into 6 independent flow channels covering 4 sensors each. Each channel has an inlet and an outlet that can be connected to flow tubing through steel cannulas. Flow connections of the array sensor measurement cell were configured to create three different isolated flow paths with 8 sensors each to monitor the same experiment using three different characterization methods: reference impedance spectrometry method, AWSFM-T and AWSFM-FF.

S2. Parametric study workflow

This section details the workflow we have followed to carry out a parametric study to evaluate the accuracy of the AWSFM characterization method under different operation conditions. This study is based on the offline post-processing of real experimental data. Main steps of the study are summarized in Figure S2, and described below:

1) Experimental data have been gathered through classical impedance spectrometry that we use as a reference method. AWS X1 platform measures 200 points of the sensor electrical admittance spectrum around resonance every 0.5 seconds and fits the data to a "phase-shifted-Lorentzian" function, providing over time six parameters ($f_r, \Gamma, G_{max}, G_{off}, B_{off}, \phi$) that model the response of the QCM sensor according to Eq. 10 and 11.

2) Parameters obtained in the experimental campaign ($f_r, \Gamma, G_{max}, G_{off}, B_{off}, \phi$) have been used to numerically simulate, through Eq.10 and 11, both the sensor conductance and susceptance responses over the duration of the whole experiment at any required driving frequency. A custom software code has been developed for this purpose. Those six parameters have also been used to obtain the initial values of C_m and C_0 by using Eq. (12) to (15) in the main paper.

3) Resonance frequency and resonance half-bandwidth shifts provided by AWSFM method have been obtained from the emulated values of $G(\omega_t)$and $B(\omega_t)$ and from the initial estimation of C_m and C_0 by using Eq. (6) to (9) in the main paper. A custom software code has been developed for this purpose. FFD method equations proposed by Guha and co-workers [1] have also been implemented for comparison purposes.

Using this approach, we have been able to compare the performance of AWSFM-FF, AWSFM-T and FFD methods. Moreover, the offline processing has also allowed us to study the influence of small variations in the initial values of the testing frequency and C_0 parameter on the accuracy of the measured resonance frequency and resonance half-bandwidth shifts.

Two different experimental cases have been chosen to collect data required for our analysis: 1) a copper electrodeposition and 2) a water to water-glycerol mixture (25%) medium exchange. Experimental cases were selected with the aim of studying the performance of the characterization methods for different representative sensor

behaviors: a rigid layer contacting a Newtonian medium and a semi-infinite Newtonian medium exchange, respectively.

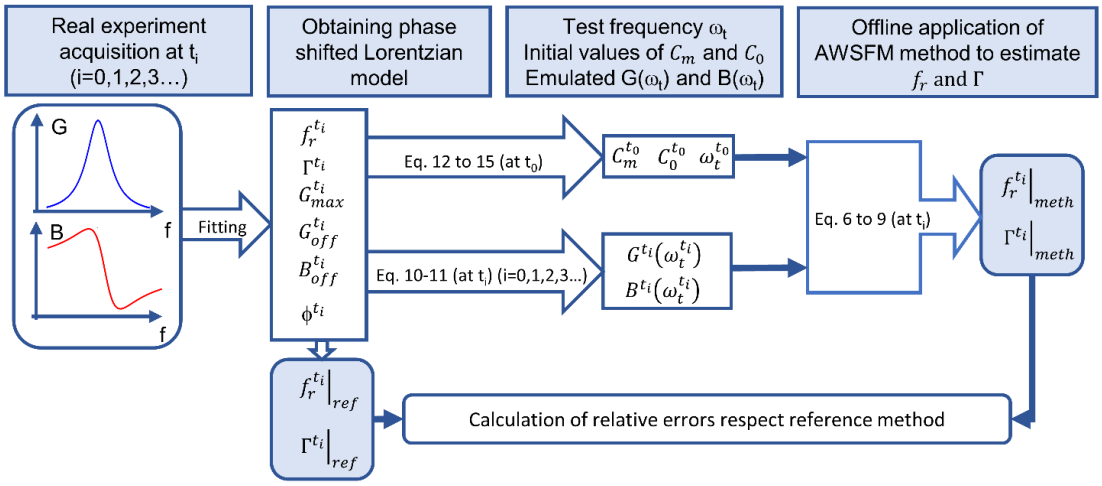

Fig S2. Flow diagram of the offline simulations performed.

S3. QUALITATIVE STUDY OF THE FREQUENCY SPECTRUM EVOLUTION

Dissipation or half-bandwidth information is a fundamental pillar to fully understand QCMD results and to properly interpret the phenomena occurring over the sensor surface. Effects such as viscoelastic and conformational changes [2]–[4], chemical and morphological properties of a surface, such as hydrophilicity, hydrophobicity, surface roughness and stress [5], [6], pressure or slip, are directly reflected on ΔΓ (or ΔR_m, or ΔD). From the parametric study described in SII, we have noticed that the fixed-frequency based implementation of AWSFM method (AWSFM-FF) fails to estimate accurately ΔΓ when changes in f_r are larger than changes in Γ, i.e., a rigid layer contacting a Newtonian medium experiment. However, AWSFM-FF offers good ΔΓ results when changes in Γ and f_r are similar, i.e., semi-infinite Newtonian medium exchange experiment.

We have carried out a qualitative study of the evolution of the sensor frequency response for both cases in order to deepen in our understanding of this phenomenon. Conductance spectra acquired for a water to water-glycerol mixture (25%) medium exchange experiment (red lines) and for a copper electrodeposition (blue lines) are depicted in Figure S3. These spectra are the fitted curves obtained with AWS X1 platform working in impedance spectroscopy mode.

Clear differences can be observed in the evolution of both experiments. Water to water-glycerol (25%) mixture medium exchange decreases considerably the resonance frequency while widening the conductance peak, following the typical Newtonian liquid behavior. However, copper electrodeposition causes a similar frequency shift but without distorting so much the peak shape. As both experiments progress over time $f_{G_{max}}$, value is changing because of the process taking place on the sensor surface; thus, moving apart from the testing frequency that has been set to initial $f_{G_{max}}$ value. Although the shift in frequency value is similar in both experiments, there is an important difference between the two cases. Driving frequency remains well inside the conductance 3dB range along the whole medium exchange experiment while it is almost outside in the case of the copper electrodeposition last spectrum (t_2).

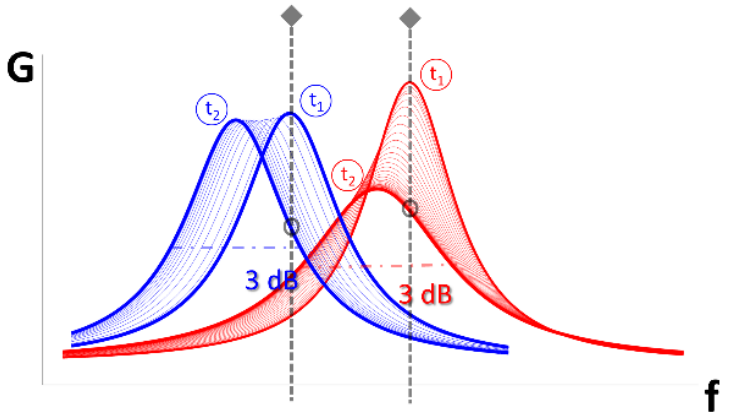

Fig. S3. Conductance spectra acquired for a water to water-glycerol mixture (25%) medium exchange experiment (red lines) and for a copper electrodeposition (blue lines). Circles tagged with t1 legend mark the first spectrum acquired while circles tagged with t2 indicate the spectrum at the end of the experiment. Black dotted lines mark the driving frequency at which the sensor is being excited in AWSFM-FF method for each experiment. Black circles represent the conductance value at the testing frequency for the last acquired spectrum.

Numerically, conductance measured at the testing frequency, $G(\omega_t)$, keeps a value around 200% higher than the 3dB limit for the last spectrum (t2) of the medium exchange experiment. On the other hand, $G(\omega_t)$is hardly 11.5% higher than the 3dB limit for the last spectrum (t_2) of the copper electrodeposition experiment. This is a consequence of the spectrum widening in the former case. Considering Figure S3 and our results in the parametric study (see S4 to S7 of this document), we think there is a direct relation between the accuracy of the fixed-frequency method and the relative proximity of the testing frequency to $f_{G_{max}}$ in terms of 3dB spans. Absolute distance in frequency seems not to be so relevant as the monitored region of the conductance spectrum. The closer the testing frequency is to leave the 3dB bandwidth the higher the error.

S4. INFLUENCE OF THE WORKING FREQUENCY SELECTION ON THE CHARACTERIZATION METHODS ACCURACY

We have analyzed the influence of the testing frequency selection in the accuracy of the resonance frequency and half-bandwidth determination using the simulation approach described in section SII. Since AWSFM-T is directly based on the continuous update of the testing frequency, we just calculated the influence of ft selection for AWSFM-FF and FFD methods. Four different testing frequencies have been evaluated: 1) $f_{G_{max}}$, 2) $f_{G_{max}}$ shifted half 3 dB span, 3) $f_{G_{max}}$ shifted one 3 dB span and 4) $f_{G_{max}}$ shifted two 3 dB spans. Relative error has been calculated with respect to the absolute values of Γ and f_r obtained from real experimental data in the third overtone both for a semi-infinite Newtonian medium exchange experiment (water to water-glycerol (25%) mixture exchange) and for a rigid layer contacting a Newtonian medium experiment (copper electrodeposition experiments).

Figure S4 and Figure S5 show the error in ppm for AWSFM-FF and FFD methods, respectively. AWSFM-FF presents a very low error in f_r determination: less than 5 ppm in the worst case. Impact of the testing frequency selection is not high in this case. However, testing frequency selection is determinant in Γ error, which increases by an order of magnitude when testing frequency is selected 2 spans away from $f_{G_{max}}$. On the other hand, FFD method shows a strong dependence on the testing frequency for both Γ and f_r and for all the experimental cases. AWSFM-FF Γ error turns from 5221 ppm to 72656 ppm when the frequency is selected two 3 dB spans away from the optimal $f_{G_{max}}$ in the water-glycerol exchange. FFD method Γ error turns from 82178 ppm to 625480 ppm in the same case.

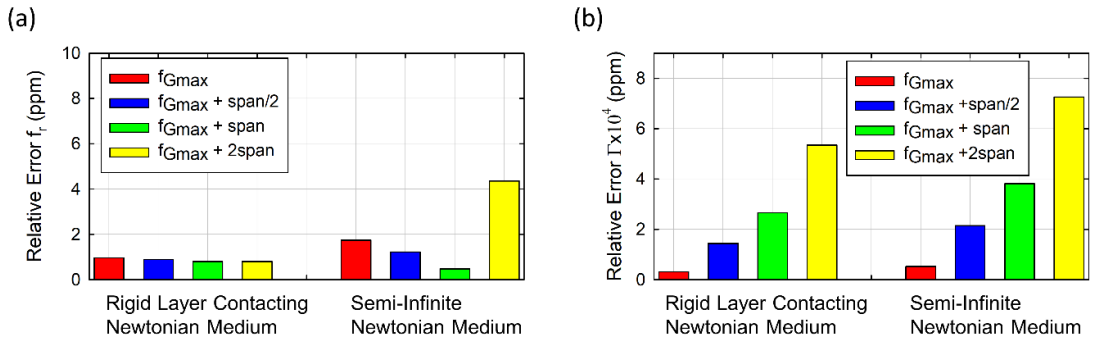

Fig. S4. AWSFM-FF method relative error vs driving frequency selection for: (a) f_r and (b) Γ.

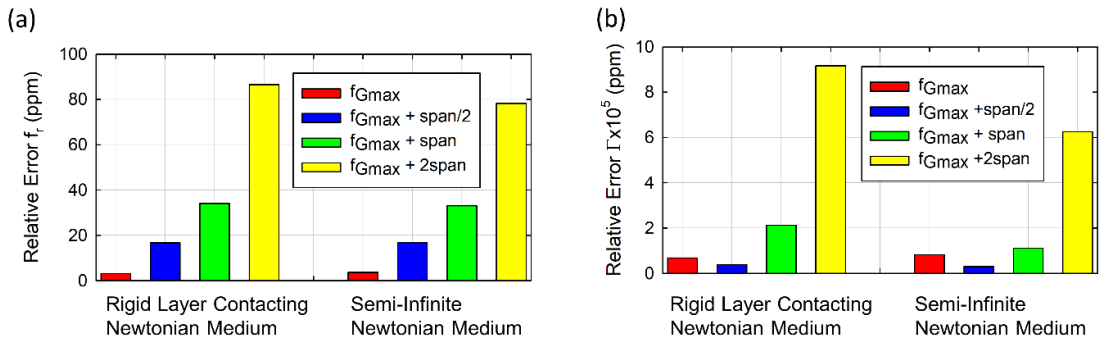

Fig. S5. FFD method relative error vs driving frequency selection for: (a) f_r and (b) Γ

S5. Influence Of The Electrical Artefacts On The Characterization Methods Accuracy

We have analysed the relevance of accounting for parasitic capacitance effects in the experimental setup on AWSFM-FF, AWSFM-T and FFD method accuracy. C_0 is especially sensitive to the parasitic capacitances produced by calibration issues, wires, connectors and electrical contacts in the measurement cells and it is normally responsible of most electrical artefacts affecting the sensor response. We have calculated the influence of small variations in the initial value of C_0 on the error in the determination of resonance frequency and half-bandwidth. Four different C_0 values have been evaluated: 1) C_0 obtained from the initial parameters (C_0^0), 2) a deviation of 1%, 3) a deviation of 3% and 4) a deviation of 5%.

Relative error has been calculated with respect to the absolute values of Γ and f_r obtained from real experimental data both for a semi-infinite Newtonian medium exchange experiment (water to water-glycerol (25%) mixture exchange) and for a rigid layer contacting a Newtonian medium experiment (copper electrodeposition experiments) in the third overtone.

Figure S6, Figure S7 and Figure S8 show the error in ppm for AWSFM-T, AWSFM-FF and FFD method, respectively. Our results show that the influence of the initial value of C_0 in the resonance frequency accuracy is relatively low for the three methods. It is interesting to note that frequency error tends to increase as C_0 deviates from its initial value for AWSFM-FF and AWSFM-T methods while FFD error is less dependent on C_0 variations. We think that this behavior is due to the nature of the equations used to calculate the resonance frequency by the different methods. AWSFM equation requires

admittance values as input data and C_0 is used in the calculation. However, FFD equation requires impedance values as input data and C_0 is subtracted from the sensor impedance at the very first calculation step.

In the case of the determination of the half bandwidth, error caused by C_0 variations is not negligible. Concretely, in AWSFM-T method applied to the copper electrodeposition experiment, half bandwidth relative error increases from 761 ppm to 1646 ppm when the C_0 value changes 5%. For the same experimental case, half bandwidth relative error in AWSFM-FF increases from 3154 ppm to 13954 ppm. In the case of FFD method, since the error in Γ determination is larger than in the other methods, the influence of C_0 variation on this error is not so pronounced. A 5% change in C_0 turns the error from 82178 ppm to 91797 ppm.

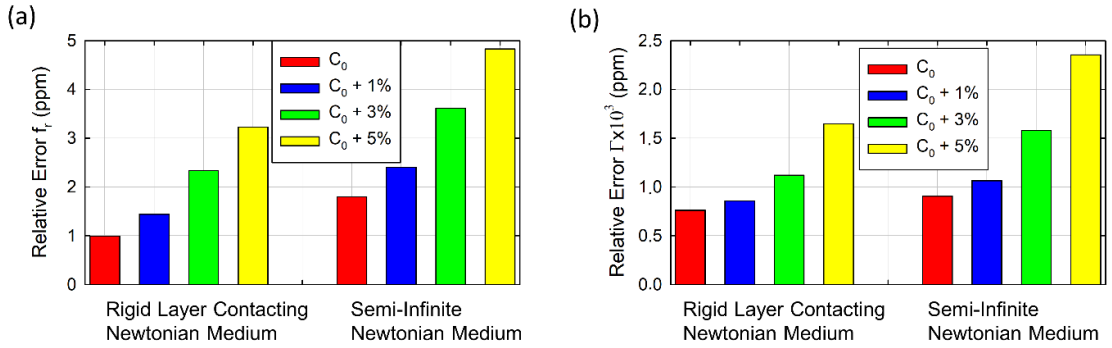

Fig. S6. AWSFM-T method relative error vs C0 selection for: (a) f_r and (b) Γ.

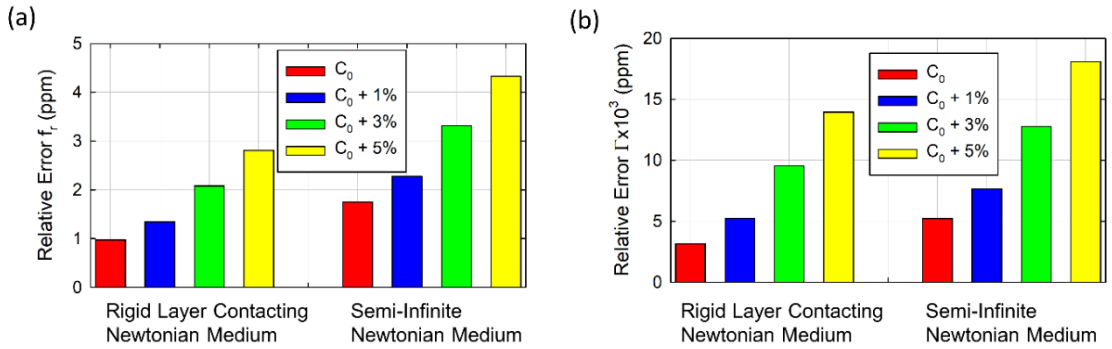

Fig. S7. AWSFM-FF method relative error vs C0 selection for: (a) f_r and (b) Γ.

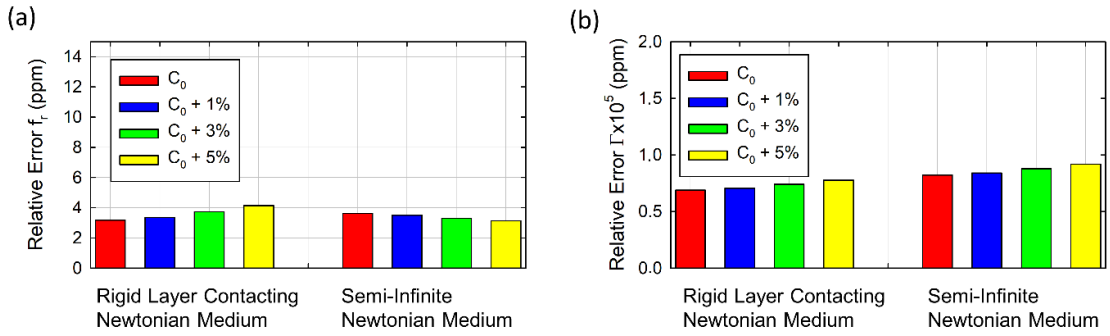

Fig. S8. FFD method relative error vs. C0 selection for: (a) f_r and (b) Γ.

References

[1] A. Guha, N. Sandström, V. P. Ostanin, W. van der Wijngaart, D. Klenerman, and S. K. Ghosh, "Simple and ultrafast resonance frequency and dissipation shift measurements using a fixed frequency drive," Sensors Actuators B Chem., vol. 281, pp. 960–970, Feb. 2019.

[2] G. A. McCubbin et al., "QCM-D fingerprinting of membrane-active peptides," Eur. Biophys. J., vol. 40, no. 4, pp. 437–446, 2011.

[3] G. Papadakis, A. Tsortos, and E. Gizeli, "Acoustic characterization of nanoswitch structures: Application to the DNA holliday junction," Nano Lett., vol. 10, no. 12, pp. 5093–5097, 2010.

[4] M. Saitakis, A. Tsortos, and E. Gizeli, "Probing the interaction of a membrane receptor with a surface-attached ligand using whole cells on acoustic biosensors," Biosens. Bioelectron., vol. 25, no. 7, pp. 1688–1693, 2010.

[5] L. Tan et al., "Dynamic measurement of the surface stress induced by the attachment and growth of cells on Au electrode with a quartz crystal microbalance," Biosens. Bioelectron., vol. 24, no. 6, pp. 1603–1609, 2009.

[6] M. Saitakis and E. Gizeli, "Acoustic sensors as a biophysical tool for probing cell attachment and cell/surface interactions," Cell. Mol. Life Sci., vol. 69, no. 3, pp. 357–371, 2012.

Appendix C

Supporting Information

S1. Monolithic 150 MHz HFF-QCMD sensor arrays

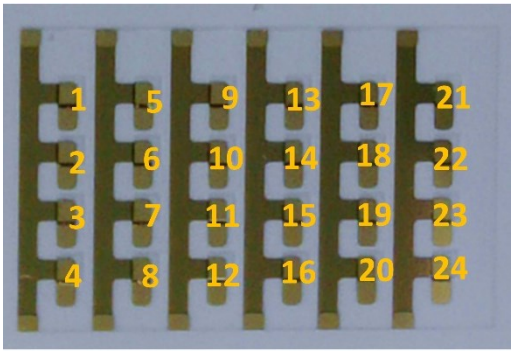

Figure S1. Monolithic 150 MHz HFF-QCMD sensor arrays. Numbers indicate the i-th element of the array, where i = r +4(c – 1) with r = 1-4 and c = 1-6 row and column indexes, respectively.

S2. Protein Adsorption and Interaction Studies

TABLE S1. QUANTIFICATION OF ADSORBED PROTEIN MASSES.

Step	Protein	Array Δm, ng/cm²	HFF Δm, ng/cm²	Protein	Array Δm, ng/cm²	HFF Δm, ng/cm²
1	Nav	700 ± 180 (23)	590 ± 200 (12)	bBSA	75 ± 73 (16)	120 ± 100 (12)
	BSA	20 ± 30 (23)	9 ± 5 (12)	BSA	230 ± 58 (16)	70 ± 42 (10)
	bBSA	340 ± 60 (15)	250 ± 70(12)	Nav	470 ± 60 (16)	390 ± 180 (12)
	BSA	24 ± 5 (15)	8 ± 5 (12)	BSA	– 11 ± 11 (8)	6 ± 4 (12)
2	Nav	780 ± 120 (23)	700 ± 120 (12)	bBSA	215 ± 34 (16)	220 ± 60 (12)
	BSA	11 ± 10 (23)	6 ± 4 (12)	BSA	29 ± 17 (16)	6 ± 4 (12)
	bBSA	250 ± 50 (23)	220 ± 50 (12)	Nav	670 ± 60 (16)	670 ± 190 (11)
	BSA	3 ± 14(23)	8 ± 5 (12)	BSA	11 ± 7 (16)	6 ± 5 (12)
3	Nav	650 ± 30 (15)	770 ± 140 (12)	bBSA	250 ± 26 (16)	220 ± 60 (12)
	BSA	8 ± 11(15)	6 ± 4 (12)	BSA	6 ± 9 (16)	7 ± 5 (12)
	bBSA	190 ± 37 (15)	280 ± 60 (8)	Nav	700 ± 26 (8)	660 ± 200 (11)

Masses of the surface-adsorbed proteins calculated using the Sauerbrey [1] relationship from the frequency shifts for the arrays and the individual HFF resonators. On each type of sensor, the measurements were performed in two directions: starting from Nav (left columns) and starting from bBSA (right columns). Errors are standard deviations, number of individual measurements in the averages are shown in brackets. The data correspond to the plots shown in Figure 3 of the main manuscript.

TABLE S2. LITERATURE VALUES FOR THE DIMENSIONS AND ADSORBED LAYER MASSES FOR BSA, BBSA, AND NAV.

	QCMD adsorbed layer masses [ng/cm²]				Dimensions [nm][a]	Expected mass [ng/cm²][b]
Surface	**Gold[c]**	**bSLB[c]**	**bSAM**	**MUASAM[c]**		
Nav	707 < [c]; 908 – 1261[d]	566 < [c]	N/D	N/D	6 × 5 × 4	460 – 650
Sav	530 ± 35 [c]; 540 [e], 447 [e]	495 ± 35 [c]	446 ± 27 [f]	575 ± 10 [f]		
Surface	**Gold**	**Nav on gold**	**Nav on bSLBs**			
BSA	535 ± 92 [g] ;532h; ~ 450[i]	N/A	N/A	~ 450[i]	3 × 4 × 8	344 – 917
bBSA	Table S1	> 177 [c]	168 ± 18[c]	N/A		

[a] Sizes per molecule were directly obtained from the protein crystallographic dimensions, pdb codes 2avi and 4f5s for avidin and albumin, respectively. Both proteins are ~ 66 kDa. [b] Expected masses were calculated for the three different orientations assuming a homogeneous protein layer of a given height and a density ~ 1.15 g/cm³ [2]. This approach takes into account that QCMD senses solvated, as opposed to dry, mass [3] and works well for streptavidin (Sav), where the corresponding dry masses that have been measured by SPR [4,5] and ellipsometry [6], are ~ 200 – 380 ng/cm² for

the oriented and random adsorption of streptavidin on biotinylated lipid layers or SAMs, respectively. [c] Wolny et al. [7]; [d] Boujday et al. [8]; Tsortos et al. [9,10]; Hays et al. [11]; Kasper et al. [12]; [e] Höök et al. [2]; Larsson et al. [4]; [f] Su et al. [5]; [g] Reimhult et al. [13]; [h] Min et al. [14]; [i] Thourson et al. [15]; N/A: not applicable. N/D: not determined.

It is interesting to examine the ratios of adsorbed bBSA mass to the mass of the adsorbed Nav. In the case of the Nav adsorbed on gold followed by the adsorption of bBSA, the ratio is (340 ng/cm^2 / 700 ng/cm^2) ~ 0.48 (Table S1).

Given the mass of Sav adsorbed on gold of ~ 530 ng/cm^2 and molecular dimensions of ~ 6x5x4 nm (Table S2), the expected area per molecule is ~ 24 nm^2. Furthermore, assuming that the packing density of the molecules on gold is given by the two-dimensional random sequential adsorption (RSA) model, ~ 0.547 [14], the area per molecule corrected for the RSA packing density is ~ 43 nm^2 (the distance between the molecules is ~ 3.7 nm).

The dimensions of BSA are 3x4x8 nm, giving an area per molecule of 32 nm^2 in the orientation of the protein that is consistent with the adsorbed mass of 340 ng/cm^2, and the smallest distance between the molecules of ~ 3.2 nm. Here, we assume that bBSA does not change conformation upon adsorbing to Nav.

What this means is that it is not possible for every Nav molecule adsorbed on gold to be occupied with an adsorbing bBSA molecule. It is more likely, that only every other molecule of Nav is occupied, explaining the observed ratio of ~ 0.48.

In this analysis, we used the adsorbed mass of Sav because it is unaffected by aggregation, unlike Nav; this allows a reasonable calculation of the area per molecule in the surface plane. One can perform identical analysis for the mass of bBSA adsorbed on Sav layers from ref. [7]: for the Sav on bSLBs, the ratio of bBSA to Sav masses is again ~ 0.48. In the case of Sav on gold, it is ~ 0.42. The occupancy is lower in the second case. This is because the adsorbed mass of Sav is larger, and the adsorbed mass of bBSA is smaller, than in the case of Sav adsorbing on bSLBs. Both are explained by the fact that Sav adsorbs on gold in multiple orientations, as explained in the main text of the paper; not all of the orientations have biotin sites accessible for bBSA binding.

The analysis of the ratio of adsorbed Nav mass to bBSA mass adsorbed on gold (470 / 75 ~ 6.3) is complicated by the likely change in the bBSA conformation (as compared to that of BSA) and the associated difficulties with calculating the area per molecule. On the other hand, on average, the ratio of Nav to bBSA adsorbed masses, excluding this first step, is ~ 3. This agrees well with the ratio of the limiting values of the adsorbed bBSA

and Nav masses, (230 ng/cm^2 and 700 ng/cm^2 ~ 0.33). Therefore, away from the gold surface, approximately 3 Nav molecules attach to every bBSA molecule.

S3. Peclet Numbers and Depletion Layer Thickness

Peclet numbers are a class of dimensionless numbers relevant in the study of mass transport phenomena. P_{e_H} refers to the Peclet number in the channel height direction and relates the rate of convection of a physical quantity by the flow to the rate of diffusion of the same quantity [16]:

$$Pe_H \equiv \frac{diffusive\ time}{convective\ time} \sim \frac{(2\mathrm{R})^2/D}{(2\mathrm{R})^2 2\mathrm{W}/Q} = \frac{Q}{D2W} \quad \text{(S1)}$$

Where Q is the flow rate, D is the target molecule diffusivity, 2R is the channel height and 2W is the channel width. If $P_{e_H} \gg 1$ convection dominates over diffusion, enhancing the mass transport and avoiding the propagation of the depletion layer. If $P_{e_H} \ll 1$, then diffusion dominates, and a depletion layer can propagate upwards in the flow. In our current design, width of the channel is mainly constrained by the spacing between HFF-QCM sensor columns in the array to 2W=1.46 mm. Maximum flow rate is limited by the fragility of the resonators to 100 µL/min. Commonly used samples in bioanalytic applications include proteins, antibodies, DNA or RNA. Diffusivity constant of these biomolecules varies widely in the range of 0.1 to 100 µm^{2}s^{-1}. Table S3 shows P_{e_H} calculated for different flow rates and analytes. As it can be observed, it is way larger than 1 for all the molecules and flow rates investigated.

TABLE S3. P_{e_H} CALCULATED FOR DIFFERENT FLOW RATES AND BIOMOLECULES.

	Diffusivity (µm²s⁻¹)	**Peн (Q=15µl min⁻¹)**	**Peн (Q=50µl min⁻¹)**	**Peн (Q=100µl min⁻¹)**
Neutravidin [17]	60	2854	9513	19026
BSA,66 kDa, 4 nm [18]	90	1903	6342	12684
Liposomes 20 nm [18]	25	6849	22831	45662
mRNA (various sizes) max	1	171233	570776	1141553
DNA (2311 bp) [19]	4,56	37551	125170	250340
DNA (762 bp) [19]	9,05	18921	63069	126138

A second Peclet number, P_{e_S},can be used to estimate the thickness of the depletion layer, δ_s [16]:

$$\delta_s \sim \frac{L_s}{Pe_S^{1/3}} \quad \text{(S2)}$$

P_{e_S} can be calculated according to next equation [16]:

$$Pe_S = 6\lambda^2 Pe_H \quad \text{(S3)}$$

Where, λ is the ratio $\lambda = L_s/2R$ where Ls is sensor length in the flow direction and 2R the channel height. Our HFF-QCM sensors have a lateral dimension of L_s=550 μm. Regarding the cartridge channel height, 2R, it is given by the thickness of the PDMS gasket (480 μm). Since PDMS is an elastic material, it is difficult to determine exactly its final thickness once the different parts of the cartridge are assembled and tightened. Table S4 shows P_{e_S} and δ_s values in two cases: (1) assuming no gasket deformation (2R=480 μm) and (2) assuming 20% gasket deformation (2R=380 μm).

TABLE S4. Pe_S CALCULATED FOR DIFFERENT GASKET DEFORMATION.

2R (μm)	Pe_S	Depletion layer thickness (μm)
480	29975,6	17,7
380	47828,2	15,1

References

[1] Sauerbrey, G. Verwendung von Schwingquarzen zur Wägung dünner Schichten und zur Mikrowägung. Zeitschrift für Phys. 1959, 155, 206–222.

[2] Höök, F.; Ray, A.; Nordén, B.; Kasemo, B. Characterization of PNA and DNA Immobilization and Subsequent Hybridization with DNA Using Acoustic-Shear-Wave Attenuation Measurements. Langmuir 2001, 17, 8305–8312.

[3] Reviakine, I.; Johannsmann, D.; Richter, R.P. Hearing What You Cannot See and Visualizing What You Hear: Interpreting Quartz Crystal Microbalance Data from Solvated Interfaces. Anal. Chem. 2011, 83, 8838–8848.

[4] Larsson, C.; Rodahl, M.; Höök, F. Characterization of DNA Immobilization and Subsequent Hybridization on a 2D Arrangement of Streptavidin on a Biotin-Modified Lipid Bilayer Supported on SiO 2. Anal. Chem. 2003, 75, 5080–5087.

[5] Su, X.; Wu, Y.-J.; Robelek, R.; Knoll, W. Surface Plasmon Resonance Spectroscopy and Quartz Crystal Microbalance Study of Streptavidin Film Structure Effects on Biotinylated DNA Assembly and Target DNA Hybridization. Langmuir 2005, 21, 348–353.

[6] Reiter, R.; Motschmann, H.; Knoll, W. Ellipsometric characterization of streptavidin binding to biotin-functionalized lipid monolayers at the water/air interface. Langmuir 1993, 9, 2430–2435.

[7] Wolny, P.M.; Spatz, J.P.; Richter, R.P. On the Adsorption Behavior of Biotin-Binding Proteins on Gold and Silica. Langmuir 2010, 26, 1029–1034.

[8] Boujday, S.; Bantegnie, A.; Briand, E.; Marnet, P.G.; Salmain, M.; Pradier, C.M. In-depth investigation of protein adsorption on gold surfaces: Correlating the structure and density to the efficiency of the sensing layer. J. Phys. Chem. B 2008, 112, 6708–6715.

[9] Tsortos, A.; Papadakis, G.; Gizeli, E. Shear acoustic wave biosensor for detecting DNA intrinsic viscosity and conformation: A study with QCM-D. Biosens. Bioelectron. 2008, 24, 836–841.

[10] Tsortos, A.; Papadakis, G.; Gizeli, E. Acoustic wave biosensor for detecting DNA conformation; A study with QCM-D. In Proceedings of the 2008 IEEE International Frequency Control Symposium; IEEE, 2008; Vol. 24, pp. 346–349.

[11] Hays, H.C.W.; Millner, P.A.; Prodromidis, M.I. Development of capacitance based immunosensors on mixed self-assembled monolayers. Sensors Actuators B Chem. 2006, 114, 1064–1070.

[12] Kasper, M.; Traxler, L.; Salopek, J.; Grabmayr, H.; Ebner, A. Broadband 120 MHz Impedance Quartz Crystal Microbalance (QCM) with Calibrated Resistance and Quantitative Dissipation for Biosensing Measurements at Higher Harmonic Frequencies. 2016, 1–13.

[13] Reimhult, K.; Petersson, K.; Krozer, A. QCM-D Analysis of the Performance of Blocking Agents on Gold and Polystyrene Surfaces. Langmuir 2008, 24, 8695–8700.

[14] Min, H.; Freeman, E.; Zhang, W.; Ashraf, C.; Allara, D.; van Duin, A.C.T.; Tadigadapa, S. Modified Random Sequential Adsorption Model for Understanding Kinetics of Proteins Adsorption at a Liquid–Solid Interface. Langmuir 2017, 33, 7215–7224.

[15] Thourson, S.B.; Marsh, C.A.; Doyle, B.J.; Timpe, S.J. Quartz crystal microbalance study of bovine serum albumin adsorption onto self-assembled monolayer-

functionalized gold with subsequent ligand binding. Colloids Surfaces B Biointerfaces 2013, 111, 707–712.

[16] Squires, T.M.; Messinger, R.J.; Manalis, S.R. Making it stick: convection, reaction and diffusion in surface-based biosensors. Nat. Biotechnol. 2008, 26, 417–426.

[17] Wayment, J.R.; Harris, J.M. Biotin−Avidin Binding Kinetics Measured by Single-Molecule Imaging. Anal. Chem. 2009, 81, 336–342.

[18] Osidak, E.O.; Osidak, M.S.; Akhmanova, M.A.; Domogatskii, S.P. Collagen — A Biomaterial for Delivery of Growth Factors and Tissue Regeneration. Russ. J. Gen. Chem. 2014, 84, 102–113.

[19] Pecora, R. Model Compound for Solution. Science (80-.). 1991, 251, 893–898.

Appendix D

Supporting Information

S1. Wavelet Daubechies transform

Direct and inverse wavelet transform is applied in the method presented. Concretely, a Daubechies wavelet transform with three vanishing moments (db3) and 4 decomposition levels is used [1]. Figure S1 shows the Mallat scheme used for signal decomposition and reconstruction. The decimation process previous to each stage reduces the number of samples in the subsequent stage by a factor of 2.

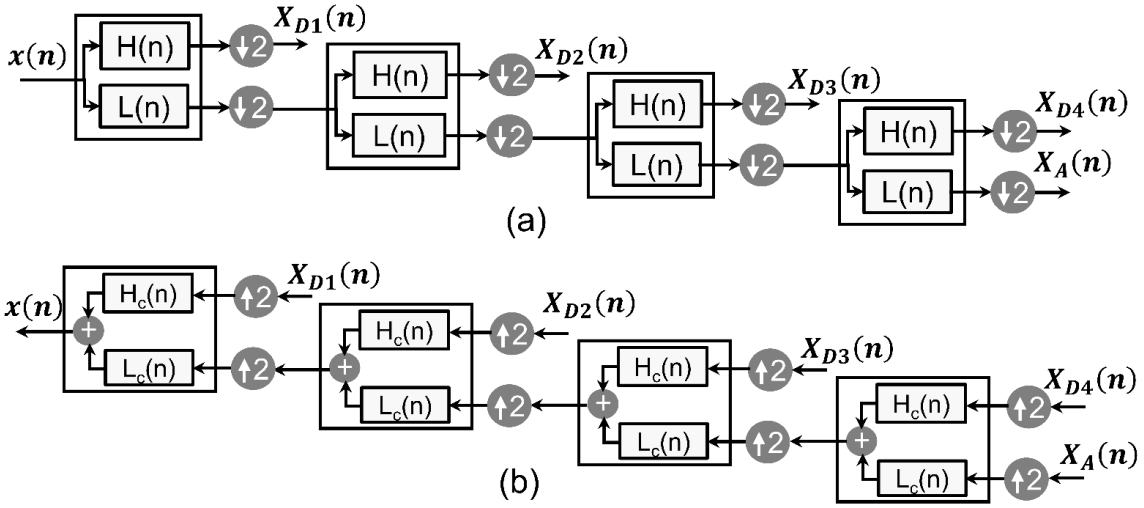

Figure S1. Mallat tree decomposition (a) and reconstruction (b) schemes implemented. H(n) and L(n) represent the high and low frequency decomposition filters respectively. H_c (n) and L_c (n) represent the high and low frequency reconstruction filters respectively. $X_A(n)$ refers to the approximation coefficient expansion and $X_{Dq}(n)$ represent the detail coefficient expansions of the different decomposition levels q. ↑2 symbol represents an interpolation operation by a factor of 2 while ↓2 represents a decimation by a factor of 2.

S2. Energy distribution of DWT coefficients

Table S1 shows the energy contribution of each DWT coefficient to the total wavelet transform energy in a typical protein adsorption experiment. Energy is clearly concentrated in the approximation coefficient $X_A(n)$, since the main components of its spectrum are located in low frequency subband.

TABLE S1. ENERGY DISTRIBUTION OF THE DIFFERENT DWT COEFFICIENTS OF Δf_r AND ΔD MONITORED IN A TYPICAL PROTEIN ADSORPTION EXPERIMENT

	$X_A(n)$	$X_{D1}(n)$	$X_{D2}(n)$	$X_{D3}(n)$	$X_{D4}(n)$
Δf_r (%)	99.9998	$9.2\cdot10^{-5}$	$6.1\cdot10^{-5}$	$4.6\cdot10^{-5}$	$4.46\cdot10^{-5}$
ΔD (%)	99.9947	0.0022	0.0014	0.0009	0.0008

S3. Experimental Setup

This section details the Monolithic QCM setup used in the real time monitoring of the protein adsorption experiment. Figure S2 (a) and (b) show top and bottom surfaces of the MQCM device, respectively. Array consists of 6 columns of 4 HFF-QCM resonator elements each. Array elements are based on a 50 MHz one-sided inverted MESA geometry and are optimized in terms of size and electrode geometry to facilitate manufacturing and integration with fluidics and electronics, spurious mode suppression, and operation in liquids. The top electrode is grounded, and it is common to all 24 array elements. This common electrode constitutes the "working" side of the array. It faces the sample. On the other side of the array, the short rectangular electrodes are connected to the driving circuitry individually.

Figure S2 (c) shows the array mounted in the flow measurement cell. Measurement cell is divided into 6 independent flow channels covering 4 sensors each. Each channel has an inlet and an outlet that can be connected to flow tubing through steel cannulas. Flow connections of the array sensor measurement cell were configured to create two separate flow regions with 12 sensors each. Region *R* contains the *reference* resonators while Region *S* contains the resonators operating as *sensors*. Figure S2 (b) and (c) show a schematic representation of both regions, *R* region columns are imbricated with *S* region columns to achieve a configuration in which each sensor has a reference one aside.

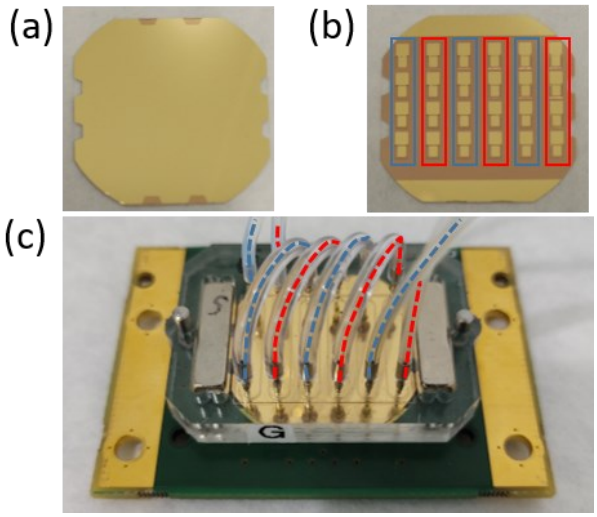

Figure S2. (a) Top and (b) bottom surfaces of the Monolithic QCM device. (c) MQCM device mounted in the flow cell. A blue dotted line is used to mark the tubing of region *R* that comprises 12 *reference* resonators while a red dotted line is used to mark the tubing of region *S* that comprises 12 resonators operating as *sensors*.

S4. Control Experiments

A set of control experiments were carried to determine the response of the NAv and bBSA protein under controlled conditions. Instrument temperature was set to 23 °C and flow rate was configured to be 20 µL/min. Figure S3 shows monitored resonance frequency and dissipation shifts at 4 different sensors integrated in the same channel of a MQCM device.

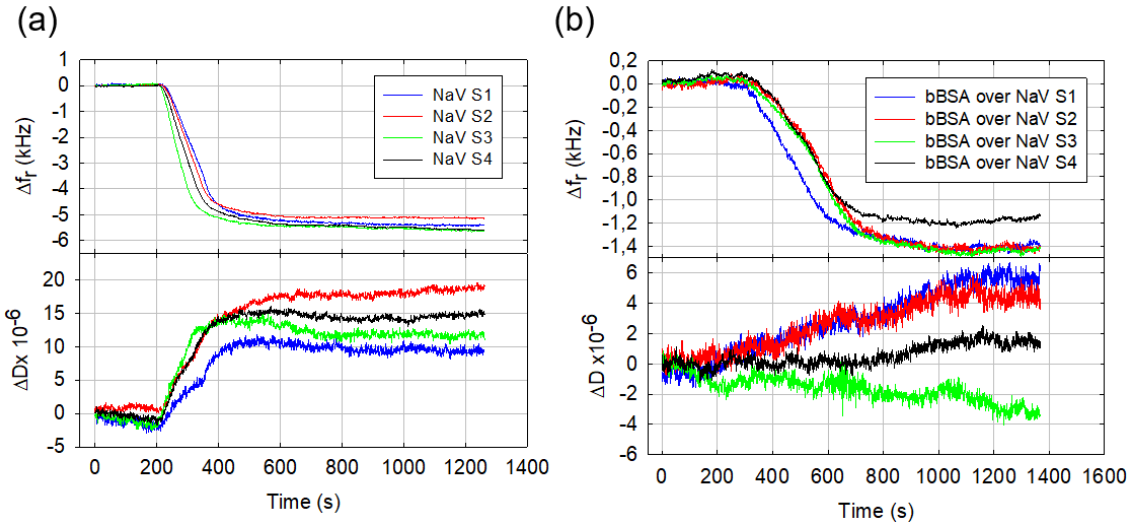

Figure S3. (a) Resonance frequency (top) and dissipation (bottom) shifts acquired in 4 HFF-QCMD sensors integrated in a MQCM channel during a NAv over gold adsorption experiment. (b) Resonance frequency (top) and dissipation (bottom) shifts acquired in 4 HFF-QCMD sensors integrated in a MQCM channel during a bBSA over NAv adsorption experiment.

Refences

[1] Mallat, S. A Wavelet Tour of Signal Processing; 2008;

Appendix E

S1. Immunoassay optimization. Comparison with individual HFF-QCM resonators.

Table S1. Optimal monoclonal antibody and conjugate assay concentrations for individual 100MHz HFF-QCMD sensors and for the 50MHz HFF-QCMD array.

Analyte	Antibody concentration (µg/mL)		Conjugate concentration (µg/mL)	
	Array	Individual	Array	Individual
Thiabendazole	1	1	5	20
Sulfathiazole	2	2	10	5

While optimal antibody concentration was the same for both analytes, conjugate concentrations differed from those of the individual. For TBZ, the concentration was four times smaller in the array than in the individual. In the case of SFZ, the concentration in the array doubled that use in the individual sensors.

S2. Immunoassay sensitivity with individual sensors

The calibration curve for PBS with MHFF-QCM (not shown) provided the analytical immunoassay parameters shown in Table S2. The table also contains those obtained for the individual sensors [1]. In this case, results are more similar for both technologies. Although lower resonance frequency would lead to an increase of the LOD and/or I_{50} parameters, a significant reduction of conjugate concentration in the array functionalization (5 µg/mL), as compared with that of the individual sensor (20 µg/mL), would lead to an improvement (decrease) of these parameters. This balance could explain the similarities in the results.

Table S2. Immunosensor analytical parameters for TBZ in PBS. Comparison between individual HFF-QCMD and HFF-QCMD array.

	Individual (µg/L)	Array (µg/L)
I_{50}	0.8	0.98
LOD	0.06	0.2
LOQ	0.16	0.33
WR	0.16 a 3.68	0.33 a 3

S3. Spiked honey samples with both compounds

Table S3. Spiked honey samples with both compounds.

Spiked level	SFZ (µg/kg)	TFZ (µg/kg)	Detected (µg/kg)	Recovery (%)	CV (%)	Detected (µg/kg)	Recovery (%)	CV (%)
			SFZ analyte			**TBZ analyte**		
0×LoD	0	0	<LOD	No false positives		<LOD	No false positives	
1×LoD	53	31	59±14	112	25	40±3	130	8
2×LoD	105	62	97±23	92	24	89±6	143	7
3×LoD	264	156	324±42	122	13	135±30	87	22
5×LoD	529	313	502±75	94	14	297±89	95	30

* Average of 8 independent determinations for HFF-QCM and 6 independent replicates for LC-MS/MS came from the same original honey sample
[1] Sample dilution factor 1/100

References

[1] L. Cervera-Chiner, Y. Jiménez, Á. Montoya, M. Juan-Borrás, N. Pascual, A. Arnau, I. Escriche, High Fundamental Frequency Quartz Crystal Microbalance (HFF-QCMD) Immunosensor for detection of sulfathiazole in honey, Food Control. 115 (2020) 107296. doi:10.1016/j.foodcont.2020.107296.

6. Scientific communications and training activities

Journal Publications

1. El Fissi, L.; Fernández, R.; García, P.; Calero, M.; García, J.V.; Jiménez, Y.; Arnau, A.; Francis, L.A. OSTEMER polymer as a rapid packaging of electronics and microfluidic system on PCB. Sensors Actuators, A Phys. 2019, 285.
2. Fernandez, R.; Calero, M.; Reviakine, I.; Garcia-Narbon, J.V.; Rocha-Gaso, M.I.; Arnau, A.; Jimenez, Y. High Fundamental Frequency (HFF) Monolithic Resonator Arrays for Biosensing Applications: Design, Simulations, and Experimental Characterization. IEEE Sens. J. 2021, 21.
3. Calero, M.; Fernández, R.; García, P.; García, J.V.; García, M.; Gamero-Sandemetrio, E.; Reviakine, I.; Arnau, A.; Jiménez, Y. A Multichannel Microfluidic Sensing Cartridge for Bioanalytical Applications of Monolithic Quartz Crystal Microbalance. Biosensors 2020, 10.
4. Fernandez, R.; Calero, M.; Garcia-Narbon, J.V.; Reiviakine, I.; Arnau, A.; Jimenez, Y. A Fast Method for Monitoring the Shifts in Resonance Frequency and Dissipation of the QCM Sensors of a Monolithic Array in Biosensing Applications. IEEE Sens. J. 2021, 21.
5. Fernández, R.; Calero, M.; Jiménez, Y.; Arnau, A. A real-time method for improving stability of monolithic quartz crystal microbalance operating under harsh environmental conditions. Sensors 2021, 21.
6. N. Naoumi et al., "Acoustic Array Biochip Combined with Allele-Specific PCR for Multiple Cancer Mutation Analysis in Tissue and Liquid Biopsy," ACS Sensors, p. acssensors.1c02245, Jan. 2022.
7. Calero, M.; Fernández, R.; García, M.; Juan-Borrás, M.; Escriche, I.; Arnau, A.; Montoya, A; Jiménez, Y. High Fundamental Frequency (HFF) Monolithic Resonator Array for the simultaneous detection of pesticides and antibiotics in complex food. Analytica Chemical Acta: **under review**.

Poster in International Congress

María Calero, Román Fernández, Pablo García, José V. García, Yolanda Jiménez, Antonio Arnau, "A PoCT microfluidic device based on monolithic HFF-QCM sensor array", 7th International Symposium on Sensor Science, Naples, Italy, May 2019

Poster in National Congress

María Calero, Román Fernández, María García, Ángel Montoya, Yolanda Jiménez, Antonio Arnau, “Inmunosensor basado en un array HFF-QCM para la detección multianalito de residuos en alimentos”, Congreso Anual de la Sociedad de Ingeniería Biomédica (CASEIB 2020), Virtual Edition, November 2020

Patent

Fernández Díaz, R.; García Narbón, J. V.; Calero Alcarria, M.; Jiménez Jiménez, Y.; Arnau Vives, A. “Método para la caracterización de la respuesta de sensors resonantes” Application Number: P202030810.

Fernández Díaz, R.; García Narbón, J. V.; Calero Alcarria, M.; Jiménez Jiménez, Y.; Arnau Vives, A. “Dispositivo y procedimiento para la mejora de la estabilidad y el límite de detección de sensores de onda acústica” Application Number: P202130351.

Training Activities

1. Training stay at AWSensors company (spin-off of the Universitat Politècnica de València). The objective of the stay was the characterization of the array and the cartridge. During this stay, the student was trained in the handle of specific instrumentation available in the facilities of the company's facilities, as well the use of the clean room.
2. Two training stays at Quartz Pro Sweden AB private company. The first stay was under the “attendance” modality. During this stay, the student was trained in the manufacturing process of quartz acoustic sensors. Additionally, some prototypes of a new sensor design were manufactured, and subsequently characterized. The student was also trained in the use of the equipment to perform quality control in a conventional manufacturing process. A second stay, under a “distance” modality, was made with the objective to characterize and analyse the behavior of the manufactured prototypes during the first stay.
3. Collaboration in teaching tasks: 280 hours in lab sessions of the course “Conversión y procesado de la Energía” and 40 hours of lab sessions of the course “Sistemas electrónicos de comunicaciones” both at Bachelor's Degree in Telecommunication Technologies and Services Engineering at Universitat Politècnica de València.
4. Some other training activities accomplished during the training period were:

“Métodos numericos con Matlab” (Numerical methods with Matlab)	20 hours
“Reescribiendo la ciencia. Como evitar errores en inglés científico escrito y hablado” (Rewriting science. How to avoid mistakes in written and spoken scientific English)	20 hours
“Documentación científica” (Scientific documentation)	20 hours
“Carrera investigadora” (Research career)	20 hours

LIST OF ABBREVIATIONS

DDT	Dichlorodiphenyltrichloroethane
EFSA	European Food Safety Authority
ELISA	Enzyme Linked Immunosorbent Assay
ESA	European Space Agency
EU	European Union
FAO	Food and Agriculture Organization
HFF-QCM	High Fundamental Frequency-QCM
HPLC	High-Performance Liquid Chromatography
HPLC-MS/MS	High-Performance Liquid Chromatography-Mass Spectrometry
MRL	Maximum Residue Limit
LoD	Limit of Detection
PcB	Polychlorinated biphenyls
QCM	Quartz Crystal Microbalance
RASFF	Rapid Alert System for Food and Feed
STZ	Sulfathiazole
TBZ	Thiabendazole
WHO	World Health Organization